

Washington University in St. Louis
Washington University Open Scholarship

Engineering and Applied Science Theses &
Dissertations

McKelvey School of Engineering


Summer 8-15-2018

Synthesis of Crumpled Graphene and Titanium Dioxide Based–Nanomaterials and the Application to Carbon Dioxide Photoreduction

Yao Nie

Washington University in St. Louis

Follow this and additional works at: https://openscholarship.wustl.edu/eng_etds

 Part of the [Chemical Engineering Commons](#), [Environmental Engineering Commons](#), [Materials Science and Engineering Commons](#), and the [Mechanics of Materials Commons](#)

Recommended Citation

Nie, Yao, "Synthesis of Crumpled Graphene and Titanium Dioxide Based–Nanomaterials and the Application to Carbon Dioxide Photoreduction" (2018). *Engineering and Applied Science Theses & Dissertations*. 376.
https://openscholarship.wustl.edu/eng_etds/376

This Dissertation is brought to you for free and open access by the McKelvey School of Engineering at Washington University Open Scholarship. It has been accepted for inclusion in Engineering and Applied Science Theses & Dissertations by an authorized administrator of Washington University Open Scholarship. For more information, please contact digital@wumail.wustl.edu.

WASHINGTON UNIVERSITY IN ST. LOUIS

School of Engineering and Applied Science

Department of Energy, Environmental and Chemical Engineering

Dissertation Examination Committee:

Pratim Biswas, Chair

John Fortner, Co-Chair

Rajan Chakrabarty,

Elijah Thimsen,

Wei-Ning Wang

Synthesis of Crumpled Graphene and Titanium Dioxide Based–Nanomaterials and the
Application to Carbon Dioxide Photoreduction

By

Yao Nie

A dissertation presented to
The Graduate School
of Washington University in
partial fulfillment of the
requirements for the degree
of Doctor of Philosophy

August 2018

St. Louis, Missouri

© 2018, Yao Nie

Contents

List of Figures.....	vii
List of Tables	xi
Acknowledgements	xii
Abstract.....	xv
Chapter 1 Introduction.....	1
1.1 Motivation.....	2
1.2 Key scientific gap	4
1.3 Objectives	7
Objective G1-Synthesis of crumpled graphene-based materials and study of their chemical and physical properties	7
Objective G2-Design and performance testing of graphene-TiO ₂ based CO ₂ photocatalysts	8
Objective G3-Kinetic model development and CO ₂ photoreduction performance prediction	9
1.4 Dissertation organization	9
Reference	13
Chapter 2 Mobility and Bipolar Diffusion Charging Characteristics of Crumpled Reduced Graphene Oxide Nanoparticles Synthesized in a Furnace Aerosol Reactor	16
Abstract.....	17
2.1 Introduction.....	18
2.2 Experimental section.....	21
2.2.1Material synthesis	21
2.2.2 Material characterization	22
2.3 Results and Discussion	29
2.3.1 Mobility study.....	29
2.3.2 Charging characteristics study.....	34
2.4 Conclusions.....	39
Acknowledgements.....	40

References.....	41
Chapter 2 Supporting Information.....	47
Chapter 3 Graphene Synthesized as by-Product of Gas Purification in Long-term Space Missions and its Lithium-ion Battery Application.....	53
Abstract.....	54
3.1 Introduction.....	55
3.2 Experimental section.....	58
3.2.1 Carbonaceous byproduct formation.....	58
3.2.2 Carbonaceous byproduct characterization.....	60
3.2.3 Application of the carbonaceous byproduct.....	61
3.3 Results and discussion.....	63
3.3.1 Carbonaceous byproduct characterization.....	63
3.3.2 The performance of the LIBs.....	71
3.4 Conclusions.....	73
Acknowledgements.....	73
References.....	75
Chapter 3 Supporting Information.....	78
Chapter 4 Crumpled Reduced Graphene Oxide–Amine–Titanium Dioxide Nanocomposites for Simultaneous Carbon Dioxide Adsorption and Photoreduction	82
Abstract.....	83
4.1 Introduction.....	84
4.2 Experimental section.....	87
4.2.1 Precursor Solution Preparation.....	87
4.2.2 CGOATI Nanocomposite Synthesis.....	87
4.2.3 Materials Characterization.....	88
4.2.4 CO ₂ Photoreduction Analysis.....	89
4.2.5 Isotope Experiments.....	91
4.3 Results and discussion.....	91
4.3.1 Morphology characterization.....	91
4.3.2 CO ₂ adsorption and photoreduction.....	94

4.3.3 Surface chemistry characterization for CO ₂ photoreduction mechanism.....	98
4.3.4 Recyclability test	106
4.4 Conclusion	107
Acknowledgements.....	108
References	109
Chapter 4 Supporting Information.....	113
Chapter 5 N-doped Reduced Graphene Oxide Promoted Nano TiO₂ as A Bifunctional Adsorbent/Photocatalyst for CO₂ Photoreduction: Effect of N Species	124
Abstract.....	125
5.1 Introduction.....	126
5.2 Experimental section.....	128
5.2.1 Preparation of TiO ₂ /NrGO composites.....	128
5.2.2 Characterization.....	129
5.3 Results and discussion	131
5.3.1 Characterization.....	131
5.3.2 Photocatalytic reduction of CO ₂ with H ₂ O.....	139
5.3.3 Mechanism of photocatalytic enhancement.....	144
5.4 Conclusions.....	152
Acknowledgments	153
References.....	154
Chapter 5 Supporting Information.....	162
Chapter 6 Surface Defect-Induced Performance Enhancement in CO₂ Photoreduction: An Applied Electric Potential Approach	169
Abstract.....	170
6.1 Introduction.....	171
6.2 Materials and methods	173
6.2.1 Synthesis of columnar TiO ₂ single crystals.....	173
6.2.2 Materials characterization.....	173
6.2.3 Design of the configuration to apply electric potential.....	174
6.2.4 CO ₂ photoreduction analysis	175

6.2.5 In situ diffuse reflectance infrared Fourier transform spectroscopy (DRIFTS) analysis	177
6.3 Results and discussion	177
6.3.1 CO ₂ photoreduction analysis	178
6.3.2 Characterizations of OTDs	181
6.3.3 Recyclability test	187
6.3.4 Proposed mechanisms.....	188
6.4 Conclusions.....	195
Acknowledgements.....	195
References.....	196
Chapter 6 Supporting Information	199
Chapter 7 A Kinetic Model of Gas-Phase Photoreduction of CO₂ over TiO₂ Thin Films with Different Morphologies in A Continuous Flow Reactor	206
Abstract.....	207
7.1 Introduction.....	208
7.2 Experimental methods	210
7.2.1 Material synthesis	210
7.2.2Material characterization	211
7.2.3 CO ₂ photoreduction analysis	211
7.3 Model development	211
7.3.1 Light-induced generation of electron and hole pairs	213
7.3.2 Adsorption of reactants and products on the accessible surface of TiO ₂	214
7.3.3 Photostationary state assumption for the reaction intermediates.....	216
7.3.4 CO yield rate as a function of different reaction parameters.....	217
7.4 Results and discussions.....	218
7.4.1 Material characterizations.....	218
7.4.2 Model parameters of TiO ₂ thin films with different morphologies.....	220
7.4.3 Solving for the reaction parameters by fitting the model with experimental data	222
7.4.4 CO ₂ photoreduction predictions of TiO ₂ thin films with different morphologies	223

7.5 Conclusions.....	229
Acknowledgements.....	229
References.....	230
Chapter 7 Supporting Information.....	232
Chapter 8 Conclusions and Future Directions.....	235
8.1 Conclusions.....	236
8.2 Future directions	239
8.2.1 Material synthesis	239
8.2.2 CO ₂ Photocatalytic mechanisms.....	240
8.2.3 Model development	240
Appendix A. MATLAB Code of the Kinetic Modeling of the CO₂ photoreduction over TiO₂ thin films	242
A.1 Obtaining the model coefficients by fitting the model with experimental data...	243
A.2 Predictions of the CO yield of the TiO ₂ films with different morphologies.....	246
A.2.1 Columnar film.....	246
A.2.2 Dense film.....	253
A.2.3 Granular film.....	256
Appendix B. Curriculum Vitae.....	261

List of Figures

Figure 1.1 U.S. greenhouse gas emission in 2015 ³	2
Figure 1.2 Human sources of carbon dioxide ⁶	3
Figure 2.1 Schematic diagram of the CGO particles synthesis and mobility study system.	22
Figure 2.2 Schematic diagram of the charging characteristics study system.	25
Figure 2.3 (a) Particle size distribution of CGO particles synthesized at 400 oC; TEM images of CGO particles synthesized at 400 oC with different electrical mobility sizes, (b) 60 nm, (c) 100 nm, (d) 140 nm, (e) 180 nm.....	31
Figure 2.4 Projected area equivalent d_p correlated to electrical mobility d_p of CGO synthesized at (a) 200 °C, (b) 400 °C, (c) 600 °C, (d) 800 °C.....	34
Figure 2.5 Charge distribution of 80 nm mobility equivalent size CGO particles synthesized at 400 °C. (a) Second DMA with no neutralizer, (b) Second DMA with neutralizer.	36
Figure 2.6 Charging fractions of CGO nanoparticles synthesized at 200, 400, 600, 800 oC. a) The fractions of particles carrying +1 charge as a function of size; b) The fractions of particles carrying +2 charges as a function of size.	38
Figure 3.1 Methane post-processing initial architecture concept diagram.	57
Figure 3.2 Photographs of (a) a fully assembled PPA prototype; (b) PPA reactor installed on a microwave development test stand; (c) cylindrical screen type carbon trap assembly inside the PPA reactor. (Image source17).....	60
Figure 3.3 (a) SEM image of the carbon particulates; TEM images of carbon particulates: (b) low magnitude image of agglomerates, (c) low magnitude image of a single particle, (d) high magnitude image of agglomerates.	64
Figure 3.4 HRTEM images of the carbon particulates, (a) ordered crystal structure outlined by a red rectangle, (b) structures near the edge outlined by a red rectangle. (c) Electron diffraction pattern of the carbon particulates.	65
Figure 3.5 XRD spectrum of the carbon particulates.	66
Figure 3.6 Raman spectrum of the carbon particulates.....	67
Figure 3.7 XPS survey spectrum of the carbon particulates. The insert is the curve fitting of the C1s peak.....	68

Figure 3.8 Nitrogen adsorption/desorption analysis of the carbon particulates. The insert is the pore size distribution of the sample. 70

Figure 3.9 Electrochemical characteristics of the crumpled graphene LIBs. (a) charge (delithiation) capacities at various rates as marked, (b) capacity and Coulombic efficiency at the designated rate of 500 mA g⁻¹ for 100 cycles. 72

Figure 4.1 Schematic diagram of the FuAR and CO₂ photoreduction system 88

Figure 4.2 Images of CGOATI (TiO₂/GO 20%, EDA/GO 15:1, at 200 °C): (a) SEM image with lower magnification, (b) SEM image with higher magnification, (c) TEM image with lower magnification, (d) TEM image with higher magnification..... 93

Figure 4.3 CO₂ photoreduction of (a) CGOTI nanocomposites with different TiO₂/GO percentages at 200 °C (Table 1, test 1(1)), (b) CGOATI nanocomposites with different EDA/GO ratios, TiO₂/GO percentage was fixed at 20%, at 200 °C (Table 1, test 1(2)), (c) CGOATI nanocomposites prepared at different synthesis temperatures, with the EDA/GO ratio at 15:1 and TiO₂/GO percentage at 20% (Table 1, test 1(3)). 95

Figure 4.4 FTIR analysis of pristine CGOTI (TiO₂/GO 20%, at 200 °C), pristine CGOATI (TiO₂/GO 20%, EDA/GO 15:1, at 200 °C). Also shown are the spectra for the samples, CGOATI after CO₂ adsorption (only) and CO₂ adsorption and photoreduction. 99

Figure 4.5 (a) XPS survey spectra of pristine CGOTI (TiO₂/GO 20%, at 200 °C) and pristine CGOATI (TiO₂/GO 20%, EDA/GO 15:1, at 200 °C), (b) N1s XPS spectrum of pristine CGOATI, (c) N1s XPS spectrum of CGOATI after CO₂ adsorption (only), (d) N1s XPS spectrum of CGOATI after CO₂ adsorption and photoreduction. 101

Figure 4.6 C1s XPS spectra of (a) pristine CGOTI (TiO₂/GO 20%, at 200 °C), (b) CGOTI after CO₂ photoreduction, (c) pristine CGOATI (TiO₂/GO 20%, EDA/GO 15:1, at 200 °C), (d) CGOATI after CO₂ photoreduction. 102

Figure 4.7 Proposed reaction mechanisms of the insertion of EDA on r-GO, and CO₂ adsorption and photoreduction on CGOATI nanocomposites..... 103

Figure 4.8 Raman analysis of (a) CGOTI (TiO₂/GO 20%, at 200 °C) samples and (b) CGOATI (TiO₂/GO 20%, EDA/GO 15:1, at 200 °C) samples before and after CO₂ adsorption and CO₂ photoreduction..... 105

Figure 5.1 Schematic of the experimental setup for photoreduction of CO₂ with H₂O.. 131

Figure 5.2 XRD patterns of TiO₂, TiO₂/rGO, and TiO₂/NrGO samples 132

Figure 5.3 (A) Diffuse reflectance UV-vis spectra and (B) plots of the square root of Kubelka-Munk function versus the photon energy of TiO ₂ , TiO ₂ /rGO, and TiO ₂ /NrGO samples.....	134
Figure 5.4 (A) SEM image, (B) TEM image, (C) XPS spectra and (D) XPS N 1s of TiO ₂ /NrGO-300 samples.	136
Figure 5.5 Raman spectra of samples. (a) TiO ₂ /rGO, (b) TiO ₂ /NrGO-100, (c) TiO ₂ /NrGO-200, (d) TiO ₂ /NrGO-300, (e) TiO ₂ /NrGO-400 and (f) TiO ₂ /NrGO-500.....	139
Figure 5.6 (A) Time course of the photocatalytic production rate of CO; (B) total yield of CO over TiO ₂ , TiO ₂ /rGO, and TiO ₂ /NrGO under UV-vis irradiation; (C) Time-dependent CO production rate and volumetric ratio of O ₂ /N ₂ over TiO ₂ /NrGO-300 catalyst, and (D) Recycling tests for CO ₂ photoreduction over over TiO ₂ , TiO ₂ /rGO, and TiO ₂ /NrGO-300.	143
Figure 5.7 CO ₂ adsorption isotherms of TiO ₂ /rGO and TiO ₂ /NrGO samples.....	146
Figure 5.8 Photocurrent response vs. time of the TiO ₂ , TiO ₂ /rGO, and TiO ₂ /NrGO samples with an electrode potential of 0 V vs. Ag/AgCl.....	147
Figure 5.9 Possible reaction mechanisms for photoreduction of CO ₂ with H ₂ O over (A) TiO ₂ and (B) TiO ₂ /NrGO-300 samples.....	152
Figure 6.1 Schematic diagram of the CO ₂ photoreduction system.....	176
Figure 6.2 (a) SEM image and (b) TEM image of a typical columnar TiO ₂ sample.	178
Figure 6.3 CO ₂ photoreduction of columnar TiO ₂ on (a) FTO substrate, (b) SS substrate and ITO substrate, with different electric powers. (Note: 0 W means no voltage applied; ~ 0 W means 12 V voltage applied, almost 0 A current, and 0 W power obtained.).....	180
Figure 6.4 HRTEM images of (a) pristine TiO ₂ (inset is the digital picture), (b) 4W TiO ₂ (inset is the digital picture). FFT analysis of (c) pristine TiO ₂ , and (d) 4W TiO ₂	182
Figure 6.5 (a) UV-vis adsorption spectra and (b) Tauc's plot obtained for different columnar TiO ₂ samples.....	184
Figure 6.6 (a) Raman spectra and (b) magnified Raman spectra in range of 300 to 800 nm, of different columnar TiO ₂ samples, including pristine TiO ₂ ; 4W TiO ₂ ; 4W_postUV TiO ₂ ; photoreduced TiO ₂	186

Figure 6.7 (a) Ti 2p XPS spectra of different columnar TiO ₂ samples, including pristine TiO ₂ , 4W TiO ₂ , and 4W_postUV TiO ₂ . Deconvoluted Ti 2p XPS spectra of (b) pristine TiO ₂ ; (c) 4W TiO ₂ ; and (d) 4W_postUV TiO ₂	187
Figure 6.8 CO ₂ photoreduction of the columnar TiO ₂ for five cycles (1 st 4W on; 2 nd off; 3 rd 4W on; 4 th off; 5 th 4W on).....	188
Figure 6.9 In situ DRIFTS analysis (red: defective TiO ₂ (4W TiO ₂), blue: pristine TiO ₂): (a) CO ₂ adsorption kinetics; (b) and (c) IR spectra obtained after adsorption for 15 min.	193
Figure 6.10 Schematic diagram of OTDs formation and healing and CO ₂ photoreduction mechanism for the columnar TiO ₂ with electric potential.	194
Figure 7.1 Reaction scheme of an illuminated TiO ₂ particle.....	213
Figure 7.2 (a) SEM and (b) AFM images of a typical columnar TiO ₂ thin film.	219
Figure 7.3 (a) Incident light intensity spectrum. (b) Light transmission spectrum of a typical TiO ₂ thin film.....	219
Figure 7.4 Schematic diagram of top and side views of TiO ₂ thin films with different morphologies: (a) columnar film, (b) dense film, and (c) granular film.....	221
Figure 7.5 Fitting of the kinetic model with the experimental data.....	223
Figure 7.6 Model predictions for columnar TiO ₂ thin films. (a) Y _{CO,m} and (b) Y _{CO,A} as a function of a radius of the single column (r ₂); (c) Y _{CO,m} and (d) Y _{CO,A} as a function of the top cone taper length (s); (e) Y _{CO,m} and (f) Y _{CO,A} as a function of the thickness of the film (d _F).	225
Figure 7.7 Model prediction for dense TiO ₂ thin films. (a) Y _{CO,m} and (b) Y _{CO,A} as a function of the thickness of the film (d _F).	227
Figure 7.8 Model prediction for granular TiO ₂ thin films. (a) Y _{CO,m} and (b) Y _{CO,A} as a function of a radius of the primary particle diameter (d _p); (c) Y _{CO,m} and (d) Y _{CO,A} as a function of the thickness of the film (d _F).	228

List of Tables

Table 2.1 Experimental plan.....	29
Table 3.1 Experimental plan.....	62
Table 4.1 Experimental plan.....	90
Table 4.2 The conductivity of CGOTI (TiO ₂ /GO 20%) samples synthesized under different temperatures (before and after CO ₂ photoreduction).....	98
Table 5.1 Physicochemical properties of TiO ₂ , TiO ₂ /rGO and TiO ₂ /NrGO samples.....	137
Table 6.1 Experimental plan.....	176
Table 6.2 Estimated band gap energies of different TiO ₂ samples: pristine, 0.25 W, 1 W, 2.25 W, 4 W.....	184
Table 6.3 Color change and OTDs status change of TiO ₂ samples under different conditions.....	189
Table 6.4 Assignment of the IR bands.....	192

Acknowledgements

I would like to express my deepest and most sincere thanks to my advisors, Drs. Pratim Biswas and John Fortner, for their great guidance and endless support through my whole doctoral research progress. I thank them for initiating my doctoral project and inspiring me whenever I was stuck with my research. They are both outstanding scientists and kind people. Through frequent discussions with them, I came up with good research ideas, and they always provided me with freedom to explore my research interests. They also helped me to develop very good research habits and to think positively, creatively, and critically, which will be a treasure through my entire life.

I would also like to acknowledge other members on my committee. I am especially grateful to Dr. Wei-Ning Wang for his mentoring in the first year of my Ph.D. study, and his valuable suggestions and tremendous help whenever I came to him. Drs. Chakrabarty and Elijah Thimsen were also very helpful and supportive, and their comments and suggestions helped to improve the quality of my research. I really thank them for all the time and effort they put in.

I want to thank all my colleagues in the Aerosol & Air Quality Research Laboratory and the Fortner Laboratory for providing help and assistance. Special thanks to my collaborators on the nanoparticle synthesis and application projects: Dr. Yi Jiang, Dr. Liang-Yi Lin, Dr. Yang Wang, Dr. Ramesh Raliya, Shaline Kavadiya, Begum Karakocak, Clayton Kacica, Dr. Fei Wu for their contributions to this work. Also, many thanks go to Dr. Marit Meyer and Dr. Robert Green from NASA for our great collaboration, and I would also like to thank Caroline Avery for her help with this project.

Tremendous thanks go to the McDonnell International Scholars Academy for providing me with a fellowship to pursue my Ph.D, offering me opportunities to broaden my horizon outside my own research lab, improving my communication skills, increasing my confidence, and developing my leadership. I really appreciate Director James Wertsch and Vice Director Teresa Sarai for their thoughtful caring and career suggestions. I am so proud to be one of the McDonnell Scholars, forever.

I would also like to thank all my friends and the staff in the EECE department, and Mr. Ballard from the Engineering Communications Center for helping with manuscript editing.

Finally, and most importantly, I want to thank my parents, my husband, Yue Wu and my daughter, Kaitlyn Wu. Without their unconditional love and support, I could have never reached where I am, and have never accomplished what I have earned.

Yao Nie

Washington University in St. Louis

August 2018

Dedicated to my dear parents, Qingju Wu and Ninghai Nie,
my husband, Dr. Yue Wu, and my daughter, Kaitlyn Wu

ABSTRACT OF THE DISSERTATION

Synthesis of Crumpled Graphene and Titanium Dioxide Based–Nanomaterials and the
Application to Carbon Dioxide Photoreduction

By

Yao Nie

Doctor of Philosophy in Energy, Environment & Chemical Engineering

Washington University in St. Louis, 2018

Professor Pratim Biswas, Chair

Professor John Fortner, Co-Chair

With the rapid development of the economy, increasing combustion of fossil fuels has caused an increase in the atmospheric carbon dioxide (CO₂) level, and has led to global climate change. As a mitigation approach, CO₂ capture and conversion (CCC) can not only capture CO₂, but also convert it to useable products, such as hydrocarbon fuels. Photocatalytic reduction is an attractive CCC option that directly harnesses inexpensive and abundant solar energy. Titanium dioxide (TiO₂) is a widely used semiconductor for photocatalysis, and graphene nanosheets are a promising material for use in fabricating graphene-TiO₂ hybridized photocatalysts. To realize the application of these materials for CO₂ photoreduction, synthesis methods and pertinent material properties need to be investigated. In addition, a simple but practical kinetic model that can predict CO₂ photoreduction performance is also needed, not only to save cost, but also to guide synthesis procedures.

Research presented in this dissertation bridges scientific and engineering gaps in CO₂ photoreduction technologies that incorporate TiO₂ with or without graphene materials.

The work was conducted in three broad steps: material synthesis, photocatalyst design and testing, and kinetic model development.

(1) Synthesis of crumpled graphene-based materials and study of their chemical and physical properties

A furnace aerosol reactor (FuAR) was used to synthesize crumpled graphene oxide (CGO) nanoparticles, and their mobility and charging characteristics were systematically investigated. The projected area equivalent diameter was found to be approximately equal to the electrical mobility diameter for the CGO particles, regardless of their morphology. A differential mobility analyzer (DMA) is a convenient and efficient tool to classify CGO particles according to their physical diameters. In the charging characteristics study, Fuch's theory fits the experimental data better than Boltzmann's theory for most of the measured charging fractions, indicating that the conductivity of CGO particles plays an important role in affecting their charging characteristics. In addition to studying FuAR synthesized material, we also characterized the carbon material formed as a side product in a NASA plasma reactor for methane post-processing. It was crumpled graphene with a low oxygen content, and was only a few layers in thickness. This crumpled graphene material was used to synthesize the anodes of lithium-ion batteries, which showed high electrochemical performance.

(2) Design and performance testing of graphene-TiO₂ based CO₂ photocatalysts

We used a single-step aerosol method to synthesize aminated, reduced graphene-based nanocomposites consisting of crumpled r-GO with encapsulated TiO₂ nanoparticles, thus creating open core-shell nanostructures (referred to as CGOATI). Furthermore, we synthesized TiO₂/nitrogen doped reduced graphene oxide (NrGO) composites by a one-

step urea-assisted hydrothermal method. Both two types of N-modified graphene-TiO₂ materials were used for simultaneous gas-phase CO₂ adsorption and photoreduction. The mechanisms of graphene and N modification in enhancing the CO₂ photoreduction performance were investigated systematically.

Aerosol chemical vapor deposition (ACVD) was used to synthesize TiO₂ thin films with columnar morphologies. To increase the CO yield of this columnar TiO₂, oxygen vacancies and Ti-related defects (OTDs) were generated by applying electric potential to TiO₂ under UV irradiation. We gained a mechanistic understanding of the formation and healing of these OTDs, and of enhanced CO₂ photoreduction by defective TiO₂ (TiO_{2-x}) with electric potential.

(3) Kinetic model development and CO₂ photoreduction performance prediction

We developed a kinetic model of gas-phase CO₂ photoreduction over TiO₂ thin films in a continuous flow reactor, considering three aspects: 1) light activation, 2) surface adsorption of reactants and products, and 3) reaction kinetics. The reaction rate constants were estimated by fitting the model with the experimental data, and used to further predict the CO yield for TiO₂ thin films with different morphology parameters.

This work identifies and addresses several key issues regarding the synthesis of (crumpled) graphene-TiO₂ based materials for CO₂ photoreduction. The findings and conclusion from this work, will impact such fields as the aerosol processing of materials, and the morphology design of photocatalysts.

Chapter 1 Introduction

1.1 Motivation

Global warming, also known as climate change, is the observed rise in the average temperature of the Earth's climate system and its related effects on a century-scale.¹ In 2013, the intergovernmental Panel on Climate Change (IPCC) Fifth Assessment Report concluded that "It is very likely that human influence has been the dominant cause of the warming observed since the mid-20th century."² In a climate model in this report, it is predicted that during the 21st century, the global surface temperature is likely to rise further, by 0.3 to 1.7 °C (0.5 to 3.1 °F) in the lowest emissions scenario, and by 2.6 to 4.8 °C (4.7 to 8.6 °F) in the highest emissions scenario.² The major human activity that causes the increasing greenhouse effect is the increasing emission of greenhouse gases, including carbon dioxide (CO₂), methane (CH₄), and nitrous oxide (NO_x) and fluorinated gases. In the U.S., among these greenhouse gases, CO₂ emissions account for over 80% of the total emissions in 2015, as shown in Figure 1.1.

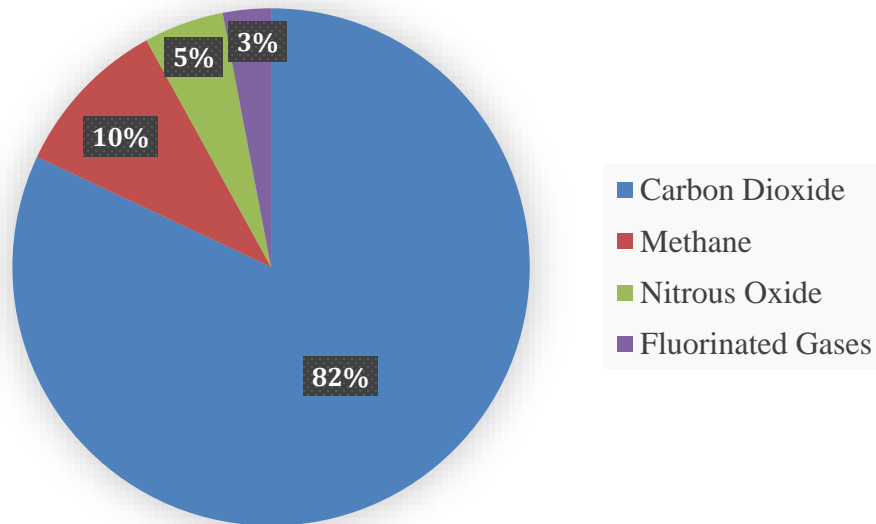


Figure 1.1 U.S. greenhouse gas emission in 2015³

As shown in Figure 1.2, the largest human source of CO₂ emission is the burning of fossil fuels, such as coal, natural gas, and oil, which provides enormous energy to meet the demand of growing economies. It has been well studied that the positive correlation between global economy and the burning of fossil fuels.^{4,5} Therefore, in order to reduce the greenhouse effect without slowing the economic growth, strategies to mitigate CO₂ before it is emitted into atmosphere have attracted global attention.

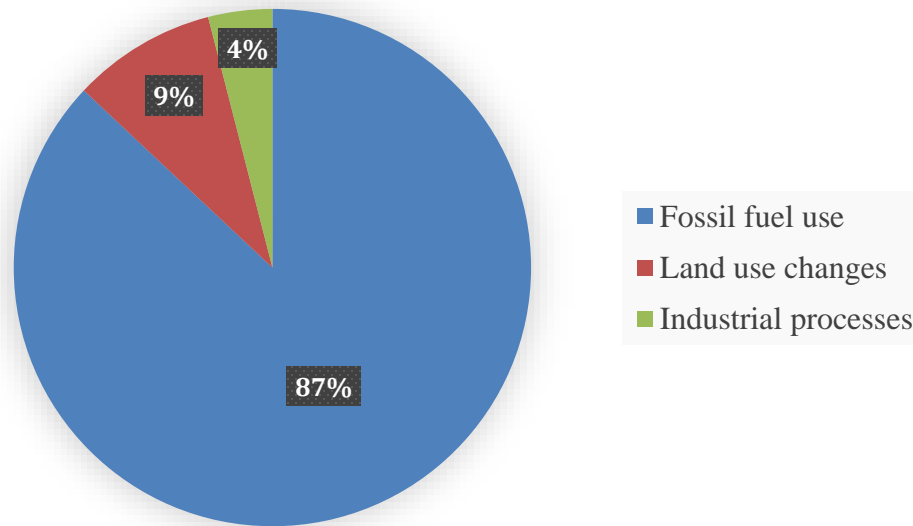


Figure 1.2 Human sources of carbon dioxide⁶

Metz et al.⁷ proposed CO₂ capture and sequestration (CCS) technology as a feasible approach to address this problem. However, this technology is energy intensive^{8,9} and has potential risks of CO₂ leakage from geological sequestration sites.¹⁰ An alternative process, CO₂ capture and conversion (CCC), can reduce risks by not only capturing CO₂, but also converting it to useable products such as hydrocarbon fuels. Thermochemical,¹¹ electrochemical,¹² and photocatalytic^{13, 14} methods are possible ways to realize the reduction of CO₂. Among these methods, photocatalytic reduction is a promising option that directly harnesses inexpensive and abundant solar energy. In the photocatalytic

process, a semiconductor photocatalyst absorbs light energy, bridging its band gap and producing electron-hole (e^-h^+) pairs to support reduction and oxidation reactions.^{15, 16} However, the efficiency of photocatalytic reduction of CO_2 is relatively low due to several limiting steps, such as CO_2 adsorption on the photocatalyst surface¹⁵ and recombination of e^-h^+ pairs¹⁶. Therefore, a modified material that could enhance CO_2 adsorption or/and retard recombination of e^- and h^+ would increase the CO_2 photoreduction efficiency.

Titanium dioxide (TiO_2) is a widely used semiconductor for photocatalysis, due to its comparatively low cost, low toxicity,¹⁷ and ability to resist photo-corrosion.¹⁸ However, the CO_2 photoreduction efficiency of TiO_2 materials is usually low, which results from their wide band gap (3.2 eV for anatase), low surface area, and rapid recombination of electrons and holes. A number of methods have been reported to modify TiO_2 to address these limitations, such as metal^{19, 20} or non-metal doping,^{21, 22} morphology modification,^{16, 23} and defects engineering.²⁴⁻²⁶ Graphene nanosheets are a promising material for use in fabricating graphene- TiO_2 hybrids for CO_2 photoreduction:^{27, 28} They have excellent electronic conductivity, which promotes the trapping of electrons and retards the recombination of electrons and holes, and have an extremely large specific surface area (theoretically $2630\text{ m}^2\text{g}^{-1}$),^{29, 30} which could enhance adsorption of CO_2 .^{31, 32} Although the potential for graphene- TiO_2 based material technologies in CO_2 photoreduction is easy to imagine, the science and engineering that enable the production and performance prediction remain relatively nascent.

1.2 Key scientific gap

To apply graphene materials with different sizes, qualities, and morphologies in CO_2 photoreduction, the first step is to identify the most applicable and advantageous types

and adopt a low cost, facile, and scalable production and processing technique for their synthesis. Graphene is a family of materials composed of pure graphene which is a 2D framework of carbon atoms, and derivatives. Defect-free graphene has excellent electrical conductivity and shows great potential for electronic/energy applications, and it is usually synthesized using chemical vapor deposition (CVD). However, these perfect graphene nanosheets are hydrophobic and has a strong tendency to restack due to strong π - π interactions, reducing the accessible surface area and material's efficacy.³³ "Imperfect" graphene, graphene oxide (GO), is heavily oxygenated, strongly hydrophilic, and contains many functional groups, making it a good candidate as a support for the photoactive center, such as TiO₂, to promote CO₂ photoreduction. In addition, to solve the restacking problem of GO sheet, one feasible approach is to convert a two-dimensional sheet to a crumpled three-dimensional structure via aerosol routes, which improves the stability and maintains the outstanding electrical properties of graphene-based materials.

However, crumpled graphene oxide (CGO) poses the potential health risks from airborne exposure, which motivates our second step: The key properties of CGO, including its dimensional properties and charging characteristics, have to be precisely and accurately known.

Third, incorporating CGO and photoactive centers, such as TiO₂ to make novel CO₂ photoreduction catalysts is essential to realizing the practical applications of CGO and TiO₂ based materials. CGO has a hollow structure that can encapsulate other nanoscale functional materials, forming a quasi-spherical hybrid. In addition, enhancing the CO₂ adsorption on the surface, by surface or structural modification of the graphene support, is also worthy of consideration. To achieve efficient simultaneous CO₂ adsorption and

photoreduction, simple methods are needed to synthesize hybrids of surface or structural modified graphene and TiO₂ for use in photocatalysis.

Fourth, to enhance the CO₂ photoreduction capability of the catalysts, another approach is to modify the photoactive center, TiO₂. The photoactivity of TiO₂ can be significantly affected by its size, structure, and morphology. The surface properties of TiO₂ are largely influenced by defects, and the dominant defects are oxygen vacancies and Ti-related defects (OTDs). In addition, to avoid introducing excess foreign elements, the effects of OTDs have been widely studied as a form of so-called “self-doping”³⁴, which is considered a green and promising strategy for efficient and environmentally friendly engineering of photocatalysts. The reported methods to generate OTDs usually require high energy inputs and an intense and special synthesis environment. A method that uses a low energy input and requires only an ambient environment would be a large environmental step forward.

Finally, to not only save cost but also to guide synthesis procedures, we need to predict the CO₂ photoreduction performance of TiO₂ with different sizes, structures and morphologies without conducting the photocatalytic experiment. To address this concern, developing a simple but practical kinetic model of CO₂ photoreduction reactions will be the foundation for such predictions. In the literature, most the kinetic models of photocatalytic processes are for liquid phase reactions and continuous stirred-tank reactors (CSTRs). A model that works for gas-phase reactions and a mixed flow reactor (MFR), which fits our experimental conditions, will be more applicable for our system, and can be obtained by combining parts of the experimental results.

1.3 Objectives

This work addresses most of the key issues highlighted above, bridging scientific and engineering gaps in CO₂ photoreduction technologies which incorporate TiO₂, with or without graphene materials. The overall goals for this work are to fabricate novel photocatalysts using TiO₂ and/or graphene-based materials, to characterize their chemical and physical properties, to demonstrate the CO₂ photoreduction mechanisms, and to offer guidance in designing the morphologies and sizes using model prediction.

Three specific research objectives, are as follows:

Objective G1-Synthesis of crumpled graphene-based materials and study of their chemical and physical properties

- (1) Synthesize crumpled graphene oxide (CGO) nanoparticles via aerosol routes
- (2) Investigate the mobility and charging characteristics of the CGO nanoparticles
- (3) Characterize the crumpled graphene synthesized in a plasma reactor at NASA

CGO particles are synthesized in a furnace aerosol reactor (FuAR) with a broad size distribution, and the morphologies of CGO particles with different sizes are also different. The synthesis temperature plays an important role in controlling their size and morphology. Here, we investigate the mobility and charging characteristics of the CGO nanoparticles as a function of particle size. By using a differential mobility analyzer (DMA), CGO particles of uniform mobility are classified and collected. The morphology and size of these CGO nanoparticles are characterized by transmission electron microscopy (TEM). The projected area equivalent diameter of CGO calculated from TEM images is correlated to the electrical mobility diameter of CGO measured by a scanning mobility particle sizer (SMPS) system, consisting of a DMA and a condensation particle counter. In addition, the bipolar diffusion

charging characteristics of CGO particles synthesized at different temperatures are also studied with a tandem DMA system, and the multiply charged fraction of CGO particles are estimated.

In addition, the by-products of an integrated NASA system for use in space missions are characterized as useful crumpled graphene particles. Their chemical and physical properties are analyzed, and potential applications were also investigated.

Objective G2-Design and performance testing of graphene-TiO₂ based CO₂ photocatalysts

- (4) Synthesize graphene-TiO₂ based high-performance CO₂ photocatalysts
- (5) Investigate the effects of the addition of nitrogen into the graphene-TiO₂ catalytic system and fundamentally describe the reaction mechanisms
- (6) Engineer defect engineering in the TiO₂ thin films and study the mechanism of the resulting enhanced CO₂ photoreduction performance

A single step aerosol method is described to synthesize aminated, reduced graphene-based nanocomposites consisting of crumpled r-GO with encapsulated TiO₂ nanoparticles, resulting in the formation of open core-shell nanostructures (referred to as CGOATI). Furthermore, TiO₂/nitrogen-doped reduced graphene oxide (NrGO) composites are synthesized as bifunctional adsorbents/photocatalysts for gas-phase photoreduction of CO₂ with H₂O vapor. Systematic studies are conducted to investigate the roles of amine surface modification and N structural dopants on the catalytic activities of photocatalysts, and possible mechanisms for the functioning of N modifications are proposed. The aerosol chemical vapor deposition (ACVD) process is used to synthesize TiO₂ thin films with columnar morphologies. To increase the CO yield of this columnar TiO₂, OTDs are

generated by applying electric potential to TiO_2 under UV irradiation. Mechanistic explanations are proposed for the formation and healing of these OTDs, and for CO_2 photoreduction by defective TiO_2 (TiO_{2-x}) with electric current.

Objective G3-Kinetic model development and CO_2 photoreduction performance prediction

(7) Develop the kinetic model of gas-phase CO_2 photoreduction over TiO_2 thin films

(8) Predict the CO_2 photoreduction performance of TiO_2 thin films with different morphology parameters.

A kinetic model of gas-phase CO_2 photoreduction over TiO_2 thin films in a continuous flow reactor is developed, incorporating three aspects: 1) light activation; 2) surface adsorption of reactants and products; and 3) reaction kinetics. The reaction rate constants are estimated by fitting the model with the experimental data, and are used to further predict the CO yield for TiO_2 thin films with different morphology parameters.

1.4 Dissertation organization

The dissertation begins by identifying key scientific and engineering issues to be addressed, followed by a review of the current technical literature. In Chapter 2, CGO nanoparticles are synthesized by atomizing a solution of graphene oxide sheets (GO) in a FuAR, in which GO is thermally reduced. By using a DMA, CGO nanoparticles of uniform mobility sizes are classified and collected. The morphology and sizes of these CGO nanoparticles are characterized by TEM. The projected area equivalent size of CGO calculated from TEM images (offline measurements) is correlated to the electrical mobility size of CGO measured by a SMPS system (online measurements), and a reasonable match between the two sizes is observed. Further, the bipolar diffusion charging characteristics

of CGO synthesized at different temperatures are studied with a tandem differential mobility analyzer (TDMA) system, from which the charge fractions of CGO are determined. Overall, this chapter describes the synthesis method of CGO and reveals some chemical and physical properties of CGO.

Chapter 3 considers another possible source of crumpled graphene materials. To support long-term missions in space, it is important to recycle valuable consumables, such as oxygen (O_2) and water. In a Sabatier reactor, hydrogen is employed to reduce carbon dioxide (CO_2) to methane (CH_4) and O_2 , then an integrated system recycles hydrogen from CH_4 . This system includes a methane purification assembly (MePA), a plasma pyrolysis assembly (PPA), and an acetylene separation assembly (ASepA). In the PPA reactor, carbon particulates are formed as a by-product. In this chapter, this carbon material is characterized, and a significant fraction is found to be graphene with a low oxygen content. To explore potential uses for this material, the crumpled graphene is used to synthesize anodes of lithium-ion batteries (LIBs), which are then tested for their electrochemical performance.

Chapter 4 offers a method to synthesize crumpled reduced graphene oxide-amine-titanium dioxide nanocomposites (CGOATI) by a one-step aerosol technique. The CGOATI product enables simultaneous CO_2 adsorption and photoreduction. The enhancement of CO_2 photoreduction is attributed to higher CO_2 adsorption on the amine-functionalized reduced-GO (r-GO) surface and the strong electron trapping capability of r-GO. The insertion of amine groups on r-GO nanosheets, the adsorption of CO_2 by amine groups, and the photoreduction of the adsorbed CO_2 are confirmed by FTIR and XPS spectra analysis. The r-GO nanosheets themselves are simultaneously photoreduced during

CO₂ photoreduction. Raman spectroscopy and conductivity measurements show that photoreduced r-GO has a higher electronic conductivity than thermally reduced r-GO, and leads to more effective CO₂ photoreduction.

Chapter 5 discusses about the synthesis of a series of TiO₂/nitrogen (N) doped reduced graphene oxide (TiO₂/NrGO) nanocomposites with varying concentrations and bonding configurations of nitrogen, produced by a one-step urea-assisted hydrothermal method and applied to photoreduction of CO₂. The promoting effects of N dopants on the structure and activity of TiO₂/NrGO are investigated. It is demonstrated that NrGO with an appropriate N quantity and N-bonding configuration acts as a dual-functional promoter, simultaneously enhancing CO₂ adsorption on the catalyst surface and facilitating electron-hole separation, and eventually boosting the photocatalytic performance.

Chapter 6 addresses how to enhance CO₂ photoreduction, with a particular focus on the role of TiO₂. A new method to generate oxygen vacancies and Ti-related defects (OTDs) in columnar titanium dioxide (TiO₂) thin film under UV irradiation with electric potential is described. The formation and healing of OTDs are confirmed by color changes (white to yellow, and back to white) and by HETEM images, UV-Vis adsorption, Raman spectra, and XPS spectra. The enhancement of the TiO_{2-x} in CO₂ photoreduction with electric potential can be attributed to 1) the narrowed band gap energy, 2) the enhanced chemical adsorption of CO₂, and 3) the better separation of electrons and holes. This study offers new insights into engineering OTDs in TiO₂ for photocatalysis, using an easy and gentle method in ambient environment.

Drawing on the experimental results from Chapter 6, in Chapter 7 a kinetic model of gas-phase photoreduction of CO₂ over TiO₂ thin films with different morphologies in a

continuous flow reactor is developed, based on the mechanistic steps, including the photo-generation of electrons and holes, the adsorption of the reactants on the surface of the thin films, and reaction kinetics. Reaction rate constants are obtained by fitting the model with the experimental data. The CO₂ photoreduction performances of the TiO₂ thin films with different morphology parameters are predicted by using the kinetic model with the calculated reaction rate constants. CO yields are discussed on the bases of both the catalyst mass and the irradiation area. The results of this study emphasize a strong effect of morphology and size parameters on photoactivity and offer new insights into designing the morphology of highly efficient CO₂ photoreduction catalysts.

Finally, Chapter 8 summarizes the dissertation's key findings and details its major contributions. Concluding remarks discuss the implications of these findings within a broader context of crumpled graphene and TiO₂ based materials for CO₂ photoreduction, and offer perspectives on potential future directions of such technologies.

Reference

1. Gillis, J., Short answers to hard questions about climate change. *The New York Times*, 2015. **25**.
2. Stocker, T.F., Climate change 2013: the physical science basis: summary for policymakers, a report of Working Group I of the IPCC, technical summary, a report accepted by Working Group I of the IPCC but not approved in detail and frequently asked questions: part of the Working Group I contribution to the fifth assessment report of the Intergovernmental Panel on Climate Change. 2013: Intergovernmental Panel on Climate Change.
3. Federici, S., et al., New estimates of CO₂ forest emissions and removals: 1990–2015. *Forest Ecology and Management*, 2015. **352**: p. 89-98.
4. Saidi, K. and S. Hammami, The impact of CO₂ emissions and economic growth on energy consumption in 58 countries. *Energy Reports*, 2015. **1**: p. 62-70.
5. Antonakakis, N., I. Chatziantoniou, and G. Filis, Energy consumption, CO₂ emissions, and economic growth: An ethical dilemma. *Renewable and Sustainable Energy Reviews*, 2017. **68**: p. 808-824.
6. Le Quéré, C., et al., The global carbon budget 1959–2011. *Earth System Science Data Discussions*, 2012. **5**(2): p. 1107-1157.
7. Metz, B., et al., Carbon dioxide capture and storage. 2005.
8. Rao, A.B. and E.S. Rubin, A technical, economic, and environmental assessment of amine-based CO₂ capture technology for power plant greenhouse gas control. *Environmental Science & Technology*, 2002. **36**(20): p. 4467-4475.
9. Singh, D., et al., Techno-economic study of CO₂ capture from an existing coal-fired power plant: MEA scrubbing vs. O₂/CO₂ recycle combustion. *Energy Conversion and Management*, 2003. **44**(19): p. 3073-3091.
10. Halbwachs, M. and J.-C. Sabroux, Removing CO₂ from Lake Nyos in Cameroon. *Science (New York, NY)*, 2001. **292**(5516): p. 438.
11. Chueh, W.C., et al., High-flux solar-driven thermochemical dissociation of CO₂ and H₂O using nonstoichiometric ceria. *Science*, 2010. **330**(6012): p. 1797-1801.

12. Pérez-Rodríguez, S., et al., Pd catalysts supported onto nanostructured carbon materials for CO₂ valorization by electrochemical reduction. *Applied Catalysis B: Environmental*, 2015. **163**: p. 83-95.
13. Kočí, K., et al., Effect of silver doping on the TiO₂ for photocatalytic reduction of CO₂. *Applied Catalysis B: Environmental*, 2010. **96**(3): p. 239-244.
14. Kočí, K., et al., Effect of TiO₂ particle size on the photocatalytic reduction of CO₂. *Applied Catalysis B: Environmental*, 2009. **89**(3): p. 494-502.
15. Linsebigler, A.L., G. Lu, and J.T. Yates Jr, Photocatalysis on TiO₂ surfaces: principles, mechanisms, and selected results. *Chemical reviews*, 1995. **95**(3): p. 735-758.
16. Wang, W.-N., et al., Size and Structure Matter: Enhanced CO₂ Photoreduction Efficiency by Size-Resolved Ultrafine Pt Nanoparticles on TiO₂ Single Crystals. *Journal of the American Chemical Society*, 2012. **134**(27): p. 11276-11281.
17. Carp, O., C.L. Huisman, and A. Reller, Photoinduced reactivity of titanium dioxide. *Progress in solid state chemistry*, 2004. **32**(1): p. 33-177.
18. Xu, Y. and M.A. Schoonen, The absolute energy positions of conduction and valence bands of selected semiconducting minerals. *American Mineralogist*, 2000. **85**(3-4): p. 543-556.
19. Mao, J., et al., Pt-loading reverses the photocatalytic activity order of anatase TiO₂ {001} and {010} facets for photoreduction of CO₂ to CH₄. *Applied Catalysis B: Environmental*, 2014. **144**: p. 855-862.
20. Hou, W., et al., Photocatalytic conversion of CO₂ to hydrocarbon fuels via plasmon-enhanced absorption and metallic interband transitions. *ACS Catalysis*, 2011. **1**(8): p. 929-936.
21. Zhou, S., et al., Facile in situ synthesis of graphitic carbon nitride (gC₃N₄)-N-TiO₂ heterojunction as an efficient photocatalyst for the selective photoreduction of CO₂ to CO. *Applied Catalysis B: Environmental*, 2014. **158**: p. 20-29.
22. Asahi, R., et al., Nitrogen-doped titanium dioxide as visible-light-sensitive photocatalyst: designs, developments, and prospects. *Chemical reviews*, 2014. **114**(19): p. 9824-9852.

23. An, W.-J., E. Thimsen, and P. Biswas, Aerosol-chemical vapor deposition method for synthesis of nanostructured metal oxide thin films with controlled morphology. *The Journal of Physical Chemistry Letters*, 2009. **1**(1): p. 249-253.
24. Liu, L. and X. Chen, Titanium dioxide nanomaterials: self-structural modifications. *Chemical reviews*, 2014. **114**(19): p. 9890-9918.
25. Liu, L., et al., Hydrogenation and disorder in engineered black TiO₂. *Physical review letters*, 2013. **111**(6): p. 065505.
26. Teng, F., et al., Preparation of black TiO₂ by hydrogen plasma assisted chemical vapor deposition and its photocatalytic activity. *Applied Catalysis B: Environmental*, 2014. **148**: p. 339-343.
27. Gusain, R., et al., Reduced graphene oxide–CuO nanocomposites for photocatalytic conversion of CO₂ into methanol under visible light irradiation. *Applied Catalysis B: Environmental*, 2016. **181**: p. 352-362.
28. Tan, L.-L., et al., Visible-light-active oxygen-rich TiO₂ decorated 2D graphene oxide with enhanced photocatalytic activity toward carbon dioxide reduction. *Applied Catalysis B: Environmental*, 2015. **179**: p. 160-170.
29. Novoselov, K.S., et al., Electric field effect in atomically thin carbon films. *science*, 2004. **306**(5696): p. 666-669.
30. Stoller, M.D., et al., Graphene-based ultracapacitors. *Nano letters*, 2008. **8**(10): p. 3498-3502.
31. Cheng, J., et al., Photoelectrocatalytic Reduction of CO₂ into Chemicals Using Pt-Modified Reduced Graphene Oxide Combined with Pt-Modified TiO₂ Nanotubes. *Environmental Science & Technology*, 2014. **48**(12): p. 7076-7084.
32. Tu, W., et al., An In Situ Simultaneous Reduction-Hydrolysis Technique for Fabrication of TiO₂-Graphene 2D Sandwich-Like Hybrid Nanosheets: Graphene-Promoted Selectivity of Photocatalytic-Driven Hydrogenation and Coupling of CO₂ into Methane and Ethane. *Advanced Functional Materials*, 2013. **23**(14): p. 1743-1749.
33. Wang, Y., et al., Preventing graphene sheets from restacking for high-capacitance performance. *The Journal of Physical Chemistry C*, 2011. **115**(46): p. 23192-23197.
34. Lo, H.-H., N.O. Gopal, and S.-C. Ke, Origin of photoactivity of oxygen-deficient TiO₂ under visible light. *Applied Physics Letters*, 2009. **95**(8): p. 083126.

Chapter 2 Mobility and Bipolar Diffusion Charging Characteristics of Crumpled Reduced Graphene Oxide Nanoparticles Synthesized in a Furnace Aerosol Reactor

The results reported in this chapter were published in - Nie, Yao, Yang Wang, and Pratim Biswas. "Mobility and Bipolar Diffusion Charging Characteristics of Crumpled Reduced Graphene Oxide Nanoparticles Synthesized in a Furnace Aerosol Reactor." The Journal of Physical Chemistry C 121.19 (2017): 10529-10537. Reproduced with permission from American Chemical Society, copyright 2017.

Abstract

Crumpled graphene oxide (CGO) nanoparticles were synthesized by atomizing a solution of graphene oxide sheets (GO) into a furnace aerosol reactor (FuAR), in which GO was thermally reduced. By using a differential mobility analyzer (DMA), CGO nanoparticles of uniform mobility sizes were classified and collected. The morphology and sizes of these CGO nanoparticles were characterized by transmission electron microscope (TEM). The projected area equivalent size of CGO calculated from TEM images (offline measurements) was correlated to the electrical mobility size of CGO measured by a scanned mobility particle sizer system (SMPS), that consisted of a DMA and a condensation particle counter (CPC) (online measurements), and a reasonable match between the two sizes was observed. Further, the bipolar diffusion charging characteristics of CGO synthesized at different temperatures were studied with a tandem differential mobility analyzer (TDMA) system, from which the charge fractions of CGO were determined. The synthesis temperature affected the charge fractions of CGO with the same electrical mobility size, which was attributed to the different conductivities of CGO thermally reduced at different temperatures. CGO nanoparticles synthesized at 400 °C had the highest conductivity and the largest fraction of charged particles.

2.1 Introduction

Graphene nanosheets, monolayers of sp^2 -bonded carbon atoms,¹ have shown great potential for use in nanoelectronics,² biosensors³ and photocatalysis,⁴⁻⁵ due to their excellent electronic conductivity and large specific surface area.⁶⁻⁷ However, with high hydrophobicity, graphene nanosheets cannot be well dispersed in water. Unlike graphene, graphene oxide (GO) nanosheets are heavily oxygenated, strongly hydrophilic, and contain many functional groups, such as hydroxyl, epoxy and carboxyl groups.¹ Many researchers have employed GO nanosheets as precursors to synthesize graphene by controlled thermal,⁸ photo⁹ or chemical⁹⁻¹⁰ reduction methods. However, graphene and GO nanosheets are unstable and tend to restack due to strong π - π interactions.¹¹ Restacking of these sheets reduces the accessible surface area and affects the material's efficacy in various applications.¹² To improve the stability and maintain the outstanding electrical properties of graphene-based materials, converting a two-dimensional sheet to a crumpled three-dimensional structure is a feasible approach.¹³⁻¹⁶ Our previous study on the DLVO analysis showed that,¹⁷ these crumpled GO (CGO) nanoparticles are much more stable than GO sheets and can support and encapsulate other nanoscale functional materials, such as Si,¹¹ TiO₂,^{18,19} and Pt,²⁰ to form a quasi-spherical hybrid, which can be used as a photocatalyst⁴ or a biosensor.³

As described above, CGO is a promising material for a variety of applications. However, its material properties are not fully known, which limits its applications.^{21,8} Furthermore, the increasing gas-phase production of CGO and carbon-based materials has led to many concerns over the potential health risks from exposure in the atmospheric and laboratory environments.²² The key properties of CGO, including its dimensional

properties and charging characteristics, have to be studied precisely and accurately. The correlations of various CGO properties are very important to establish functionality.^{23,24} In our previous study,¹⁴ CGO synthesized in a furnace aerosol reactor (FuAR) had a broad size distribution, and the morphologies of CGO with different sizes were also different. The synthesis temperature played an important role in controlling the size and morphology of the CGO particles. The difference in sizes and morphologies could lead to many uncertainties in the performance of the materials. Therefore, there is an urgent need to 1) characterize CGO particles of different sizes, 2) correlate the morphology of CGO particles with their mobility size, and 3) further classify CGO particles with uniform properties by size.

To evaluate the fate and transport of CGO nanoparticles, their charging characteristics need to be established, as particle charging affects the measurement²⁵⁻²⁷, synthesis process²⁸, and gas-phase aerosol dynamics²⁹⁻³² of nanoparticles. The crumpled structure of these nanoparticles further adds uncertainties in their charging characteristics, which may lead to inaccurate size and concentration measurement results by traditional aerosol instruments. By investigating the charging characteristics of CGO nanoparticles under a wide range of conditions, we can obtain a comprehensive understanding of their properties. Diffusion charging, thermionization, and photoionization are three major mechanisms that charge nanoparticles.³³ Diffusion charging dominates under most conditions, since the effect of thermionization is minimal below 2200 K, and photoionization relies on strong radiation to separate electrons from particles. In diffusion charging, bipolar/unipolar ions freely diffuse to the surface of the particles, where the charges are transferred. It takes place in a wide range of processes from gas reactions and

particle formation in the atmosphere³⁴ to particle removal in industrial or household devices.³⁵ The diffusion charging of particles is commonly realized by introducing particles into an environment that contains radioactive materials, where radiation generates ions that actively collide with the particles.³⁶ Currently, two theories exist in describing the diffusion charging of spherical particles. Boltzmann charging theory assumes the charging states of the particles in equilibrium, and the fraction of particles carrying certain charges is a function of temperature only.³⁷ Fuchs' charging theory, on the other hand, assumes that the charge transfer between the ions and the particles is irreversible, and the charging process is in a steady state.³⁸⁻³⁹ Furthermore, Fuchs' charging theory considers the effect of the particle's conductivity, since the induced dipole effect enhances the collision between an ion and a particle. The charge distributions of particles predicted by these two theories differ quite significantly below the size of 100 nm (which will be shown in this work); however, each of the theories has been validated by existing studies for different materials.⁴⁰⁻⁴² Hence, it is also interesting to study which theory is more predictive of the diffusion charging of CGO nanoparticles.

In this study, we investigated the mobility and charging characteristics of CGO nanoparticles as a function of particle size. By using a differential mobility analyzer (DMA), CGO particles of uniform mobility sizes were classified and collected. The morphology and size of these CGO nanoparticles were characterized by transmission electron microscopy (TEM). The projected area equivalent diameter of CGO calculated from TEM images was correlated to the electrical mobility diameter of CGO measured by a scanned mobility particle sizer (SMPS) system, that consisted of a DMA and a condensation particle counter. In addition, the bipolar diffusion charging characteristics of

CGO synthesized at different temperatures were studied with a tandem DMA system, and the multiply charged fraction of CGO particles was estimated. The effect of synthesis temperature on the properties of CGO particles was also studied, because the synthesis temperature can affect the size, morphology, and electrical conductivity of CGO particles.¹⁴

2.2 Experimental section

2.2.1 Material synthesis

Graphene oxide nanosheets were prepared by using the modified Hummers method,⁴³ reported in detail in our previous work.¹⁴ Briefly, graphite powder (45 μm) was oxidized by potassium permanganate (KMnO_4) with concentrated sulfuric acid (H_2SO_4), and then washed and dried overnight. The resultant graphite oxide powder was redispersed in DI water, then ultrasonicated and centrifuged to obtain single nanosheets. The supernatant was collected to prepare the GO stock solution.

A schematic diagram of the system for synthesizing the CGO particles is shown in Figure 2.1. The solutions (50 mg/L GO) were first atomized into micrometer-sized droplets by a Collison nebulizer (BGI Incorporated). The droplets with mean size around 5.1 μm , measured by an aerodynamic particle sizer (APS, TSI Inc.), (the droplet size was a function of pressure used, not the concentration of precursors¹⁴), were then carried by nitrogen gas (N_2) at a flow rate of 12.4 L/min (at 96.53 kPa) into a tubular alumina furnace aerosol reactor (FuAR, 1 m long \times 25 mm ID) maintained at various set temperatures (200 ~ 800 $^\circ\text{C}$). In the residence time of around 1 ~ 2 s in the FuAR, the GO nanosheets were thermally reduced and also crumpled by capillary force due to rapid solvent evaporation, as detailed in our previous work.¹⁴

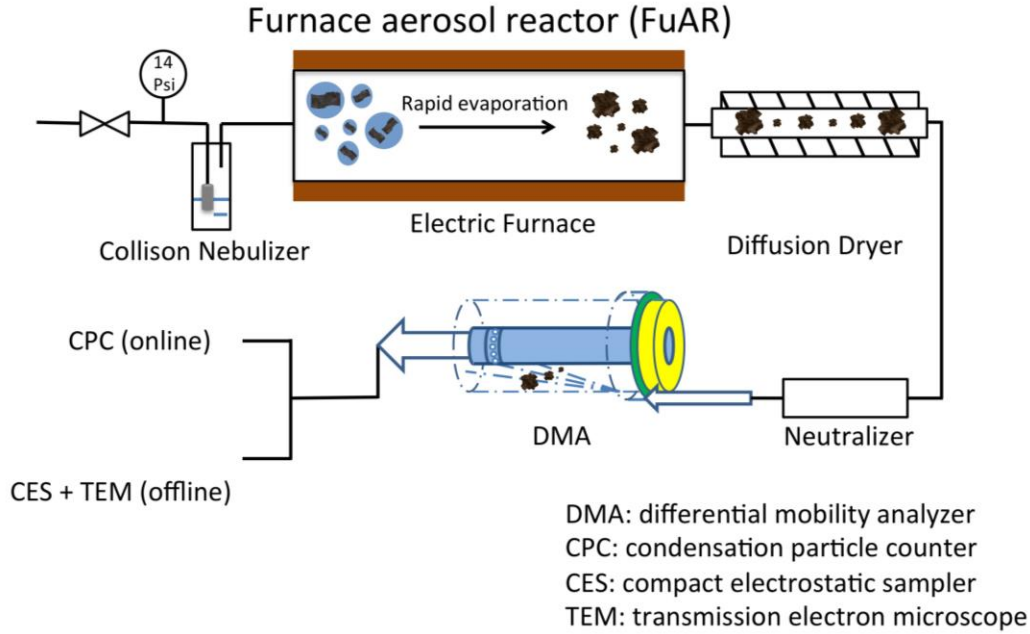


Figure 2.1 Schematic diagram of the CGO particles synthesis and mobility study system.

2.2.2 Material characterization

2.2.2.1 Size distribution

Online measurements: SMPS (electrical mobility size)

To measure the electrical mobility size, the CGO particles synthesized in the FuAR were introduced into a SMPS, that consisted of a DMA (Model 3081, TSI Inc.) and a condensation particle counter (CPC, model 3776, TSI Inc.). Based on the balance of electrical force and drag force, CGO particles of a certain size could pass through the DMA at a certain voltage:

$$\frac{d_p}{C(d_p)} = \frac{2L}{3 \ln\left(\frac{R_2}{R_1}\right)} \frac{V_{DMA} n e}{\mu Q_{sheath}}, \quad (2.1)$$

where d_p is the electrical mobility diameter of the CGO particles that pass through the DMA, L , R_2 , and R_1 are the length, outer diameter, and inner diameter of the DMA; V_{DMA}

is the voltage of DMA; C is the Cunningham slip correction factor, which is a function of particle diameter; m is the viscosity of the sheath flow gas; and Q_{sheath} is the sheath flow rate. By scanning the DMA voltage from 0 to 10 kV, the particle size distribution of the CGO particles can be obtained. The sheath flow rate and sample flow rate of the DMA were maintained at 3.0 and 0.3 L/min, respectively, and 60, 100, and 140 nm polystyrene latex nanospheres (PSL, Bangs Inc.) were used for the external calibration of the mobility size.

Offline measurement: TEM (physical size)

By setting the voltage of the DMA, CGO particles with a selected uniform electrical mobility size could pass through it. A homemade compact electrostatic sampler (CES)⁴⁴ was connected downstream of the DMA to collect the CGO particles with uniform mobility size. The morphology and projected area of the CGO particles were investigated using a TEM (Tecnai TM Spirit, FEI Co.). ImageJ was used to process the TEM images and measure the projected area of the CGO particles. After the projected area equivalent size was obtained from the measured projected area, the relationship between electrical mobility size and projected area equivalent size was established.

2.2.2.2 Resistivity measurement

The CGO samples synthesized at different temperatures were collected downstream the FuAR using a borosilicate glass membrane. The electric resistivity was measured by a JANIS probe station (ST500-1-2CX), and a Keithley 2400 source measurement unit, both fully controlled by a LabVIEW program. Details were reported in our previous paper.⁴⁵

2.2.2.3 Charging characteristics

Measuring the charging characteristics of CGO particles

Figure 2.2 is a schematic of the charging characteristics study system. The outlet aerosol existing FuAR was first introduced into a charged particle remover (CPR), where the CGO particles charged in the FuAR were removed. Neutralizer1 provided CGO particles with a specific but unknown charged particle size distribution. Then CGO particles with uniform equivalent electrical mobility sizes were classified by DMA1, at a set voltage. In the next steps, CGO particles with uniform equivalent electrical mobility sizes were recharged, if DMA1 was followed by neutralizer2. If a dummy neutralizer (which has the same geometric size as normal neutralizer, but has no radioactive materials) was used, it was assumed that the difference in the particle size distributions of the dummy neutralizer outlet and the DMA1 outlet was only attributed to the diffusion loss in the transport of particles. The neutralizers used in this study were Kr-85 neutralizer with an original activity of 370 MBq (Model 3077A, TSI Inc.). They were manufactured on 10/1/2013. Kr-85 has a half-life of 10.756 years. A study comparing six bipolar chargers with different ion source, source activity, geometry, and flow rate showed that the stationary state charge distributions could be achieved when the source activity was higher than 70 MBq for Kr-85 sources.⁴⁶ A SMPS system measured the scanned charged particle size distribution.

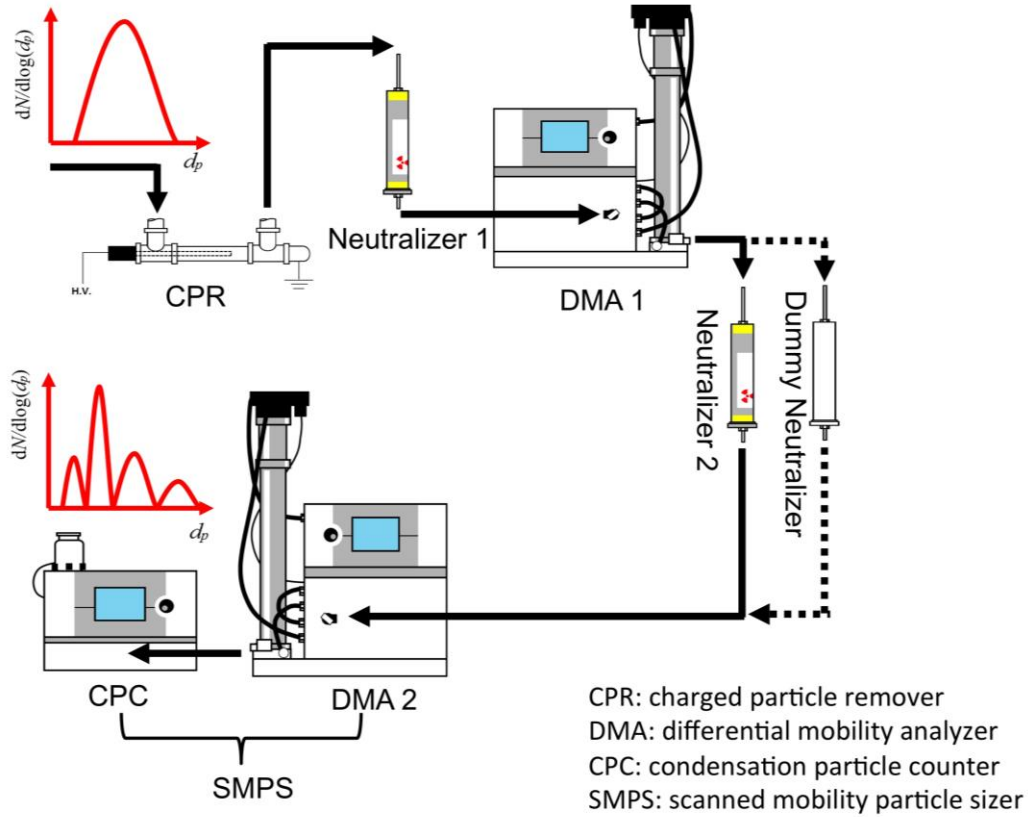


Figure 2.2 Schematic diagram of the charging characteristics study system.

Theoretical diffusion charging models

The Boltzmann and Fuchs' charging theories are widely used to predict the particle charging characteristics, which are commonly represented as the fractions of particles carrying certain charges ($0, \pm 1, \pm 2, \pm 3, \dots$) among the total particles of a given size (d_p). These two theories are introduced briefly as follows, so that we can compare the theoretical and experimental results on the charging characteristics of CGO nanoparticles.

The Boltzmann charging theory uses the balance relationships in classical equilibrium theories and predicts that

$$N_i = N_0 \exp\left(-\frac{i^2 e^2}{d_p kT}\right), \quad (2.2)$$

where N_i and N_0 are the number concentrations of particles carrying i (e.g., $\pm 1, \pm 2, \pm 3, \dots$) charges and 0 charge ($\#/m^3$), e is the electronic charge of an electron (C), d_p is the particle size (m), k is Boltzmann's constant (m^2kg/s^2K), and T is the temperature (K). The fraction of particles with a charge state of i and a diameter of d_p using Boltzmann charging theory is hence calculated by

$$f_{i,B} = \frac{N_i}{\sum_{k=-\infty}^{k=+\infty} N_k}. \quad (2.3)$$

Since i appears as the second power in the inverse exponential term, $f_{i,B}$ decreases significantly with an increasing number of charges carried by the particle. We should also note that the fractions of particles carrying $-i$ and $+i$ charges are the same in this charging theory, while the ion properties and material type of particles does not affect the charging characteristics.

Fuchs' charging theory, on the other hand, assumes that the charging process is in a steady state and a limiting sphere exists around each particle. Outside the limiting sphere, the ions travel freely according to convection diffusion equations, while inside the limiting sphere, the diffusion of ions is neglected and the detailed trajectory of ions is calculated. Fuchs' charging theory predicts particle charging characteristics based on the assumption that the number concentrations of bipolar ions are significantly higher than those of particles^{38, 47-48}, which is the case in commonly used aerosol neutralizers. This high concentration of bipolar ions will not smear the effect of materials, since the mass and mobilities of ions are different in each polarity⁴⁹⁻⁵². According to these studies, negative ions have smaller mass and higher mobility values than those of positive ions. This different results with an asymmetry in the characteristics of particle charging with different

polarities, which is proven by various laboratory studies of particles with different size and composition using the tandem differential mobility analysis^{48,53-55}. Fuchs' charging theory further considers the material dependence of the particles in the electrostatic potential between an ion and a particle, where

$$\phi(r) = - \int_{\infty}^r F_e(r) dr = \frac{e^2}{4\pi\epsilon_0} \left[\frac{i}{r} - K \frac{a^3}{2r^2(r^2 - a^2)} \right]. \quad (2.4)$$

In this equation, ϵ_0 is the permittivity of vacuum (C/Vm), i is the product of the numbers of charges on the particle and on the ion (i is positive if the particle and ion are of same polarity, and is negative if particle and ion are of different polarity), and a is the radius of the particle (m). K is the conductivity of the particle and is calculated by $K = (\epsilon_p - 1)/(\epsilon_p + 2)$, where ϵ_p is the dielectric constant of the material that composes the particle. The dielectric constants range from 1 to infinity from perfectly insulating materials to perfectly conducting materials. Hence, K takes value from 0 to 1 and for a perfectly conducting particle, $K = 1$. The conductivity of particle is considered since it decides the strength of the image charge and the induced dipole that the ion creates in the particle, affecting the magnitude of the electrostatic force. Currently, there have not been studies reporting the influence of particle conductivity on bipolar charging characteristics. However, experiments using different types of materials (Ag, NaCl, and sucrose) were conducted for unipolar charging⁵⁶, showing that the different particle conductivity values indeed caused different charging characteristics, which agreed with Fuchs' charging theory. The attachment coefficient η_i , representing the combination rate between ions and particles carrying i charges, is solved by:

$$\eta_i = \frac{n_0 \beta_i \exp\left(-\frac{\phi_i(\delta)}{kT}\right)}{1 + \exp(-\phi_i(\delta)/kT) (\beta_i/4\pi D) \int_{\delta}^{\infty} \rho^{-2} \exp(-\phi_i(\rho)/kT) d\rho} \quad (2.5)$$

where β_i is the flux of ions through the limiting sphere, ϕ_i is the electrical potential around the particle, δ is the radius of the limiting sphere, and D is the diffusion coefficient of the ion. The dynamics of ion-particle collisions dictate that the particles carrying $+i$ ($i=1, 2, 3\dots$) charges are generated from the collision of a positive ion with a particle carrying $+(i-1)$ charges and the collision of a negative ion with a particle carrying $+(i+1)$ charges; while they are lost by the collision of a positive/negative ion with a particle carrying $+i$ charges. Furthermore, by using the steady-state assumption, we can derive

$$\begin{aligned} \frac{dN_{+i}}{dt} &= \eta_{+(i-1)\&+1} n_{+1} N_{+(i-1)} + \eta_{+(i+1)\&-1} n_{-1} N_{+(i+1)} - \eta_{+i\&+1} n_{+1} N_{+i} - \eta_{+i\&-1} n_{-1} N_{+i} \\ &= 0, \end{aligned} \quad (2.6)$$

where N_{+i} is the number concentration of particles with a charging state of $+i$, $\eta_{+i\&+1} / \eta_{+i\&-1}$ is the attachment coefficient of positive/negative ions onto the particles carrying $+i$ charges, and n_{+1} / n_{-1} is the number concentration of positive/negative ions infinitely far away. Eq. 4.5 can be solved by induction, and a relationship between the number concentrations of neutral particles (N_0) and particles carrying $+i$ charges is obtained as $N_{+i} = A_{+i} N_0$, where A_{+i} is a function of the attachment coefficients and the number concentrations of positive and negative ions. Similarly, for negatively charged particles, $N_{-i} = A_{-i} N_0$. The fraction of d_p -sized particles carrying i charges is hence calculated by:

$$f_{i,F} = \frac{N_i}{\sum_{k=-m}^{k=+m} N_k}, \quad (2.7)$$

In this study of the charging characteristics of CGO nanoparticles, $f_{i,B}$ and $f_{i,F}$ for $i = +1, +2$ were calculated and compared with the experimentally determined values. The effect of synthesis conditions on the conductivity of CGO nanoparticles was further investigated through a comparison of charging fractions.

All the experimental plans are included in Table 2.1.

Table 2.1 Experimental plan.

Test number	Objective	Methodology	Results
1	Size distribution & morphology	SMPS TEM	Figure 2.3 (400 °C)
2	Mobility correlated to projected area equiv. size	SMPS TEM	Figure 2.4 (200, 400, 600, 800 °C)
3	Charge distribution	Tandem DMA with & without neutralizer	Figure 2.5 (80 nm equiv. size at 400 °C)
4	Charge fraction compared to Fuchs' & Boltzmann theory prediction	Tandem DMA with & without neutralizer (models)	Figure 2.6 (200, 400, 600, 800 °C)

2.3 Results and Discussion

2.3.1 Mobility study

Figure 2.3(a) shows the number concentration of CGO particles synthesized at 400 °C as a function of electrical mobility diameter. This mobility diameter distribution has a

high polydispersity, with a full-width at half-maximum of around 60 nm, which was attributed to the aerosol synthesis method.¹⁴ By using a DMA, we can successfully measure the full mobility diameter distribution. When the voltage of the DMA was set at a fixed value, monodispersed CGO particles with a certain electrical mobility diameter could be classified and further collected by a CES.

Orthogonally, TEM was employed to investigate the morphology and physical diameter (which was represented by the projected area equivalent diameter) of the CGO particles. In Figure 2.3(b-e), it can be seen that CGO particles have various morphologies with different electrical mobility diameters. Particles with a mode diameter of around 60 nm are GO fragments, not CGO particles. However, particles with electrical mobility diameters larger than 100 nm are CGO particles. The difference in size and morphology could be due to the broad size distribution of GO sheets in the precursor solution. As discussed in our previous work,¹⁴ the crumpling of the GO sheets is an evaporation-induced process. The equation describing capillary force is:

$$F = ABC^{\frac{1}{\delta D}} D_P^{-\frac{1}{\delta}} \left(\frac{\kappa T_d}{P_d D_g} \right)^{3/\delta D}, \quad (2.8)$$

where F is the capillary force, A and B are constants, C is the mass concentration of the precursor solution, D_P is the diameter of the CGO particles, κ is the evaporation rate of solvent, T_d is the droplet surface temperature, P_d is the vapor pressure of the solvent at the surface of the droplet, D_g is the gas-phase diffusion coefficient of the solvent, δ is the force scaling exponent, and D is the characteristic fractal dimension.

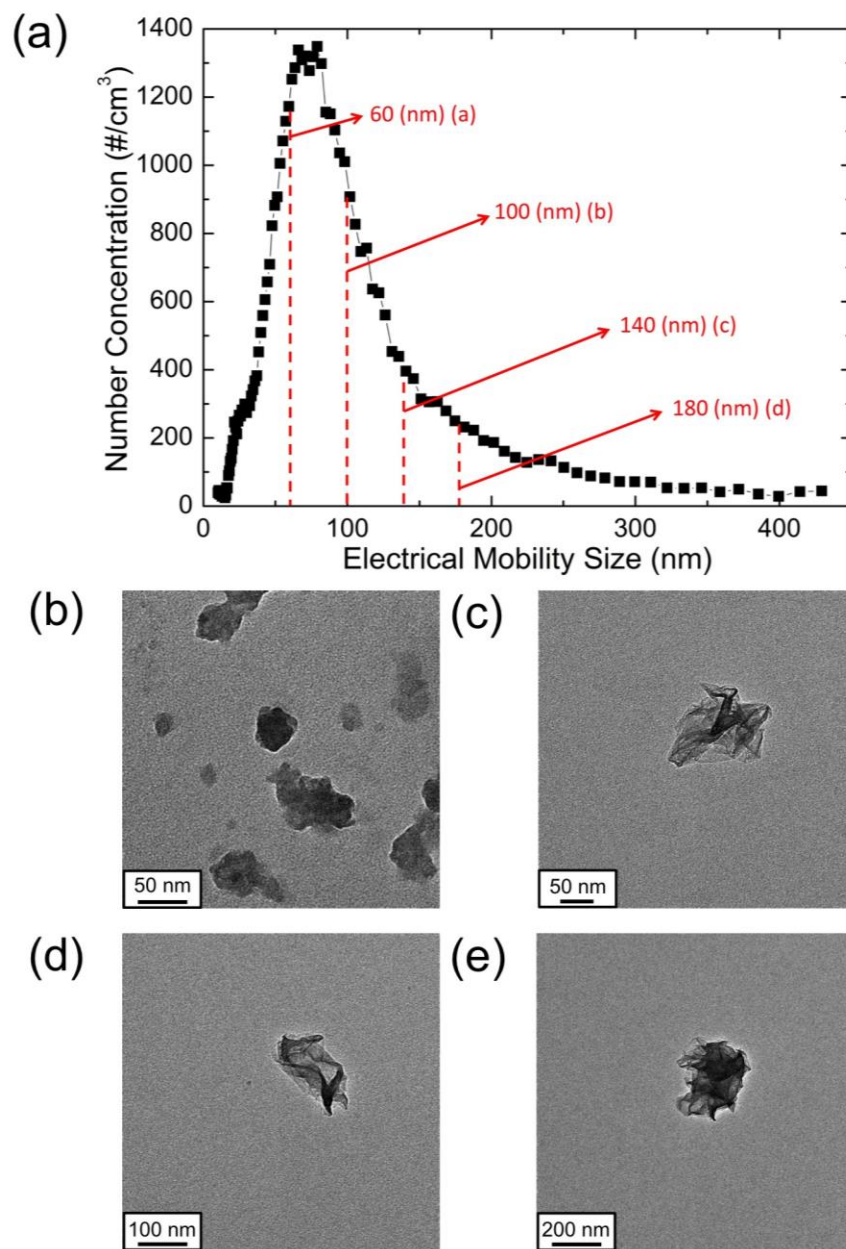


Figure 2.3 (a) Particle size distribution of CGO particles synthesized at 400 oC; TEM images of CGO particles synthesized at 400 oC with different electrical mobility sizes, (b) 60 nm, (c) 100 nm, (d) 140 nm, (e) 180 nm.

From this equation, F is inversely proportional to D_p . For a small piece of the GO sheet in the precursor solution, D_p is expected to be small as well. To obtain a small particle, the capillary force must be large. Therefore, with other parameters held constants, the

larger GO sheets crumpled more easily when the solvent evaporated. In addition, another possible reason for this phenomena could be that the larger GO sheets were more aggregated and led the more crumpled CGO particles after the evaporation-induced self-assembly (EISA).⁵⁷ In future work, we will seek to narrow the size distribution of CGO particles by controlling the sheet size (the size distribution GO sheets in the precursor solution was quite broad¹⁴) and improving the monodispersity of the GO sheets in the precursor solution (i.e., by decreasing the sonication time and the sonication power).

Even though the SMPS is an effective and convenient tool to characterize CGO particles by size, there has been no report on the relationship between the electrical mobility diameter and the physical diameter (represented by projected area equivalent diameter) of the CGO particles. Although they have a roughly spherical shape, we cannot assume CGO nanoparticles to be spheres, because the interior of the nanoparticle is not densely packed, and a fractal dimension of 2.5 is commonly observed for the crumpled structures.⁵⁸ To correlate the electrical mobility diameter and the physical diameter (represented by projected area equivalent diameter) of the CGO particles, the online SMPS data was compared with offline TEM data. The projected area equivalent diameter (d_A) was calculated from the projected area (A_P), using the following equation:

$$A_P = \frac{\pi d_A^2}{4}. \quad (2.9)$$

As shown in Figure 2.4, the projected area equivalent diameter is almost proportional to the electrical mobility diameter of CGO particles synthesized at different temperatures. In our previous study,¹⁴ the synthesis temperature played an important role in affecting the evaporation rate of the solvent, the confinement force, and the morphology of the CGO particles. To better understand the relationship between the projected area

equivalent diameter and the electrical mobility diameter, the flow regime of the CGO particles needs to be discussed. The Knudsen number (K_n), which is the ratio of the molecular mean free path to the particle diameter, was calculated to determine the flow regime, using the following equation:³⁷

$$K_n = \frac{2\lambda}{d_p}. \quad (2.10)$$

The sizes of the CGO particles that we studied ranged from 60 nm to 200 nm, and K_n was calculated to be around 1, which indicates that the CGO particles were in transition regimes. It has been theoretically validated that the electrical mobility diameter can be approximately estimated by the projected area equivalent diameter in the free molecular regime.⁵⁹ In the free molecular regime, the drag force can be considered as the collective effect of collisions of ballistic gas molecules on the particle. The probability of collision is proportional to the available cross-sectional area (projected area) of the particle. The electrical mobility diameter is calculated based on the balance between electrical force and drag force. Therefore, under such circumstances, the electrical mobility diameter and the projected area equivalent diameter are approximately equal. Although there is no theoretical evidence to show the validity of this conclusion in the transition regime, many researchers have verified this approximation in experimental studies.⁵⁹⁻⁶¹ In our study, the projected area equivalent diameter was found to be approximately equal to the electrical mobility diameter for the CGO particles, regardless of the morphology. Therefore, DMA can be employed as a convenient and efficient tool to classify CGO particles according to their physical diameters. This property is advantageous when the application of CGO nanoparticles requires a uniform size and structure distribution, such as in membranes and solar cell assembly.

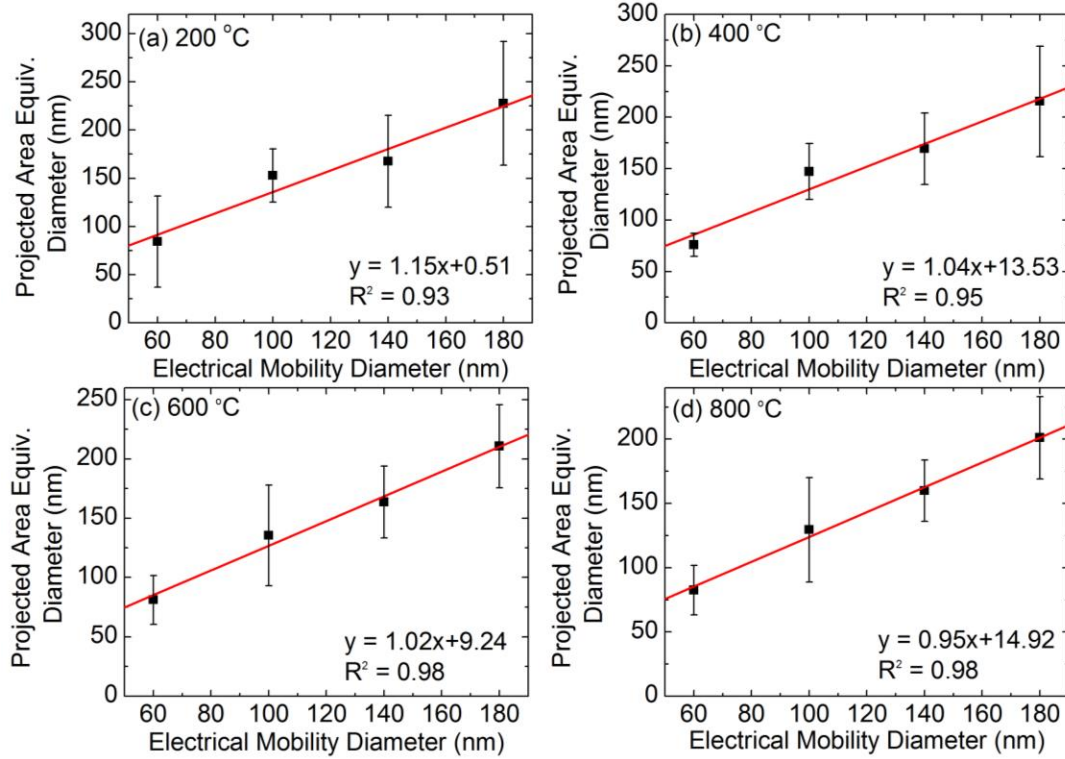


Figure 2.4 Projected area equivalent d_p correlated to electrical mobility d_p of CGO synthesized at (a) 200 °C, (b) 400 °C, (c) 600 °C, (d) 800 °C.

2.3.2 Charging characteristics study

2.3.2.1 Measurement of particles with different charging states

In the study of CGO nanoparticles' charging characteristics, the total number concentration of CGO particles with a mobility size of d_{mob1} (controlled by the voltage of the first DMA) was measured when using a dummy neutralizer (Figure 2.5(a)). After set the voltage of the first DMA, CGO particles with a certain electrical mobility were selected. When these monodispersed CGO particles passed through the dummy neutralizer, the number concentration would remain the same, except for the diffusion loss. If we passed all these CGO particles from the outlet of the dummy neutralizer into a CPC, the total number concentration of CGO particles of this certain electrical mobility size was obtained. However, this classified aerosol (CGO particles of the same certain electrical mobility size)

contained singly charged particles with a size of d_{mob1} , and possibly doubly charged particles with a size of d_{mob2} and triply charged particles with a size of d_{mob3} ($d_{mob3} > d_{mob2} > d_{mob1}$), and so on. By using a second neutralizer, the charges on the CGO particles with the same certain electrical mobility size could be redistributed, and a scanned charged particle size distribution could be obtained after these recharged particles were introduced into a SMPS system (b). In Figure 2.5(b), the left side of the red line corresponds to the singly charged particles in the first neutralizer, and the right side corresponds to the multiply charged particles. Because the concentration of the multiply charged particles is very small compared to the concentration of the singly charged particles, the concentration presented in Figure 2.5(a) can be regarded as the total concentration of CGO particles with a size of d_{mob1} .

In Figure 2.5(b), the highest peak corresponds to singly charged particles with a size of d_{mob1} , and the peak on the left of the highest peak corresponds to doubly charged d_{mob1} -sized particles. Fractions of singly charged or doubly charged particles were calculated by dividing the concentration of singly charged or doubly charged CGO by the total concentration of CGO. The equations are as follows:

$$\text{Fraction of singly charged particles} = \frac{C_{d_{mob1}(+)}}{C_{d_{mob1}(total)}}, \quad (2.11)$$

$$\text{Fraction of doubly charged particles} = \frac{C_{d_{mob1}(++)}}{C_{d_{mob1}(total)}}. \quad (2.12)$$

By varying the voltage of the first DMA, CGO particles with different mobility sizes can be selected, and the charging characteristics of CGO particles were further investigated as a function of particle size.

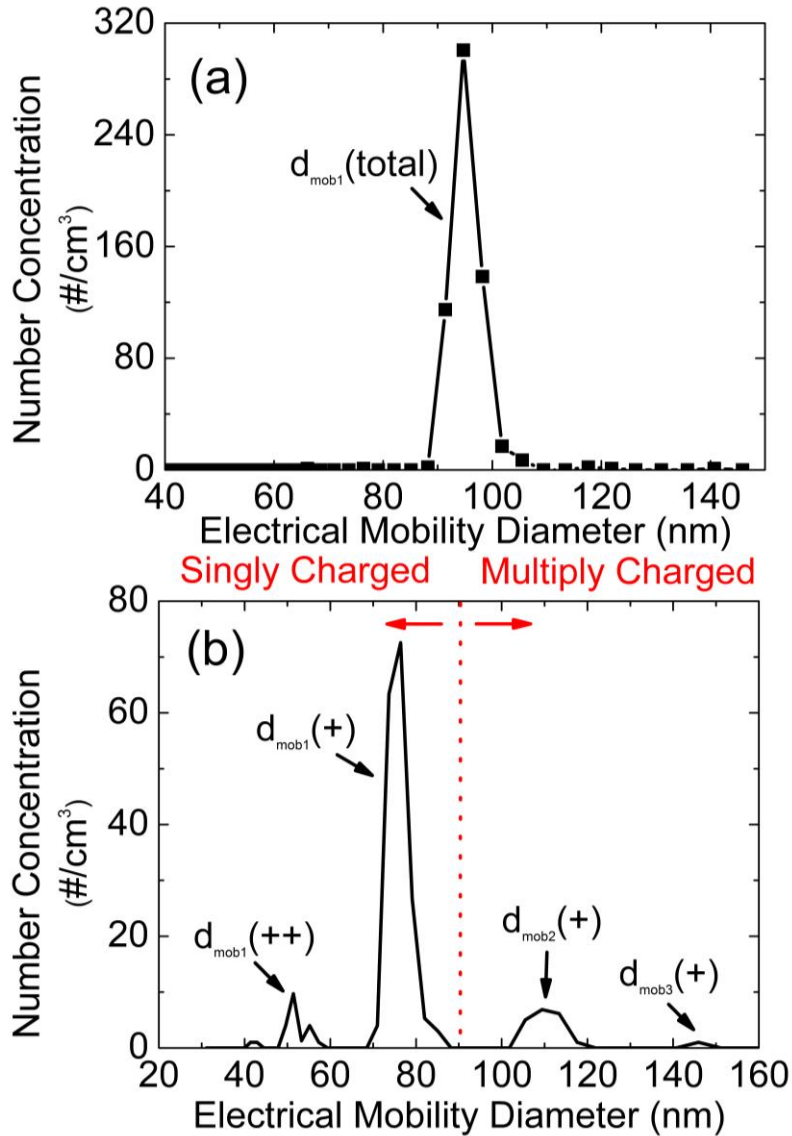


Figure 2.5 Charge distribution of 80 nm mobility equivalent size CGO particles synthesized at 400 °C. (a) Second DMA with no neutralizer, (b) Second DMA with neutralizer.

2.3.2.2 Charging characteristics of CGO nanoparticles synthesized at different temperatures.

Figure 2.6 (Figure 2.6(a) refers to singly charged particles, and Figure 2.6(b) refers to doubly charged particles) shows the charging fractions of CGO nanoparticles

synthesized at different furnace temperatures. The charging fractions calculated by the Boltzmann charging theory and Fuchs' charging theory using conductivity (K) values of 0 and 1 are also plotted. It could be seen that the charging fractions predicted by the Boltzmann charging theory were higher than those of Fuchs' charging theory. This difference arose because the Boltzmann theory does not consider the effect of ion polarity on the particle charging process. The positively charged particles are mainly produced by collisions between particles with positive ions, while the positive ions generated in neutralizers have higher masses and smaller electrical mobilities, as indicated by previous studies.^{49, 62} This asymmetry in the ion properties could lead to a lower fraction of particles carrying positive charges, as shown in the calculation results. It was also found that the conductivity of the nanoparticles indeed affected the charging fractions according to Fuchs' model. When the conductivity value (K) changed from 0 to 1, the charging fraction increased by up to three-fold times in the tested size ranges (Figure. 6(b), 60 nm), while the decreasing and overlapping of the charging fractions, as shown in Figure 6(a), is a result of the increased fractions of particles carrying more than +1 charges.

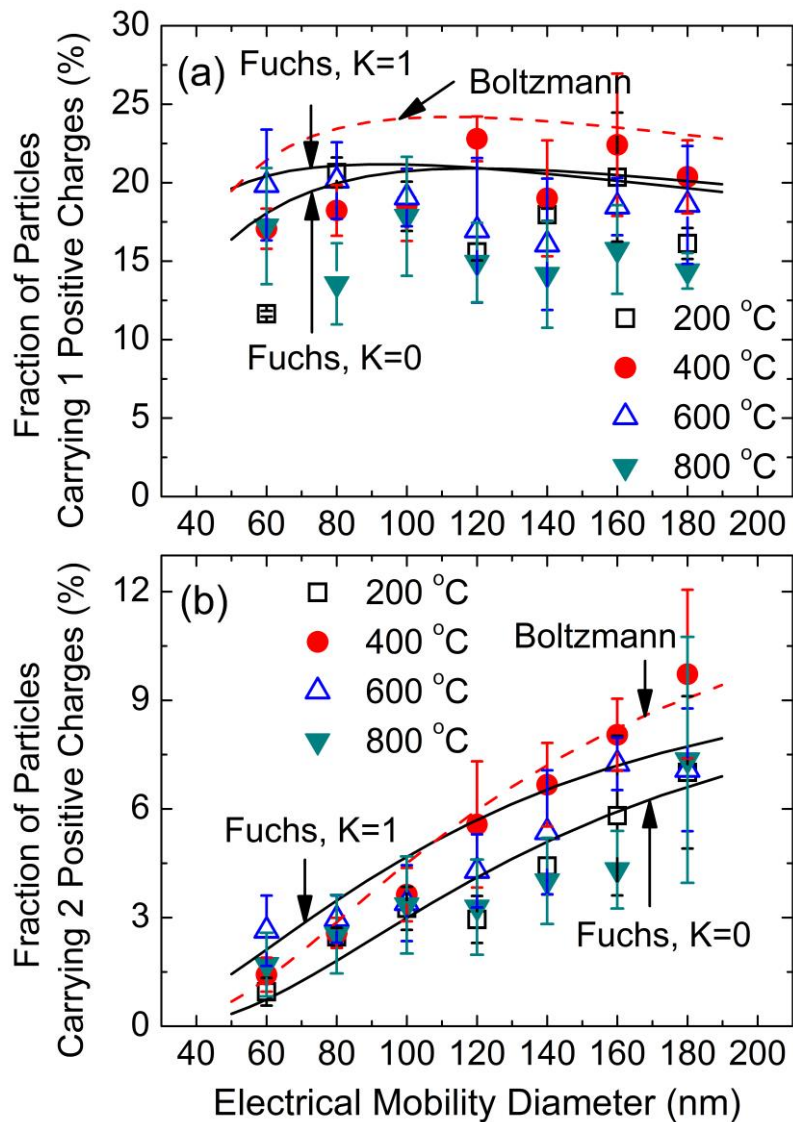


Figure 2.6 Charging fractions of CGO nanoparticles synthesized at 200, 400, 600, 800 °C. a) The fractions of particles carrying +1 charge as a function of size; b) The fractions of particles carrying +2 charges as a function of size.

Figure 2.6 displays that Fuchs' theory fits the experimental data better for most of the measured charging fractions, compared to the Boltzmann theory. For the fractions of particles carrying 2 positive charges, Fuchs' theory can fit most of the measured charging fractions. However, the contribution of particle conductivity on charging was not easy to be identified quantitatively since the data points had relatively large standard deviations.

CGO particles synthesized at different furnace temperatures differ quite significantly in their charging characteristics. Nanoparticles synthesized at 400 °C provide the highest charging fraction among the tested conditions, which may be a result of higher particle conductivity, since all the other parameters were the same according to Fuchs' charging theory. It is well documented that GO can be thermally reduced, and the conductivity can also be partially restored by the removal of surface functional groups, under high temperature. From the resistivity test,⁴⁵ we found that 400 °C is the optimal furnace temperature for reducing CGO nanoparticles and obtaining the highest conductivity. The conductivity decreases with a further increase of temperature (over 400 °C) due to the formation of surface defects, such as carbon vacancies.⁶³ Since the conditions for charging the CGO nanoparticles are the same, this higher charging fraction at 400 °C can be attributed to the higher particle conductivity only. Measurements of charge fractions further confirmed temperature's influence on the surface chemistry and the electrical conductivity of CGO particles.

2.4 Conclusions

By using a DMA, CGO nanoparticles of uniform mobility sizes were classified and then collected. The projection size of CGO calculated from offline measurements were correlated with the electrical mobility size of CGO measured by online measurements. Further, the bipolar diffusion charging characteristics of CGO synthesized at different temperatures were studied with a tandem DMA system, from which the charge fractions of CGO were determined. The synthesis temperature significantly affected the charge fractions of CGO with the same mobility, which was attributed to the different conductivities of CGO (thermally) reduced at different temperatures.

Acknowledgements

Y.N. thanks the McDonnell International Scholars Academy and the McDonnell Academy Global Energy and Environment Partnership (MAGEEP) for the fellowship to pursue a Ph.D. at Washington University in St. Louis. Partial support from the Solar Energy Research Institute for India and the United States (SERIUS), DE-AC36-OSGO28308 funded by the US Department of Energy at Washington University in St. Louis is gratefully acknowledged. Electron microscopy work was performed at the Nano Research Facility (NRF) at Washington University in St. Louis.

References

1. Stankovich, S.; Dikin, D. A.; Dommett, G. H. B.; Kohlhaas, K. M.; Zimney, E. J.; Stach, E. A.; Piner, R. D.; Nguyen, S. T.; Ruoff, R. S., Graphene-Based Composite Materials. *Nature* **2006**, *442*, 282-286.
2. Westervelt, R., Graphene Nanoelectronics. *Science* **2008**, *320*, 324-325.
3. Shao, Y.; Wang, J.; Wu, H.; Liu, J.; Aksay, I. A.; Lin, Y., Graphene Based Electrochemical Sensors and Biosensors: A Review. *Electroanalysis* **2010**, *22*, 1027-1036.
4. Wang, W.-N.; Jiang, Y.; Fortner, J. D.; Biswas, P., Nanostructured Graphene-Titanium Dioxide Composites Synthesized by a Single-Step Aerosol Process for Photoreduction of Carbon Dioxide. *Environ. Eng. Sci.* **2014**, *31*, 428-434.
5. Gusain, R.; Kumar, P.; Sharma, O. P.; Jain, S. L.; Khatri, O. P., Reduced Graphene Oxide–CuO Nanocomposites for Photocatalytic Conversion of CO₂ into Methanol under Visible Light Irradiation. *Appl. Catal., B* **2016**, *181*, 352-362.
6. Novoselov, K. S.; Geim, A. K.; Morozov, S.; Jiang, D.; Zhang, Y.; Dubonos, S.; Grigorieva, I.; Firsov, A., Electric Field Effect in Atomically Thin Carbon Films. *Science* **2004**, *306*, 666-669.
7. Stoller, M. D.; Park, S.; Zhu, Y.; An, J.; Ruoff, R. S., Graphene-Based Ultracapacitors. *Nano Lett.* **2008**, *8*, 3498-3502.
8. Tai, J.-T.; Lai, Y.-C.; Yang, J.-H.; Ho, H.-C.; Wang, H.-F.; Ho, R.-M.; Tsai, D.-H., Quantifying Nanosheet Graphene Oxide Using Electrospray-Differential Mobility Analysis. *Analytical chemistry* **2015**, *87*, 3884-3889.
9. Pei, S.; Cheng, H.-M., The Reduction of Graphene Oxide. *Carbon* **2012**, *50*, 3210-3228.
10. Park, S.; Dikin, D. A.; Nguyen, S. T.; Ruoff, R. S., Graphene Oxide Sheets Chemically Cross-Linked by Polyallylamine. *J. Phys. Chem. C* **2009**, *113*, 15801-15804.
11. Luo, J.; Zhao, X.; Wu, J.; Jang, H. D.; Kung, H. H.; Huang, J., Crumpled Graphene-Encapsulated Si Nanoparticles for Lithium Ion Battery Anodes. *J. Phys. Chem. Lett.* **2012**, *3*, 1824-1829.
12. Wang, Y.; Wu, Y.; Huang, Y.; Zhang, F.; Yang, X.; Ma, Y.; Chen, Y., Preventing Graphene Sheets from Restacking for High-Capacitance Performance. *J. Phys. Chem. C* **2011**, *115*, 23192-23197.

13. Chen, Y.; Guo, F.; Jachak, A.; Kim, S.-P.; Datta, D.; Liu, J.; Kulaots, I.; Vaslet, C.; Jang, H. D.; Huang, J., Aerosol Synthesis of Cargo-Filled Graphene Nanosacks. *Nano Lett.* **2012**, *12*, 1996-2002.
14. Wang, W.-N.; Jiang, Y.; Biswas, P., Evaporation-Induced Crumpling of Graphene Oxide Nanosheets in Aerosolized Droplets: Confinement Force Relationship. *J. Phys. Chem. Lett.* **2012**, *3*, 3228-3233.
15. Jiang, Y.; Wang, W.-N.; Liu, D.; Nie, Y.; Li, W.; Wu, J.; Zhang, F.; Biswas, P.; Fortner, J. D., Engineered Crumpled Graphene Oxide Nanocomposite Membrane Assemblies for Advanced Water Treatment Processes. *Environ. Sci. Technol.* **2015**.
16. Ma, X.; Zachariah, M. R.; Zangmeister, C. D., Reduction of Suspended Graphene Oxide Single Sheet Nanopaper: The Effect of Crumpling. *J. Phys. Chem. C* **2013**, *117*, 3185-3191.
17. Jiang, Y.; Raliya, R.; Fortner, J. D.; Biswas, P., Graphene Oxides in Water: Correlating Morphology and Surface Chemistry with Aggregation Behavior. *Environ. Sci. Technol.* **2016**, *50*, 6964-6973.
18. Jiang, Y.; Wang, W.-N.; Biswas, P.; Fortner, J. D., Facile Aerosol Synthesis and Characterization of Ternary Crumpled Graphene–TiO₂–Magnetite Nanocomposites for Advanced Water Treatment. *ACS Appl. Mater. Interfaces* **2014**, *6*, 11766-11774.
19. Jang, H. D.; Kim, S. K.; Chang, H.; Roh, K.-M.; Choi, J.-W.; Huang, J., A Glucose Biosensor Based on TiO₂–Graphene Composite. *Biosensors Bioelectron.* **2012**, *38*, 184-188.
20. Jang, H. D.; Kim, S. K.; Chang, H.; Choi, J.-W.; Luo, J.; Huang, J., One-Step Synthesis of Pt-Nanoparticles-Laden Graphene Crumples by Aerosol Spray Pyrolysis and Evaluation of Their Electrocatalytic Activity. *Aerosol Sci. Technol.* **2013**, *47*, 93-98.
21. Kostarelos, K.; Novoselov, K. S., Exploring the Interface of Graphene and Biology. *Science* **2014**, *344*, 261-263.
22. Kulkarni, P.; Deye, G. J.; Baron, P. A., Bipolar Diffusion Charging Characteristics of Single-Wall Carbon Nanotube Aerosol Particles. *Journal of Aerosol Science* **2009**, *40*, 164-179.
23. Akhavan, O.; Ghaderi, E., Toxicity of Graphene and Graphene Oxide Nanowalls against Bacteria. *ACS nano* **2010**, *4*, 5731-5736.

24. Liu, S.; Zeng, T. H.; Hofmann, M.; Burcombe, E.; Wei, J.; Jiang, R.; Kong, J.; Chen, Y., Antibacterial Activity of Graphite, Graphite Oxide, Graphene Oxide, and Reduced Graphene Oxide: Membrane and Oxidative Stress. *Acs Nano* **2011**, *5*, 6971-6980.
25. Knutson, E.; Whitby, K., Aerosol Classification by Electric Mobility: Apparatus, Theory, and Applications. *Journal of Aerosol Science* **1975**, *6*, 443-451.
26. Fang, J.; Wang, Y.; Attoui, M.; Chadha, T. S.; Ray, J. R.; Wang, W.-N.; Jun, Y.-S.; Biswas, P., Measurement of Sub-2 Nm Clusters of Pristine and Composite Metal Oxides During Nanomaterial Synthesis in Flame Aerosol Reactors. *Anal. Chem.* **2014**, *86*, 7523-7529.
27. Wang, Y.; Fang, J.; Attoui, M.; Chadha, T. S.; Wang, W.-N.; Biswas, P., Application of Half Mini Dma for Sub 2 Nm Particle Size Distribution Measurement in an Electrospray and a Flame Aerosol Reactor. *J. Aerosol Sci.* **2014**, *71*, 52-64.
28. Vemury, S.; Pratsinis, S. E., Charging and Coagulation During Flame Synthesis of Silica. *Journal of aerosol science* **1996**, *27*, 951-966.
29. Wang, Y.; Sharma, G.; Koh, C.; Kumar, V.; Chakrabarty, R.; Biswas, P., Influence of Flame-Generated Ions on the Simultaneous Charging and Coagulation of Nanoparticles During Combustion. *Aerosol Science and Technology* **2017**, just accepted.
30. Wang, Y.; Kangasluoma, J.; Attoui, M.; Fang, J.; Junninen, H.; Kulmala, M.; Petäjä, T.; Biswas, P., The High Charge Fraction of Flame-Generated Particles in the Size Range Below 3 Nm Measured by Enhanced Particle Detectors. *Combust. Flame* **2017**, *176*, 72-80.
31. Wang, Y.; Liu, P.; Fang, J.; Wang, W.-N.; Biswas, P., Kinetics of Sub-2 Nm TiO₂ Particle Formation in an Aerosol Reactor During Thermal Decomposition of Titanium Tetraisopropoxide. *J. Nanopart. Res.* **2015**, *17*, 1-13.
32. Wang, Y.; Kangasluoma, J.; Attoui, M.; Fang, J.; Junninen, H.; Kulmala, M.; Petäjä, T.; Biswas, P., Observation of Incipient Particle Formation During Flame Synthesis by Tandem Differential Mobility Analysis-Mass Spectrometry (Dma-MS). *Proceedings of the Combustion Institute* **2017**, *36*, 745-752.
33. Jiang, J.; Lee, M.-H.; Biswas, P., Model for Nanoparticle Charging by Diffusion, Direct Photoionization, and Thermionization Mechanisms. *Journal of electrostatics* **2007**, *65*, 209-220.

34. Enghoff, M.; Svensmark, H., The Role of Atmospheric Ions in Aerosol Nucleation—a Review. *Atmospheric Chemistry and Physics* **2008**, *8*, 4911-4923.
35. Jing, H.; Wang, X.; Wang, W.-N.; Biswas, P., Elemental Mercury Oxidation in an Electrostatic Precipitator Enhanced with in Situ Soft X-Ray Irradiation. *Journal of the Air & Waste Management Association* **2015**, *65*, 455-465.
36. Wiedensohler, A.; Fissan, H., Bipolar Charge Distributions of Aerosol Particles in High-Purity Argon and Nitrogen. *Aerosol Science and Technology* **1991**, *14*, 358-364.
37. Friedlander, S. K., *Smoke, Dust, and Haze*; Oxford university press New York, 2000; Vol. 198.
38. Fuchs, N., On the Stationary Charge Distribution on Aerosol Particles in a Bipolar Ionic Atmosphere. *Geofisica pura e applicata* **1963**, *56*, 185-193.
39. Hoppel, W. A.; Frick, G. M., Ion—Aerosol Attachment Coefficients and the Steady-State Charge Distribution on Aerosols in a Bipolar Ion Environment. *Aerosol Science and Technology* **1986**, *5*, 1-21.
40. Maricq, M. M., Bipolar Diffusion Charging of Soot Aggregates. *Aerosol Sci. Technol.* **2008**, *42*, 247-254.
41. Kim, S.; Woo, K.; Liu, B.; Zachariah, M., Method of Measuring Charge Distribution of Nanosized Aerosols. *J. Colloid Interface Sci.* **2005**, *282*, 46-57.
42. Sahu, M.; Park, J.; Biswas, P., In Situ Charge Characterization of Tio₂ and Cu–Tio₂ Nanoparticles in a Flame Aerosol Reactor. *Journal of Nanoparticle Research* **2012**, *14*, 1-11.
43. Hummers Jr, W. S.; Offeman, R. E., Preparation of Graphitic Oxide. *J. Am. Chem. Soc.* **1958**, *80*, 1339-1339.
44. Jing, H.; He, S.; Ou, Q.; Hsiao, T.-C.; Chen, D.-R., Development of a Compact Electrostatic Nanoparticle Sampler for Offline Aerosol Characterization. *Mapan* **2013**, *28*, 217-226.
45. Nie, Y.; Wang, W.-N.; Jiang, Y.; Fortner, J.; Biswas, P., Crumpled Reduced Graphene Oxide–Amine–Titanium Dioxide Nanocomposites for Simultaneous Carbon Dioxide Adsorption and Photoreduction. *Catal. Sci. Technol.* **2016**.
46. Jiang, J.; Kim, C.; Wang, X.; Stolzenburg, M. R.; Kaufman, S. L.; Qi, C.; Sem, G. J.; Sakurai, H.; Hama, N.; McMurry, P. H., Aerosol Charge Fractions Downstream of Six

Bipolar Chargers: Effects of Ion Source, Source Activity, and Flowrate. *Aerosol Science and Technology* **2014**, *48*, 1207-1216.

47. Hoppel, W. A.; Frick, G. M., Ion-Aerosol Attachment Coefficients and the Steady-State Charge Distribution on Aerosols in a Bipolar Ion Environment. *Aerosol Sci. Technol.* **1986**, *5*, 1-21.

48. Reischl, G.; Mäkelä, J.; Karch, R.; Nucid, J., Bipolar Charging of Ultrafine Particles in the Size Range Below 10 Nm. *J. Aerosol Sci.* **1996**, *27*, 931-949.

49. Kallinger, P.; Steiner, G.; Szymanski, W. W., Characterization of Four Different Bipolar Charging Devices for Nanoparticle Charge Conditioning. *Journal of Nanoparticle Research* **2012**, *14*, 1-8.

50. Maißer, A.; Thomas, J. M.; Larriba-Andaluz, C.; He, S.; Hogan, C. J., The Mass-Mobility Distributions of Ions Produced by a Po-210 Source in Air. *J. Aerosol Sci.* **2015**, *90*, 36-50.

51. Steiner, G.; Reischl, G. P., The Effect of Carrier Gas Contaminants on the Charging Probability of Aerosols under Bipolar Charging Conditions. *Journal of aerosol science* **2012**, *54*, 21-31.

52. Tigges, L.; Jain, A.; Schmid, H.-J., On the Bipolar Charge Distribution Used for Mobility Particle Sizing: Theoretical Considerations. *J. Aerosol Sci.* **2015**, *88*, 119-134.

53. Gopalakrishnan, R.; McMurry, P. H.; Hogan Jr, C. J., The Bipolar Diffusion Charging of Nanoparticles: A Review and Development of Approaches for Non-Spherical Particles. *Aerosol Sci. Technol.* **2015**, *49*, 1181-1194.

54. Wiedensohler, A., An Approximation of the Bipolar Charge Distribution for Particles in the Submicron Size Range. *Journal of Aerosol Science* **1988**, *19*, 387-389.

55. Wiedensohler, A.; Fissan, H. J., Bipolar Charge Distributions of Aerosol Particles in High-Purity Argon and Nitrogen. *Aerosol Science and Technology* **1991**, *14*, 358-364.

56. Shin, W. G.; Qi, C.; Wang, J.; Fissan, H.; Pui, D. Y., The Effect of Dielectric Constant of Materials on Unipolar Diffusion Charging of Nanoparticles. *Journal of Aerosol Science* **2009**, *40*, 463-468.

57. Brinker, C. J.; Lu, Y.; Sellinger, A.; Fan, H., Evaporation-Induced Self-Assembly: Nanostructures Made Easy. *Adv. Mater.* **1999**, *11*, 579-585.

58. Wen, X.; Garland, C. W.; Hwa, T.; Kardar, M.; Kokufuta, E.; Li, Y.; Orkisz, M.; Tanaka, T., Crumpled and Collapsed Conformation in Graphite Oxide Membranes. **1992**.
59. Sorensen, C., The Mobility of Fractal Aggregates: A Review. *Aerosol Sci. Technol.* **2011**, *45*, 765-779.
60. Chakrabarty, R. K.; Moosmüller, H.; Arnott, W. P.; Garro, M. A.; Slowik, J. G.; Cross, E. S.; Han, J.-H.; Davidovits, P.; Onasch, T. B.; Worsnop, D. R., Light Scattering and Absorption by Fractal-Like Carbonaceous Chain Aggregates: Comparison of Theories and Experiment. *Appl. Opt.* **2007**, *46*, 6990-7006.
61. Rogak, S. N.; Flagan, R. C.; Nguyen, H. V., The Mobility and Structure of Aerosol Agglomerates. *Aerosol Sci. Technol.* **1993**, *18*, 25-47.
62. Maißer, A.; Thomas, J. M.; Larriba-Andaluz, C.; He, S.; Hogan, C. J., The Mass-Mobility Distributions of Ions Produced by a Po-210 Source in Air. *Journal of Aerosol Science* **2015**, *90*, 36-50.
63. Bagri, A.; Mattevi, C.; Acik, M.; Chabal, Y. J.; Chhowalla, M.; Shenoy, V. B., Structural Evolution During the Reduction of Chemically Derived Graphene Oxide. *Nat Chem* **2010**, *2*, 581-587.

Chapter 2 Supporting Information

Table of Contents

S2.1 Extra TEM images of typical CGO synthesized at 200 °C

S2.2 Extra TEM images of typical CGO synthesized at 400 °C

S2.3 Extra TEM images of typical CGO synthesized at 600 °C

S2.4 Extra TEM images of typical CGO synthesized at 800 °C

S2.5 The distributions of projected area equiv. diameter of CGO

S2.1 TEM images of typical CGO synthesized at 200 °C, 60 nm (1a-1d), 100 nm (2a-2d), 140 nm (3a-3d), 180 nm (4a-4d). (Note: the scale bars are different in different images)

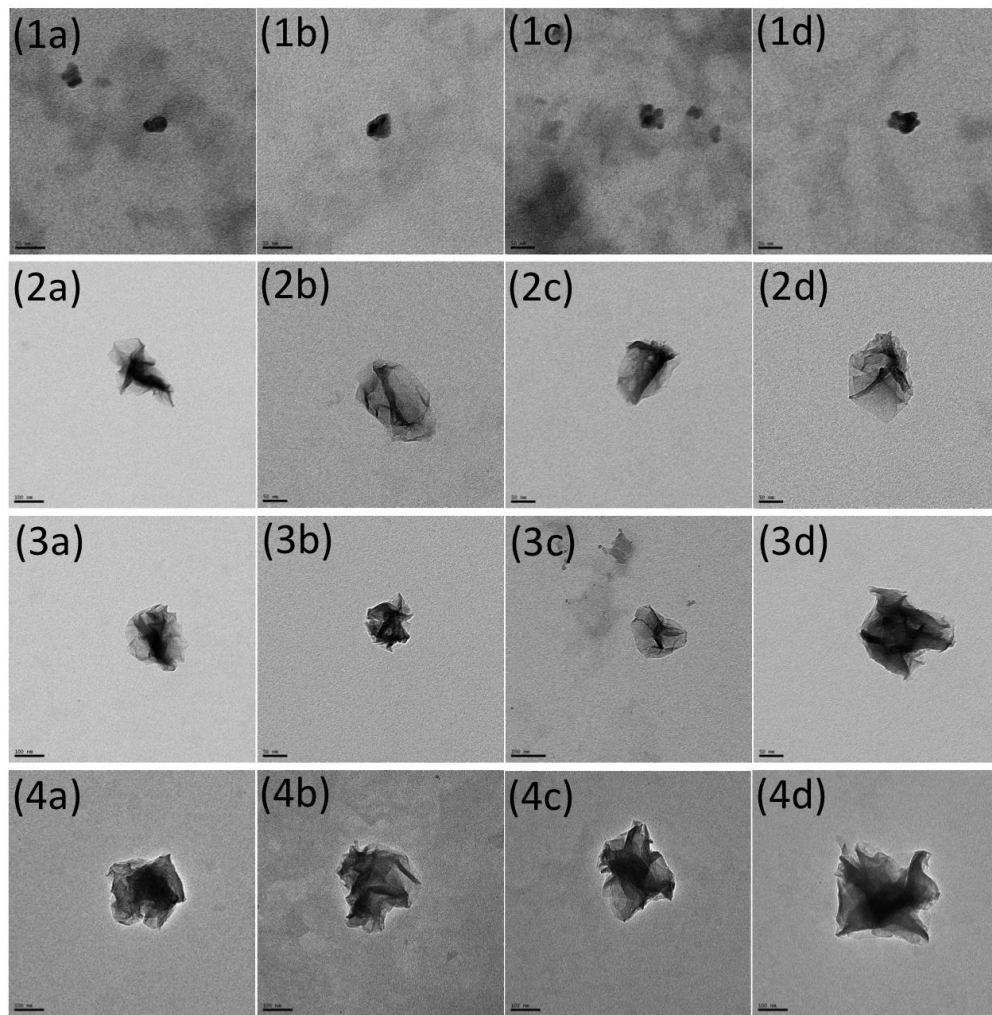


Figure S2.1 TEM images of typical CGO synthesized at 200 °C, 60 nm (1a-1d), 100 nm (2a-2d), 140 nm (3a-3d), 180 nm (4a-4d).

S2.2 TEM images of typical CGO synthesized at 400 °C, 60 nm (1a-1d), 100 nm (2a-2d), 140 nm (3a-3d), 180 nm (4a-4d). (Note: the scale bars are different in different images)

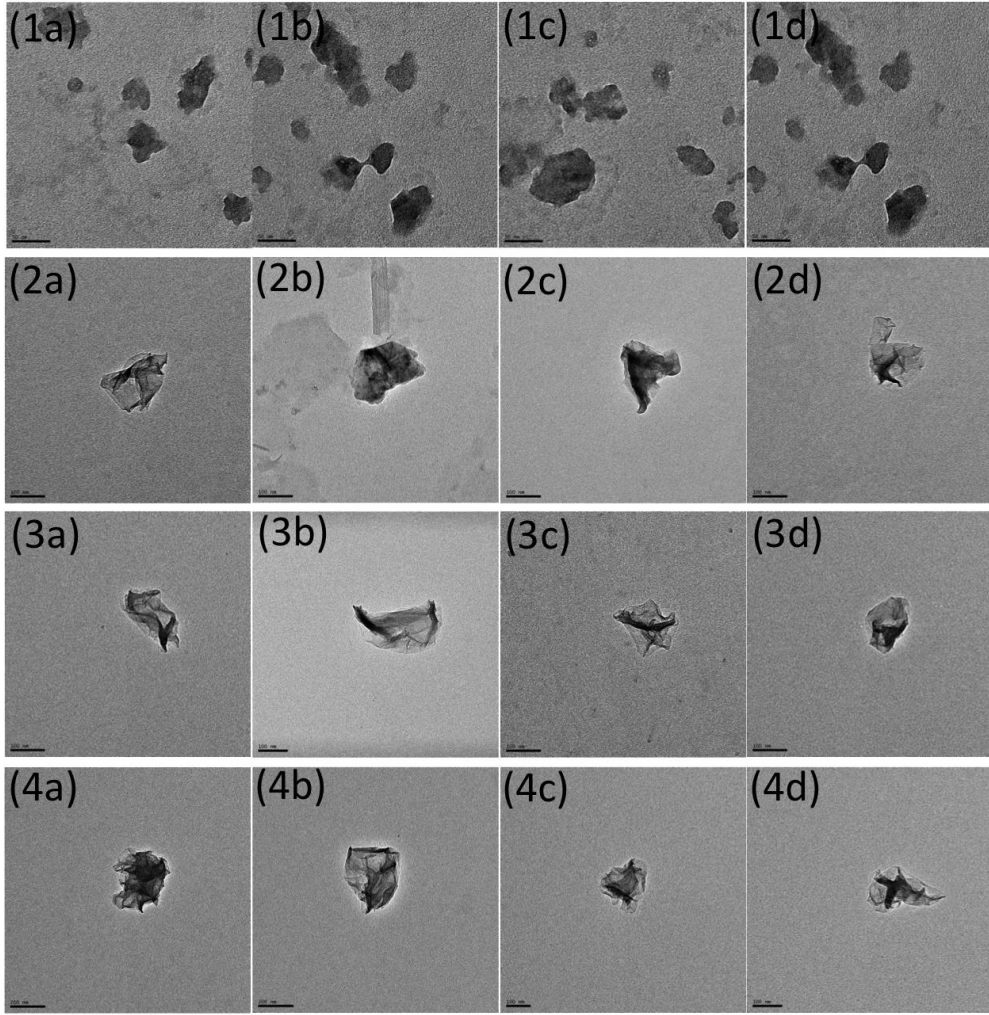


Figure S2.2 TEM images of typical CGO synthesized at 400 °C, 60 nm (1a-1d), 100 nm (2a-2d), 140 nm (3a-3d), 180 nm (4a-4d).

S2.3 TEM images of typical CGO synthesized at 600 °C, 60 nm (1a-1d), 100 nm (2a-2d), 140 nm (3a-3d), 180 nm (4a-4d). (Note: the scale bars are different in different images)

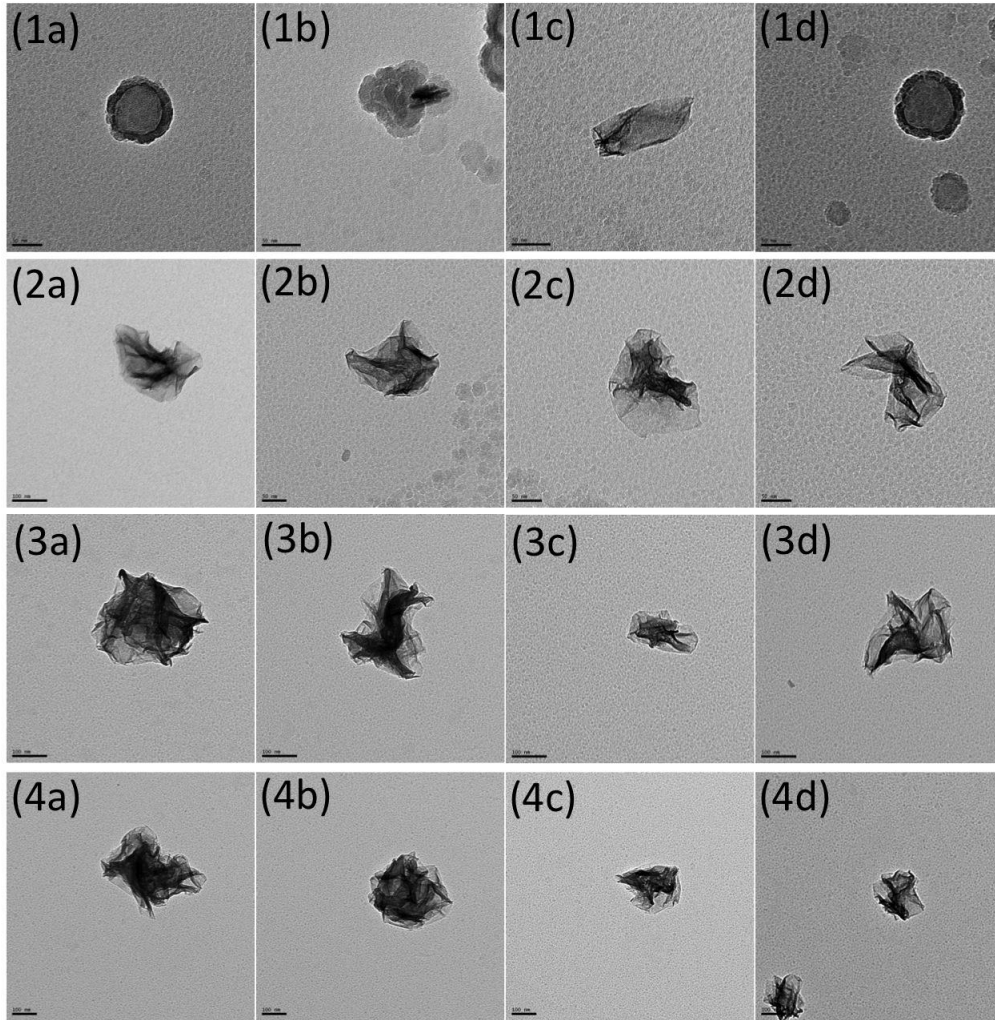


Figure S2.3 TEM images of typical CGO synthesized at 600 °C, 60 nm (1a-1d), 100 nm (2a-2d), 140 nm (3a-3d), 180 nm (4a-4d).

S2.4 TEM images of typical CGO synthesized at 800 °C, 60 nm (1a-1d), 100 nm (2a-2d), 140 nm (3a-3d), 180 nm (4a-4d). (Note: the scale bars are different in different images)

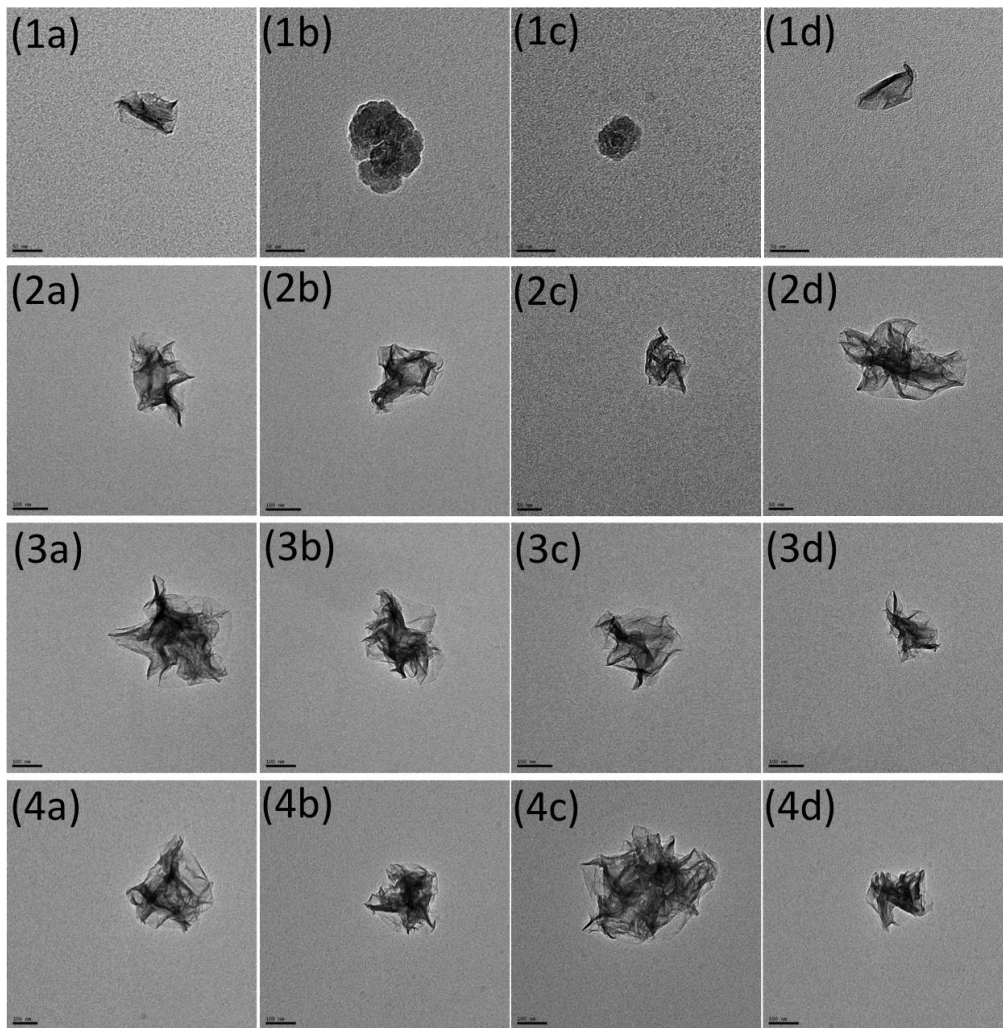


Figure S2.4 TEM images of typical CGO synthesized at 800 °C, 60 nm (1a-1d), 100 nm (2a-2d), 140 nm (3a-3d), 180 nm (4a-4d).

S2.5 The distributions of projected area equiv. diameter of CGO synthesized at 200 °C, 60, 100, 140, 180 nm (1a-1d), 400 °C, 60, 100, 140, 180 nm (2a-2d), 600 °C, 60, 100, 140, 180 nm (3a-3d), 800 °C, 60, 100, 140, 180 nm (4a-4d).

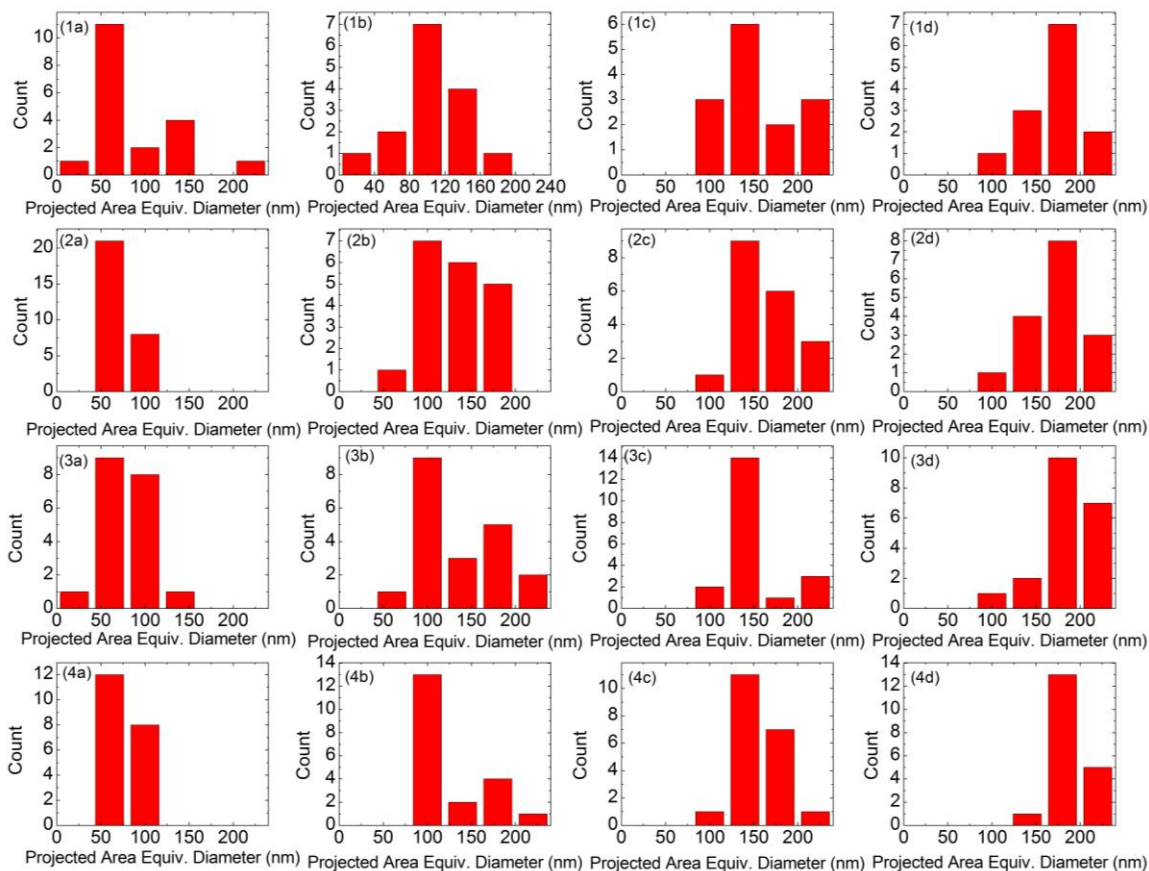


Figure S2.5 The distributions of projected area equiv. diameter of CGO synthesized at 200 °C, 60, 100, 140, 180 nm (1a-1d), 400 °C, 60, 100, 140, 180 nm (2a-2d), 600 °C, 60, 100, 140, 180 nm (3a-3d), 800 °C, 60, 100, 140, 180 nm (4a-4d).

Chapter 3 Graphene Synthesized as by-Product of Gas Purification in Long-term Space Missions and its Lithium-ion Battery Application

The results reported in this chapter were published in - Nie, Yao, Clayton Kacica, Marit E. Meyer, Robert D. Green, and Pratim Biswas. "Graphene Synthesized as by-Product of Gas Purification in Long-term Space Missions and its Lithium-ion Battery Application." Advances in Space Research 62, 5, (2018): 1015-1024. Reproduced with permission from Elsevier, copyright 2018.

Abstract

To support long-term missions in space, it is important to recycle valuable consumables, such as oxygen (O₂) and water. In a Sabatier reactor, hydrogen is employed to reduce carbon dioxide (CO₂) to methane (CH₄) and O₂, then an integrated system is designed to recycle hydrogen from CH₄, which includes a methane purification assembly (MePA), a plasma pyrolysis assembly (PPA), an acetylene separation assembly (ASepA). In the PPA reactor, carbon particulates were observed to form as a by-product. In this study, this carbon material was characterized, and a significant fraction is graphene with a low oxygen content. HRTEM images clearly showed a partially crystalline hexagonal structure, which is a characteristic graphene signature. The specific surface area of the graphene was measured to be 258.5 m²/g, only one tenth of the theoretical value of single layer graphene, which can be attributed to stacking of the few layers and partial crumpling of this material. To explore potential uses of this material, the crumpled graphene was used to synthesize anodes of lithium-ion batteries (LIBs), which were then tested for their electrochemical performance. In long-term cycle tests, LIBs made with crumpled graphene demonstrated a high retention rate after the first cycle, indicating very little additional degradation of the electrode. The high stability of the cells can be attributed to the greater variety and higher number of lithium ion storage sites in the crumpled graphene, compared with bulk graphite. Considering the crumpled graphene as a by-product and the high electrochemical performance of the crumpled graphene LIBs, crumpled graphene synthesized in the NASA plasma reactor has great promise in better supporting the long-duration space missions.

3.1 Introduction

As planning proceeds for the Mars Mission, it will be imperative that humans can stay for longer durations in space.¹ NASA has an ambitious goal of sending human beings to Mars in the 2030s. During short-duration missions of days or weeks, open-loop life-support systems are usually adopted due to their simplicity and reliability. In these open-loop systems, stored consumables, such as water and oxygen, are used once and discarded in forms of metabolic wastes, like exhaled carbon dioxide (CO₂) and volatile organic compounds. However, for longer-term missions with duration of months and years, such as humans going to Mars, the mass of consumables needed is greater, and it becomes more advantageous to recover water and oxygen from the metabolic wastes. From this perspective, closed-loop air revitalization architecture, in which 100% of oxygen and water are recovered, is highly desirable. Presently, the Carbon Dioxide Removal Assembly (CDRA) on the International Space Station (ISS) removes CO₂ from the cabin atmosphere by temperature swing adsorption onto regenerable zeolite beds.² The Carbon Dioxide Reduction Assembly (CRA) reduces this captured CO₂ to water and methane (CH₄) via the Sabatier reaction,³ $CO_2 + 4H_2 \rightarrow 2H_2O + CH_4$.

The H₂ required for the Sabatier reaction is generated by the Oxygen Generation Assembly (OGA) that electrolyzes water to provide breathable oxygen for the cabin atmosphere. Unfortunately, the generated CH₄ is treated as a waste product, and the stoichiometry of this system results in only a 50% hydrogen recovery rate due to the hydrogen lost from the CH₄ vented overboard.³ The extra water required to balance this hydrogen loss is supplied to the ISS by resupply from Earth, but for a long-duration mission to Mars or another planet, the logistics would be more formidable. It would be highly

desirable to develop a technology to close the loop, or at least achieve a substantial increase in the hydrogen recovery rate.

To improve the hydrogen recovery rate of the CRA, NASA has under development a Plasma Pyrolysis Assembly (PPA), to convert the CH_4 to acetylene (C_2H_2) and recover a larger portion of the hydrogen. The integrated system currently planned for use on the International Space Station is shown in Figure 3.1 and consists of: the CRA which includes the Sabatier reactor, the PPA, and a Hydrogen Purification Assembly (HyPA).³⁻⁵ This combined system has the potential to increase the hydrogen recovery rate to 75%. In the CRA, a condenser removes H_2O , which is recycled for other uses, and CO_2 is compressed and stored until sufficient H_2 is available from the OGA. Additional H_2 is introduced into the PPA reactor, where CH_4 is decomposed, via plasma pyrolysis, into different hydrocarbon species based on the reactions, $\text{CH}_4 \rightarrow \text{CH}_x + y\text{H}_2$. In the HyPA, the H_2 is purified and becomes available for the CRA, thus largely closing the loop. At this time, acetylene will be vented out of the spacecraft as a waste product, but eventually it could be stored and used for fuel or cold-gas thrust. It is worth noting that unwanted carbon particulates could also be generated in the plasma reactor, which would deposit on the reactor and affect the performance.

There have been a lot of reports on the synthesis of carbon materials in a plasma enhanced chemical vapor deposition (PECVD) system.⁶⁻¹¹ Compared with common thermal chemical vapor deposition (T-CVD), PECVD have advantages, such as a lower substrate temperature, higher growth selectivity and better control in nanostructure ordering/patterning of the final products, which are due to the presence of energetic electrons, excited molecules and atoms, free radicals, photons, and other active species in

the plasma region.¹²⁻¹⁵ On the other hand, growth of carbon atoms on the substrate is a more complex process, compared with T-CVD methods, and the morphology and structure of the final carbon products are highly dependent on the plasma source and a series of operation parameters, such as gas precursors, temperature, pressure, and type of substrate.¹⁶

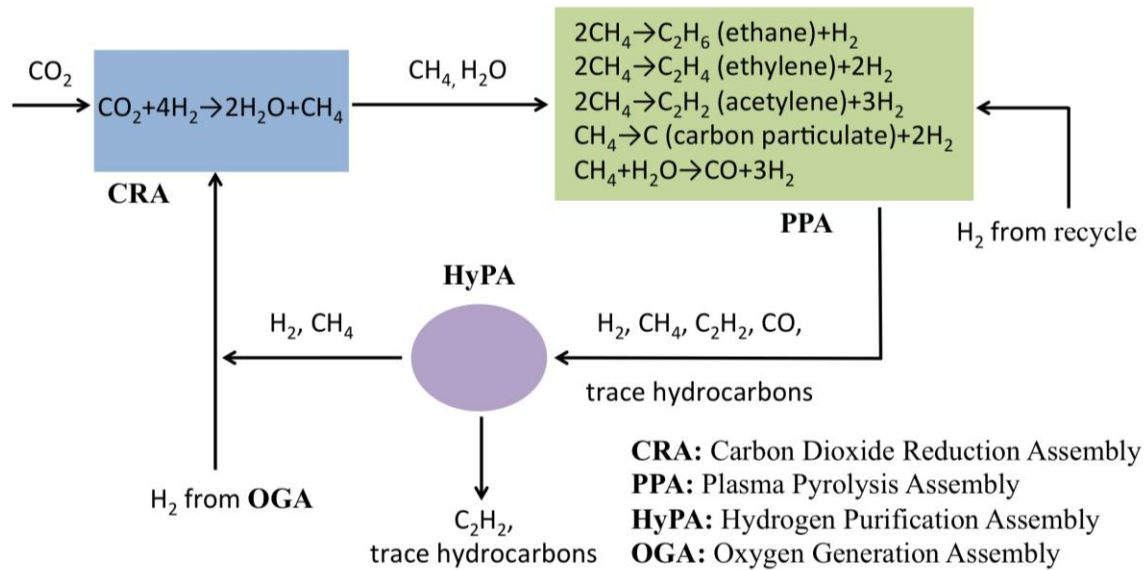


Figure 3.1 Methane post-processing initial architecture concept diagram.

Based on NASA's previous research,^{3-4, 17} the decomposition efficiency of CH_4 and the formation rate of particulate carbon largely depends on the ratio of H_2 to CH_4 in the reactant gas, because the H_2 was found to be a co-catalyst in graphene synthesis and also an etching reagent that controls the size and shape of the carbon domains.¹⁸⁻¹⁹ A hydrogen rich stream, i.e. ratio of H_2/CH_4 gas of 5:1, was used in this test to minimize the formation of carbon particulates.⁴ A stainless steel cylindrical carbon trap was placed inside the plasma reactor, which acted as a substrate for the carbon formation. After the plasma pyrolysis, the carbon material was scraped off the trap and collected for further characterization and application.

The objectives of this study are to examine by-products produced in the integrated NASA system to be used in space missions. Specifically, the synthesis process of the carbon material formed in a PPA reactor will be studied. The as-produced carbon material will be analyzed for its chemical and physical properties. The potential applications of the as-produced carbonaceous material will be investigated.

3.2 Experimental section

The first part of the study was to use the integrated NASA system to recycle methane produced in the Sabatier reaction to generate hydrogen and a carbonaceous byproduct. The second part of the study was characterization of the carbonaceous byproduct. The final part was to explore potential application of this byproduct.

3.2.1 Carbonaceous byproduct formation

To reduce CH_4 after the Sabatier reaction and recycle H_2 , NASA's integrated system will include a CRA, a PPA, and a HyPA. In the Sabatier reactor, CO_2 is reduced by H_2 to form CH_4 and H_2O . In the CRA condenser, residual water vapor is removed, and the CH_4 and additional H_2 are introduced into the PPA. In the PPA reactor, CH_4 decomposes to different hydrocarbon species, and there is also unwanted carbon particulate generated from a side reaction. Based on NASA's previous research, the formation rate of carbon particulate largely depends on the ratio of H_2 to CH_4 in the reactant gas. A ratio of H_2/CH_4 gas of 5:1 was used in this test to minimize the formation of carbon particulates.⁴

A fully assembled PPA prototype and the PPA reactor that was used for tests are shown in Figure 3.2 (a) and (b) respectively.¹⁷ In order to collect and remove the carbon particulate, a final carbon trap was placed inside the PPA reactor (Figure 3.2 (c)). This trap design consists of six 0.5 in. diameter cylindrical screens positioned equally around the

outer circumference of an internal 0.5 in. diameter cartridge heater and confined by a 1.5 in. diameter outer screen. The ends of this assembly are captured by custom aluminum end-rings. The inlet end-ring has six holes equally spaced around its face that line up with the inside end of each of the six screen cylinders. This relatively simple geometric design benefits from carbon in close proximity to the internal cartridge heater and therefore should experience higher regeneration temperatures where needed at the point of highest loading. Each of the six internal (40 mesh, 0.01 inch diameter, 316 ss) screens uses its entire length to capture carbon. The external (80 mesh, 0.0037 inch diameter, 316 ss) screen provides a secondary, smaller hole size, surface for further carbon capture. The effluent gas stream then passes out around the external circumference at the opposite end of the trap. During the PPA reaction, carbon particulates are formed and collected by the carbon trap. After the reaction, these carbon particulates are scraped off the carbon trap for subsequent use. The average production rate of the crumpled graphene with these settings is about 0.05 g/h. (Wheeler et al. , 2014) However, this is the lowest rate and could be increased with different reactor settings.

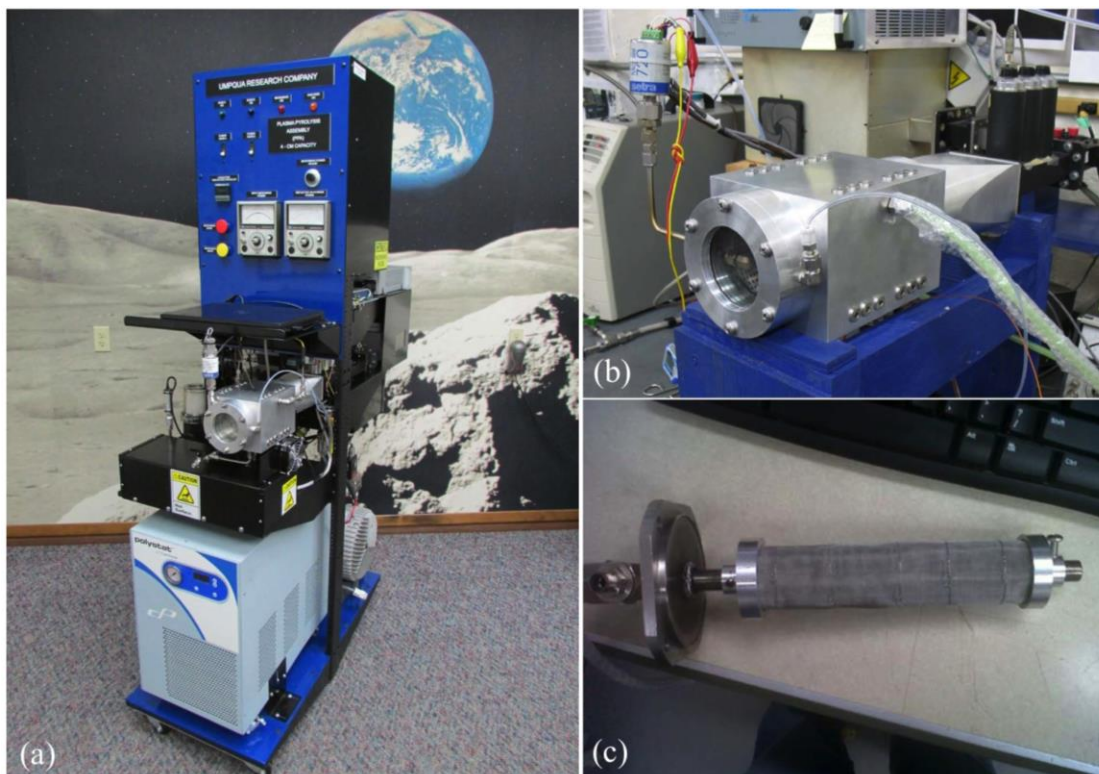


Figure 3.2 Photographs of (a) a fully assembled PPA prototype; (b) PPA reactor installed on a microwave development test stand; (c) cylindrical screen type carbon trap assembly inside the PPA reactor. (Image source17)

3.2.2 Carbonaceous byproduct characterization

The morphology and size of these carbon particulates were examined by field emission scanning electron microscopy (FE-SEM, NOVA NanoSEM 230, FEI Co.), and transmission electron microscopy (TEM, Tecnai TM Spirit, FEI Co.), and high resolution-TEM (HR-TEM, JEOL 2100) with an accelerating voltage of 200 kV. The specific surface area, pore diameter, and total pore volume of the synthesized materials were measured using a surface area and pore diameter distribution analyzer (Micromeritics, ASAP 2020, USA). Pore volumes were obtained from the volumes of nitrogen adsorbed at $P/P_0 = 0.95$ or in the vicinity. The crystal phase was determined by X-ray Diffraction (XRD) (Geigerflex D-MAX/A, Rigaku Denki) with Cu $K\alpha$ radiation ($\lambda = 1.548 \text{ \AA}$). The surface

chemical properties, including molecular bonds and functional groups, were analyzed by laser Raman spectrometry (Renishaw InVia Reflex confocal Raman spectrometer, with a 514 nm laser) and X-ray photoelectron spectroscopy (XPS, PHI 5000 VersaProbe II equipped with a monochromatic Al K α (1486.6 eV) X-ray source). XPS data analysis was performed using PHI MultiPak software, after performing a Shirley background correction.

3.2.3 Application of the carbonaceous byproduct

Since the PPA does generate a carbonaceous byproduct that is not recycled, it is beneficial to recycle of this waste product to something useful during a long-duration mission. In past technology development of Bosch reactor and other carbon formation reactor work, suggested applications of the solid carbon waste product included using in in-situ building materials or plant growing media. But given the initial characterization work performed by NASA on the PPA carbon particulates indicated the possibility the material may be graphene-based,²⁰ more valuable applications would include water filtration membranes²¹ or filter media, and intercalation matrices for Li-ion battery electrodes. In this paper, we perform a preliminary investigation of the feasibility of this second suggestion.

3.2.3.1 Fabrication of electrodes and coin cell batteries

A slurry casting technique was used to fabricate the working electrodes on a piece of 25- μ m thick stainless-steel foil (SS316, ESPI Metals, OR, USA). The slurry consisted of the carbonaceous material (90 wt%) and a binder polyvinylidene fluoride (10 wt%) in N-methylpyrrolidinone solvent. The electrodes were dried at 120°C in a vacuum oven for 24 hours. The mass loading of the electrodes ranged between 2.74 -3.40 mg/cm².

Coin cells (CR2032) were assembled using the carbonaceous material working electrodes and lithium foil as the counter electrode. An Ar-glovebox (Unilab, MBraun Inc, USA) with O₂ and H₂O concentrations maintained at <0.1 ppm levels was used to fabricate the cells. The electrolyte was composed of 1 M LiPF₆ salt dissolved in ethylene carbonate/dimethyl carbonate/diethyl carbonate (EC/DMC/DEC = 1:1:1 volume ratio) (MTI corporation, CA, USA). The cells were aged for 24 hours before testing.

3.2.3.2 Electrochemical testing of the LIBs performance

All electrochemical characterization was performed on coin cell type cells assembled as described above, using a multichannel potentiostat/galvanostat (Bio-logic USA, TN, USA). Cyclic voltammetry was performed at a sweep rate of 1 mV/s between 0.05 – 3.2 V for a total of 5 cycles. A rate capability analysis was performed by using galvanostatic charge/discharge cycles at various rates, including 300, 500, 1000, and 3000 mA g⁻¹, for a total of 6 cycles per rate. The long-term stability of the electrodes was tested by performing 100 galvanostatic charge/discharge cycles at a rate of 500 mA g⁻¹.

All the experimental plans are included in Table 3.1.

Table 3.1 Experimental plan

Test number	Test conducted	Instuments/ methodology used	Detailed objective
1	Material characterization of crumpled graphene (morphology and size)	SEM, TEM, HRTEM	Investigate the morphology and size of the carbon material synthesized in the plasma reactor from NASA

2	Material characterization of crumpled graphene (crystal structure and surface chemistry)	XRD, Raman, XPS, specific surface area, pore size distribution	Characterise the carbon material to be crumpled graphene, and investigate the chemical properties of the material for better future application
3	Fabrication of electrodes and coin cell batteries	Slurry casting technique/ Ar-glovebox	Fabricate crumpled graphene LIBs for further testing
4	Electrochemical performance test	Multichannel potentiostat/galvanostat	Study the rate capacity and Coulombic efficiency of the LIBs; investigate the stability of the LIBs as a function of cycle number

3.3 Results and discussion

3.3.1 Carbonaceous byproduct characterization

Figure 3.3(a) shows a SEM image of typical carbon particulate agglomerates. It can be seen that the crumpled primary particles agglomerate with each other, which makes the boundaries of a single primary particle undistinguishable. Because the scale bar in the image is 1 μm , the sizes of the primary particles are around several hundred nanometers. Figure 3.3(b) and 3.3(c) show the TEM images of typical carbon particulate agglomerates and a single primary particle, respectively. To prepare the TEM grid for examination, the carbon particulates were first dissolved into dimethylformamide (DMF) solution. Then a drop was placed onto the grid surface and let dry. This procedure was repeated for several times to ensure enough carbon particulates were deposited onto the grid. As seen in Figure 3.3(b), the particles agglomerated at a high concentration, and some large carbon flakes were also observed. A single particle was measured to be around 300-400 nm and had a crumpled ball-like structure, as shown in Figure 3.3(c). This crumpled structure could minimize the contact area of each particle and reduce possible restacking. In a higher

resolution image of a typical agglomerate (Figure 3.3(d)), most part of the imaged agglomerate is transparent, indicating the small number of layers in these particulates.

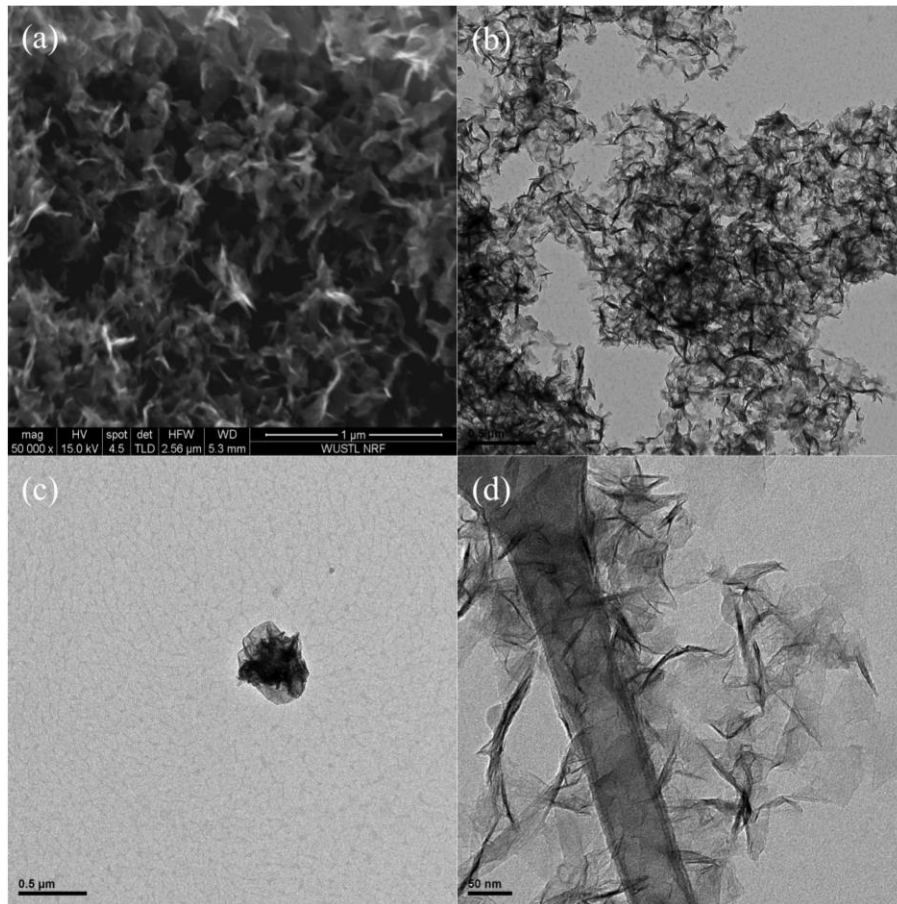


Figure 3.3 (a) SEM image of the carbon particulates; TEM images of carbon particulates: (b) low magnification image of agglomerates, (c) low magnification image of a single particle, (d) high magnification image of agglomerates.

To further observe the thickness of these crumpled particles and also the lattice structure, HRTEM and electron diffraction characterization was employed. In Figure 3.4(a), a clear lattice pattern is observed, with multiple phases. As outlined in the red rectangle, an array of atoms is arranged in a hexagonal atomic arrangement, which is typical of graphene. The lattice size (in-plane interatomic distance) was measured to be around 0.22 nm. The rectangular area outlined in Figure 3.4(b) shows the edge region of

the particulate. There are around 5 layers, each with a thickness of around 0.36 nm (inter-plane distance between neighboring carbon atoms). The ring-shaped electron diffraction pattern also confirms the multiple phase property. The two rings correspond to the (100) and (110) planes for hexagonal crystals, respectively.²² HRTEM images imply that these carbon particulates have similar atom arrangement and electron diffraction pattern typical of graphene. However, further surface chemistry and crystal structure characterizations were needed.

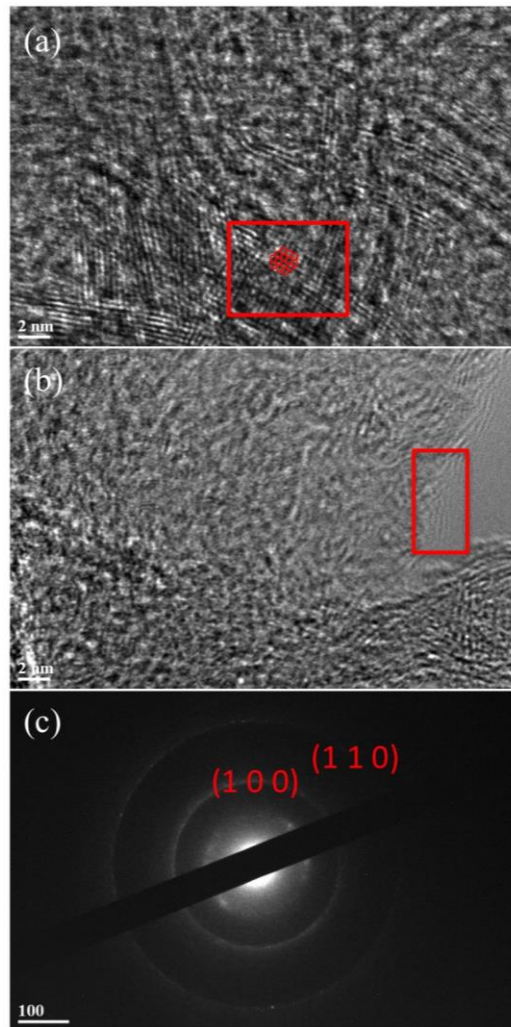


Figure 3.4 HRTEM images of the carbon particulates, (a) ordered crystal structure outlined by a red rectangle, (b) structures near the edge outlined by a red rectangle. (c) Electron diffraction pattern of the carbon particulates.

Figure 3.5 shows the XRD spectrum of the carbon particulates. Several characteristic peaks, which correspond to known peak values for graphite, can be found in this spectrum. The peaks at 26.4° and 77.8° are the C(002) and C(110) peaks, respectively, and were used to calculate the in-plane atomic distance and inter-plane distance.²³ Because the wavelength of the X-rays used in the experiment was 1.548 \AA , the in-plane atomic distance and the inter-plane distance were calculated to be 0.25 nm and 0.34 nm , which are consistent with our HRTEM results, and are also consistent, within the experimental error, with the theoretical graphite values.²⁴

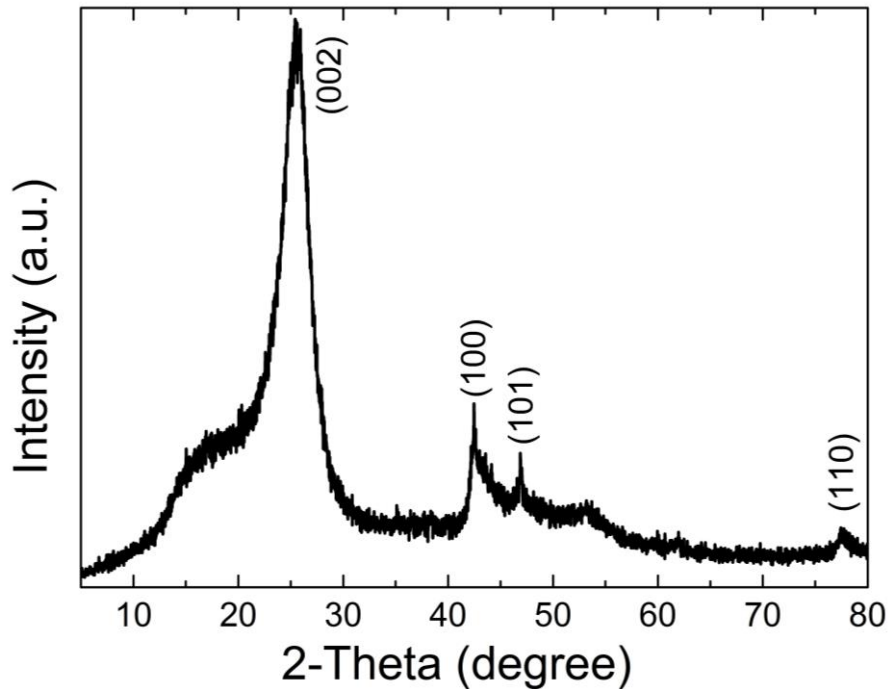


Figure 3.5 XRD spectrum of the carbon particulates.

Figure 3.6 shows the Raman spectrum of the carbon particulate, where three major peaks can be found. The first peak, around 1350 cm^{-1} , is the D band, which is disorder-induced and caused by phonon scattering at defect sites and impurities.²⁵ The next major peak on the Raman spectrum is the G band, at 1570 cm^{-1} , which is related to phonon

vibrations in sp^2 carbon material. The intensity ratio of the D band to the G band is denoted as the R value, which is by definition inversely proportional to quality and is ideally zero for highly ordered graphite.²⁶ The R value was measured to be around 0.55 for this carbon material, indicating the existence of defects in the sample, which is consistent with the HRTEM results. The third notable peak lies at around 2700 cm^{-1} , and is the G' or 2D band, a characteristic band for graphite-based materials. However, the shape of the 2D band, more specifically the absence of a typical graphite shoulder at 2680 cm^{-1} , is a characteristic feature of this carbon material,²⁷ indicating it is more like graphene than bulk graphite.

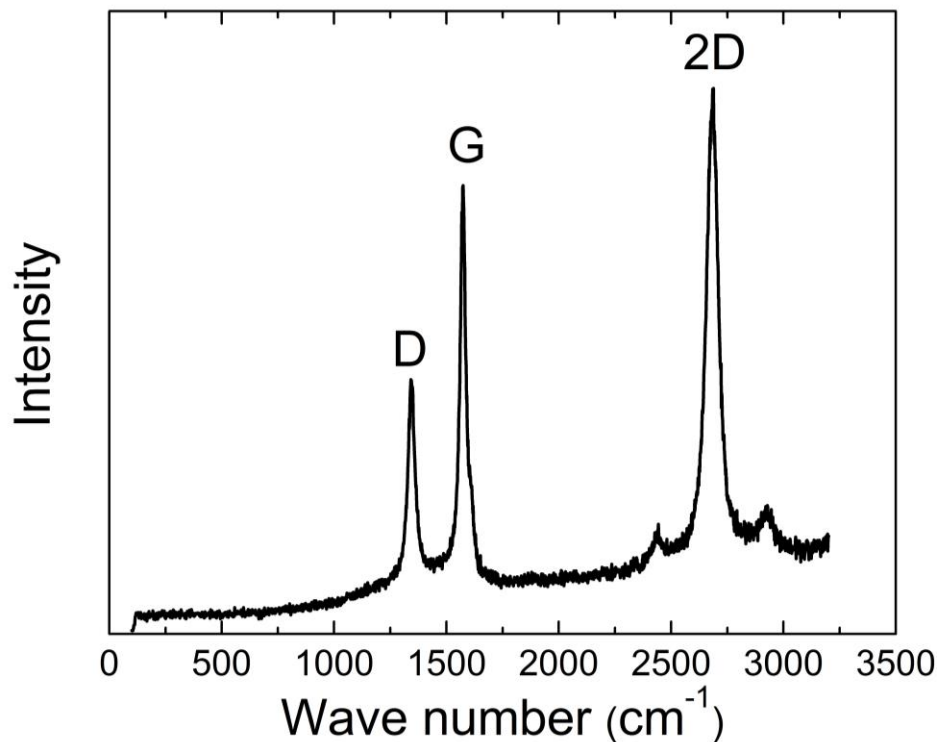


Figure 3.6 Raman spectrum of the carbon particulates.

A survey spectrum of the carbon particulates is shown in Figure 3.7 showing a strong C1s peak at 284.6 eV and a small O1s peak at 532.8 eV. The concentrations of carbon and oxygen were estimated to be 93.8% and 6.1%, respectively. The small amount

of oxygen concentration is possibly due to the oxidation of the graphene after being exposed to the ambient environment. The small figure inset of Figure 3.7 displays a fitting result of the C1s peak. Three components at 284.6, 284.9, and 286.4 eV can be assigned to graphite C=C species,²⁸ carbon defects,²⁹ and C-O bonds,³⁰ which are all commonly found in graphene.¹⁰ Considering all the characterization results, it can be concluded that the carbon particulates synthesized as a by-product in the NASA plasma reactor are crumpled graphene with a low oxygen content and a thickness of only a few layers.

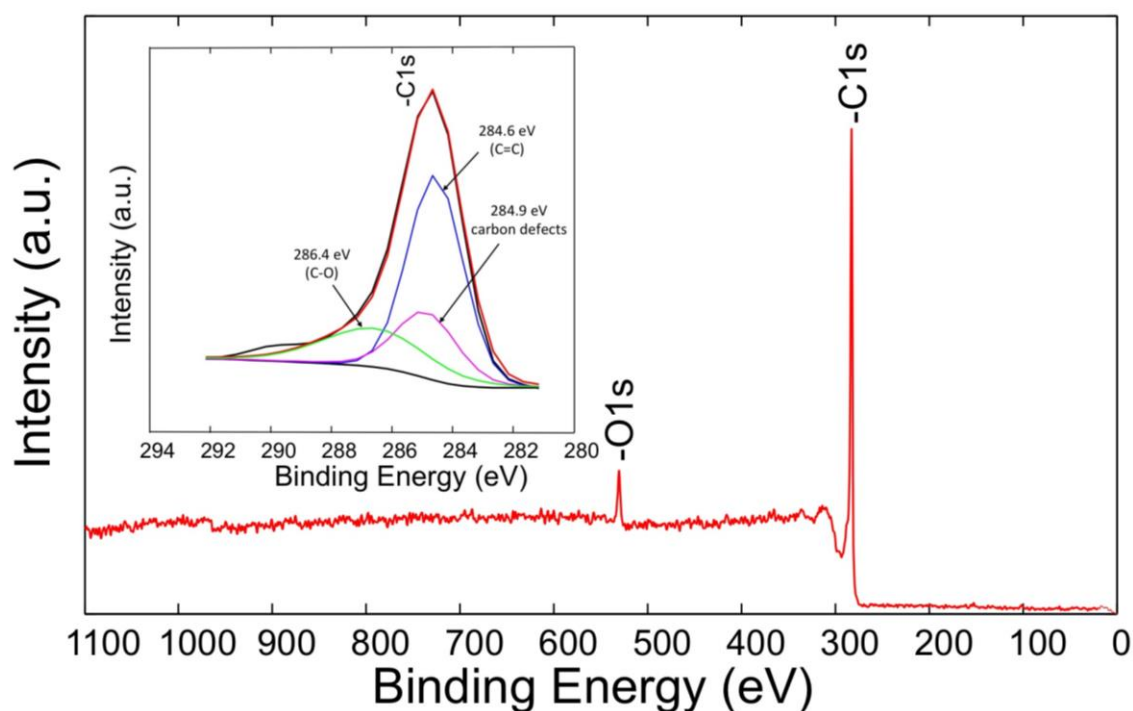


Figure 3.7 XPS survey spectrum of the carbon particulates. The insert is the curve fitting of the C1s peak.

The N₂ adsorption-desorption plots of the crumpled graphene sample (Figure 3.8) show a type III isotherm³¹⁻³⁴ with a steep increase in nitrogen absorption at a high relative pressure ($P/P_0 = 0.80-0.99$), indicating the multilayer adsorption. The specific surface area of the graphene samples was analyzed to be 258.5 m²/g, which is around one tenth of the

theoretical surface area of graphene (2630 m²/g).³⁵ The difference in surface area between the NASA sample and theoretical value could be attributed to stacking of the few layers in our sample (shown in the HRTEM images, Figure 3.4), as well as the crumpling of the graphene sheets (shown in the SEM and TEM images, Figure 3.3). It is noted that the IV type isotherm indicates the graphene sample is a mesoporous material,³¹⁻³³ which is also consistent with the results shown in the pore size distribution plot inset of Figure 3.8. Based on a classification of hysteresis by de Boer,³¹⁻³² materials with shape of adsorption-desorption isotherm shape have slit-shaped pores, revealing that they are non-rigid aggregates of plate-like particles, due to unlimited adsorption at high P/P₀. The N₂ adsorption/desorption measurement confirms with our previous analysis of the morphology characteristics of the graphene sample.

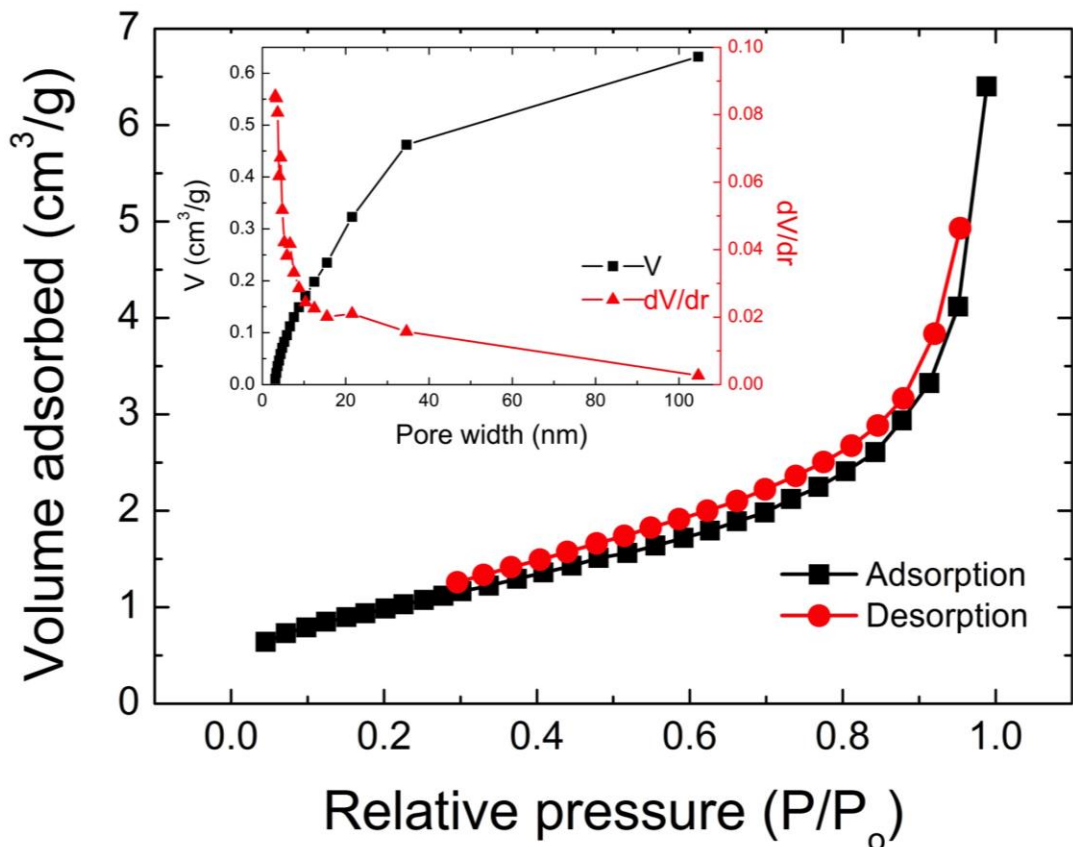


Figure 3.8 Nitrogen adsorption/desorption analysis of the carbon particulates. The insert is the pore size distribution of the sample.

Materials based on graphene, a single layer of carbon atoms arranged in a honeycomb network, are promising candidates for use in next generation lithium-ion batteries (LIBs),³⁶⁻³⁷ due to graphene's superior electrical conductivity, high surface-to-volume ratio, ultrathin thickness, structural flexibility, and chemical stability.³⁸⁻⁴⁰ Graphene based materials can have different morphologies, sizes, and properties. It is now well recognized that graphene properties are highly dependent on the synthesis process. In general, the two main methods are top-down or bottom-up methods.⁴¹ Reduction of graphene oxide (GO) and chemical vapor deposition (CVD) are the representatives of these two synthesis methods, respectively.⁴² However, both two approaches have their own

drawbacks, which can limit the application of graphene-based materials. Reduction of GO can cause a high oxygen content in the final product and introduce structural defects,⁴³ while CVD methods have higher cost and may also introduce undesired contaminants.⁴⁴ Another general consideration is that, the application of these flat-structured graphene materials can also be significantly limited by restacking of the two-dimensional (2D) sheets. Restacking of these sheets, which results from strong π - π interactions,⁴⁵⁻⁴⁶ reduces the accessible surface area and thus affects the overall material efficacy.⁴⁷ However, crumpled graphene nanosheets do not have the same issue with restacking that flat sheets suffer from,^{46, 48-49} and this allows more lithium storage sites to remain available. Therefore, the crumpled graphene material, with a low oxygen content and a relatively large specific surface area, formed in the NASA's PPA reactor, shows a promising applicability in LIBs.

3.3.2 The performance of the LIBs

A rate capability analysis was performed to determine the performance of the crumpled graphene electrode at various charge-discharge rates within a voltage window of 0.05-3.25 V, the results of which can be seen in Figure 3.9(a). At charging rates of 300, 500, 1000, and 3000 mA g⁻¹, stable capacities of 803, 585, 405, and 290 mAh g⁻¹ were obtained, and no rapid capacity loss was seen even at high charge-discharge rates. Furthermore, when the charge-discharge rate was lowered back to 500 mA g⁻¹, the capacity increased back to 579 mAh g⁻¹, representing a recovery of 99% of the original capacity. This high retention of capacity indicates that the electrodes are stable even at high charge-discharge rates, without experiencing irreversible degradation.

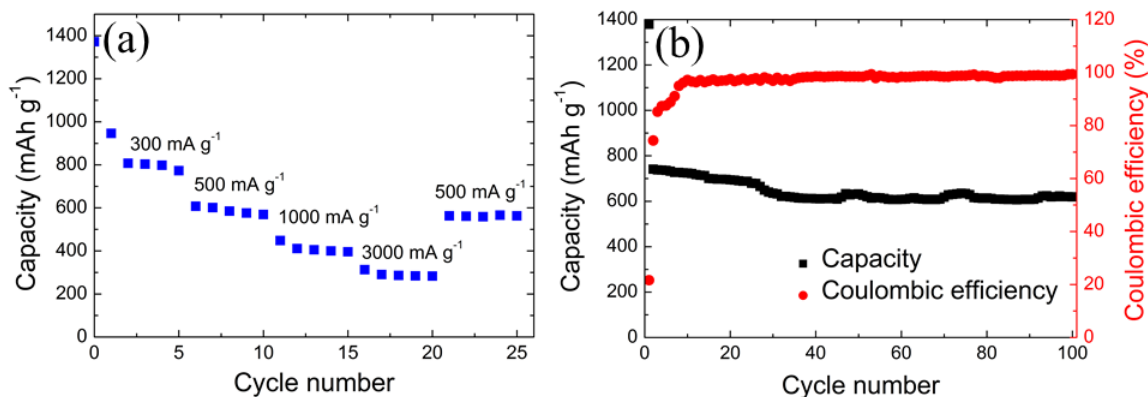


Figure 3.9 Electrochemical characteristics of the crumpled graphene LIBs. (a) charge (delithiation) capacities at various rates as marked, (b) capacity and Coulombic efficiency at the designated rate of 500 mA g⁻¹ for 100 cycles.

The long-term cycle performance of the prepared electrodes was determined by charging and discharging them at a current density of 500 mA g⁻¹ in a voltage window of 0.05-3.25 V for 100 cycles, and the results are shown in Figure 3.9(b). The first cycle discharge capacity was found to be 1379 mAh g⁻¹, while the second cycle dropped to 741 mAh g⁻¹, slightly higher than the values reported by Guo et al, of 1233 mAh g⁻¹ and 672 mAh g⁻¹ for graphene nanosheets.⁵⁰ The large irreversible capacity drop in the first cycle can be attributed to the formation of a solid-electrolyte interphaser (SEI) layer on the surface of the graphene electrode, and the reaction of lithium ions with oxygen containing functional groups. During the first 33 cycles, the capacity dropped slowly until it reached a stable capacity of 621 mAh g⁻¹, a retention of 84% of the capacity from the 2nd cycle. Compared to the values reported by Yoo et al.⁵¹ of 540 mAh g⁻¹ or Wang et al.⁵² of 460 mAh g⁻¹ after 100 cycles at a rate of 1 C, the results presented here show a marked improvement. Additionally, it can be seen that the Coulombic efficiency was approximately 51% for the first cycle due to the irreversible reactions mentioned previously, but then quickly rose to over 99% after the first 10 cycles. Other detailed

electrochemical characteristics of the crumpled graphene LIBs, including the voltage profiles and cyclic voltammograms can be found in Supporting Information (Figure S3.1).

3.4 Conclusions

The carbon material formed as a side product in a NASA plasma reactor for methane post-processing was characterized as crumpled graphene with a low oxygen content and only a few layers in thickness. HRTEM images clearly show a partially crystalline hexagonal structure, which is a characteristic graphene signature. The specific surface area of the graphene was measured to be 258.5 m²/g, one tenth of the theoretical value of single layer graphene, which can be attributed stacking of the layers and partial crumpling of this material. This crumpled graphene material was used to synthesize the anodes of LIBs, which were tested for electrochemical performance. The LIB cells showed large irreversible capacity drop only in the first cycle, which may be due to the side reactions breaking down the electrolytes and the formation of an SEI layer on the surface of the graphene layer. However, the crumpled graphene LIBs demonstrated a high retention rate after the first cycle, indicating very little degradation of the electrode. The high stability of the cells can be attributed to the greater variety and higher number of lithium ion storage sites in the crumpled graphene, compared with bulk graphite. Considering the crumpled graphene as a by-product and the high electrochemical performance of the crumpled graphene LIBs, our study provided an insightful approach to recycle this by-product and better support the long-duration space missions.

Acknowledgements

Y.N. thanks the McDonnell International Scholars Academy and the McDonnell Academy Global Energy and Environment Partnership (MAGEEP) for partial support of

this work and through a fellowship to pursue a Ph.D. at Washington University in St. Louis. Ramesh Raliya is acknowledged for the help with HR-TEM characterization. Zachary Greenwood and Morgan Abney are gratefully acknowledged for providing the material samples. Electron microscopy work was performed at the Nano Research Facility (NRF) at Washington University in St. Louis.

References

1. Goodliff, K.; Troutman, P.; Craig, D.; Caram, J.; Herrmann, N. In *AIAA SPACE 2016*, 2016; p 5456.
2. Knox, J. C.; Stanley, C. M., **2015**.
3. Abney, M.; Miller, L.; Williams, T. In *Sabatier reactor system integration with microwave plasma methane pyrolysis post-processor for closed-loop hydrogen recovery*, 40th International Conference on Environmental Systems, 2010; p 6274.
4. Abney, M. B.; Miller, L. A.; Greenwood, Z.; Iannantuono, M.; Jones, K. In *Methane post-processor development to increase oxygen recovery beyond state-of-the-art carbon dioxide reduction technology*, 43rd International Conference on Environmental Systems, 2013; p 3513.
5. Greenwood, Z. W.; Abney, M. B.; Perry, J. L.; Miller, L. A.; Dahl, R. W.; Hadley, N. M.; Wambolt, S. R.; Wheeler, R. R., **2015**.
6. Bo, Z.; Yang, Y.; Chen, J.; Yu, K.; Yan, J.; Cen, K., *Nanoscale* **2013**, 5 (12), 5180-5204.
7. Kim, J.; Ishihara, M.; Koga, Y.; Tsugawa, K.; Hasegawa, M.; Iijima, S., *Appl. Phys. Lett.* **2011**, 98 (9), 091502.
8. Tatarova, E.; Henriques, J.; Luhrs, C.; Dias, A.; Phillips, J.; Abrashev, M.; Ferreira, C., *Appl. Phys. Lett.* **2013**, 103 (13), 134101.
9. Wang, Q.; Wang, X.; Chai, Z.; Hu, W., *Chem. Soc. Rev.* **2013**, 42 (23), 8821-8834.
10. Wang, Z.; Shoji, M.; Ogata, H., *Appl. Surf. Sci.* **2011**, 257 (21), 9082-9085.
11. Yamada, T.; Kim, J.; Ishihara, M.; Hasegawa, M., *J. Phys. D: Appl. Phys.* **2013**, 46 (6), 063001.
12. Cappelli, E.; Orlando, S.; Mattei, G.; Scilletta, C.; Corticelli, F.; Ascarelli, P., *Applied Physics A: Materials Science & Processing* **2004**, 79 (8), 2063-2068.
13. Dikonimos, T.; Giorgi, L.; Giorgi, R.; Lisi, N.; Salernitano, E.; Rossi, R., *Diamond Relat. Mater.* **2007**, 16 (4), 1240-1243.
14. Ostrikov, K.; Xu, S., *Plasma-aided nanofabrication: from plasma sources to nanoassembly*. John Wiley & Sons: 2007.
15. Vizireanu, S.; Stoica, S.; Luculescu, C.; Nistor, L.; Mitu, B.; Dinescu, G., *Plasma Sources Sci. Technol.* **2010**, 19 (3), 034016.
16. Ostrikov, K., *Plasma nanoscience*. John Wiley & Sons: 2008.

17. Wheeler, R. R.; Hadley, N. M.; Wambolt, S. R.; Abney, M. B. In *Third Generation Advanced PPA Development*, 44th International Conference on Environmental Systems: 2014.
18. Park, J.; Mitchel, W. C.; Grazulis, L.; Smith, H. E.; Eyink, K. G.; Boeckl, J. J.; Tomich, D. H.; Pacley, S. D.; Hoelscher, J., *Adv. Mater.* **2010**, 22 (37), 4140-4145.
19. Vlassioun, I.; Regmi, M.; Fulvio, P.; Dai, S.; Datskos, P.; Eres, G.; Smirnov, S., *ACS nano* **2011**, 5 (7), 6069-6076.
20. Green, R. D.; Meyer, M. E.; Agui, J. H.; Berger, G. M.; Vijayakumar, R.; Abney, M. B.; Greenwood, Z., **2015**.
21. Tunuguntla, R. H.; Henley, R. Y.; Yao, Y.-C.; Pham, T. A.; Wanunu, M.; Noy, A., *Science* **2017**, 357 (6353), 792-796.
22. Wang, G.; Yang, J.; Park, J.; Gou, X.; Wang, B.; Liu, H.; Yao, J., *J. Phys. Chem. C* **2008**, 112 (22), 8192-8195.
23. Malesevic, A.; Vitchev, R.; Schouteden, K.; Volodin, A.; Zhang, L.; Van Tendeloo, G.; Vanhulsel, A.; Van Haesendonck, C., *Nanotechnology* **2008**, 19 (30), 305604.
24. Brown, T. L.; LeMay, H. E.; Bursten, B. E.; Brunauer, L. S., *Chemistry: the central science*. Prentice Hall Englewood Cliffs, NJ: 1994; Vol. 8.
25. Dresselhaus, M. S.; Dresselhaus, G.; Saito, R.; Jorio, A., *Physics reports* **2005**, 409 (2), 47-99.
26. Kastner, J.; Pichler, T.; Kuzmany, H.; Curran, S.; Blau, W.; Weldon, D.; Delamesiere, M.; Draper, S.; Zandbergen, H., *Chem. Phys. Lett.* **1994**, 221 (1-2), 53-58.
27. Ferrari, A. C.; Meyer, J.; Scardaci, V.; Casiraghi, C.; Lazzeri, M.; Mauri, F.; Piscanec, S.; Jiang, D.; Novoselov, K.; Roth, S., *Phys. Rev. Lett.* **2006**, 97 (18), 187401.
28. Yang, D.-Q.; Sacher, E., *Surf. Sci.* **2002**, 504, 125-137.
29. Estrade-Szwarckopf, H., *Carbon* **2004**, 42 (8), 1713-1721.
30. Paredes, J. I.; Villar-Rodil, S.; Solís-Fernández, P.; Martínez-Alonso, A.; Tascon, J., *Langmuir* **2009**, 25 (10), 5957-5968.
31. Broekhoff, J., *Stud. Surf. Sci. Catal.* **1979**, 3, 663-684.
32. Lowell, S.; Shields, J. E.; Thomas, M. A.; Thommes, M., *Characterization of porous solids and powders: surface area, pore size and density*. Springer Science & Business Media: 2012; Vol. 16.

33. Zhao, X. S.; Lu, G.; Millar, G. J., *Industrial & Engineering Chemistry Research* **1996**, 35 (7), 2075-2090.
34. Sing, K. S., *Pure Appl. Chem.* **1985**, 57 (4), 603-619.
35. Zhu, Y.; Murali, S.; Stoller, M. D.; Ganesh, K.; Cai, W.; Ferreira, P. J.; Pirkle, A.; Wallace, R. M.; Cychosz, K. A.; Thommes, M., *Science* **2011**, 332 (6037), 1537-1541.
36. Ji, F.; Li, Y.-L.; Feng, J.-M.; Su, D.; Wen, Y.-Y.; Feng, Y.; Hou, F., *J. Mater. Chem.* **2009**, 19 (47), 9063-9067.
37. Wang, D.; Choi, D.; Li, J.; Yang, Z.; Nie, Z.; Kou, R.; Hu, D.; Wang, C.; Saraf, L. V.; Zhang, J., *ACS nano* **2009**, 3 (4), 907-914.
38. Geim, A. K., *Science* **2009**, 324 (5934), 1530-1534.
39. Novoselov, K.; Jiang, D.; Schedin, F.; Booth, T.; Khotkevich, V.; Morozov, S.; Geim, A., *Proc. Natl. Acad. Sci. U. S. A.* **2005**, 102 (30), 10451-10453.
40. Novoselov, K. S.; Geim, A. K.; Morozov, S. V.; Jiang, D.; Zhang, Y.; Dubonos, S. V.; Grigorieva, I. V.; Firsov, A. A., *Science* **2004**, 306 (5696), 666-669.
41. Ferrari, A. C.; Bonaccorso, F.; Fal'Ko, V.; Novoselov, K. S.; Roche, S.; Bøggild, P.; Borini, S.; Koppens, F. H.; Palermo, V.; Pugno, N., *Nanoscale* **2015**, 7 (11), 4598-4810.
42. Wei, D.; Astley, M. R.; Harris, N.; White, R.; Ryhänen, T.; Kivioja, J., *Nanoscale* **2014**, 6 (16), 9536-9540.
43. Raccichini, R.; Varzi, A.; Passerini, S.; Scrosati, B., *Nat. Mater.* **2015**, 14 (3), 271-279.
44. Wei, D.; Kivioja, J., *Nanoscale* **2013**, 5 (21), 10108-10126.
45. Luo, J.; Zhao, X.; Wu, J.; Jang, H. D.; Kung, H. H.; Huang, J., *J. Phys. Chem. Lett.* **2012**, 3 (13), 1824-1829.
46. Nie, Y.; Wang, W.-N.; Jiang, Y.; Fortner, J.; Biswas, P., *Catal. Sci. Technol.* **2016**.
47. Ma, X.; Zachariah, M. R.; Zangmeister, C. D., *Nano Lett.* **2011**, 12 (1), 486-489.
48. Nie, Y.; Wang, Y.; Biswas, P., *J. Phys. Chem. C* **2017**, 121 (19), 10529-10537.
49. Wang, W.-N.; Jiang, Y.; Biswas, P., *J. Phys. Chem. Lett.* **2012**, 3 (21), 3228-3233.
50. Guo, P.; Song, H.; Chen, X., *Electrochem. Commun.* **2009**, 11 (6), 1320-1324.
51. Yoo, E.; Kim, J.; Hosono, E.; Zhou, H.-s.; Kudo, T.; Honma, I., *Nano Lett.* **2008**, 8 (8), 2277-2282.
52. Wang, G.; Shen, X.; Yao, J.; Park, J., *Carbon* **2009**, 47 (8), 2049-2053.

Chapter 3 Supporting Information

Table of Contents

S3.1 The performance of the LIBs

S3.1. The performance of the LIBs

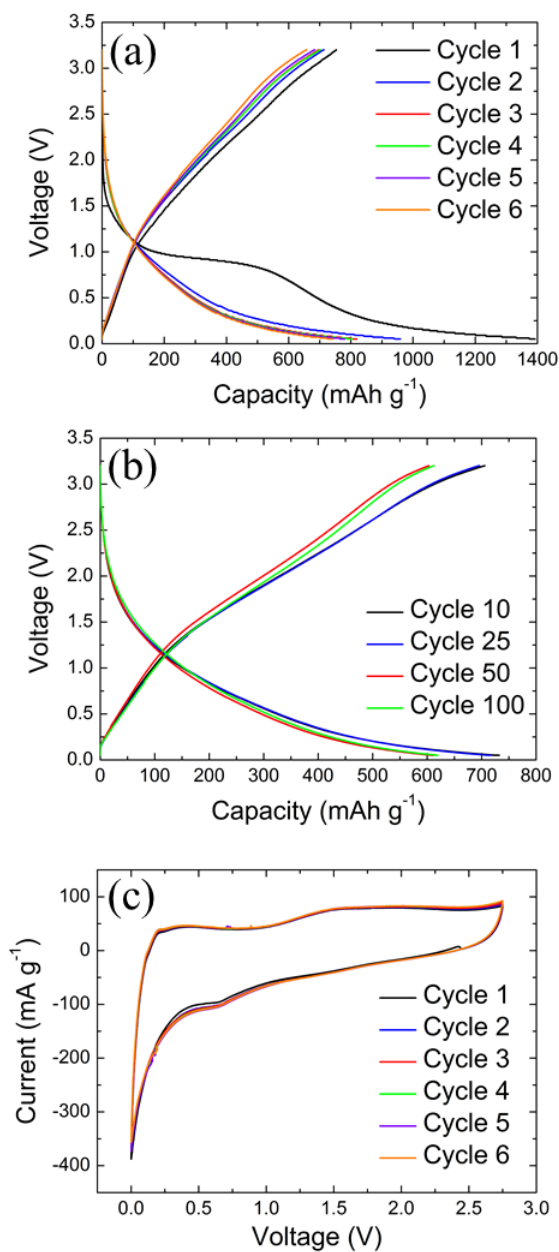


Figure S3.1. Electrochemical characteristics of the crumpled graphene LIBs. (a) Voltage profiles for the first 6 cycles, (b) voltage profiles for up to 100 cycles, and (c) cyclic voltammograms of the crumpled graphene LIBs for the first 6 cycles at a scanning rate of 1mV/s.

Supplemental Figure S3.1(a) shows the voltage profiles for the first six charge-discharge cycles of the crumpled graphene electrodes vs Li/Li⁺. The first cycle has a plateau at approximately 1 V, which may be attributed to side reactions involved in the breakdown of the electrolyte and the formation of a SEI layer on the surface of the graphene electrode, which are also the cause of the large irreversible capacity drop seen in the first cycle.¹⁻³ These side reactions, considered irreversible, are linked to the specific surface area of the electrodes and are typically observed in lithium-ion cells.⁴ However, from the second cycle onwards, the voltage profiles do not show any distinguishable plateaus, which suggests that Li-ions are stored in a variety of sites, created by the disordered and non-crystalline stacking of the crumpled graphene sheets.^{3, 5, 6} This variety of storage sites is dissimilar from currently used bulk graphite, which stores lithium solely between two carbon sheets to form the intercalation compound LiC₆.

Supplemental Figure S3.1(b) shows the voltage profiles for the 10th, 25th, 50th, and 100th charge-discharge cycles. It can be seen that the 50th and 100th cycle voltage profiles are very similar, indicating that very little degradation of the electrode occurred between the 50th and 100th cycles. This matches well with the results of the cycling experiments discussed previously.

Cyclic voltammogram (CV) curves for the crumpled graphene electrodes are shown in Supplemental Figure S3.1(c). These curves demonstrate highly reversible behavior and match well with the voltage profiles shown earlier. No large peaks were observed in the CV curves, indicating a variety of lithium ion storage sites rather than the single site type available in bulk graphite, which is consistent with previous work.

References

1. Wu, Z.-S.; Ren, W.; Xu, L.; Li, F.; Cheng, H.-M., Doped graphene sheets as anode materials with superhigh rate and large capacity for lithium ion batteries. *ACS nano* 2011, 5 (7), 5463-5471.
2. Lin, J.; Peng, Z.; Xiang, C.; Ruan, G.; Yan, Z.; Natelson, D.; Tour, J. M., Graphene Nanoribbon and Nanostructured SnO₂ Composite Anodes for Lithium Ion Batteries. *ACS Nano* 2013, 7 (7), 6001-6006.
3. Li, X.; Geng, D.; Zhang, Y.; Meng, X.; Li, R.; Sun, X., Superior cycle stability of nitrogen-doped graphene nanosheets as anodes for lithium ion batteries. *Electrochem. Commun.* 2011, 13 (8), 822-825.
4. Mukherjee, R.; Thomas, A. V.; Krishnamurthy, A.; Koratkar, N., Photothermally reduced graphene as high-power anodes for lithium-ion batteries. *ACS Nano* 2012, 6 (9), 7867-7878.
5. Chen, J.; Xu, L.; Li, W.; Gou, X., α -Fe₂O₃ nanotubes in gas sensor and lithium-ion battery applications. *Adv. Mater.* 2005, 17 (5), 582-586.
6. Menachem, C.; Peled, E.; Burstein, L.; Rosenberg, Y., Characterization of modified NG7 graphite as an improved anode for lithium-ion batteries. *J. Power Sources* 1997, 68 (2), 277-282.

Chapter 4 Crumpled Reduced Graphene Oxide–Amine–Titanium Dioxide Nanocomposites for Simultaneous Carbon Dioxide Adsorption and Photoreduction

The results reported in this chapter were published in - Nie, Yao, Wei-Ning Wang, Yi Jiang, John Fortner, and Pratim Biswas. "Crumpled Reduced Graphene Oxide–Amine–Titanium Dioxide Nanocomposites for Simultaneous Carbon Dioxide Adsorption and Photoreduction." Catalysis Science & Technology 6 (2016): 6187-6196. (Back cover paper). Reproduced with permission from Royal Society of Chemistry, copyright 2016.

Abstract

Crumpled reduced graphene oxide-amine-titanium dioxide nanocomposites (CGOATI) were synthesized by an one-step aerosol technique to enable simultaneous carbon dioxide (CO₂) adsorption and photoreduction. Graphene oxide (GO), chemically modified by ethylenediamine (EDA), was crumpled using an aerosol process, encapsulating TiO₂ nanoparticles to form core-shell nanostructures. The three-dimensional (3D) structure largely prevented the crumpled graphene nanosheets from restacking by minimizing π - π interactions, thus enhancing the stability of the catalyst by retaining its higher surface area. A combination of a 20% mass percentage of TiO₂/GO, a 15:1 mass ratio of EDA/GO in precursor solution, and a 200 °C synthesis temperature led to the highest CO yield (65 μ mol/g/h, with an apparent quantum efficiency of 0.0094%), which was two-fold higher than that of crumpled reduced GO-TiO₂ (CGOTI) and four-fold higher than that of TiO₂ alone. The enhancement of CO₂ photoreduction was attributed to higher CO₂ adsorption on the amine-functionalized reduced-GO (r-GO) surface and the strong electron trapping capability of r-GO. The insertion of EDA on r-GO nanosheets, the adsorption of CO₂ by amine groups, and the photoreduction of the adsorbed CO₂ were confirmed by FTIR and XPS spectra analysis. The r-GO nanosheets themselves were simultaneously photoreduced during CO₂ photoreduction. Raman spectroscopy and conductivity measurements showed that photoreduced r-GO had a higher electronic conductivity than thermally reduced r-GO, and led to more effective CO₂ photoreduction. This study offers new insights into the design and fabrication of graphene-based photocatalysts for CO₂ photoreduction.

4.1 Introduction

With the rapid development of the world's economy, increasing amounts of fossil fuels are being consumed every year to meet the growing energy demand.¹ The burning of fossil fuels is widely considered to be the main anthropogenic source of atmospheric carbon dioxide (CO₂) emissions.² The atmospheric CO₂ concentration is reported to have increased by 100 parts per million (ppm) from the 1700s to 2005, and to be causing global climate change.^{3, 4} Therefore strategies to urgently mitigate CO₂ have attracted global attention. Metz et al.⁵ proposed CO₂ capture and sequestration (CCS) technology as a feasible approach to address this problem. However, this technology is energy intensive^{6, 7} and has potential risks due to the CO₂ leakage from geological sequestered sites.⁸

An alternative process, CO₂ capture and conversion (CCC), can reduce risks by capturing and reducing CO₂ to useable products such as hydrocarbon fuels. Thermochemical,⁹ electrochemical,¹⁰ and photocatalytic^{11, 12} methods are possible ways to realize the reduction of CO₂. Among these methods, photocatalytic reduction is a promising option that directly harnesses inexpensive and abundant solar energy, and titanium dioxide (TiO₂) is a commonly used photocatalyst.^{13, 14} In the photocatalytic process, a semiconductor photocatalyst absorbs light energy, bridging its band gap and producing electron-hole (e⁻ - h⁺) pairs to support reduction and oxidation reactions.^{15, 16} However, the efficiency of photocatalytic reduction of CO₂ is relatively low due to several limiting steps, such as CO₂ adsorption on the photocatalyst surface¹⁷ and recombination of e⁻ - h⁺ pairs.¹⁸ Therefore, a modified material that could enhance CO₂ adsorption or/and retard recombination of e⁻ and h⁺ would increase the CO₂ photoreduction efficiency.

Coating the photocatalyst with metal nanoparticles (NPs), such as platinum,¹⁹ copper,²⁰ or silver,²¹ is a viable approach to realize the separation of e^- and h^+ , since metals have a high electron conductivity and work as an e^- sink. However, such coated materials tend to be unstable due to coagulation of the required sub-nanometer metal NPs.^{22, 23} Nanocarbon hybrid photocatalysts have demonstrated their potential applicability for CO_2 photoreduction due to their stability, as well as their electronic and optical properties. Graphene nanosheets are a promising material for use as a CO_2 photoreduction catalyst: They have excellent electronic conductivity and an extremely large specific surface area (theoretically $2630\text{ m}^2\text{g}^{-1}$),^{24, 25} which could enhance adsorption of CO_2 on the graphene.^{26, 27} However, the application of these flat-structured materials can be significantly limited by restacking of the two-dimensional (2D) sheets. Restacking of these sheets, which results from strong π - π interactions,²⁸ reduces the accessible surface area and thus affects the overall material efficacy.²⁹ Converting the flat 2D sheet to a 3D crumpled structure by an aerosol technique is a feasible approach to overcome the above hurdles without compromising its electrical properties.³⁰⁻³² Furthermore, crumpled graphene has a hollow structure that can encapsulate other nanoscale functional materials, such as Si,³³ TiO_2 ,^{31, 34} and Pt,³⁵ and resulting in the formation of a quasi-spherical hybrid. In our recent work,³² crumpled reduced graphene oxide (CGO)- TiO_2 (CGOTI) nanocomposites was shown to result in a multi-fold enhancement of CO_2 photoreduction performance compared to pure TiO_2 .³¹

Another important aspect is the enhancement of the CO_2 adsorption on the surface, and this has not been extensively studied. Amine modification is one of the most commonly applied techniques in this regard.³⁶ Triamine-modified pore-mesoporous silica MCM-41

was shown to exhibit high CO₂ adsorption capacity and high selectivity for CO₂ over N₂ and O₂.³⁷ Zhao et al.³⁸ used ethylenediamine (EDA), diethylenetriamine (DETA) and triethylene tetraamine (TETA) to modify graphite oxide to improve CO₂ adsorption, and EDA modified graphite oxide showed the best CO₂ adsorption performance with the highest capacity and longest breakthrough time. The insertion of amine groups is promoted by reactions between amine groups and oxygen-containing groups on GO, such as carboxyl groups and epoxy groups.³⁹ However, to the best of our knowledge, no study has reported the use of aminated GO for combined CO₂ adsorption and photoreduction.

This paper reports on methods to develop a simultaneous CO₂ adsorption-photoreduction catalyst. A single step aerosol method to synthesize aminated, reduced graphene-based nanocomposites consisting of crumpled r-GO with encapsulated TiO₂ nanoparticles resulting in the formation of open core-shell nanostructures (referred to as CGOATI in this paper) is described. It is demonstrated that this 3D structure obtained by crumpling is not as prone to agglomeration as the 2D sheets thus enhancing the stability. Moreover, photoreduction reactions can be promoted by the addition of graphene, because the electrons can be trapped by the reduced graphene oxide shell. Besides, amine functionalization of the graphene-titanium dioxide nanocomposite, was demonstrated for the first time to enhance CO₂ adsorption with simultaneous photoreduction. The TiO₂/GO percentage, EDA/GO ratio, and synthesis temperature were optimized to obtain the best CO₂ conversion performance. The role of the amine groups in enhancing CO₂ adsorption followed by its photoreduction was unraveled by Fourier transform infrared (FTIR) spectroscopy, X-ray photoelectron spectroscopy (XPS) and Raman spectroscopy. A

mechanistic understanding of the simultaneous CO₂ adsorption and photoreduction on CGOATI is presented.

4.2 Experimental section

4.2.1 Precursor Solution Preparation

Graphene oxide nanosheets were prepared by using the modified Hummers method,⁴⁰ and also reported in detail in our previous work.⁴¹ Briefly, graphite powder (45 μm) was oxidized by potassium permanganate (KMnO₄) with concentrated sulfuric acid (H₂SO₄), and then washed and dried overnight. The resultant graphite oxide powder was redispersed in DI water, then ultrasonicated and centrifuged to obtain single nanosheets. The supernatant was collected to prepare the graphene oxide (GO) stock solution. To obtain the CGOATI nanocomposites, this GO stock solution was mixed with TiO₂ NPs (AERODISP[®] W740X, Evonik Degussa Co.), ethylenediamine (EDA, ≥ 99.5%, Sigma Aldrich), and DI water in different ratios (shown in Figure 4.3), to prepare the precursor solutions for feed to the aerosol reactor. The precursor solutions were ultrasonicated for 30 min to allow EDA to react with GO prior to the aerosolization.

4.2.2 CGOATI Nanocomposite Synthesis

The schematic diagram of the system to synthesize the crumpled CGOATI nanocomposite is shown in Figure 4.1. The solutions were first atomized into micrometer-sized droplets by a Collison Nebulizer (BGI Incorporated). The droplets were then carried by nitrogen gas (N₂) at a flow rate of 12.4 L/min (at 96.53 kPa) into a tubular alumina furnace aerosol reactor (FuAR, 1 m long × 25 mm ID) maintained at various set temperatures (200 ~ 800 °C). In the residence time of around 1 ~ 2 s in the FuAR, the GO was thermally reduced and also crumpled by the imposed capillary force due to rapid

solvent evaporation, as detailed in our previous work.⁴¹ The TiO₂ particles were effectively encapsulated by the crumpled reduced GO (r-GO). Finally, these nanocomposites were further dried and collected downstream.

4.2.3 Materials Characterization

The morphology and size of the CGOATI particles were examined by field emission scanning electron microscopy (FE-SEM, NOVA NanoSEM 230, FEI Co.), and

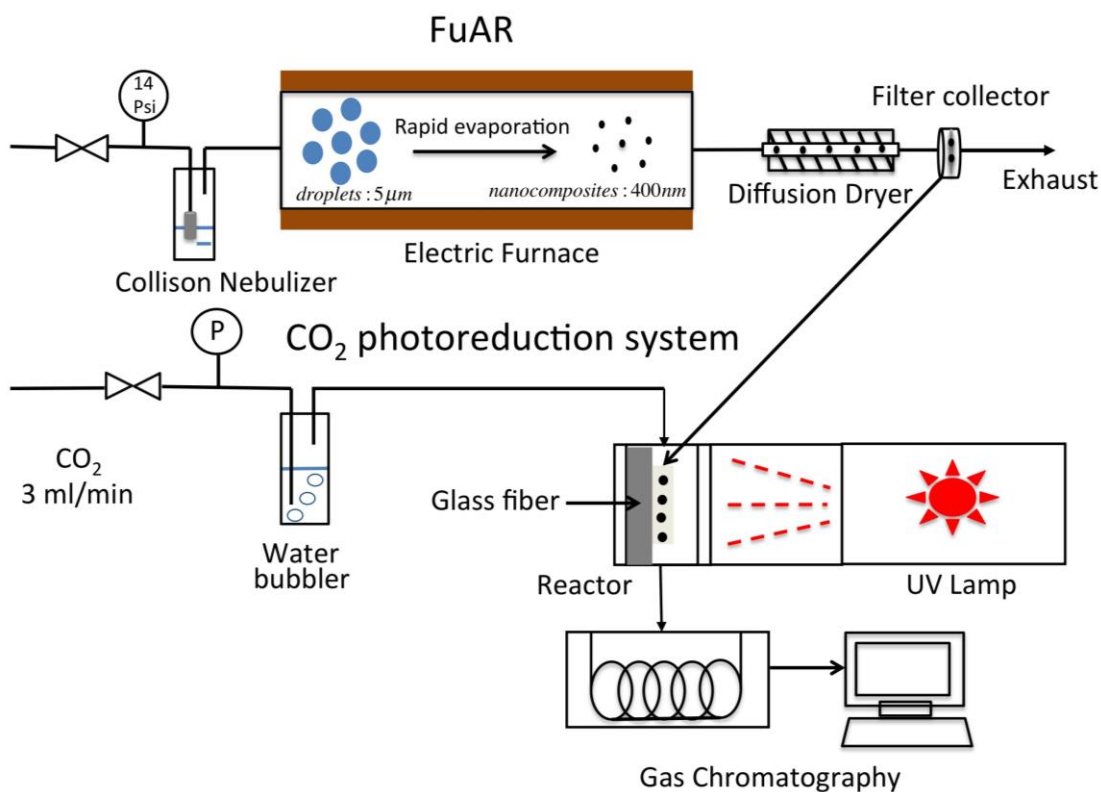


Figure 4.1 Schematic diagram of the FuAR and CO₂ photoreduction system

transmission electron microscopy (TEM, Tecnai TM Spirit, FEI Co.). The surface chemical properties, including molecular bonds and functional groups, were analyzed by Fourier transform infrared spectrometry (FTIR, Nicolette Nexus 470), laser Raman spectrometry (Renishaw InVia Reflex confocal Raman spectrometer, with a 514 nm laser) and X-ray photoelectron spectroscopy (XPS, PHI 5000 VersaProbe II equipped with a

monochromatic Al K α (1486.6 eV) X-ray source). XPS data analysis was performed using the PHI MultiPak software, after performing a Shirley background correction. Calibration was carried out by aligning of the spectra with reference to the C 1s line at 284.5 eV, which is associated with graphitic carbon. The electric resistivity was measured by a JANIS probe station (ST500-1-2CX), and a Keithley 2400 source measurement unit, both fully controlled by a LabVIEW program. Samples were dried in vacuum overnight to eliminate moisture. The mass of different samples was controlled to be the same, and the probes were placed in the same positions for different samples. The optical properties of TiO₂, CGOTI and CGOATI aqueous dispersions (20mg/L) were measured using a UV-Vis spectrophotometer (Varian Bio 50) (see Figure S4.1, Supporting information for more details).

4.2.4 CO₂ Photoreduction Analysis

Compressed CO₂ (Instrument Gr. 4, Airgas, Inc.) was the carbon source, and was passed through a water bubbler to generate a mixture of CO₂ and water vapor. The gaseous mixture was then introduced into a homemade continuous flow reactor where the catalysts were loaded. The reactor was cylindrical with a quartz window vertically facing the light source, which was a Xe lamp (Oriel 66021, Newport Co.) operating at 450 W with an accumulated intensity of 11.5 mW/cm² (the light spectrum was measured by a spectroradiometer (ILT-900R, Polytec GmbH), see Figure S4.2, Supporting information) in the effective UV range (250-388 nm). The photoreduction analysis system was reported in detail in our previous publications.^{16, 31, 42} Before each test, the reactor loaded with samples was initially purged with CO₂ and water vapor at 100 ml/min for 0.5 hr, and then the flow rate was decreased and maintained at 3 ml/min for the test period. The light source

was turned on ($t = 0$ hr) and measurements were made for 8 hours. The concentrations of effluent gases (CO_2 , CO , CH_4 , O_2 , and N_2) as a function of irradiation time were recorded automatically by gas chromatography (GC, 6895N, Agilent Technologies, Inc.) through an automated gas valve, using helium as the carrier gas. The GC was equipped with a PLOT capillary column (Supelco Carboxen-1010) and a thermal conductivity detector (TCD). To evaluate the reusability of the CGOATI nanocomposites, the procedure was repeated. An overall experimental plan is outlined in Table 1.

Table 4.1 Experimental plan

Test number	Test conducted	Instuments/ methodology used	Detailed objective
1	Material synthesis & characterization	FuAR, TEM, SEM	Optimize synthesis conditions: TiO_2/GO percentage, EDA/GO ratio, synthesis temperature: (1) TiO_2/GO (%) (no EDA): 1, 5, 10, 20, 30 (2) $\text{TiO}_2/\text{GO} = 20\%$, EDA/GO: 0, 3, 15, 45, 75 (3) $\text{TiO}_2/\text{GO} = 20\%$, EDA/GO = 15, synthesis temperature: 200, 300, 400 °C
2	Blank test	CO_2 photoreduction analysis system	Confirm that any carbon containing products originated from the photo conversion of the CO_2 reactant. Cases tested: (1) Mixture of CO_2 and H_2O vapor without catalysts, with/without glass fiber membrane, with/without UV irradiation (2) Mixture of N_2 and H_2O vapor with catalysts, glass fiber membrane and UV irradiation
3	CO_2 photoreduction test	CO_2 photoreduction analysis system	Test the CO_2 photoreduction performance of CGOATI samples
4	Surface chemistry	FTIR, XPS, Raman, UV-Vis	Study the change of surface chemistry of r-GO in CO_2 adsorption and photoreduction

5	Recyclability	CO ₂ photoreduction analysis system	Test the stability of CGOATI
---	---------------	---------------------------------------------------------	------------------------------

4.2.5 Isotope Experiments

Isotope experiments were performed in the same reactor with the UV lamp. ¹³CO₂ (Sigma-Aldrich) was used as the source gas. The products in the reactor after 2h UV-irradiation was analyzed by a GC (7890A, Agilent Technologies, Inc.), equipped with a PLOT capillary column (Supelco Carboxen-1006), and a mass spectrometer (5975C, Agilent Technologies, Inc.).

4.3 Results and discussion

4.3.1 Morphology characterization

As described earlier, the precursor solutions were prepared by mixing different ratios of GO nanosheets, TiO₂ NPs, and EDA solution in DI water. Representative CGOATI samples with the best CO₂ photoreduction performance were characterized by FE-SEM and TEM. From the SEM images (Figure 4.2a, b), it can be seen that the r-GO nanosheets are crumpled and the TiO₂ particles are encapsulated inside them. These nanocomposites form a porous structure on the support membrane (borosilicate glass), with an average macropore size of 385±108 nm (estimated from SEM images). The size and morphology of each nanocomposite can be seen clearly from these TEM images (Figure 4.2(c)(d)). The dark dots are TiO₂ NPs with an average size of 22±6 nm (calculated from TEM images), which are inside the crumpled r-GO nanosheets (the transparent crumpled structure). The diameter of a typical CGOATI nanocomposite is around 480 nm (estimated from TEM images). Assuming the particles are solid with a spherical morphology, the size of the particle can be calculated using the one-droplet to one-particle (ODOP) mechanism⁴³

$$D_{V,P} = D_{V,d} \left(\frac{C}{\rho} \right)^{1/3}, \quad (4.1)$$

where $D_{V,P}$, is the volume mean diameter of the nanocomposite (μm), $D_{V,d}$ is the volume mean diameter of droplets (μm), C is the precursor concentration (g/ml), and ρ is the product particles density (g/ml), respectively.

Using assumptions similar to those for the ODOP mechanism, Eq. (4.2) can be applied to calculate the CGOATI nanocomposite size in the two component system (the amount of EDA is negligibly small). The geometric mean size of droplets, $5.1 \mu\text{m}$, was measured by an aerodynamic particle sizer (APS, TSI Inc.).⁴¹ The nanocomposite size was thus calculated to be 254 nm , using

$$D_{V,P} = D_{V,d} = \left(\frac{C_{GO}}{\rho_{GO}} + \frac{C_{TiO_2}}{\rho_{TiO_2}} \right)^{1/3}. \quad (4.2)$$

There is a large discrepancy between the calculated and measured particle sizes, indicating that the nanocomposites are partially hollow particles. The void factor of the nanocomposites, estimated from the calculated nanocomposite size and measured nanocomposite size is given by

$$\text{void factor} = 1 - \frac{V_{\text{calculated}}}{V_{\text{measured,TEM}}} = 1 - \left(\frac{D_{\text{calculated}}}{D_{\text{measured,TEM}}} \right)^3. \quad (4.3)$$

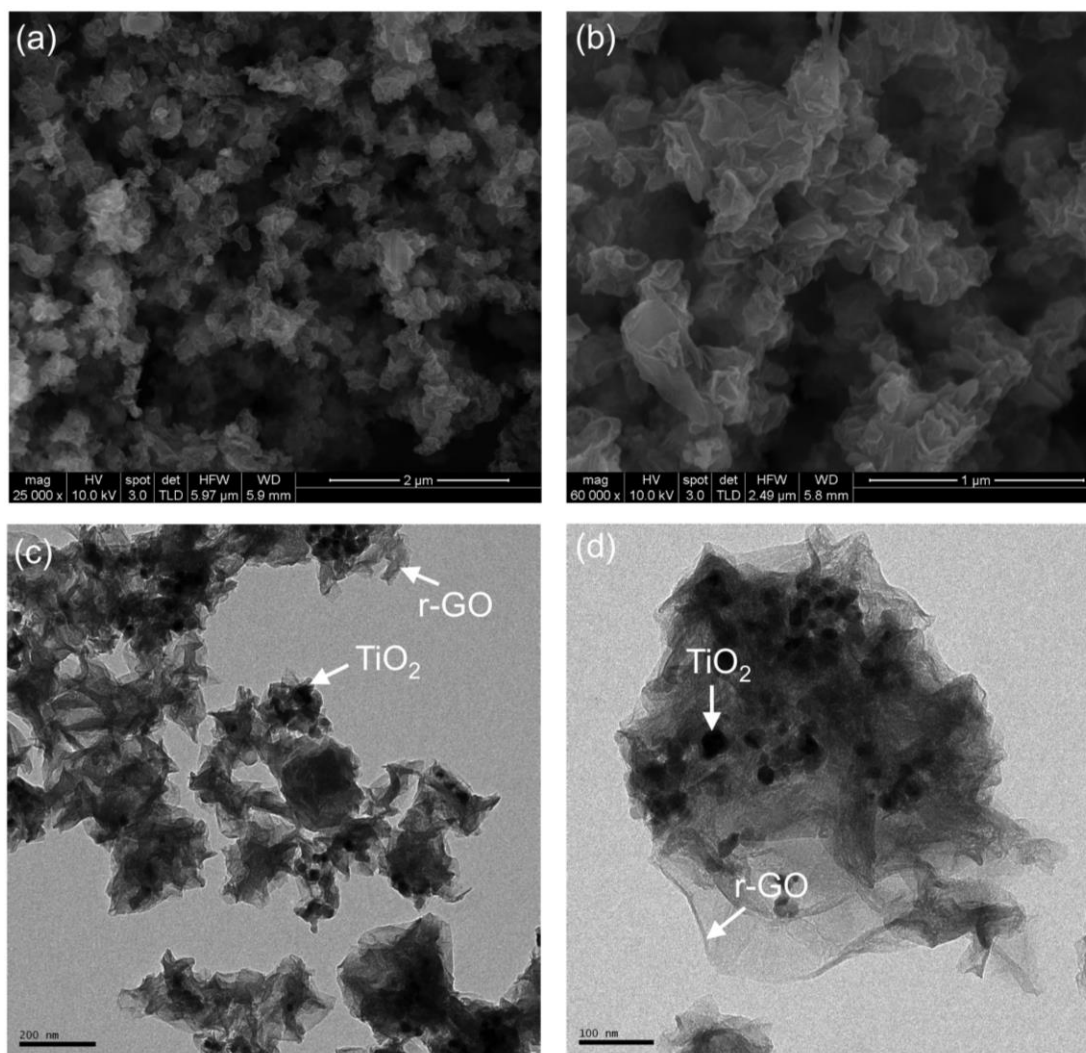


Figure 4.2 Images of CGOATI (TiO₂/GO 20%, EDA/GO 15:1, at 200 °C): (a) SEM image with lower magnification, (b) SEM image with higher magnification, (c) TEM image with lower magnification, (d) TEM image with higher magnification.

The void factor is about 85%, and the calculated number of TiO₂ NPs encapsulated in one nanocomposite particle is about 1550, and the average distance between two TiO₂ NPs is around 20 nm (see Supporting information S4.3 for details). Therefore, the TiO₂ NPs are expected to be well separated, and the interparticle e⁻-h⁺ recombination is not significant. In addition, intraparticle e⁻-h⁺ recombination can also be retarded because the electrons can be rapidly trapped by r-GO nanosheets.⁴⁴ Moreover, it can be inferred that

this hollow structure allows r-GO nanosheets to have a higher possibility of adsorbing moisture and CO₂, which can also enhance the CO₂ photoreduction efficiency.

4.3.2 CO₂ adsorption and photoreduction

A series of background tests (Table 1, test 2) were conducted to confirm that any carbon-containing products in the effluent gas measured by GC originated from the photo-conversion of the CO₂ reactant, and not from the nanocomposite particles. The following cases were tested with a mixture of CO₂ and H₂O vapor passing through the reactor: (1) without any nanocomposite catalysts or glass fiber membrane, (2) blank glass fiber membrane in the reactor. No CO₂ conversion products (CO or CH₄) were detected whether the light was on or off. To further confirm that no CO was produced by decomposition of CGOATI, a background test with CGOATI present in the reactor, using nitrogen and H₂O vapor was conducted. When the light was on, CO was not detected, although a small amount of CO₂ was detected, which was much smaller compared to the baseline flow of the CO₂ (Supporting information, Figure S4.3, S4.4). The products were only observed when CO₂ was passed over CGOATI that was irradiated with light. In addition, isotope tracer analyses using ¹³CO₂ were conducted for the optimized CGOATI. Figure S4.5 (Supporting information) shows the mass chromatography spectra of the gas samples in the reactor before UV-irradiation, and after 2h UV-irradiation. A peak corresponding to ¹³CO ($m/z = 13$) was detected in the spectrum after 2h UV-irradiation. Therefore, it can be concluded that CO was derived from CO₂ in the feed gas, and not from the decomposition of the catalyst. Volumetric ratio of O₂/N₂ was also monitored as a function of irradiation time, which shows a very similar tendency as that of CO yield, implying the ratio of oxidation and reduction products meets stoichiometry (see Supporting Information, S4.7).

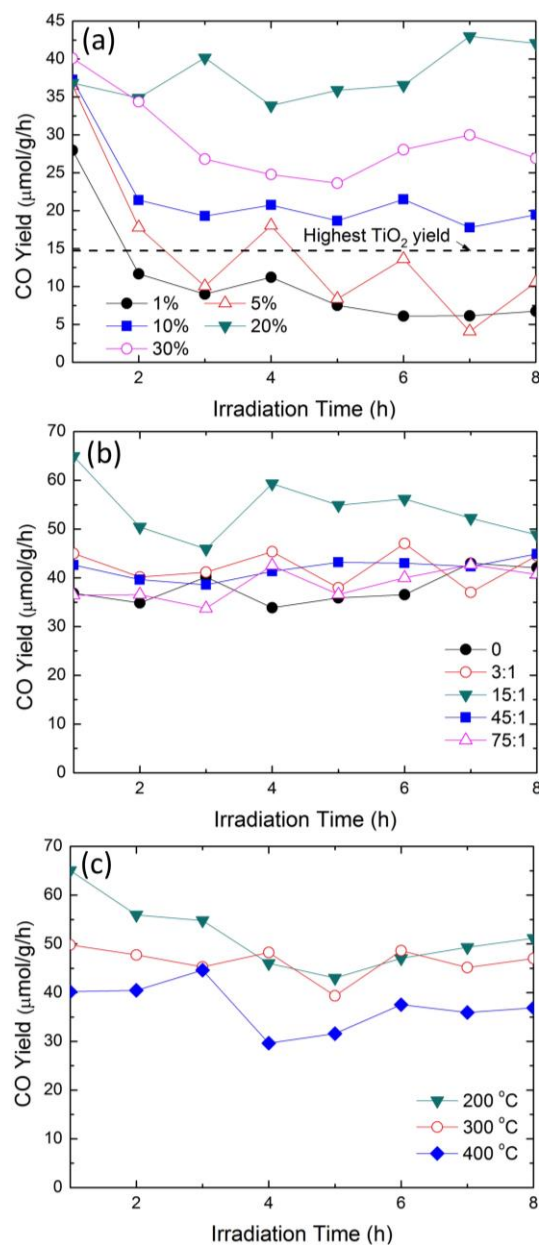


Figure 4.3 CO₂ photoreduction of (a) CGOTI nanocomposites with different TiO₂/GO percentages at 200 °C (Table 1, test 1(1)), (b) CGOATI nanocomposites with different EDA/GO ratios, TiO₂/GO percentage was fixed at 20%, at 200 °C (Table 1, test 1(2)), (c) CGOATI nanocomposites prepared at different synthesis temperatures, with the EDA/GO ratio at 15:1 and TiO₂/GO percentage at 20% (Table 1, test 1(3)).

CO₂ photoreduction results for nanocomposites synthesized with different TiO₂/GO percentages (mass ratios of TiO₂ to GO) are shown in Figure 4.3a, with CO yield

normalized by the mass of the entire catalyst (r-GO and TiO₂). For all the samples, the CO yield reached a peak value within 1 hour. The optimal performance was obtained at 20% TiO₂/GO, with a CO yield of about 40 μmol/g/h. The fact that lower TiO₂/GO loading percentages yielded low CO values might have been due to the fewer active catalyst sites available for photoreduction. The CO yield, however, decreased with further increases in the TiO₂/GO percentage after the optimal value (20%). Based on our previous studies,^{31, 32} TiO₂/GO percentages beyond 20% increased the possibility of agglomeration of TiO₂ NPs both inside and outside the r-GO nanosheets. The overall CO₂ photoreduction efficiency will be affected by both the interparticle e⁻-h⁺ recombination due to the agglomeration of TiO₂ NPs inside the r-GO nanosheets, and the intraparticle e⁻-h⁺ recombination resulting from free TiO₂ NPs outside the r-GO nanosheets.

To investigate the effect of the EDA/GO ratio (mass ratio), CGOATI nanocomposites were also synthesized with different mass ratios of EDA to GO, but the same optimal TiO₂/GO percentage (20%) and synthesis temperature (200 °C). As shown in Figure 4.3b, the optimal mass ratio of EDA to GO in the precursor solution was 15:1, with the highest CO yield of 65 μmol/g/h. The relatively low EDA/GO ratio enhanced the photoreduction performance; however, the CO yield decreased with higher EDA /GO ratios. The excessive EDA on the surface of the nanocomposite affects the conductivity of CGOATI after CO₂ photoreduction, and this is discussed in detail later, along with resistivity and Raman analysis results (Figure 4.8).

The effect of synthesis temperature on CO₂ photoreduction performance was also investigated, and the results are shown in Figure 4.3c. The results indicate that the sample synthesized at 200 °C has the highest CO yield (65 μmol/g/h), and this decreases to 40

$\mu\text{mol/g/h}$ as the synthesis temperature was increased to $400\text{ }^\circ\text{C}$. During the synthesis process in the furnace, the GO nanosheets were reduced to r-GO by thermal removal of surface functional groups. Temperature played an important role in tailoring r-GO surface functional groups. The resistivity of CGOTI samples synthesized under different temperatures (before and after CO_2 photoreduction) is summarized in Table 2. With thermal reduction of GO, the conductivity first increased and then decreased after $400\text{ }^\circ\text{C}$, based on the conductivity results of CGOTI samples before CO_2 photoreduction. It is well documented that GO has a much lower conductivity than graphene due to the surface defects of functional groups.⁴⁵ With the removal of surface functional groups by thermal reduction, the conductivity can be partially restored. However, with a further increase of temperature (over $400\text{ }^\circ\text{C}$), more surface defects, such as carbon vacancy, are created due to the reactions during the thermal removal of surface functional groups.⁴⁶ Thus temperatures below $400\text{ }^\circ\text{C}$ were only investigated, and the optimal temperature was $200\text{ }^\circ\text{C}$. At these low temperatures, the thermal reduction of r-GO nanosheets was limited (the conductivity of r-GO synthesized under $200\text{ }^\circ\text{C}$ was the lowest before CO_2 photoreduction), but the r-GO underwent simultaneous photoreduction during CO_2 photoreduction. From Table 2, it is clear that the resistivity of the $200\text{ }^\circ\text{C}$ sample decreased dramatically from $>6.43\text{ M}\Omega\cdot\text{m}$ to about $0.02\text{ M}\Omega\cdot\text{m}$, indicating a significant increase in conductivity due to the photoreduction of r-GO simultaneously occurring during the CO_2 photoreduction process. The temperature in the reactor was measured (by a K-type thermocouple) to be around $70\text{ }^\circ\text{C}$, which was not high enough for photothermal reduction of r-GO. Therefore, the photoreduction of r-GO was a photochemical process. The resistivity of the samples prepared at higher temperatures (over $400\text{ }^\circ\text{C}$), did not change

significantly after photoreduction, implying that most surface functional groups on those samples were removed prior by thermal processes reduction during synthesis. The simultaneous photoreduction method is a softer reduction method than the intense thermal reduction, since 200 °C CGOTI samples had a higher conductivity (electron trapping capability) than 400 °C CGOTI samples after photoreduction. This softer reduction explains why the samples prepared at lower temperatures demonstrated better performance than their counterparts synthesized at higher temperatures.

Table 4.2 The conductivity of CGOTI (TiO₂/GO 20%) samples synthesized under different temperatures (before and after CO₂ photoreduction).

Synthesis temperature (°C)		200	400	600	800
Resistance (Ω)	Before CO ₂ photoreduction	>10G	~180M	~1G	~1.7G
	After CO ₂ photoreduction	~30M	~170M	~800M	~1.5G

4.3.3 Surface chemistry characterization for CO₂ photoreduction mechanism

FTIR spectroscopy is employed to assess the bonding chemistry during the CO₂ adsorption and photoreduction processes. In Figure 4.4 (the spectrum for the range 650-2000 cm⁻¹ can be found in Figure S4.7, Supporting information), the FTIR spectrum of pristine (original material before CO₂ adsorption and photoreduction) CGOTI shows typical absorption peaks of oxygen-based functional groups: The broad peak at 3400 cm⁻¹ is assigned to the -OH groups, and the peaks at 1727 cm⁻¹ and 1620 cm⁻¹, correspond to carboxyl and carbonyl groups, respectively, and the peaks at 1066 cm⁻¹ and 1000 cm⁻¹ correspond to alkoxy C-O and epoxy C-O, respectively.⁴⁷ After the modification of graphene oxide with EDA, the peak at 1727 cm⁻¹ disappears, and meanwhile a new broad

peak at 1626 cm^{-1} emerges, which corresponds to the stretching vibration of the C=O group in $-\text{CONH}-$,⁴⁸ showing evidence of reactions between carboxyl groups and amine groups.

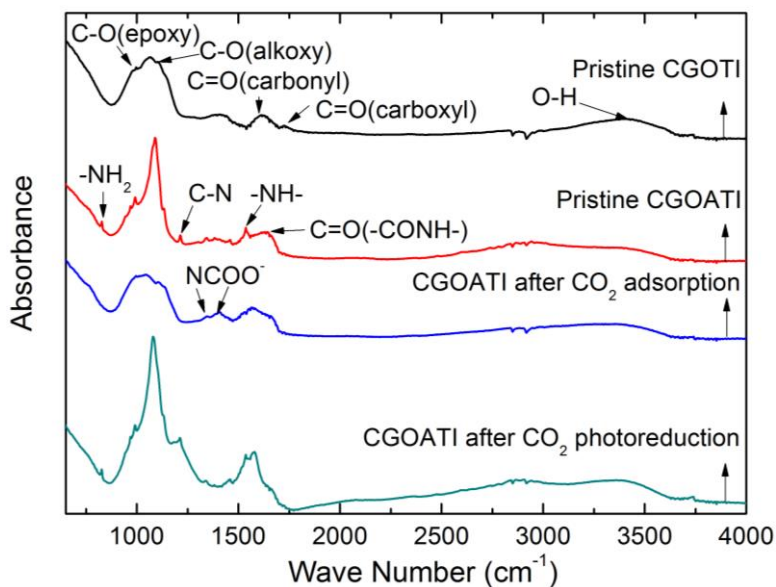


Figure 4.4 FTIR analysis of pristine CGOTI (TiO_2/GO 20%, at $200\text{ }^\circ\text{C}$), pristine CGOATI (TiO_2/GO 20%, EDA/GO 15:1, at $200\text{ }^\circ\text{C}$). Also shown are the spectra for the samples, CGOATI after CO_2 adsorption (only) and CO_2 adsorption and photoreduction.

Furthermore, a new peak at 1220 cm^{-1} corresponds to C-N stretching vibration,⁴⁹ and the new peaks at 1535 cm^{-1} and 830 cm^{-1} correspond to $-\text{NH}-$ and $-\text{NH}_2$ bending vibrations,⁵⁰ respectively, which indicates that a ring-opening reaction occurred between the amine groups and epoxy groups on the r-GO surface. To verify the adsorption and photoreduction of CO_2 , the FTIR spectra of CGOATI after CO_2 adsorption and after photoreduction were also obtained (Figure 4.4). After CO_2 adsorption, a significant decrease in intensity of $-\text{NH}-$ and $-\text{NH}_2$ peaks is observed. The new peaks at 1320 and 1410 cm^{-1} are assigned to NCOO^- skeletal vibration of alkylammonium carbamate species.⁵¹ In the spectrum of CGOATI after CO_2 photoreduction, the peaks at 1320 and 1410 cm^{-1}

disappear. However, the -NH- and -NH₂ peaks are observed again, implying that the NCOO⁻ groups are reduced and amine groups are regenerated after CO₂ photoreduction.

The C- and N- containing groups in pristine CGOATI were also identified from the XPS spectrum, where the peaks corresponding to C, N and O elements are apparent (Figure 4.5a). However, only C and O elements are clearly distinguished in the spectrum of pristine CGOTI (Figure 4.5a). There is a small N peak in the CGOTI spectrum, which may be caused by impurity formed in the synthesis process. In the N 1s XPS spectra of the CGOATI, the two peaks at ~400.8 eV and ~399.5 eV are assigned to C(O)-N and C-N(H)-C or C-NH₂ species.⁵² As shown in Figure 4.5(b, c, d), the percentage of C-N(H)-C or C-NH₂ species decreases from 61.8% to 52.9% after CO₂ adsorption on CGOATI, but increases to 61.7% after CO₂ photoreduction, which verifies the formation of alkylammonium carbamate species due to CO₂ adsorption and the reduction of carbamate after photoreduction. The deconvoluted C 1s spectrum (Figure 4.6a) of pristine CGOTI shows a strong C_{epoxide} signal (286.5 eV),⁵² which decreases in intensity in the spectrum of pristine CGOATI. In addition, two new peaks corresponding to C(O)-N (287.4 eV) and C-N (286.6 eV)⁵² appear in the C 1s spectrum of pristine CGOATI (Figure 4.6c), which confirms the ring-opening reaction between the amine groups and epoxy groups. As shown in Figure 4.6(b, d), a significant decrease in intensity of oxygen-containing groups (especially hydroxyl (285.9 eV) and epoxy groups (286.5 eV)⁵²) is observed in the spectra of both CGOATI and CGOTI after photoreduction, compared to the pristine samples. This decrease indicates the simultaneous photoreduction of r-GO in the CO₂ photoreduction process.

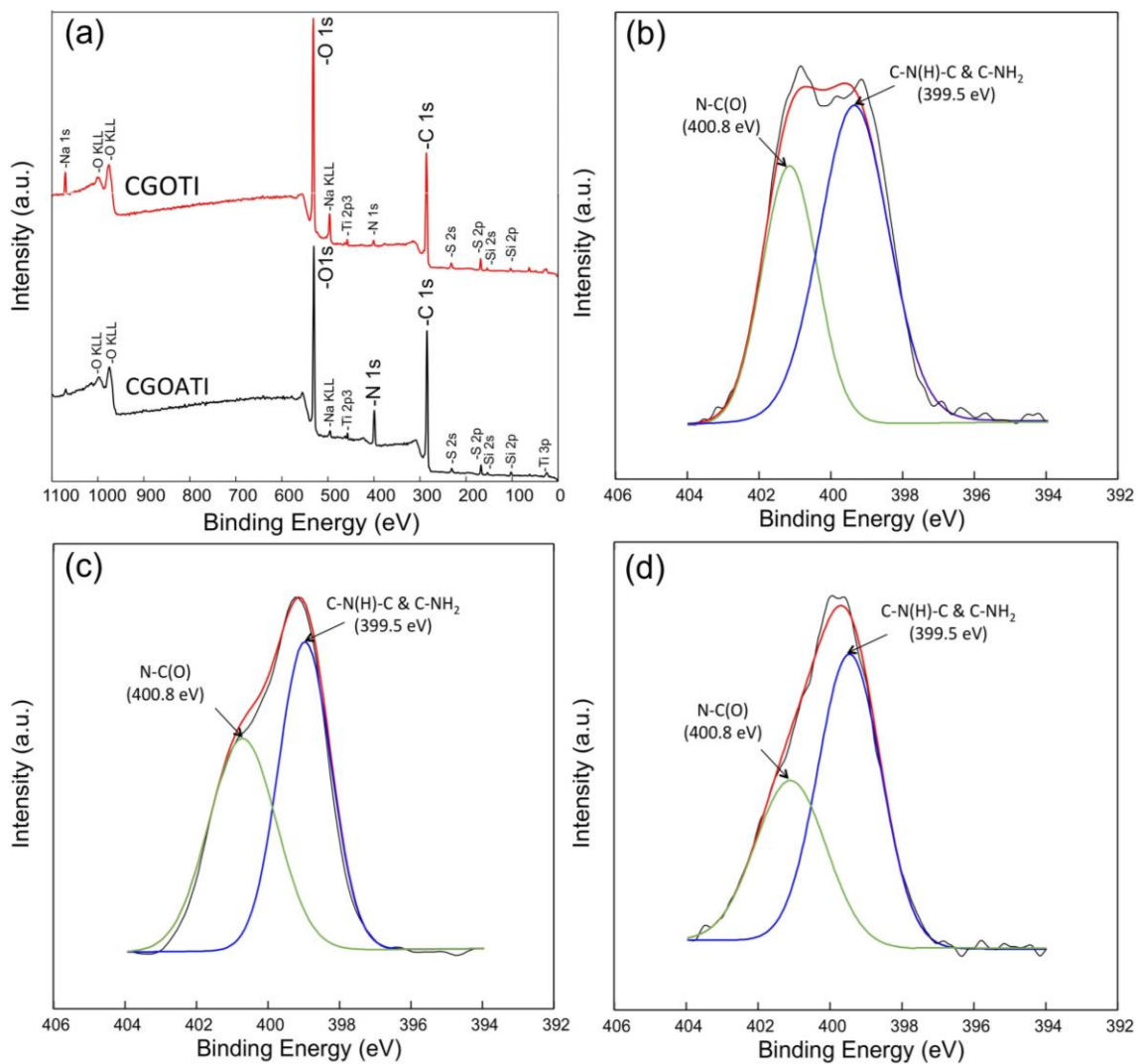


Figure 4.5 (a) XPS survey spectra of pristine CGOTI (TiO₂/GO 20%, at 200 °C) and pristine CGOATI (TiO₂/GO 20%, EDA/GO 15:1, at 200 °C), (b) N1s XPS spectrum of pristine CGOATI, (c) N1s XPS spectrum of CGOATI after CO₂ adsorption (only), (d) N1s XPS spectrum of CGOATI after CO₂ adsorption and photoreduction.

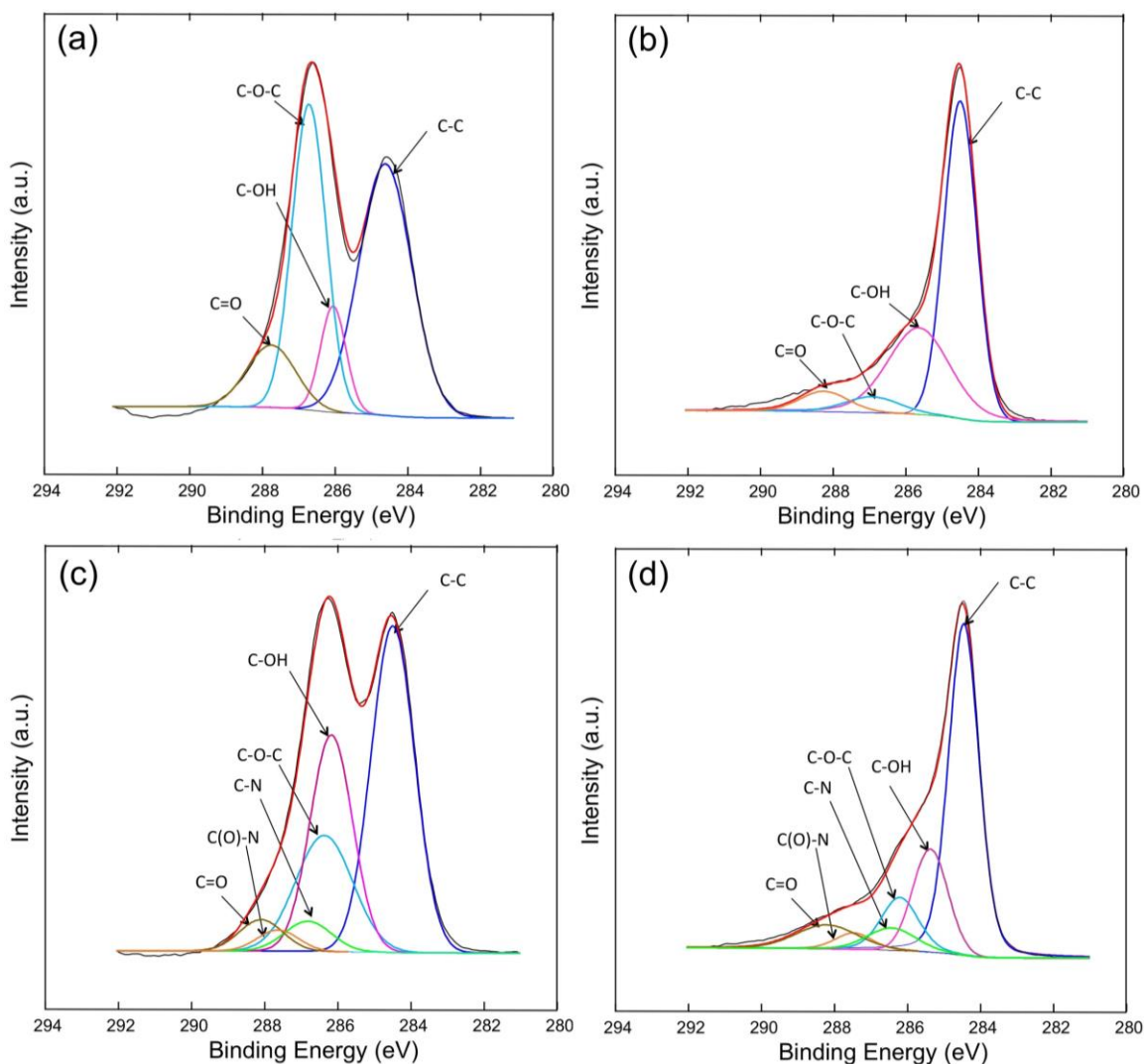


Figure 4.6 C1s XPS spectra of (a) pristine CGOTI (TiO₂/GO 20%, at 200 °C), (b) CGOTI after CO₂ photoreduction, (c) pristine CGOATI (TiO₂/GO 20%, EDA/GO 15:1, at 200 °C), (d) CGOATI after CO₂ photoreduction.

Based on the above characterization results, overall reaction mechanisms of the insertion of amines on r-GO, and the CO₂ adsorption and photoreduction using CGOATI are illustrated in Figure 4.7. The first step is the addition of EDA by the reactions between amine groups of EDA and the epoxy and carboxyl groups on the r-GO surface.^{39,53} This is followed by the free amine groups of EDA adsorbing CO₂ to form alkylammonium carbamate species.^{51,54} The carbamate species are then photoreduced by TiO₂ under UV

light to generate CO and regenerate the amine groups, during which r-GO is simultaneously photoreduced by removal of oxygen-containing groups.

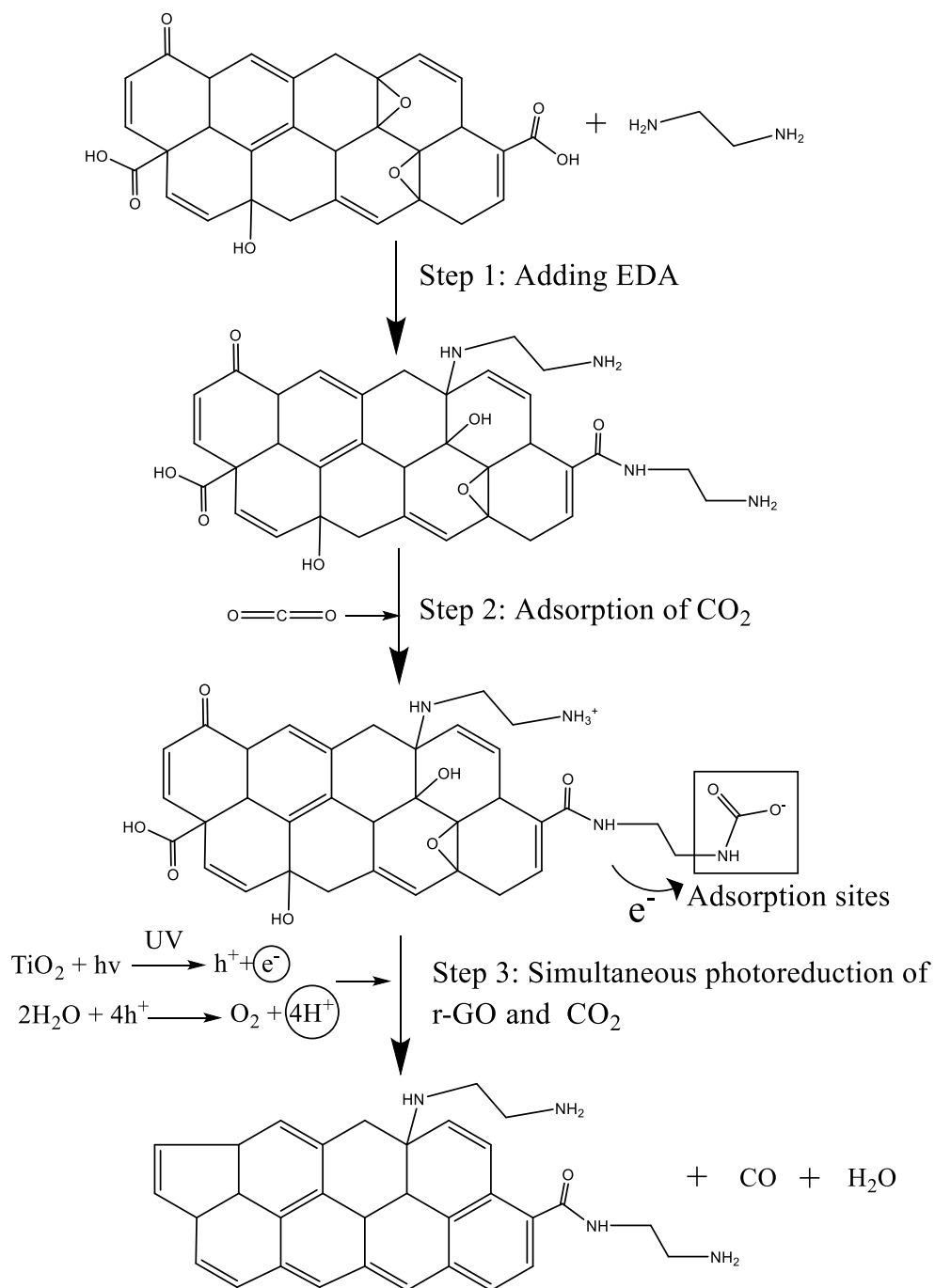


Figure 4.7 Proposed reaction mechanisms of the insertion of EDA on r-GO, and CO_2 adsorption and photoreduction on CGOATI nanocomposites.

To further verify the change in surface characteristics of these graphene-based nanocomposites, samples of CGOTI and CGOATI before and after CO₂ adsorption and photoreduction were analyzed by Raman spectroscopy. As seen in Figure 9, two characteristic bands of r-GO are observed. These are the D band (~1350 cm⁻¹, a measure of hexagonal carbon pattern distortions, such as defects) and the G band (~1600 cm⁻¹, a measure of pure sp² hybridized graphene carbon).⁵⁵ The ratio I_D/I_G is usually used to determine defect density, however, each ratio can correspond to two different defect densities, above or below the maximum ratio, as found in previous reports.⁵⁶ Based on the width of G bands (full width at half-maximum (FWHM) > critical value ~ 14 cm⁻¹), we determined that the defect regime of our r-GO material was in the so-called stage-2 regime, where the I_D/I_G ratios increase with decreased defect densities.⁵⁶ From Figure 8(a), there was no significant change in the I_D/I_G ratio of CGOTI samples before (0.89±0.03) and after (0.89±0.02) CO₂ adsorption. However, it increased to 1.04 after CO₂ photoreduction, which showed the decrease of defect densities, indicating simultaneous photoreduction of r-GO. This observation is consistent with the trends reported in our previous work on CO₂ photoreduction of CGOTI³¹ and is confirmed by our conductivity measurements in Table 4.2.

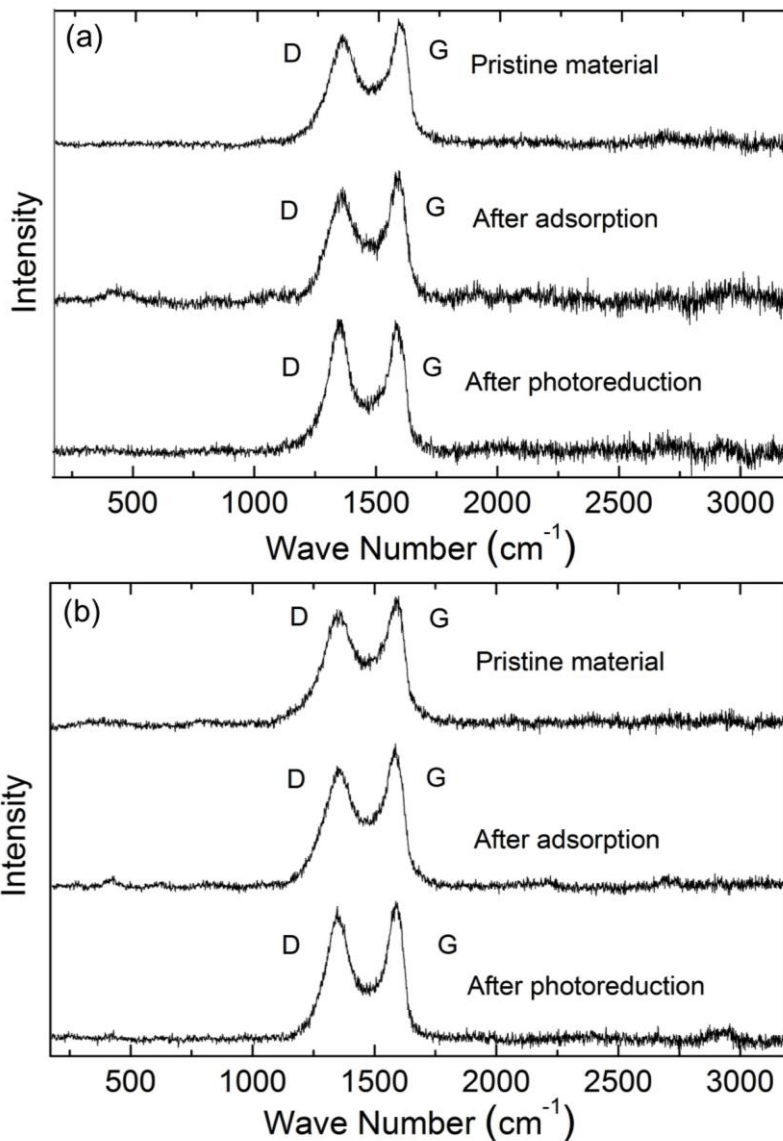


Figure 4.8 Raman analysis of (a) CGOTI (TiO₂/GO 20%, at 200 °C) samples and (b) CGOATI (TiO₂/GO 20%, EDA/GO 15:1, at 200 °C) samples before and after CO₂ adsorption and CO₂ photoreduction.

For CGOATI samples, an increase in I_D/I_G ratio after photoreduction (from 0.88 ± 0.01 to 0.97 ± 0.01) was also observed, but the increase was not as significant as that of CGOTI ($I_D/I_G = 1.04$). The addition of EDA breaks epoxy groups to form hydroxyl groups and C-N bonds, as identified by FTIR and XPS analyses. While reduction of r-GO was mainly due to the removal of hydroxyl and epoxy groups (XPS spectra), the removal

of the C-N bond may have been quite difficult, since the N atom was also bonded with the C atom in the EDA molecules. This difficulty could possibly explain why CGOATI was harder to photoreduce compared to CGOTI (see the final I_D/I_G ratios). Figure S8 (Supporting information) shows the I_D/I_G ratios and electrical resistivity of CGOTI samples synthesized under different temperatures. A larger I_D/I_G ratio (meaning lower defect densities in the stage-2 regime) was observed in materials with higher conductivity (lower resistivity). The conductivity of pristine CGOATI samples was similar to that of pristine CGOTI samples synthesized at 200 °C, which indicated that the addition of EDA didn't significantly affect the conductivity of CGOTI. However, CGOATI samples were measured to have a lower conductivity than CGOTI samples after photoreduction, which is consistent with the Raman measurement showing that the I_D/I_G ratio of CGOATI was lower than that of CGOTI. Taken together with the adsorption experimental results, it can be generalized that the optimized CO₂ photoreduction performance with the addition of EDA was mainly a compromise between CO₂ adsorption and r-GO conductivity.

4.3.4 Recyclability test

The CO₂ photoreduction performance of CGOATI after two run cycles was investigated (see Figure S9, Supporting information). In the first cycle, the CO yield decreased after 1h and reached a steady value of 35 μmol/g/h after 2 h. In the second cycle, the CO yield remained in this steady state, which confirmed the stability of this material. Pure TiO₂ is reported to be unstable, with decreasing photoreduction performance after 4 h.⁵⁷ The decrease in performance of pure TiO₂ may be attributed to diminishment of the adsorption power of the particles.¹⁶ In the case of CGOATI, the adsorption of CO₂ can be

maintained for a longer time due to the regeneration of amine groups after photoreduction (FTIR and XPS spectra), which leads to a higher stability.

4.4 Conclusion

CGOATI nanocomposites were readily prepared using a one-step aerosol technique in a furnace aerosol reactor. The effects of TiO₂/GO percentage, EDA/GO ratio, and synthesis temperature on CO₂ photoreduction were investigated systematically. The isotope experiment and background tests verified that the CO originated from CO₂, not from the decomposition of the CGOATI. The optimal conditions for CO₂ photoreduction were established: a 20% TiO₂/GO percentage, a 15:1 EDA/GO mass ratio in precursor solution, and a 200 °C synthesis temperature. CGOATI nanocomposites synthesized under these conditions had a maximal CO yield of 65 μmol/g/h, (the apparent quantum efficiency is 0.0094%, see Supporting information S11 for detailed calculations), which is four-fold higher than that of pure TiO₂, even when it is normalized by the entire catalyst mass. A mechanistic understanding of the various pathways was unravelled. The modification of GO by EDA, the adsorption of CO₂ by CGOATI, and the photoreduction of adsorbed CO₂ were confirmed by FTIR and XPS spectra. EDA played an important role in improving CO₂ adsorption and further enhancing overall CO₂ photoreduction. EDA enhanced the adsorption of CO₂ and then formed alkylammonium carbamate species; the carbamate species were photoreduced by irradiated TiO₂, generating CO and then regenerating the amine groups. The XPS spectra also verified the photoreduction of r-GO by TiO₂. From the Raman analysis, the ratio of I_D/I_G was observed to increase after CO₂ photoreduction, which indicated the simultaneous photoreduction of r-GO by TiO₂ during the CO₂ photoreduction process. The photoreduction of GO is a softer method than thermal

reduction of GO, since it can restore a higher conductivity of r-GO and enhance CO₂ photoreduction performance. The stability of the CGOATI was also better than that of pure TiO₂.

Acknowledgements

Y.N. thanks the McDonnell International Scholars Academy and the McDonnell Academy Global Energy and Environment Partnership (MAGEEP) for the fellowship to pursue a Ph.D. at Washington University in St. Louis. Partial support from the Consortium for Clean Coal Utilization (CCCU) and the Solar Energy Research Institute for India and the United States (SERIUS) funded by the US Department of Energy at Washington University in St. Louis is gratefully acknowledged. Electron microscopy work was performed at the Nano Research Facility (NRF) at Washington University in St. Louis, a member of the National Nanotechnology Infrastructure Network (NNIN), supported by the National Science Foundation under Grant No. ECS-0335765.

References

1. P. Biswas, W.-N. Wang and W.-J. An, *Front. Environ. Sci. Eng. China*, 2011, **5**, 299-312.
2. M. R. Raupach, G. Marland, P. Ciais, C. Le Quéré, J. G. Canadell, G. Klepper and C. B. Field, *Proc. Natl. Acad. Sci. U. S. A.*, 2007, **104**, 10288-10293.
3. D. Etheridge, L. Steele, R. Langenfelds, R. Francey, J. M. Barnola and V. Morgan, *J. Geophys. Res.: Atmos.*, 1996, **101**, 4115-4128.
4. D. Hofmann, J. Butler, E. Dlugokencky, J. Elkins, K. Masarie, S. Montzka and P. Tans, *Tellus B*, 2006, **58**, 614-619.
5. B. Metz, O. Davidson, H. De Coninck, M. Loos and L. Meyer, 2005.
6. A. B. Rao and E. S. Rubin, *Environ. Sci. Technol.*, 2002, **36**, 4467-4475.
7. D. Singh, E. Croiset, P. L. Douglas and M. A. Douglas, *Energy Convers. Manage.*, 2003, **44**, 3073-3091.
8. M. Halbwachs and J.-C. Sabroux, *Science (New York, NY)*, 2001, **292**, 438.
9. W. C. Chueh, C. Falter, M. Abbott, D. Scipio, P. Furler, S. M. Haile and A. Steinfeld, *Science*, 2010, **330**, 1797-1801.
10. S. Sen, D. Liu and G. T. R. Palmore, *ACS Catalysis*, 2014, **4**, 3091-3095.
11. W. Hou, W. H. Hung, P. Pavaskar, A. Goepfert, M. Aykol and S. B. Cronin, *ACS Catalysis*, 2011, **1**, 929-936.
12. S. C. Roy, O. K. Varghese, M. Paulose and C. A. Grimes, *Acs Nano*, 2010, **4**, 1259-1278.
13. L. Liu, C. Zhao, H. Zhao, D. Pitts and Y. Li, *Chem. Commun.*, 2013, **49**, 3664-3666.
14. Q. Zhang, Y. Li, E. A. Ackerman, M. Gajdardziska-Josifovska and H. Li, *Appl. Catal., A*, 2011, **400**, 195-202.
15. A. L. Linsebigler, G. Lu and J. T. Yates Jr, *Chem. Rev.*, 1995, **95**, 735-758.
16. W.-N. Wang, W.-J. An, B. Ramalingam, S. Mukherjee, D. M. Niedzwiedzki, S. Gangopadhyay and P. Biswas, *J. Am. Chem. Soc.*, 2012, **134**, 11276-11281.
17. C.-C. Lo, C.-H. Hung, C.-S. Yuan and J.-F. Wu, *Sol. Energy Mater. Sol. Cells*, 2007, **91**, 1765-1774.

18. W.-N. Wang, J. Soulis, Y. J. Yang and P. Biswas, *Aerosol Air Qual. Res.*, 2014, **14**, 533-549.
19. B. Pan, S. Luo, W. Su and X. Wang, *Appl. Catal., B*, 2015, **168**, 458-464.
20. I. Tseng, J. Wu and H.-Y. Chou, *J. Catal.*, 2004, **221**, 432-440.
21. L. Zhang, J. C. Yu, H. Y. Yip, Q. Li, K. W. Kwong, A.-W. Xu and P. K. Wong, *Langmuir*, 2003, **19**, 10372-10380.
22. H. Eckstein and U. Kreibitz, *Zeitschrift für Physik D Atoms, Molecules and Clusters*, 1993, **26**, 239-241.
23. K. Kimura, *J. Phys. Chem.*, 1994, **98**, 11997-12002.
24. K. S. Novoselov, A. K. Geim, S. Morozov, D. Jiang, Y. Zhang, S. Dubonos, I. Grigorieva and A. Firsov, *Science*, 2004, **306**, 666-669.
25. M. D. Stoller, S. Park, Y. Zhu, J. An and R. S. Ruoff, *Nano Lett.*, 2008, **8**, 3498-3502.
26. J. Cheng, M. Zhang, G. Wu, X. Wang, J. Zhou and K. Cen, *Environ. Sci. Technol.*, 2014, **48**, 7076-7084.
27. W. Tu, Y. Zhou, Q. Liu, S. Yan, S. Bao, X. Wang, M. Xiao and Z. Zou, *Adv. Funct. Mater.*, 2013, **23**, 1743-1749.
28. J. Luo, H. D. Jang, T. Sun, L. Xiao, Z. He, A. P. Katsoulidis, M. G. Kanatzidis, J. M. Gibson and J. Huang, *Acs Nano*, 2011, **5**, 8943-8949.
29. X. Ma, M. R. Zachariah and C. D. Zangmeister, *Nano Lett.*, 2011, **12**, 486-489.
30. Y. Chen, F. Guo, A. Jachak, S.-P. Kim, D. Datta, J. Liu, I. Kulaots, C. Vaslet, H. D. Jang and J. Huang, *Nano Lett.*, 2012, **12**, 1996-2002.
31. W.-N. Wang, Y. Jiang, J. D. Fortner and P. Biswas, *Environ. Eng. Sci.*, 2014, **31**, 428-434.
32. Y. Jiang, W.-N. Wang, P. Biswas and J. D. Fortner, *ACS Appl. Mater. Interfaces*, 2014, **6**, 11766-11774.
33. J. Luo, X. Zhao, J. Wu, H. D. Jang, H. H. Kung and J. Huang, *J. Phys. Chem. Lett.*, 2012, **3**, 1824-1829.
34. H. D. Jang, S. K. Kim, H. Chang, K.-M. Roh, J.-W. Choi and J. Huang, *Biosensors Bioelectron.*, 2012, **38**, 184-188.
35. H. D. Jang, S. K. Kim, H. Chang, J.-W. Choi, J. Luo and J. Huang, *Aerosol Sci. Technol.*, 2013, **47**, 93-98.

36. M. A. Alkhabbaz, P. Bollini, G. S. Foo, C. Sievers and C. W. Jones, *J. Am. Chem. Soc.*, 2014, **136**, 13170-13173.
37. R. Serna-Guerrero, Y. Belmabkhout and A. Sayari, *Chem. Eng. J.*, 2010, **158**, 513-519.
38. Y. Zhao, H. Ding and Q. Zhong, *Appl. Surf. Sci.*, 2012, **258**, 4301-4307.
39. K. P. Loh, Q. Bao, P. K. Ang and J. Yang, *J. Mater. Chem.*, 2010, **20**, 2277-2289.
40. W. S. Hummers Jr and R. E. Offeman, *J. Am. Chem. Soc.*, 1958, **80**, 1339-1339.
41. W.-N. Wang, Y. Jiang and P. Biswas, *J. Phys. Chem. Lett.*, 2012, **3**, 3228-3233.
42. W.-N. Wang, J. Park and P. Biswas, *Catal. Sci. Technol.*, 2011, **1**, 593-600.
43. W.-N. Wang, W. Widiyastuti, I. W. Lenggoro, T. O. Kim and K. Okuyama, *J. Electrochem. Soc.*, 2007, **154**, J121-J128.
44. Y. Zhang, Z.-R. Tang, X. Fu and Y.-J. Xu, *ACS nano*, 2010, **4**, 7303-7314.
45. P. V. Kamat, *J. Phys. Chem. Lett.*, 2011, **2**, 242-251.
46. A. Bagri, C. Mattevi, M. Acik, Y. J. Chabal, M. Chhowalla and V. B. Shenoy, *Nat Chem*, 2010, **2**, 581-587.
47. W.-H. Liao, S.-Y. Yang, J.-Y. Wang, H.-W. Tien, S.-T. Hsiao, Y.-S. Wang, S.-M. Li, C.-C. M. Ma and Y.-F. Wu, *ACS Appl. Mater. Interfaces*, 2013, **5**, 869-877.
48. W. Hou, B. Tang, L. Lu, J. Sun, J. Wang, C. Qin and L. Dai, *RSC Advances*, 2014, **4**, 4848-4855.
49. C. Shan, H. Yang, D. Han, Q. Zhang, A. Ivaska and L. Niu, *Langmuir*, 2009, **25**, 12030-12033.
50. H.-J. Chen, Z.-H. Zhang, R. Cai, X. Chen, Y.-N. Liu, W. Rao and S.-Z. Yao, *Talanta*, 2013, **115**, 222-227.
51. X. Wang, V. Schwartz, J. C. Clark, X. Ma, S. H. Overbury, X. Xu and C. Song, *J. Phys. Chem. C*, 2009, **113**, 7260-7268.
52. D. Lee, M.-C. Choi and C.-S. Ha, *J. Polym. Sci., Part A: Polym. Chem.*, 2012, **50**, 1611-1621.
53. Y. Jiang, W.-N. Wang, D. Liu, Y. Nie, W. Li, J. Wu, F. Zhang, P. Biswas and J. D. Fortner, *Environ. Sci. Technol.*, 2015, **49**, 6846-6854.
54. J. Yu, Y. Le and B. Cheng, *RSC Advances*, 2012, **2**, 6784-6791.
55. S. Stankovich, D. A. Dikin, R. D. Piner, K. A. Kohlhaas, A. Kleinhammes, Y. Jia, Y. Wu, S. T. Nguyen and R. S. Ruoff, *Carbon*, 2007, **45**, 1558-1565.

56. L. G. Cançado, A. Jorio, E. H. M. Ferreira, F. Stavale, C. A. Achete, R. B. Capaz, M. V. O. Moutinho, A. Lombardo, T. S. Kulmala and A. C. Ferrari, *Nano Lett.*, 2011, **11**, 3190-3196.
57. Y. Li, W.-N. Wang, Z. Zhan, M.-H. Woo, C.-Y. Wu and P. Biswas, *Appl. Catal., B*, 2010, **100**, 386-392.

Chapter 4 Supporting Information

Table of Contents

S4.1 UV-Vis absorption spectrum

S4.2 Light spectrum of the Xe lamp

S4.3 Calculation of the average distance between two TiO₂ NPs

S4.4 Background CO test

S4.5 Background CO₂ test

S4.6 Isotope experiments

S4.7 Reaction stoichiometry

S4.8 Magnified FTIR spectrum

S4.9 The I_D/I_G ratio and resistivity of CGOTI

S4.10 Recyclability test

S4.11 Apparent quantum efficiency calculation

S4.1 UV-Vis absorption spectrum of TiO₂, CGO (at 200 °C), CGOTI (TiO₂/GO 20%, at 200 °C) and CGOATI (TiO₂/GO 20%, EDA/GO 15:1, at 200 °C) (20mg/L)

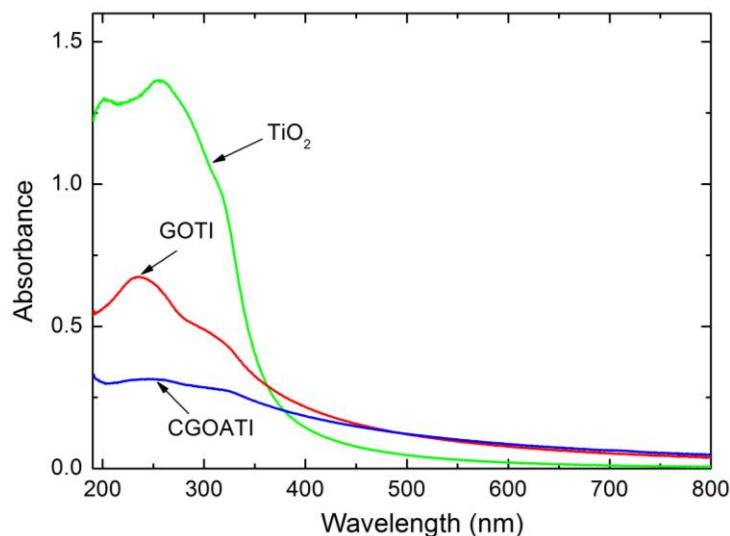


Figure S1. UV-Vis absorption spectrum of TiO₂, (at 200 °C), CGOTI (TiO₂/GO 20%, at 200 °C) and CGOATI (TiO₂/GO 20%, EDA/GO 15:1, at 200 °C) (20mg/L).

From the figure above, an extended absorption range was observed when compared to bare TiO₂, which is due to the band gap narrowing of TiO₂ when participating in Ti-O-C interactions¹. This extension makes the graphene-modified TiO₂ have an advantage over bare TiO₂ in the utilization of light.

S4.2 Light spectrum of the Xe lamp

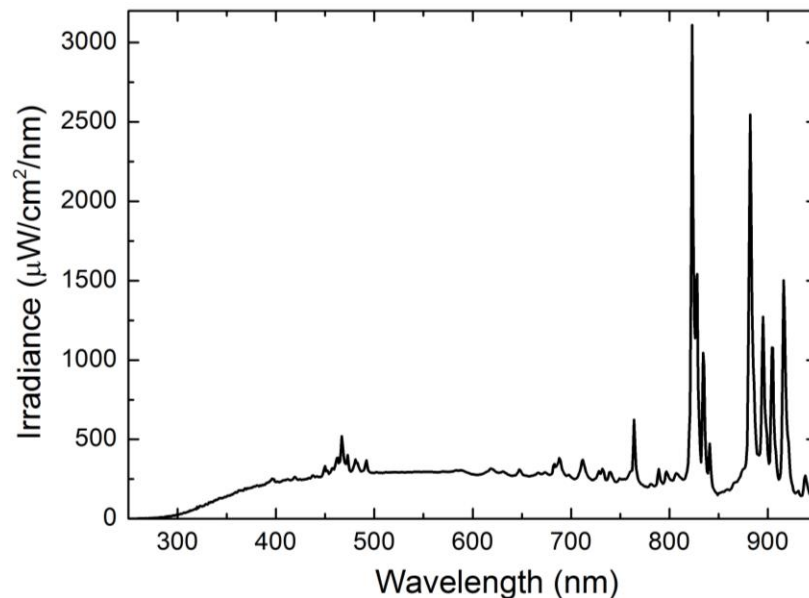


Figure S4.2. Light spectrum of the Xe lamp.

For TiO_2 nanoparticles with a bandgap of 3.2 eV, the effective UV range is 250 – 388 nm. By integration, the accumulated intensity in this effective UV range was calculated to be 11.5 mW/cm^2 .

S4.3 Calculation of the average distance between two TiO₂ NPs in a typical CGOATI nanocomposite

By assuming the TiO₂ NPs are spherical with average size 22±6 nm (calculated from TEM images), the number of TiO₂ NPs in a typical nanocomposite (480nm) with an 85% void factor can be estimated using the following equation,

$$n_{TiO_2NPs} = \frac{V_{measured,TEM} \times (1 - void\ factor\ \%)}{V_{TiO_2NPs}} = \frac{(D_{measured,TEM})^3 \times (1 - void\ factor\ \%)}{(D_{TiO_2NPs})^3}, \quad (S4.1)$$

where $V_{measured,TEM}$, V_{TiO_2NPs} are the volumes of the typical nanocomposite and TiO₂ NP, and $D_{measured,TEM}$, D_{TiO_2NPs} are the diameters of the typical nanocomposite and the TiO₂ NP measured from TEM images respectively.

In this specific condition, the number of TiO₂ NPs encapsulated in the typical nanocomposite is about 1550. With the assumption that all the TiO₂ NPs are evenly distributed inside the nanocomposite, the average distance between two TiO₂ NPs can be calculated as.

$$d = \left(\frac{V_{measured,TEM}}{n_{TiO_2NPs} \frac{\pi}{6}} \right)^{1/3} - D_{TiO_2NPs} = \left(\frac{D_{measured,TEM}}{n_{TiO_2NPs}} \right)^{\frac{1}{3}} - D_{TiO_2NPs}, \quad (S4.2)$$

The average distance between two TiO₂ NPs is calculated to be around 20 nm, which indicates the TiO₂ NPs (22±6 nm) are well separated.

S4.4 Background testing of CGOATI nanocomposites (TiO₂/GO 20%, EDA/GO 15:1, at 200 °C) with light on, where nitrogen (N₂) was the source gas.

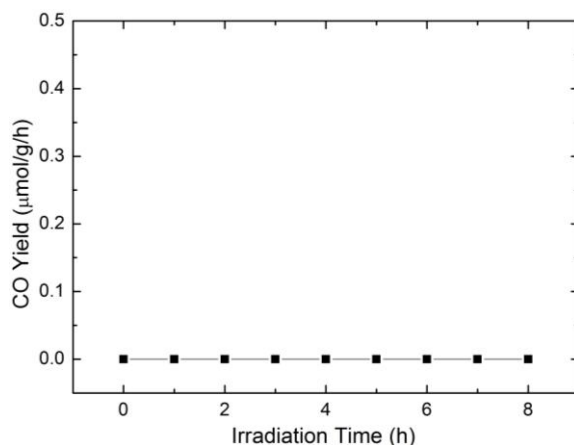


Figure S4.3. Background testing of CGOATI nanocomposites (TiO₂/GO 20%, EDA/GO 15:1, at 200 °C), where nitrogen (N₂) was the source gas. CO was either not produced or was below our detection limit during this process.

S4.5 Background testing of CGOATI nanocomposites (TiO₂/GO 20%, EDA/GO 15:1, at 200 °C) with light on, where nitrogen (N₂) was the source gas.

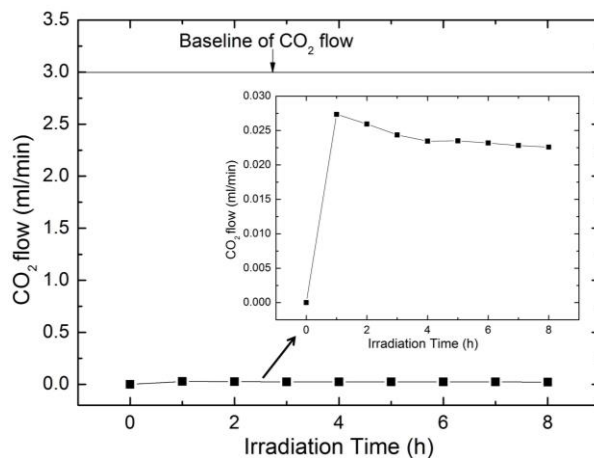


Figure S4.4 Background testing of CGOATI nanocomposites (TiO₂/GO 20%, EDA/GO 15:1, at 200 °C), where nitrogen (N₂) was the source gas. The baseline of CO₂ flow means the flow in the actual CO₂ photoreduction analysis (not control experiments). The ratio of produced CO₂ to the baseline CO₂ is about 0.01.

S4.6. Isotope experiments

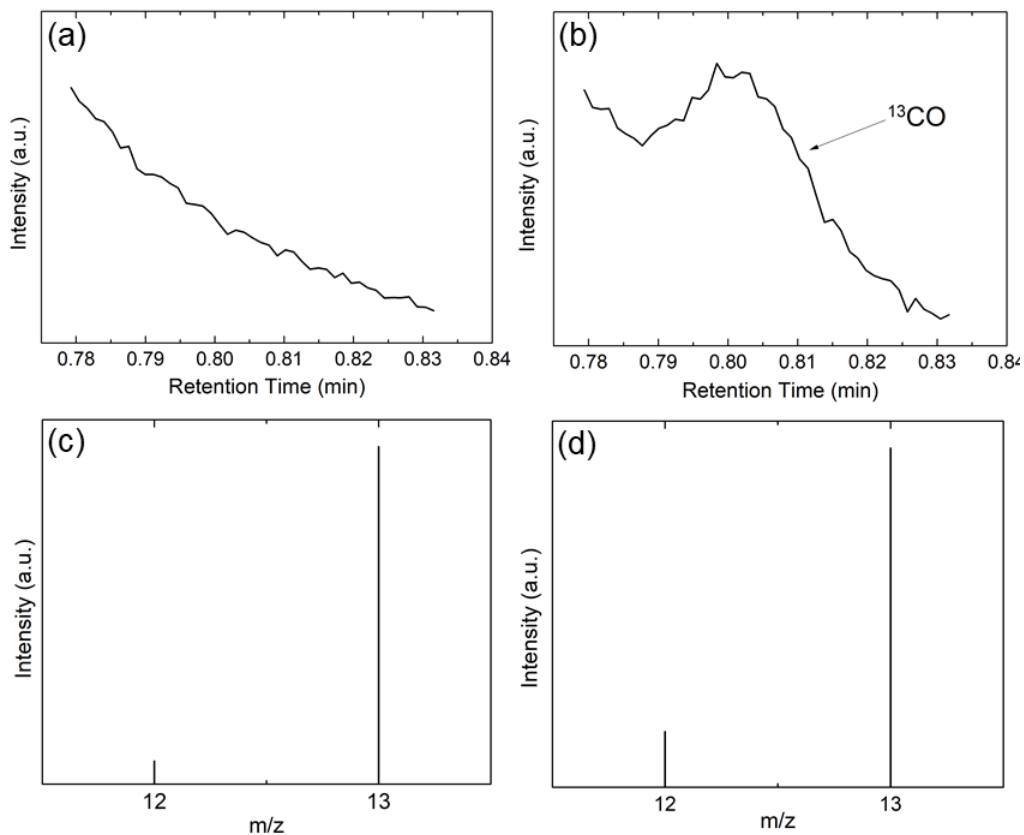


Figure S4.5 $^{13}\text{CO}_2$ as source gas, CGOATI sample (TiO_2/GO 20%, EDA/GO 15:1, at 200 °C), gas chromatography spectra (a) before UV-irradiation; (b) generated from UV-irradiated CGOATI nanocomposites after 2h. Mass chromatography spectra of (a) source $^{13}\text{CO}_2$; (d) generated CO peak after 2h UV irradiation.

S4.7 Reaction stoichiometry

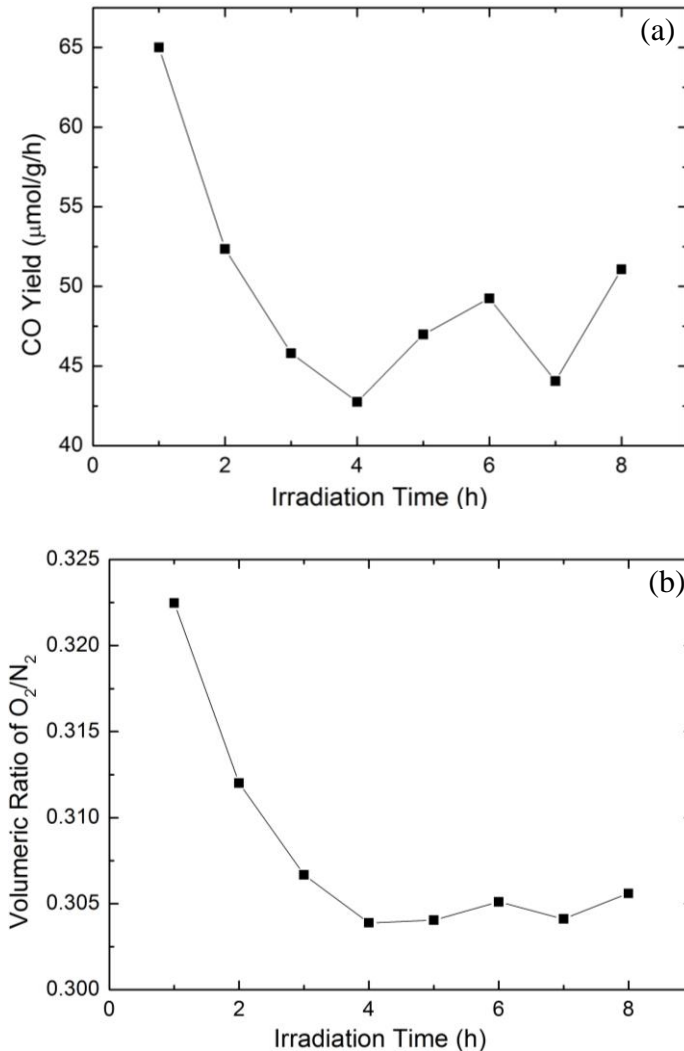


Figure S4.6 (a) The CO yield, (b) volumetric ratio of O₂/N₂, as a function of irradiation time, with CGOATI nanocomposites (TiO₂/GO 20%, EDA/GO 15:1, at 200 °C) as the catalyst.

The concentrations of O₂ and N₂ in the effluent gas were also monitored during the CO₂ photoreduction experiments using CGOATI. There was background O₂ detected in the reactor effluent gas at the beginning of the test, possibly because the reactor was not well vacuumed out before purging it with the CO₂-H₂O mixture and possibly because of

the low concentration impurity gases in the CO₂ cylinder. Hence, a better indicator of O₂ production from the photocatalytic reaction is the volumetric ratio of O₂/N₂ in the effluent gas.

S4.8 FTIR analysis of CGOTI and CGOATI samples in the range 650-2000 cm⁻¹.

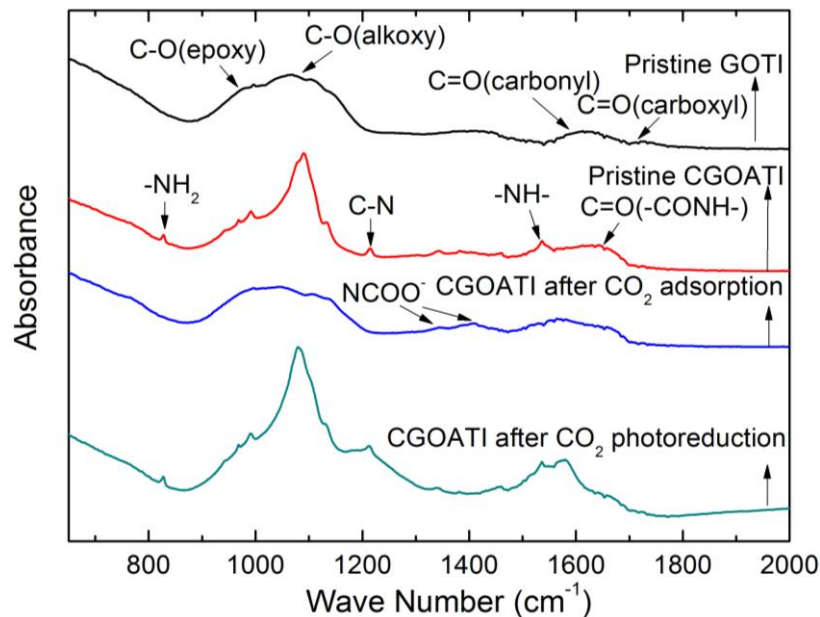


Figure S4.7 FTIR analysis of pristine CGOTI (TiO₂/GO 20%, at 200 °C), pristine CGOATI (TiO₂/GO 20%, EDA/GO 15:1, at 200 °C). Also shown are the spectra for the samples, CGOATI after CO₂ adsorption (only) and CO₂ adsorption and photoreduction.

S4.9 The I_D/I_G ratio and resistivity of CGOTI (TiO_2/GO 20%) samples with different synthesis temperatures

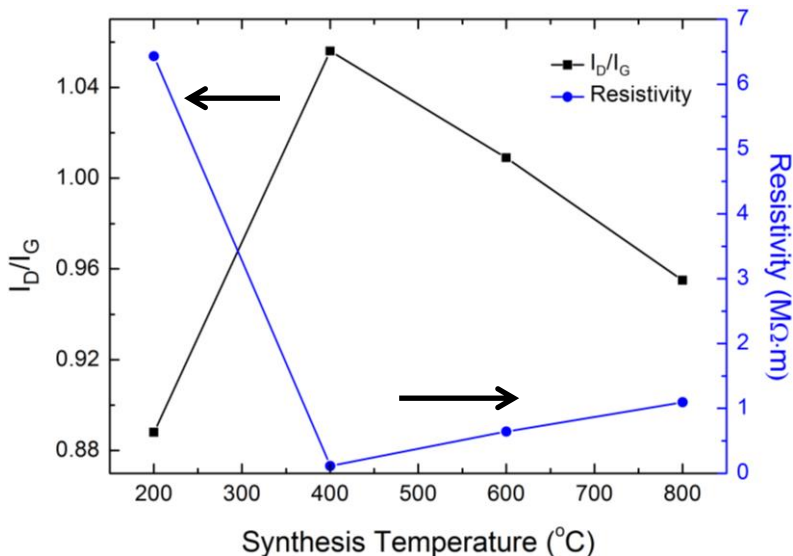


Figure S4.8 The I_D/I_G ratio and resistivity of CGOTI samples (TiO_2/GO 20%) with different synthesis temperatures.

S4.10 CO_2 photoreduction of CGOATI (TiO_2/GO 20%, EDA/GO 15:1, at 200 °C) nanocomposites after two cycles.

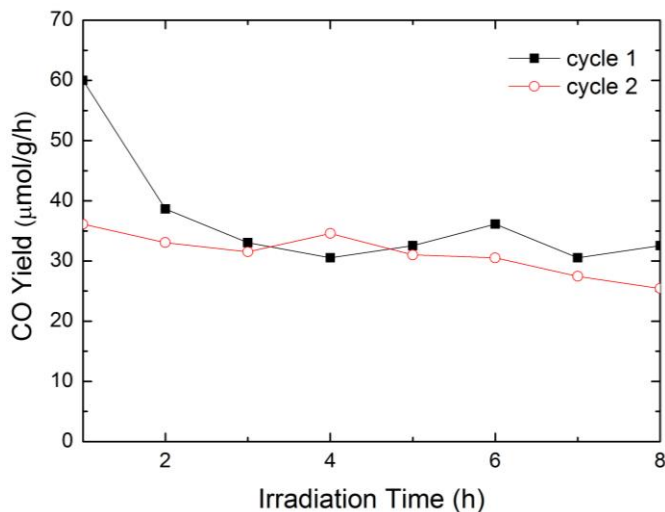


Figure S4.9 CO_2 photoreduction of CGOATI (TiO_2/GO 20%, EDA/GO 15:1, at 200 °C) nanocomposites after two cycles.

S4.11. Apparent quantum efficiency calculation

The photoreduction performance can be characterized by the photochemical apparent quantum efficiency (quantum yield), ϕ , which is defined as a measure of the molar fraction of incident photons that result in CO₂ reduction products². For the case that CO is the product, apparent quantum efficiency can be calculated by the following equation, as two electrons are required to convert one CO₂ molecule to one CO molecule³.

$$\phi(\%) = \frac{2 \times CO \text{ yield (mol)}}{\text{incident photon (mol)}} \times 100\% \quad (\text{S4.3})$$

The highest CO yield within the 8 hours UV irradiation was taken for calculation of quantum efficiency. The moles of incident photon were calculated using the following equation:

$$\text{incident photon (mol)} = \frac{\text{total incident energy}}{\text{average photon energy} \times N_A} \quad (\text{S4.4})$$

where N_A is the Avogadro's constant.

The photon energy at a certain wavelength can be calculated by:

$$E = \frac{hc}{\lambda} \quad (\text{S4.5})$$

where h , c and λ are Planck constant, speed of light and wavelength of light. The average photon energy can be estimated by averaging the photon energy from 250 to 388 nm.

The constants that were used for the calculations are listed as below:

Light intensity in the effective light range:	11.5 mW/cm ²
Deposited film diameter (circle):	4.2 cm
Average photon energy:	6.85×10 ⁻¹⁹ J
Yield of CO:	65 μmol/g/h
Mass of the catalyst used:	1.0 mg
Based on Eq. (S3), the ϕ was calculated to be 0.0094%.	

References

1. Sakthivel, S.; Kisch, H., Daylight photocatalysis by carbon-modified titanium dioxide. *Angewandte Chemie International Edition* **2003**, *42*, (40), 4908-4911.
2. Morris, A. J.; Meyer, G. J.; Fujita, E., Molecular approaches to the photocatalytic reduction of carbon dioxide for solar fuels. *Accounts of Chemical Research* **2009**, *42*, (12), 1983-1994.
3. Li, Y.; Wang, W.-N.; Zhan, Z.; Woo, M.-H.; Wu, C.-Y.; Biswas, P., Photocatalytic reduction of CO₂ with H₂O on mesoporous silica supported Cu/TiO₂ catalysts. *Applied Catalysis B: Environmental* **2010**, *100*, (1), 386-392.

Chapter 5 N-doped Reduced Graphene Oxide Promoted Nano TiO₂ as A Bifunctional Adsorbent/Photocatalyst for CO₂ Photoreduction: Effect of N Species

The results reported in this chapter were published in - Lin, Liang-Yi, Yao Nie, Shaline Kavadiya, Thiagarajan Soundappan, and Pratim Biswas. "N-doped Reduced Graphene Oxide Promoted Nano TiO₂ as A Bifunctional Adsorbent/Photocatalyst for CO₂ Photoreduction: Effect of N Species." Chemical Engineering Journal 316 (2017): 449-460. Reproduced with permission from Elsevier, copyright 2017.

Abstract

A series of TiO₂/nitrogen (N) doped reduced graphene oxide (TiO₂/NrGO) nanocomposites with varying concentration and bonding configurations of nitrogen were synthesized by a one-step urea-assisted hydrothermal method, and applied to photoreduction of CO₂ with H₂O vapor in the gas-phase under the irradiation of a Xe lamp. The effect of the N dopant (doping quantity and bonding configuration) on the catalytic performance of TiO₂/NrGO was examined. In particular, TiO₂/NrGO-300, with a 300:1 mass ratio of urea/GO in precursor solution, had the highest CO production yield (356.5 μmole g⁻¹), manifesting a significant 4.4 and 2.2-fold enhancements of CO yield over pure TiO₂ and TiO₂/rGO, respectively. More significantly, TiO₂/NrGO showed excellent catalytic stability during the prolonged reaction, while catalytic deactivation was observed for both pristine TiO₂ and TiO₂/rGO after a few hours. The promoting effects of N dopants on the structure and activity of TiO₂/NrGO were investigated. It was demonstrated that NrGO with an appropriate N quantity and N-bonding configuration acted as a dual-functional promoter, simultaneously enhancing CO₂ adsorption on the catalyst surface and facilitating electron-hole separation, while eventually boosted the photocatalytic performance. Experimental results in this work provide a better understanding of the critical roles of N dopants in the synthesized composites and also inspire the ongoing interest in better design of other N-doped graphene based materials for photoreduction of CO₂.

5.1 Introduction

CO₂ capture and storage (CCS) has been evaluated by the Inter-governmental Panel on Climate Change (IPCC) as a feasible CO₂ mitigation option.¹ The conversion of CO₂ could provide another alternative to the storage of CO₂ underground or in the deep ocean by producing value added chemicals while simultaneously addressing the energy shortage and global warming.² Among several existing technologies for CO₂ conversion to renewable fuels, photocatalytic reduction of CO₂ is a promising option that directly utilizes inexpensive and abundant solar energy.³⁻⁵ Thus far, TiO₂ is commonly investigated for CO₂ photoreduction, however, its insufficient catalytic conversion efficiency still remains as the main bottleneck. This is primarily due to a combination of several factors, including rapid electron-hole (e⁻-h⁺) recombination, limited light harvesting, and weak adsorption of CO₂ on TiO₂ surface in the presence of H₂O vapor.^{6,7} Moreover, TiO₂ is prone to deactivate (especially in a continuous gas-phase reaction), mainly due to the deposition of less reactive intermediates on the surface active sites.^{8,9}

In past years, several strategies have been pursued to improve the catalytic activity of TiO₂, such as enhancing the adsorption of CO₂ on TiO₂,^{10,11} band gap engineering,^{12,13} and combining with other semiconductors and co-catalysts.^{14,15} Particularly, improving the adsorption of CO₂ on TiO₂ to convert the thermodynamically stable CO₂ molecule into more reactive carbon species (e.g., carbamate and bicarbonate) for further reduction has been proven to effectively enhance the photocatalytic rate of CO₂ reduction.^{16,17} Hence, strategies such as increasing the surface area by either creating a porous structure or dispersing TiO₂ on high-surface-area supports^{18,19} or functionalizing the surface with

amine-containing groups^{20,21} have been proposed to enhance the adsorption and activation of CO₂.

Among the adsorbents that are currently being developed, graphene is considered as a promising adsorbent for CO₂ capture and storage, due to its high surface area and the planar structure associated with the 2D lattice structure formed by sp²-bonded carbon atoms.^{22,23} Previous studies have shown that CO₂ uptake on carbon materials can be greatly improved by selective functionalization with nitrogen dopants.^{24–27} Kim et al.²⁸ has determined the values of CO₂ adsorption amount on pristine graphene and N-graphene (nitrogen doped graphene) materials. The results demonstrate the importance of N dopants, which act as basic sites for anchoring CO₂ molecules, in determining the optimal CO₂ adsorption on N-graphene materials. Moreover, the nitrogen dopants also significantly alter the electronic properties of the graphene and change the local surface reactivity,^{29,30} increasing its potential for the use in photocatalytic applications.^{31,32} As a result, functionalization with nitrogen atoms is expected to be an effective process to enhance the CO₂ adsorption and CO₂ reactivity of graphene materials. However, there has been limited number of studies related to N-graphene based photocatalysts for CO₂ photoreduction.^{33,34} Yet, the research on N-graphene based photocatalysts for gas-phase CO₂ photoreduction has not been concerned. Furthermore, the roles of the N dopant on CO₂ photoreduction need to be further clarified.

In this study, we synthesize and study TiO₂/nitrogen doped reduced graphene oxide (NrGO) composite as a bifunctional adsorbent/photocatalyst for gas-phase photoreduction of CO₂ with H₂O vapor. Our experimental results clearly demonstrated that the photocatalytic activity of TiO₂ was improved after coupling with rGO, especially with

appropriate doping of N species. More importantly, TiO₂/NrGO showed remarkably enhanced photocatalytic stability compared to those of pristine TiO₂ and TiO₂/rGO, which deactivated after a few hours. Systematic studies were conducted to investigate the roles of N dopants on the microstructures and catalytic activities of optimized materials, and a possible mechanism for using NrGO as an effective synergist is proposed. To the best of the authors' knowledge, this is the first study reporting the promoting roles of doped N species in NrGO based materials on gas-phase CO₂ photoreduction. This work provides fundamental knowledge and may establish the basis for a better design of other N-doped graphene based materials for photoreduction of CO₂.

5.2 Experimental section

5.2.1 Preparation of TiO₂/NrGO composites

GO was prepared from graphite powder according to the modified Hummer's method.³⁵ Commercial Degussa P25 TiO₂ nanoparticle was used as the photocatalyst source. The TiO₂/NrGO composites were synthesized by a one-step hydrothermal method using urea as the chemical dopant in a GO aqueous dispersion. In preliminary studies, we demonstrated the effect of the amount of GO on the catalytic performance of the synthesized TiO₂/NrGO for the photoreduction of CO₂. When the mass ratio of GO to TiO₂ was 5%, the resulting TiO₂/NrGO showed the highest photocatalytic activity (Fig. S5.1). Accordingly, the mass ratio of GO to TiO₂ was kept at 5% in this work.

For a typical synthesis, 7 mg of GO was dispersed in 20 ml of ethanol/water (1:2), followed by the addition of 2.1 g of urea under sonication for 1 h. Then, 0.133 g of TiO₂ was added and the mixture was stirred at ambient temperature for 2 h. After that, the solution was transferred to a 25 ml Teflon-sealed autoclave and maintained at 175 °C for

20 h. Finally, the resulting solids were recovered by filtration, washed with water, and fully dried at 60 °C. The synthesized samples were denoted as TiO₂/NrGO-X, where X corresponds to the weight ratio of urea/GO in the precursor solution. For comparison, TiO₂/rGO samples were also prepared under the same experimental parameters but without adding the urea to the GO aqueous dispersion.

5.2.2 Characterization

The crystal phase of the material was determined by X-ray Diffraction (XRD) (Geigerflex D-MAX/A, Rigaku Denki) with Cu K α radiation ($\lambda = 1.548 \text{ \AA}$). The optical properties the materials were measured using a UV-Vis spectrophotometer (Varian Bio 50). The surface chemical properties were analyzed by laser Raman spectrometry (Renishaw InVia Reflex confocal Raman spectrometer, with a 514 nm laser) and X-ray photoelectron spectroscopy (XPS, PHI 5000 VersaProbe II, equipped with a monochromatic Al K α (1486.6 eV) X-ray source). The specific surface area, pore diameter, and total pore volume of the synthesized materials were measured using a surface area and pore diameter distribution analyzer (Micromeritics, ASAP 2020, USA). Pore volumes were obtained from the volumes of nitrogen adsorbed at $P/P_0 = 0.95$ or in the vicinity. CO₂ adsorption isotherms were measured using the same Micromeritics ASAP2020 equipment. All samples were degassed at 393 K overnight and sealed under vacuum prior to analysis. CO₂ was adsorbed at 195 K, and the pressure ranges from 1.8 to 850 mm Hg. The content of GO of the synthesized composite materials were analyzed by thermal gravimetric/ differential thermal analysis (TA Instruments, New Castle, DE).

Photoelectrochemical measurements were performed with a lab-built three-electrode cell setup. A Pt was the counter electrode, and an Ag/AgCl bar was the reference

electrode. The working electrode was prepared on fluoride tin oxide (FTO) conductor glass. Typically, the sample powder (5 mg) (TiO_2/NrGO) was ultrasonicated in 5 mL of ethanol to disperse it evenly and obtain a slurry, which was then coated on the FTO glass surface; the contact side had previously been protected using Teflon tape. Further the working electrode was dried at 60 °C for 4 h. Photocurrent measurements were measured using a CHI 760 bipotentiostat in 0.5 M Na_2SO_4 solution. Furthermore, linear sweep voltammetry was performed to determine the band position of the samples. Samples were prepared by deposition onto an indium tin oxide (ITO) slide. The voltage was scanned in both positive (anodic) and negative (cathodic) direction with respect to the reference electrode at a rate of 1 mV/s.

5.2.3 Photocatalytic reduction of CO_2 with H_2O vapor

Catalytic tests were performed using a lab-built photoreactor operating in continuous flow mode, as displayed in Fig. 5.1. For each test, 10 mg of catalyst was evenly dispersed onto a glass-fiber filter, which was then placed at the bottom of the photoreactor. CO_2 (99.999%, Praxair) was continuously passed through a water bubbler to obtain a gas mixture of $\text{CO}_2 + \text{H}_2\text{O}$ that flowed into the photoreactor. Prior to each reaction test, a high gas flow rate (16.0 ml min^{-1}) of CO_2 was used initially to purge air from the reactor for 40 min, and then a flow rate of 3.0 ml min^{-1} was maintained during the whole 8 h photoreaction. A 400 W Xenon lamp (Oriel 66021, Newport Co.) was the light source, and the measured light intensity (ILT-900R, International Light Technologies) was about 11.5 mW cm^{-2} in the wavelength range of 250-400 nm. The gaseous products in the reactor effluent were continuously analyzed using a gas chromatograph (GC, 6895N, Agilent Technologies, Inc.) equipped with a thermal conductivity detector (TCD) and flame

ionization detector (FID). Helium was used as the carrier gas. As additional experiments, the photoreduction of CO₂ with H₂O vapor tests were also conducted under the illumination of the same Xenon lamp equipped with a UV cut-filter ($\lambda > 400$ nm). Samples were taken at 1 hour intervals. To evaluate the reusability of the catalyst, runs were done after the 8 h photoreaction. After the end of each run, the photoreactor was purged with N₂ for 1 h to remove the gaseous products. After that, the Xe lamp was turned on again to perform the photocatalytic reaction measurements.

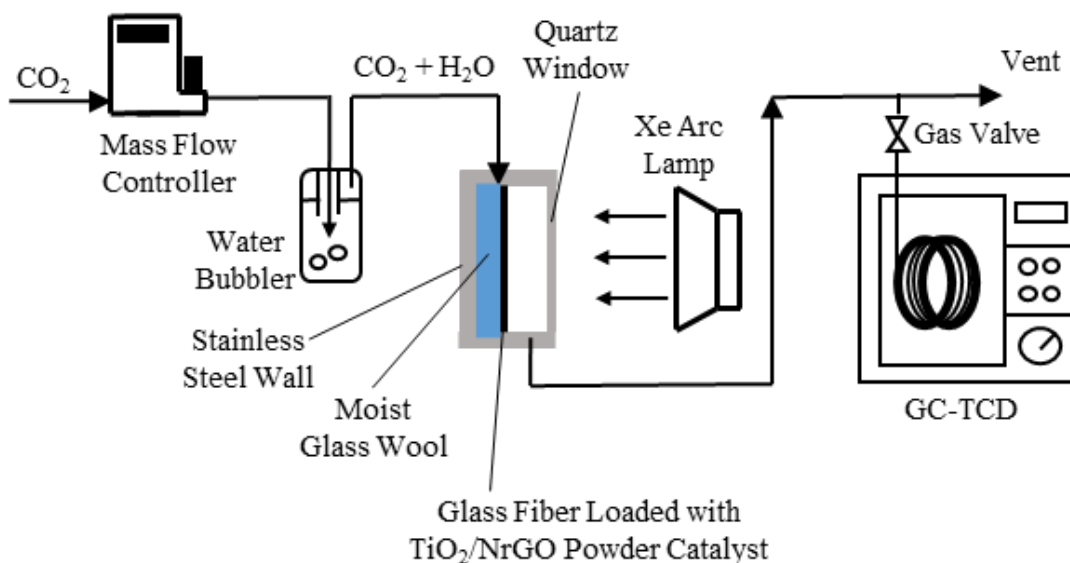


Figure 5.1 Schematic of the experimental setup for photoreduction of CO₂ with H₂O.

5.3 Results and discussion

5.3.1 Characterization

Firstly, the content of GO in the composite material was determined by the TGA analysis, with results shown in Fig. S2. All samples displayed a three-step weight loss in the range of 40-250, 250-600, and 600-700 °C. The first weight loss in the range of 40-250 °C can be ascribed to the desorption of physically and/or chemically adsorbed water on the

surface of the catalysts, while the weight losses in the range of 250-700 °C is due to the decomposition of GO or NrGO.³⁶ This is further confirmed by the differential thermal analysis (DTA) profile of TiO₂/rGO in which two main mass changes are observed in the range of 250-700 °C. The GO amount of each sample is almost identical and is in the range of 4.22-4.65 wt% in the composite, which is very close to the theoretical value (5 wt %) in the precursor solution.

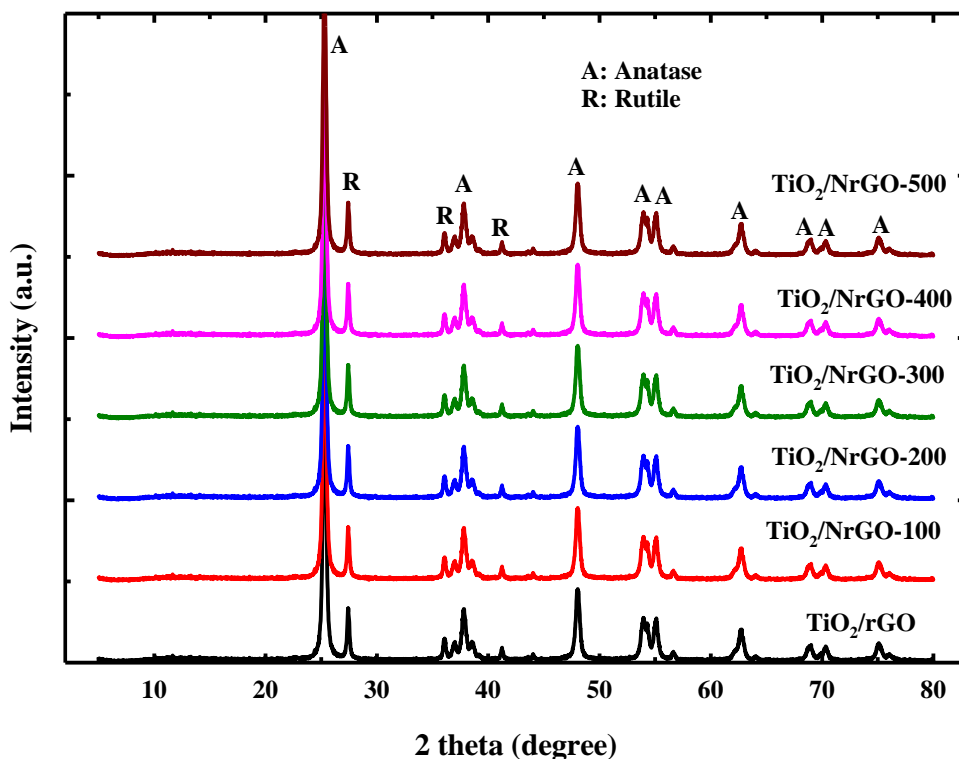


Figure 5.2 XRD patterns of TiO₂, TiO₂/rGO, and TiO₂/NrGO samples

The XRD patterns in Fig. 5.2 show that all samples exhibit almost identical TiO₂ crystal phases of anatase and rutile, which are consistent with the composition of commercial P25 TiO₂ (75% anatase and 25% rutile).^{37,38} Also, as revealed in Table 5.1, the textural properties, including surface area, pore diameter, and pore volume of all materials are nearly unchanged. As a result, coupling with small amount of either rGO or NrGO did

not result in significant changes in the phase composition, and textural properties of TiO₂. Fig. 5.3A shows the diffuse reflectance UV-Vis spectra of all samples. For the pure TiO₂ sample, a typical band-gap absorption can be observed at ca. 395 nm. After loading with either rGO or NrGO, the resultant composites show improved visible-light absorption in the range of 400-700 nm. Therefore, doping induces a red shift in the absorption spectra and alters the band gap energy of the composite TiO₂/rGO or TiO₂/NrGO material. To determine the band gap energies of all studied samples, a Tauc plot of the modified Kubelka-Munk function versus the energy of light absorbed is plotted in Fig. 5.3B. Compared to bare TiO₂, all composite samples exhibited reduced band gap energies, reported in Table S5.1. Analogous band gap narrowing of TiO₂ is also found in the case of TiO₂/CNT composite materials, which could be attributed to the chemical bonding between TiO₂ and the specific sites of carbon.³⁹ Furthermore, the band position of the valence and conduction band of the composite material was determined by linear sweep voltammetry. Three samples are considered for this measurement – TiO₂/rGO, TiO₂/NrGO-300 and TiO₂/NrGO-500. The conduction band can be obtained by scanning the voltage in the negative/backward direction (cathodic scan Fig. S5.3a) and valence band can be obtained by scanning the voltage in the positive/forward direction (anodic scan, Fig. S5.3b). The band potential is calculated by drawing a tangent (dashed line) at the onset of the oxidation and reduction peak. Band positions and the band gap are reported in the supplementary material. Band gaps calculated from electrochemical measurements are lower than that calculated from the UV-Vis absorption measurements (Tauc plot). This is because the voltage is not scanned beyond the TiO₂ valence band position, which is 2.78 V vs Ag/AgCl. The variation among the samples is the N doping in rGO, hence the N dopant should play

the main role in affecting the band positions. Thus only the potentials corresponding to rGO are considered, as described in previous studies.^{40,41} However, it is important to note that, the band positions and hence the band gap do not vary significantly with the N doping, supporting the trend obtained from Tauc plot (UV-Vis data).

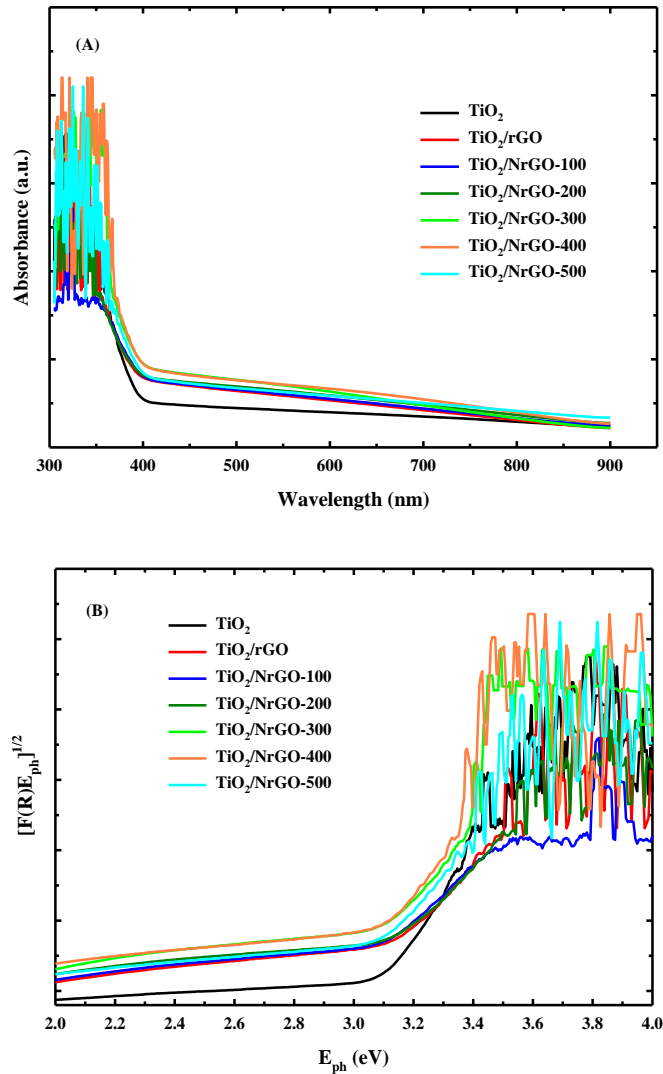


Figure 5.3 (A) Diffuse reflectance UV-vis spectra and (B) plots of the square root of Kubelka-Munk function versus the photon energy of TiO₂, TiO₂/rGO, and TiO₂/NrGO samples

The morphologies of the synthesized TiO₂/NrGO-300 sample were investigated by SEM and TEM. As displayed in Fig. 5.4A, the obtained TiO₂/NrGO-300 retains the two-dimensional sheet structure with micrometers-long wrinkles after the hydrothermal treatment. Moreover, the TEM image (Fig. 5.4B) further shows that the TiO₂ nanoparticles were uniformly deposited on the surface of the graphene sheet. The chemical species located near the catalyst surface were characterized by XPS, and a typical survey XPS spectrum of the synthesized TiO₂/NrGO-300 sample is shown in Fig. 5.4C. An N peak is obvious in the TiO₂/NrGO-300 sample. The deconvolution of the N 1s peak is useful in distinguishing the states of N species. In the N 1s spectrum (Fig. 5.4D), the peaks at 398.6, 399.5, and 401.4 can be attributed to pyridinic-N (N1), pyrrolic-N (N2), and quaternary-N (N3), respectively.^{42,43} The pyridinic-N is from the sp² hybridized N atom with two sp² hybridized C neighbors, while the pyrrolic-N is attributed to the incorporation of N atoms into a five-member heterocyclic ring.³⁸ The quaternary-N is ascribed to the replacement of C atoms by N atoms in graphene hexagonal-ring, and is sp² hybridized N atom with three sp² hybridized C neighbors.³⁹

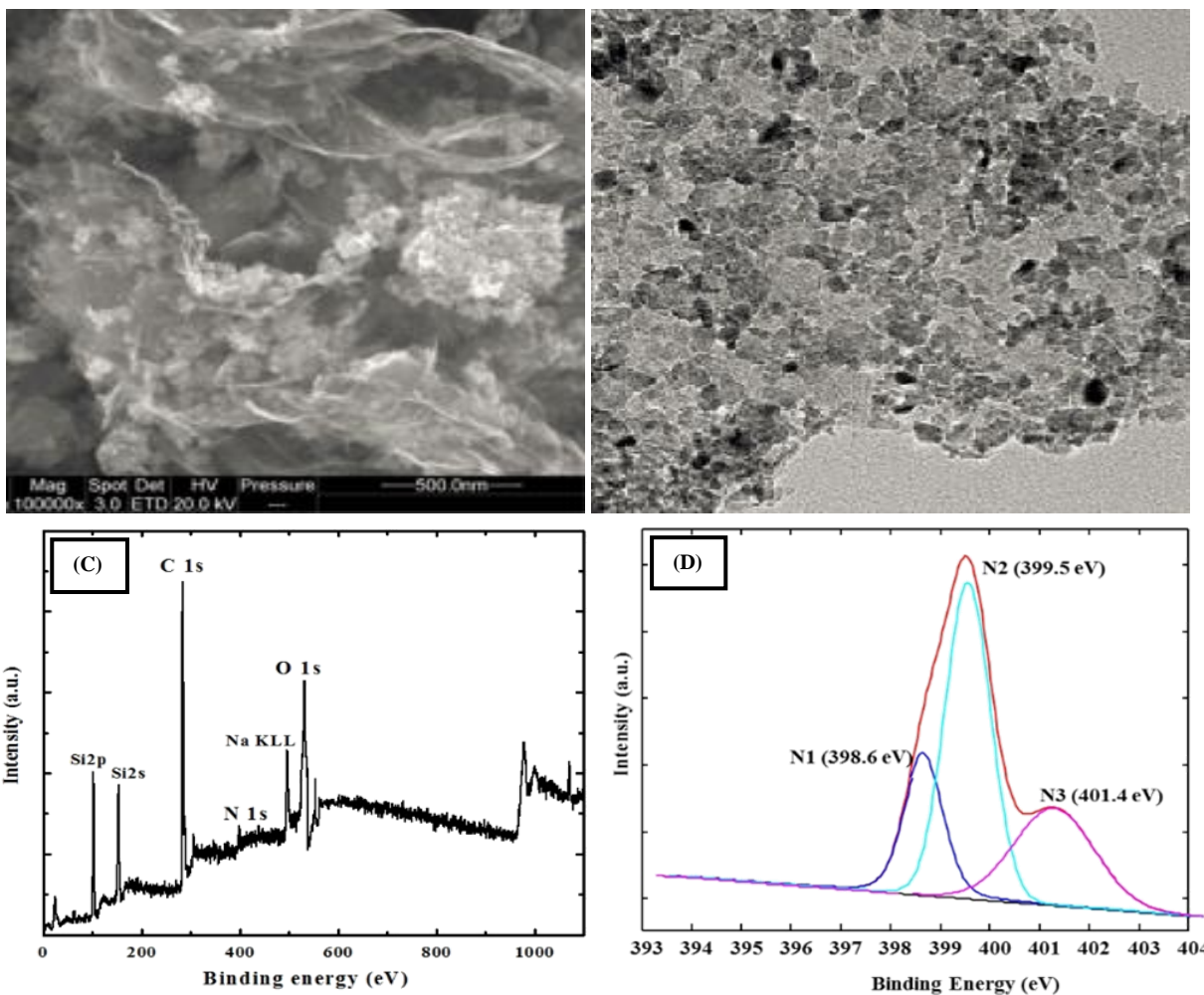


Figure 5.4 (A) SEM image, (B) TEM image, (C) XPS spectra and (D) XPS N 1s of $\text{TiO}_2/\text{NrGO-300}$ samples.

Detailed information about the surface N species is recorded in **Table 5.1**. As observed, similar to the total N, pyridinic-N, pyrrolic-N, and quaternary-N increase steadily when the urea/GO mass ratio increases to 300/1, whereas they decrease in $\text{TiO}_2/\text{NrGO-400}$ and $\text{TiO}_2/\text{NrGO-500}$ samples. Similar observations were reported by several studies on the preparation of N-graphene, which demonstrated that there was an upper limit to the amount of N that could be incorporated into the graphene network before it starts to decompose due to many defects.^{44,45} Hence, one may conclude that NrGO with the highest N content

could be prepared at a urea/GO mass ratio of 300/1. In addition, it is noted that the pyrrolic-N content increases up to 300/1, decrease at 400/1 and then increase at 500/1. A similar finding was reported previously on the synthesis of N-graphene materials using urea as a nitrogen source.⁴⁶ However, the exact formation mechanism is still unclear, and further studies must be conducted to clarify the relationship between the urea precursor and the doped nitrogen content.

Table 5.1 Physicochemical properties of TiO₂, TiO₂/rGO and TiO₂/NrGO samples.

Sample	Urea/GO mass ratio	S _{BET} (m ² g ⁻¹)	V _p (cm ³ g ⁻¹)	D _p (nm)	N _{XPS}			
					Total (Atomic %)	N1 (398.6 eV)	N2 (399.5 eV)	N3 (401.4 eV)
TiO ₂	-	57	0.23	15	-	-	-	-
TiO ₂ /rGO	-	53	0.23	14	-	-	-	-
TiO ₂ /NrGO-100	100	59	0.25	14	1.67	0.59	0.80	0.28
TiO ₂ /NrGO-200	200	62	0.25	15	2.41	0.69	0.94	0.78
TiO ₂ /NrGO-300	300	60	0.28	16	3.60	0.78	1.82	1.00
TiO ₂ /NrGO-400	400	57	0.25	18	2.65	0.89	1.24	0.52
TiO ₂ /NrGO-500	500	54	0.18	18	2.51	0.86	1.36	0.29

On the other hand, Table 5.1 also shows that unlike pyridinic-N and pyrrolic-N, which increase with increasing amounts of urea in the precursor mixture, the quaternary-N first increases and then drops, and the maximum atomic percentage of quaternary-N is 1.00 when the mass ratio of urea to GO is 300/1. Further increases in the amount of urea result

in a gradual decrease in the atomic percentage of quaternary-N. This observation is consistent with the previous studies on the synthesis of N-graphene materials.^{46,47} Different from the pyridinic-N and pyrrolic-N which locate at the edges of graphene sheets, quaternary-N is formed in the bulk of the hexagonal graphene ring. It is reported that a high concentration of urea in the system causes a large number of defects, which disrupts the π -system and results in a gradual decreased quaternary-N concentration.^{46,47}

Fig. 5.5 displays the Raman spectra of TiO₂/rGO and TiO₂/NrGO samples. Bands at around 1340 and 1580 cm⁻¹, assigned to the D and G bands, respectively, are observed for all the samples. The D band is related to defects in the hexagonal graphitic layer, and G band is associated with the graphitic carbon.⁴⁸ For heteroatom (e.g., nitrogen) doping, the substitution of carbon atom by the heteroatom usually is accompanied by the introduction of defects into the graphene surface, which are caused by the bond-angle disorder, bond-length disorder, and hybridization of the hexagon graphitic layer.^{49,50} The high intensity ratio of I_D to I_G reflects the high degree of defects. The calculated I_D/I_G value of rGO is 0.75, whereas that of the N-doped rGO becomes slightly larger, from 0.89 to 0.99, with increasing amounts of urea. This difference suggests that more defects are formed within N-doped rGO than within rGO, similar to the results reported elsewhere.⁴⁷

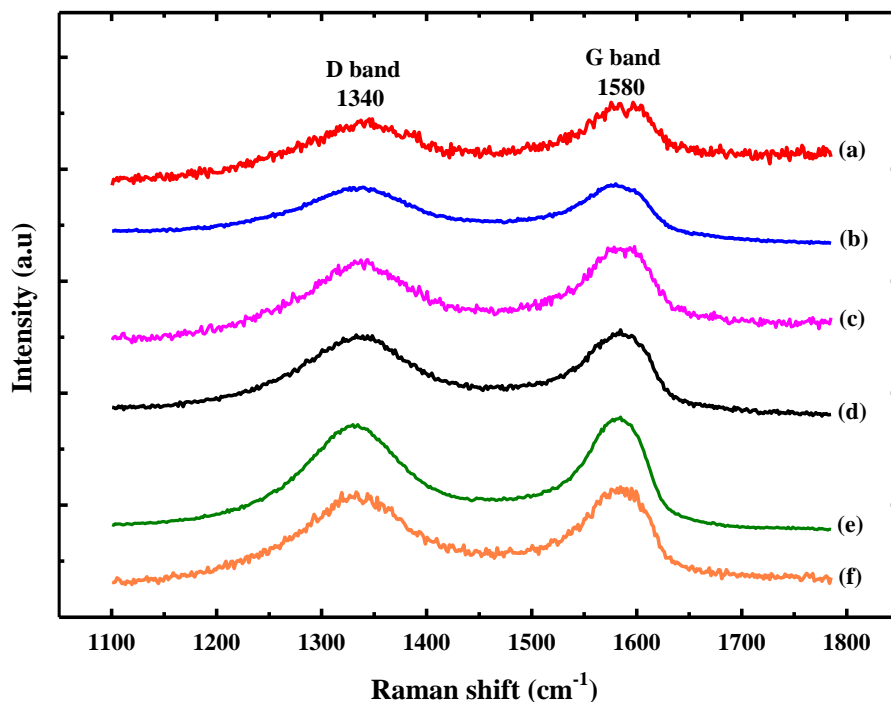


Figure 5.5 Raman spectra of samples. (a) TiO₂/rGO, (b) TiO₂/NrGO-100, (c) TiO₂/NrGO-200, (d) TiO₂/NrGO-300, (e) TiO₂/NrGO-400 and (f) TiO₂/NrGO-500.

5.3.2 Photocatalytic reduction of CO₂ with H₂O

A series of control experiments were first conducted under the following conditions to exclude the interference of surface organic contaminants on CO₂ photoreduction: (1) in the dark, catalysts were loaded on a glass-fiber filter with CO₂ + H₂O vapor, and (2) under light irradiation, catalysts were loaded on a glass-fiber filter with N₂ + H₂O vapor (in the absence of CO₂). In the former condition, no carbonaceous products were detected. A small amount of CO₂ was produced in the latter condition, and the ratio of produced CO₂ to the baseline CO₂ was about 0.01. CO was the major product in the current reaction, and was only detected when CO₂ was passed over the catalysts that were irradiated by light. Our previous isotope experiment showed that CO was formed from CO₂ in the feed gas, but not from the decomposition of the catalyst.⁵¹ On the basis of these results, we concluded that

the produced CO gases were derived from photocatalytic reduction of CO₂ + H₂O vapor under light irradiation.

It is suggested in the literature that hydrogen evolution reaction may compete with the CO₂ reduction reaction; however, due to the detection limit of the GC column, we were unable to detect very low concentration of hydrogen as compared to the major product CO, indicating that H₂O is not competing with CO₂ during the reduction process. In fact, hydrogen was barely detectable, and this indicates that it is indeed a minor reaction product.^{9,52} Also, it is suggested that produced protons would interact with the photoinduced electrons to form •H radicals, and both •H radicals and H₂ were rapidly consumed by CO₂ during the photocatalytic process.^{52,53}

In general, the photoreduction of CO₂ is based on the proton-assisted multi-electron transfer mechanism.⁹ Based on this mechanism, although the formation of hydrocarbons (e.g., methanol, formaldehyde and ethanol) is thermodynamically favorable, it requires more electrons and protons, thus resulting in kinetic limitations. Also, these products are more likely produced in CO₂ photoreduction in aqueous solutions.⁸ Since this study focused on CO₂ reduction on a gas–solid interface, CO was found as the main product in our flow reactor system as it needs a minimum number of electrons and protons and appears to be kinetically favorable. The absence of CH₄ in this study could be due to the fact that the photoreduction of CO₂ into CH₄ requires more electrons and protons, making it more difficult to generate than CO.⁴⁸ Specifically, an eight-electron reduction and available H atoms from the oxidation of water on the same catalyst surface are required for the production of CH₄. If the CO desorbs from the surface before it can be fully reduced, then the formation of CH₄ is significantly affected.

Fig. 5.6A depicts the production rates of CO from CO₂ photoreduction as a function of irradiation time over TiO₂, TiO₂/rGO, and TiO₂/NrGO samples with various N doping. Pristine TiO₂ showed a low production rate of CO with a maximum of 16.2 μmol g⁻¹ h⁻¹. Compared with pure TiO₂, the combination of TiO₂ with rGO obviously enhanced the CO production rate, probably because rGO could simultaneously enhance the adsorption of CO₂ and H₂O on the catalyst surface and improve the electron-hole separation efficiency.⁵⁴ For the TiO₂/NrGO samples, the activities of the photocatalysts were superior to that of TiO₂/rGO in the order of TiO₂/NrGO-300 > TiO₂/NrGO-200 > TiO₂/NrGO-100 > TiO₂/NrGO-400 > TiO₂/NrGO-500. Clearly, doping rGO with N species further enhanced the photoactivity of TiO₂/rGO, especially when doped with suitable amounts; particularly, the TiO₂/NrGO-300 had a maximal CO yield of 50 μmol g⁻¹h⁻¹ (the quantum efficiency is 0.0072%, see supporting information for detailed calculations). Neither pure rGO nor NrGO-300 (Fig. S5.1) alone as the catalyst showed any photoactivity under light irradiation. Fig. 5.6B shows that TiO₂/NrGO-300, among all studied samples, exhibited the highest total CO production yield of 356.5 μmol g⁻¹, a remarkable 4.4 and 2.2-fold enhancement of CO yield over pure TiO₂ (81.1 μmol g⁻¹) and TiO₂/rGO (160.5 μmol g⁻¹), respectively.

It is also noted in Fig. 5.6A that the CO production rates of both pristine TiO₂ and TiO₂/rGO did not remain steady during the 8 h reaction; rather, it decreased after reaching the peak values, indicating the deactivation and poor catalytic stability of the photocatalysts. A similar phenomenon has been observed in gas-phase CO₂ photoreduction studies involving TiO₂, Pt/TiO₂, and TiO₂/reduced graphene oxide composite materials, probably due to diminished adsorption by the catalyst and saturated adsorption sites on the

TiO₂ surface with less reactive intermediates.^{9,55,56} One should mention that promoting charge transfer simply by adding electron trapping sites (e.g., Pt) cannot prevent long-term catalyst deactivation. In contrast, all TiO₂/NrGO samples showed superior photoactivity during the 8 h test, highlighting the important role played by N dopants in NrGO in simultaneously improving the catalytic activity and stability of TiO₂/NrGO composites.

An additional experiment was conducted to monitor the production of O₂ from H₂O oxidation using TiO₂/NrGO-300. Prior to the reaction, the photoreactor was purged with a CO₂-H₂O gas mixture to purge air from the reactor. However, there was always background O₂ and N₂ in the order of a few hundred ppm detected in the reactor effluent gas even after purging for a few hours, possible because the reactor was not vacuum before purging it with CO₂-H₂O mixture and because of the low concentration impurity gases in the CO₂ cylinder. As a result, a better indicator of O₂ production from the oxidation of H₂O during the photoreaction is the volumetric ratio of O₂/N₂ in the effluent gas, which is also suggested in literature.^{51,53} As displayed in Fig. 5.6C, the time-dependent volumetric ratio of O₂/N₂ ratio correlated well with that of CO production. This similar tendency confirms that both photoreduction (CO₂ reduction to CO) and photooxidation (H₂O oxidation to O₂) reactions occurred simultaneously in the reactor system. Fig. 5.6D shows the reuse performance of TiO₂/NrGO-300 during four cycles of operation. TiO₂/NrGO-300 maintains its high CO production rate of $\approx 49 \mu\text{mol g}^{-1} \text{h}^{-1}$ for CO₂ photoreduction during consecutive reaction cycles, retaining the good photostability and reproducibility. On the other hand, the CO production rates of both pristine TiO₂ and TiO₂/rGO dropped significantly during the second tests. This could be primary related to the accumulation of

carbonaceous intermediates that occupied the active reaction sites and deactivated the catalysts.⁹

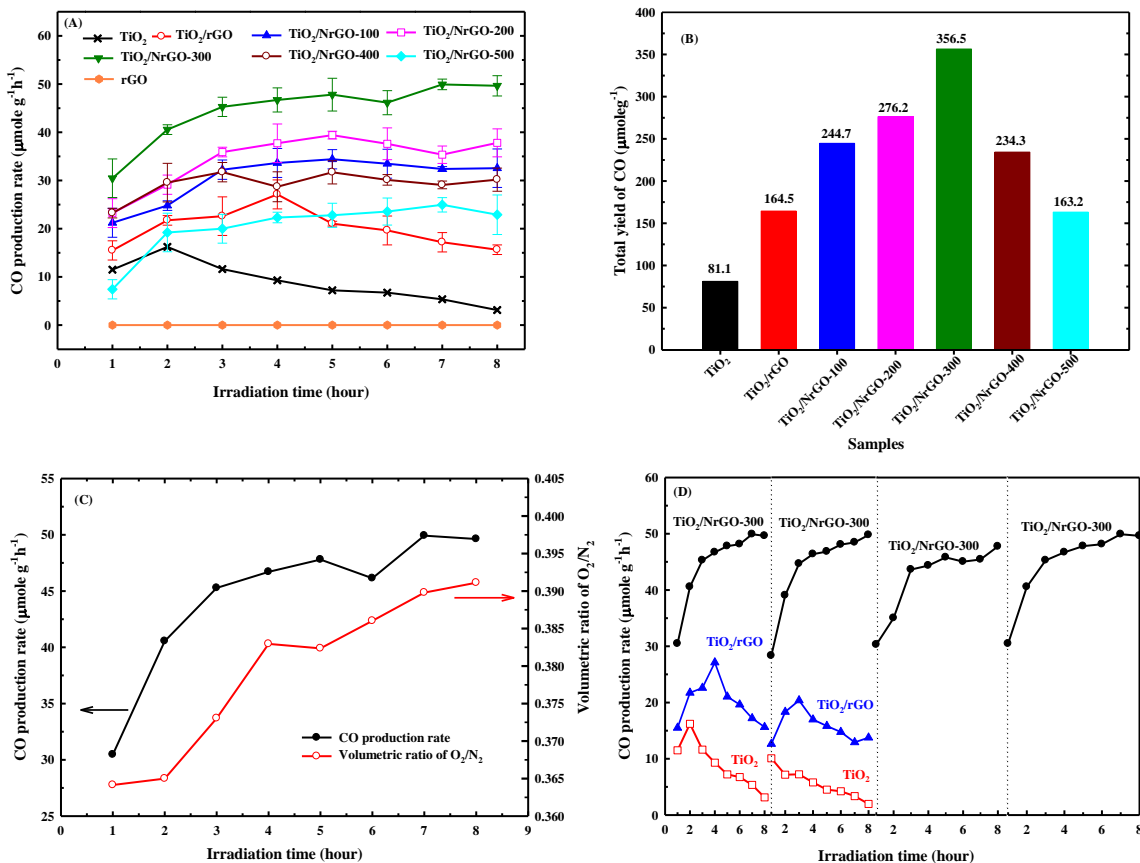


Figure 5.6 (A) Time course of the photocatalytic production rate of CO; (B) total yield of CO over TiO₂, TiO₂/rGO, and TiO₂/NrGO under UV-vis irradiation; (C) Time-dependent CO production rate and volumetric ratio of O₂/N₂ over TiO₂/NrGO-300 catalyst, and (D) Recycling tests for CO₂ photoreduction over over TiO₂, TiO₂/rGO, and TiO₂/NrGO-300.

The CO₂ photoreduction experiments were also conducted under the irradiation of the Xe arc lamp with a UV-cut off filter ($\lambda > 400$ nm) to confirm the visible-light activity of the selected samples (Fig. S5.4). Clearly, pristine TiO₂ showed no activity under visible light irradiation, while the TiO₂/NrGO-300 sample exhibited a stable CO production rate of ca. 5.1 $\mu\text{mol g}^{-1}\text{h}^{-1}$ during the reaction. Surprisingly, no CO production was detected

over the TiO₂/rGO, even though it is visible-light-responsive as revealed by the UV-Vis result. The possible reason could be related to the fast recombination of photoinduced charges that deteriorates the visible-light photocatalytic activity of TiO₂/rGO.⁵⁷

5.3.3 Mechanism of photocatalytic enhancement

The above results confirmed that the catalytic activity of TiO₂ for CO₂ photoreduction can be enhanced by coupling with rGO, especially with controlled doping of N species. It is well known that CO₂ photoreduction reactions are very complex, and the catalytic performance is related to a number of parameters, such as crystalline phase, textural properties, and separation efficiency of photogenerated electron-hole pair.⁵⁸⁻⁶¹ The XRD and nitrogen physisorption analyses suggest that the crystallinity of TiO₂ and the textural properties of the composite photocatalyst, are nearly unchanged after coupling with either rGO or NrGO, revealing that these factors are not the main reasons for the difference in the photocatalytic activities. Particularly, the visible-light-responsiveness of the TiO₂/NrGO composite materials could be one of the important factors for their enhancement in photoactivities, as confirmed by the UV-Vis spectra and visible-light-induced CO₂ photoreduction results. In addition, during the CO₂ photoreduction reaction, CO₂ and H₂O were initially adsorbed onto the surface of the photocatalysts; subsequently, the adsorbed CO₂ molecules were reduced when contacted with electrons and protons, forming CO. In this respect, the photocatalytic performance should also depend on both the CO₂ adsorption ability and photogenerated electron-hole separation efficiency of the photocatalyst. Hence, we have mainly investigated the structure-photoactivity relationship in terms of CO₂ adsorption ability and the efficiency of photogenerated electron and hole separation to learn

how NrGO influences the photocatalytic activity of composite photocatalysts for CO₂ photoreduction.

Fig. 5.7 depicts the CO₂ adsorption isotherms of TiO₂, TiO₂/rGO, and TiO₂/NrGO samples. The CO₂ adsorption amount decreased in the order of TiO₂/NrGO-300 > TiO₂/NrGO-400 ≈ TiO₂/NrGO-500 > TiO₂/NrGO-200 > TiO₂/NrGO-100 > TiO₂/rGO, which correlates well with the sequence of the total amount of nitrogen dopants, as revealed in Table 5.1. Generally, pristine graphene shows a uniform distribution of electrostatic potential on a defect-free surface. But it is more positive at the edges due to the existence of unsaturated bonds and surface defects, which have slightly higher adsorption ability and reactivity.⁶² As a result, pristine graphene has few adsorption sites and low adsorption ability. By contrast, the introduction of nitrogen dopants significantly changes the distribution of electrostatic potential on the graphene surface, producing positive electrostatic potential regions on the doped nitrogen region, and providing additional sites for CO₂ adsorption and activation.^{62,63} Based on the above studies, it is suggested that nitrogen dopants are beneficial for CO₂ adsorption in this work, and the higher the amount of nitrogen dopants, the higher the CO₂ adsorption ability, which is favorable for capturing CO₂ on the surface of TiO₂/NrGO.

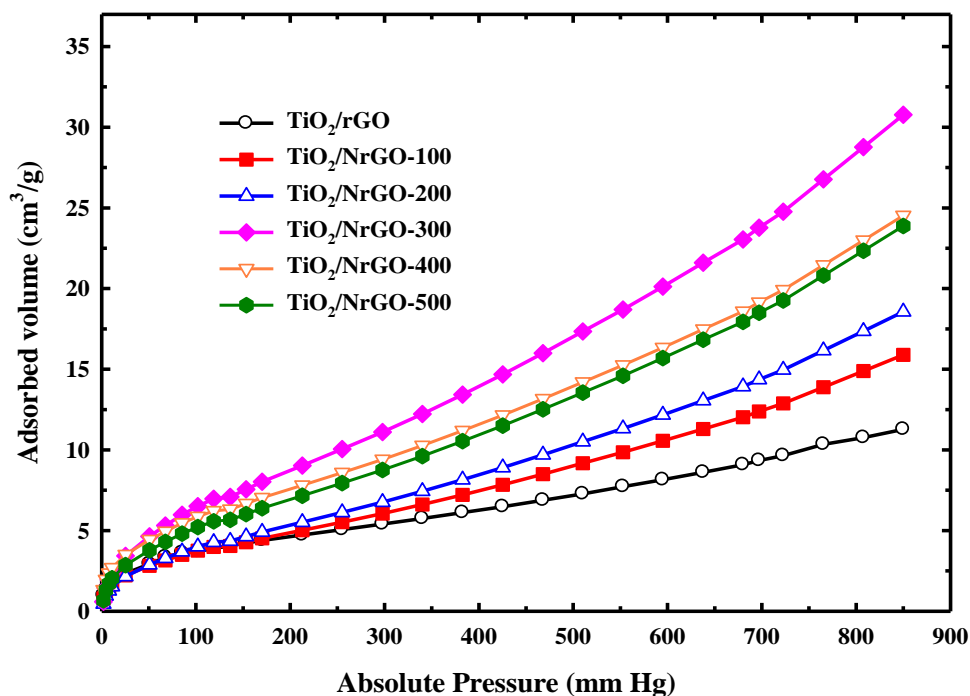


Figure 5.7 CO₂ adsorption isotherms of TiO₂/rGO and TiO₂/NrGO samples.

The photocurrent responses of TiO₂, TiO₂/rGO, and TiO₂/NrGO were investigated using a typical three-electrode cell to study the separation efficiency of photogenerated charges. The Amperometric *i-t* technique was utilized to measure the photocurrent behaviors at various electrodes. As can be seen in Fig. 5.8, for an applied potential of 0 V vs. Ag/AgCl, a steady and prompt anodic photocurrent was generated immediately in the presence of light. We interrupted the current after 50s, left it off for 50s, and then allowed it to flow again to start the next cycle. This pattern was repeated for 10 cycles, demonstrating good stability of the photocurrent for all samples. Compared with pristine TiO₂ and TiO₂/rGO, TiO₂/NrGO samples showed obvious increases in the photocurrent, indicating that the photogenerated electrons and holes in the TiO₂ transferred separately to the NrGO and the recombination of electron-hole pairs was greatly hindered. Also, the

doped N species in NrGO are clearly helpful for enhancing the photocurrent response of the composite photocatalysts.

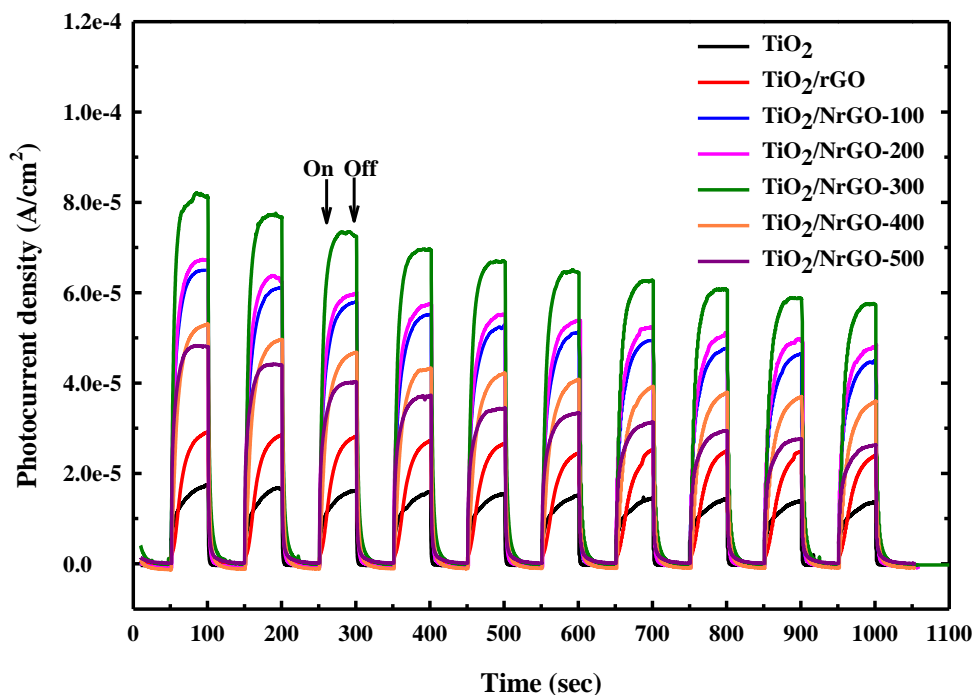


Figure 5.8 Photocurrent response vs. time of the TiO_2 , TiO_2/rGO , and TiO_2/NrGO samples with an electrode potential of 0 V vs. Ag/AgCl.

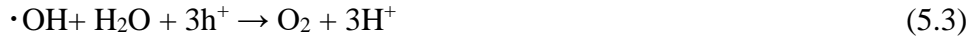
In addition, considering the results in Fig. 5.8 and Table 5.1, the photocurrent behavior of the TiO_2/NrGO samples is consistent with amount of quaternary-N in the NrGO. This consistency clearly indicates that coupling TiO_2 with NrGO that is appropriately doped with quaternary-N groups, is highly desirable for enhanced charge separation efficiency. This finding is in line with a recent study by He et al.⁴⁷ who found that the photocurrent property of N-graphene is related to the amount of quaternary-N groups, but not to either total N quantity or pyridinic-N and pyrrolic-N groups. Unlike pyridinic-N and pyrrolic-N, which are located at the edges of graphene, quaternary-N species are formed in the bulk of graphene structure. They then provide electrons to the

delocalized π -system, improving the electron-transfer mobility.⁶⁴ Consequently, more electrons and holes can participate in the reaction, driving its superior performance in CO₂ photoreduction reaction over TiO₂/NrGO-300.

One should note that the photocatalytic activities of TiO₂/NrGO-400 and TiO₂/NrGO-500 are inferior to that of TiO₂/NrGO-200, even though they have higher CO₂ adsorption abilities than TiO₂/NrGO-200, which has a relatively lower CO₂ adsorption ability but better photocurrent response. The decreased photoactivities observed of TiO₂/NrGO-400 and TiO₂/NrGO-500 could be associated with their relatively lower photocurrent properties. Therefore, it is reasonable to suggest that the charge separation efficiency of photocatalyst plays a predominant role in the current reaction scheme. In addition, a higher number of structural defects were revealed by Raman spectra (Fig. 5.5), which might also disrupt the π -system, resulting in the reduced photoactivities of TiO₂/NrGO-400 and TiO₂/NrGO-500. In brief, the quantity and configuration of doped N species in NrGO in the synthesized TiO₂/NrGO play crucial roles in affecting the CO₂ adsorption ability and charge separation efficiency, and underline the superior performance of TiO₂/NrGO-300 for CO₂ photoreduction.

Fig. 5.9A and B show the schematic mechanisms for photoreduction of CO₂ with H₂O vapor over TiO₂ and TiO₂/NrGO-300, respectively. The mechanism of CO₂ photoreduction on TiO₂ has been well developed in literature.^{11,13,19} Under light irradiation, TiO₂ is photo-excited to generate electrons (e^-) and holes (h^+) (eq 5.1), which initiate the photoreactions when contacted with CO₂ and H₂O. The H₂O vapor, which functions as a reducing agent, is oxidized by the holes from the TiO₂ surface to form hydroxyl radicals (

$\cdot\text{OH}$),⁹ which in turn produces oxygen and protons (H^+) (eq 5.2 and 5.3), with which CO_2 and the two of electrons interact to produce CO (eq 5.4).



When O_2 is also present as the surface adsorbed species, O_2 will compete with CO_2 as electron acceptors, mitigating the CO_2 reduction efficiency.⁵³ The reaction can be expressed as:



The electron scavenging effect by O_2 is supported by the experimental results in this work that no CO_2 photoreduction product was observed when the reactor influent gas was changed to a mixture of O_2/CO_2 (1:1 v/v) upstream of the water bubbler. The result implies that CO_2 photoreduction is not favorable at O_2 -rich environment.

For the TiO_2/rGO composite, heterogeneous junction between rGO and TiO_2 can be formed and lead to more efficient interelectron transfer between two components, as found in N-graphene/CdS photocatalyst.⁶⁵ The work function of rGO has been computed to be -4.42 eV, and the conduction band (CB) and valence band (VB) of TiO_2 are -4.26 and -7.46 eV, respectively. The CB of TiO_2 is smaller than work functions of rGO, making photoinduced electrons transfer from TiO_2 to rGO is energetically favorable.³⁷ These lead to the fact that the presence of rGO in the TiO_2/rGO can effectively inhibit the recombination of electron-hole pairs, and improve the CO_2 photoreduction activity. A recent study found that the carbon atoms on the graphene sheets are accessible to protons

that can readily react with the adsorbed CO₂ to produce methanol by accepting photoinduced electrons.⁶⁶ Hsu et al.⁶⁶ reported that graphene oxide as a metal-free photocatalyst showed photocatalytic activity for methanol evolution, indicating CO₂ photoreduction occurs on the surface of graphene derivatives. Therefore, the reduction of CO₂ may take place on both the surface of the TiO₂ and rGO.

However, one should mention that catalytic deactivation was observed on both pure TiO₂ and TiO₂/rGO samples, consistent with the previous studies.^{8,9,55,56} It was suggested that during the photoreduction of CO₂ with H₂O, the deposition of carbonaceous intermediates starts as HCO₃⁻ and CO₃⁻ from CO₂ coordinating with the surface OH groups and/or unsaturated O²⁻. The surface intermediates are immediately converted to CO and/or other hydrocarbon fuels when dissociative H atoms are available.⁶⁷ Otherwise, the persistent accumulation of less reactive carbonaceous intermediates on the TiO₂ surface would block the active reaction sites and suppress the oxidation of H₂O and reduction of CO₂ simultaneously, which could be the main cause of their long-term photocatalytic deactivation.

Interestingly, the presence of N dopants obviously contributes to enhance the photocatalytic activity and stability of TiO₂/NrGO composites. For the N-graphene materials, the spin density and charge distribution of carbon atoms are influenced by the neighbor nitrogen dopants, which can induce the formation of activation regions on the graphene surface.⁶⁸ In this study, the presence of different bonding configurations of N dopants may lead to produce different activation regions accordingly. It has been reported that pyridinic-N and pyrrolic-N have Lewis basicity which work as active sites for CO₂ capture and activation,⁶² while the recent studies on N-graphene/metal oxide photocatalysts

pointed out the important role of quaternary-N as an electron-mobility activation region for the effective transfer of photogenerated electrons from the CB of the semiconductor.^{47,69} It was demonstrated that the photogenerated charge transfer is positively related to the content of quaternary-N.^{47,69}

Similar to TiO₂/rGO, for the TiO₂/NrGO composites, we propose that there are the CO₂ reduction sites on both the surface of the TiO₂ and NrGO-300, but a majority of CO₂ reduction occurs on the surface of NrGO-300 because the CO₂ molecules are preferably adsorbed on the N sites due to the acid-base and/or hydrogen-bonding interactions between the N-containing functional groups and the CO₂ molecules.^{70,71} Therefore, fewer carbonaceous intermediates were deposited on the surface of TiO₂; meanwhile the photogenerated holes on the TiO₂ VB could react with the H₂O to produce protons, which can be persistently supplied for the reduction of CO₂ on the surface of NrGO-300. This could be main cause contributing to a higher and more stable activity of TiO₂/NrGO-300 over those of TiO₂ and TiO₂/rGO.

On the basis of the above results, the enhanced photocatalytic mechanism of the TiO₂/NrGO-300 can be explained by the synergistic effect of CO₂ activation sites and electron-transfer-mediator, as depicted in Fig. 5.9B. In this reaction scheme, NrGO-300 was a bifunctional co-catalyst, which can facilitate the CO₂ activation and effectively inhibit the recombination of electron-hole pairs simultaneously. The quaternary-N works as the electron-transfer-mediator, rapidly transferring the photogenerated electrons from the CB of TiO₂, and the photogenerated holes also transport to the surface of the TiO₂ easily and the oxidation of H₂O into oxygen and protons occurred. Meanwhile, with the participation of electron and protons, both the pyridinic-N and pyrrolic-N act as the CO₂

reduction active sites to improve the interfacial photocatalytic activity. Nevertheless, the proposed scheme needs further confirmation, and further studies using *in situ* diffuse reflection infrared Fourier transform spectroscopy (DRIFTS) analysis will be helpful to explore the formation of intermediates and clarify the structure-stability relationship of TiO₂/rGO and TiO₂/NrGO catalysts.

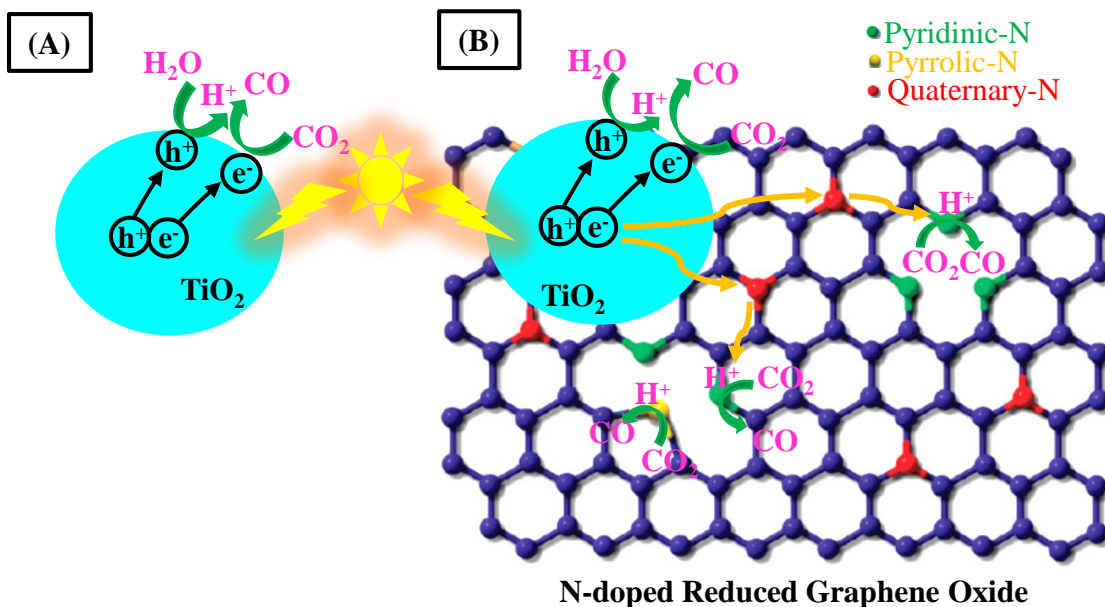


Figure 5.9 Possible reaction mechanisms for photoreduction of CO₂ with H₂O over (A) TiO₂ and (B) TiO₂/NrGO-300 samples.

5.4 Conclusions

We have successfully synthesized TiO₂/nitrogen-doped reduced graphene oxide nanocomposites for gas-phase photoreduction of CO₂ with H₂O vapor. The quantity and configuration of nitrogen dopant in the TiO₂/NrGO nanocomposites strongly influenced the catalytic performance, and the highest activity was observed for TiO₂/NrGO-300 with the highest nitrogen doping content studied and the optimal ratio of each type of nitrogen atoms. Compared with pristine TiO₂ and TiO₂/rGO, the introduction of nitrogen dopant

resulted in a synergistic effect, enhancing CO₂ adsorption on the catalyst surface and promoting photogenerated electron transfer, which together account for the superior CO₂ photoreduction rate of TiO₂/NrGO-300. This work provides a new insight into the important role of doped nitrogen in graphene in CO₂ photoreduction reaction, and it can be expected that our findings will contribute to better design of heteroatom-doped graphene-based materials for CO₂ photoreduction.

Acknowledgments

This work was partially supported by the Ministry of Science and Technology of Taiwan through grant no.: 104-2917-I-564-074. Support from the US-China Clean Energy Center funded by the US DOE is gratefully acknowledged.

References

1. S.D. Kenarsari, D. Yang, G. Jiang, S. Zhang, J. Wang, A.G. Russell, Q. Wei, M. Fan, Review of recent advances in carbon dioxide separation and capture, *RSC Adv.* 3 (2013) 22739–22773.
2. M. Tahir, N.S. Amin, Recycling of carbon dioxide to renewable fuels by photocatalysis: Prospects and challenges, *Renew. Sustain. Energy Rev.* 25 (2013) 560–579.
3. I.-H. Tseng, J.C.S. Wu, H.-Y. Chou, Effects of sol–gel procedures on the photocatalysis of Cu/TiO₂ in CO₂ photoreduction, *J. Catal.* 221 (2004) 432–440.
4. H.-Y. Wu, N.H. Nguyen, H. Bai, S. Chang, J.C.S. Wu, Photocatalytic reduction of CO₂ using molybdenum-doped titanate nanotubes in a MEA solution, *RSC Adv.* 5 (2015) 63142–63151.
5. C.-W. Lee, R. Antoniou Kourounioti, J.C.S. Wu, E. Murchie, M. Maroto-Valer, O.E. Jensen, C.-W. Huang, A. Ruban, Photocatalytic conversion of CO₂ to hydrocarbons by light-harvesting complex assisted Rh-doped TiO₂ photocatalyst, *J. CO₂ Util.* 5 (2014) 33–40.
6. J. Fu, S. Cao, J. Yu, J. Low, Y. Lei, Enhanced photocatalytic CO₂-reduction activity of electrospun mesoporous TiO₂ nanofibers by solvothermal treatment, *Dalton Trans.* 43 (2014) 9158–9165.
7. M. Manzanares, C. Fàbrega, J. Oriol Ossó, L.F. Vega, T. Andreu, J.R. Morante, Engineering the TiO₂ outermost layers using magnesium for carbon dioxide photoreduction, *Appl. Catal. B Environ.* 150–151 (2014) 57–62.
8. W.-N. Wang, J. Park, P. Biswas, Rapid synthesis of nanostructured Cu–TiO₂–SiO₂ composites for CO₂ photoreduction by evaporation driven self-assembly, *Catal. Sci. Technol.* 1 (2011) 593–600.
9. L.-L. Tan, W.-J. Ong, S.-P. Chai, A.R. Mohamed, Visible-light-activated oxygen-rich TiO₂ as next generation photocatalyst: Importance of annealing temperature on the photoactivity toward reduction of carbon dioxide, *Chem. Eng. J.* 283 (2016) 1254–1263.
10. S. Xie, Y. Wang, Q. Zhang, W. Deng, Y. Wang, MgO- and Pt-Promoted TiO₂ as an Efficient Photocatalyst for the Preferential Reduction of Carbon Dioxide in the Presence of Water, *ACS Catal.* 4 (2014) 3644–3653.

11. M. Tahir, N.S. Amin, Photocatalytic CO₂ reduction with H₂O vapors using montmorillonite/TiO₂ supported microchannel monolith photoreactor, *Chem. Eng. J.* 230 (2013) 314–327.
12. L.-L. Tan, W.-J. Ong, S.-P. Chai, A.R. Mohamed, Photocatalytic reduction of CO₂ with H₂O over graphene oxide-supported oxygen-rich TiO₂ hybrid photocatalyst under visible light irradiation: Process and kinetic studies, *Chem. Eng. J.* 308 (2017) 248–255.
13. M.M. Gui, W.M.P. Wong, S.-P. Chai, A.R. Mohamed, One-pot synthesis of Ag-MWCNT@TiO₂ core-shell nanocomposites for photocatalytic reduction of CO₂ with water under visible light irradiation, *Chem. Eng. J.* 278 (2015) 272–278.
14. X. Li, H. Liu, D. Luo, J. Li, Y. Huang, H. Li, Y. Fang, Y. Xu, L. Zhu, Adsorption of CO₂ on heterostructure CdS(Bi₂S₃)/TiO₂ nanotube photocatalysts and their photocatalytic activities in the reduction of CO₂ to methanol under visible light irradiation, *Chem. Eng. J.* 180 (2012) 151–158.
15. M. Tahir, N.S. Amin, Performance analysis of nanostructured NiO–In₂O₃/TiO₂ catalyst for CO₂ photoreduction with H₂ in a monolith photoreactor, *Chem. Eng. J.* 285 (2016) 635–649.
16. Y. Liu, Y. Yang, Q. Sun, Z. Wang, B. Huang, Y. Dai, X. Qin, X. Zhang, Chemical Adsorption Enhanced CO₂ Capture and Photoreduction over a Copper Porphyrin Based Metal Organic Framework, *ACS Appl. Mater. Interfaces.* 5 (2013) 7654–7658.
17. H.-Y. Wu, H. Bai, J.C.S. Wu, Photocatalytic Reduction of CO₂ Using Ti–MCM-41 Photocatalysts in Monoethanolamine Solution for Methane Production, *Ind. Eng. Chem. Res.* 53 (2014) 11221–11227.
18. H.-C. Yang, H.-Y. Lin, Y.-S. Chien, J.C.-S. Wu, H.-H. Wu, Mesoporous TiO₂/SBA-15, and Cu/TiO₂/SBA-15 Composite Photocatalysts for Photoreduction of CO₂ to Methanol, *Catal. Lett.* 131 (2009) 381–387.
19. M. Hussain, P. Akhter, N. Russo, G. Saracco, New optimized mesoporous silica incorporated isolated Ti materials towards improved photocatalytic reduction of carbon dioxide to renewable fuels, *Chem. Eng. J.* 278 (2015) 279–292.
20. S. Liu, J. Xia, J. Yu, Amine-Functionalized Titanate Nanosheet-Assembled Yolk@Shell Microspheres for Efficient Cocatalyst-Free Visible-Light Photocatalytic CO₂ Reduction, *ACS Appl. Mater. Interfaces.* 7 (2015) 8166–8175.

21. Y. Liao, S.-W. Cao, Y. Yuan, Q. Gu, Z. Zhang, C. Xue, Efficient CO₂ Capture and Photoreduction by Amine-Functionalized TiO₂, *Chem. – Eur. J.* 20 (2014) 10220–10222.
22. A.K. Mishra, S. Ramaprabhu, Carbon dioxide adsorption in graphene sheets, *AIP Adv.* 1 (2011) 032152-032157.
23. A. Garcia-Gallastegui, D. Iruretagoyena, V. Gouvea, M. Mokhtar, A.M. Asiri, S.N. Basahel, S.A. Al-Thabaiti, A.O. Alyoubi, D. Chadwick, M.S.P. Shaffer, Graphene Oxide as Support for Layered Double Hydroxides: Enhancing the CO₂ Adsorption Capacity, *Chem. Mater.* 24 (2012) 4531–4539.
24. J. Wang, I. Senkovska, M. Oschatz, M.R. Lohe, L. Borchardt, A. Heerwig, Q. Liu, S. Kaskel, Imine-Linked Polymer-Derived Nitrogen-Doped Microporous Carbons with Excellent CO₂ Capture Properties, *ACS Appl. Mater. Interfaces.* 5 (2013) 3160–3167.
25. M. Sevilla, J.B. Parra, A.B. Fuertes, Assessment of the Role of Micropore Size and N-Doping in CO₂ Capture by Porous Carbons, *ACS Appl. Mater. Interfaces.* 5 (2013) 6360–6368.
26. Á. Sánchez-Sánchez, F. Suárez-García, A. Martínez-Alonso, J.M.D. Tascón, Influence of Porous Texture and Surface Chemistry on the CO₂ Adsorption Capacity of Porous Carbons: Acidic and Basic Site Interactions, *ACS Appl. Mater. Interfaces.* 6 (2014) 21237–21247.
27. G. Chen, X. Wang, J. Li, W. Hou, Y. Zhou, J. Wang, Direct Carbonization of Cyanopyridinium Crystalline Dicationic Salts into Nitrogen-Enriched Ultra-Microporous Carbons toward Excellent CO₂ Adsorption, *ACS Appl. Mater. Interfaces.* 7 (2015) 18508–18518.
28. K.C. Kemp, V. Chandra, M. Saleh, K.S. Kim, Reversible CO₂ adsorption by an activated nitrogen doped graphene/polyaniline material, *Nanotechnology.* 24 (2013) 235703-235709.
29. H. Wang, T. Maiyalagan, X. Wang, Review on Recent Progress in Nitrogen-Doped Graphene: Synthesis, Characterization, and Its Potential Applications, *ACS Catal.* 2 (2012) 781–794.
30. C.N.R. Rao, K. Gopalakrishnan, A. Govindaraj, Synthesis, properties and applications of graphene doped with boron, nitrogen and other elements, *Nano Today.* 9 (2014) 324–343.

31. Z. Mou, Y. Wu, J. Sun, P. Yang, Y. Du, C. Lu, TiO₂ Nanoparticles-Functionalized N-Doped Graphene with Superior Interfacial Contact and Enhanced Charge Separation for Photocatalytic Hydrogen Generation, *ACS Appl. Mater. Interfaces*. 6 (2014) 13798–13806.
32. M.S.A. Sher Shah, W.-J. Kim, J. Park, D.K. Rhee, I.-H. Jang, N.-G. Park, J.Y. Lee, P.J. Yoo, Highly Efficient and Recyclable Nanocomplexed Photocatalysts of AgBr/N-Doped and Amine-Functionalized Reduced Graphene Oxide, *ACS Appl. Mater. Interfaces*. 6 (2014) 20819–20827.
33. S.-Q. Liu, S.-S. Zhou, Z.-G. Chen, C.-B. Liu, F. Chen, Z.-Y. Wu, An artificial photosynthesis system based on CeO₂ as light harvester and N-doped graphene Cu(II) complex as artificial metalloenzyme for CO₂ reduction to methanol fuel, *Catal. Commun.* 73 (2016) 7–11.
34. P. Kumar, H.P. Mungse, O.P. Khatri, S.L. Jain, Nitrogen-doped graphene-supported copper complex: a novel photocatalyst for CO₂ reduction under visible light irradiation, *RSC Adv*. 5 (2015) 54929–54935.
35. W.S. Hummers, R.E. Offeman, Preparation of Graphitic Oxide, *J. Am. Chem. Soc.* 80 (1958) 1339–1339.
36. Z. Wang, D. Xu, Y. Huang, Z. Wu, L. Wang, X. Zhang, Facile, mild and fast thermal-decomposition reduction of graphene oxide in air and its application in high-performance lithium batteries, *Chem Commun*. 48 (2012) 976–978.
37. H. Zhang, X. Lv, Y. Li, Y. Wang, J. Li, P25-Graphene Composite as a High Performance Photocatalyst, *ACS Nano*. 4 (2010) 380–386.
38. J. Ryu, S. Kim, H.I. Kim, E.-H. Jo, Y.K. Kim, M. Kim, H.D. Jang, Self-assembled TiO₂ agglomerates hybridized with reduced-graphene oxide: A high-performance hybrid photocatalyst for solar energy conversion, *Chem. Eng. J.* 262 (2015) 409–416.
39. Y. Zhang, Z.-R. Tang, X. Fu, Y.-J. Xu, TiO₂-Graphene Nanocomposites for Gas-Phase Photocatalytic Degradation of Volatile Aromatic Pollutant: Is TiO₂-Graphene Truly Different from Other TiO₂-Carbon Composite Materials?, *ACS Nano*. 4 (2010) 7303–7314.

40. T.-F. Yeh, C.-Y. Teng, S.-J. Chen, H. Teng, Nitrogen-Doped Graphene Oxide Quantum Dots as Photocatalysts for Overall Water-Splitting under Visible Light Illumination, *Adv. Mater.* 26 (2014) 3297–3303.
41. L.-C. Chen, T.-F. Yeh, Y.-L. Lee, H. Teng, Incorporating nitrogen-doped graphene oxide dots with graphene oxide sheets for stable and effective hydrogen production through photocatalytic water decomposition, *Appl. Catal. Gen.* 521 (2016) 118–124.
42. H.-L. Guo, P. Su, X. Kang, S.-K. Ning, Synthesis and characterization of nitrogen-doped graphene hydrogels by hydrothermal route with urea as reducing-doping agents, *J. Mater. Chem. A* 1 (2013) 2248–2255.
43. B. Jiang, C. Tian, L. Wang, L. Sun, C. Chen, X. Nong, Y. Qiao, H. Fu, Highly concentrated, stable nitrogen-doped graphene for supercapacitors: Simultaneous doping and reduction, *Appl. Surf. Sci.* 258 (2012) 3438–3443.
44. Z. Chen, D. Higgins, H. Tao, R.S. Hsu, Z. Chen, Highly Active Nitrogen-Doped Carbon Nanotubes for Oxygen Reduction Reaction in Fuel Cell Applications, *J. Phys. Chem. C* 113 (2009) 21008–21013.
45. L. Sun, L. Wang, C. Tian, T. Tan, Y. Xie, K. Shi, M. Li, H. Fu, Nitrogen-doped graphene with high nitrogen level via a one-step hydrothermal reaction of graphene oxide with urea for superior capacitive energy storage, *RSC Adv.* 2 (2012) 4498–4506.
46. L. Sun, L. Wang, C. Tian, T. Tan, Y. Xie, K. Shi, M. Li, H. Fu, Nitrogen-doped graphene with high nitrogen level via a one-step hydrothermal reaction of graphene oxide with urea for superior capacitive energy storage, *RSC Adv.* 2 (2012) 4498–4506.
47. L. He, L. Jing, Y. Luan, L. Wang, H. Fu, Enhanced Visible Activities of α -Fe₂O₃ by Coupling N-Doped Graphene and Mechanism Insight, *ACS Catal.* 4 (2014) 990–998.
48. D. Long, W. Li, L. Ling, J. Miyawaki, I. Mochida, S.-H. Yoon, Preparation of Nitrogen-Doped Graphene Sheets by a Combined Chemical and Hydrothermal Reduction of Graphene Oxide, *Langmuir*. 26 (2010) 16096–16102.
49. A.C. Ferrari, Raman spectroscopy of graphene and graphite: Disorder, electron–phonon coupling, doping and nonadiabatic effects, *Solid State Commun.* 143 (2007) 47–57.

50. Y. Shao, S. Zhang, M.H. Engelhard, G. Li, G. Shao, Y. Wang, J. Liu, I.A. Aksay, Y. Lin, Nitrogen-doped graphene and its electrochemical applications, *J. Mater. Chem.* 20 (2010) 7491–7496.
51. Y. Nie, W.-N. Wang, Y. Jiang, J. Fortner, P. Biswas, Crumpled Reduced Graphene Oxide–Amine–Titanium Dioxide Nanocomposites for Simultaneous Carbon Dioxide Adsorption and Photoreduction, *Catal. Sci. Technol.* 6 (2016) 6187–6196.
52. X. Li, Z. Zhuang, W. Li, H. Pan, Photocatalytic reduction of CO₂ over noble metal-loaded and nitrogen-doped mesoporous TiO₂, *Appl. Catal. Gen.* 429–430 (2012) 31–38.
53. L.-L. Tan, W.-J. Ong, S.-P. Chai, B.T. Goh, A.R. Mohamed, Visible-light-active oxygen-rich TiO₂ decorated 2D graphene oxide with enhanced photocatalytic activity toward carbon dioxide reduction, *Appl. Catal. B Environ.* 179 (2015) 160–170.
54. L.-L. Tan, W.-J. Ong, S.-P. Chai, A.R. Mohamed, Noble metal modified reduced graphene oxide/TiO₂ ternary nanostructures for efficient visible-light-driven photoreduction of carbon dioxide into methane, *Appl. Catal. B Environ.* 166–167 (2015) 251–259.
55. W.-N. Wang, W.-J. An, B. Ramalingam, S. Mukherjee, D.M. Niedzwiedzki, S. Gangopadhyay, P. Biswas, Size and Structure Matter: Enhanced CO₂ Photoreduction Efficiency by Size-Resolved Ultrafine Pt Nanoparticles on TiO₂ Single Crystals, *J. Am. Chem. Soc.* 134 (2012) 11276–11281.
56. W.-N. Wang, Y. Jiang, J.D. Fortner, P. Biswas, Nanostructured Graphene-Titanium Dioxide Composites Synthesized by a Single-Step Aerosol Process for Photoreduction of Carbon Dioxide, *Environ. Eng. Sci.* 31 (2014) 428–434.
57. M. Liu, X. Qiu, M. Miyauchi, K. Hashimoto, Cu(II) Oxide Amorphous Nanoclusters Grafted Ti³⁺ Self-Doped TiO₂: An Efficient Visible Light Photocatalyst, *Chem. Mater.* 23 (2011) 5282–5286.
58. K. Li, T. Peng, Z. Ying, S. Song, J. Zhang, Ag-loading on brookite TiO₂ quasi nanocubes with exposed {2 1 0} and {0 0 1} facets: Activity and selectivity of CO₂ photoreduction to CO/CH₄, *Appl. Catal. B Environ.* 180 (2016) 130–138.
59. Y. Ji, Y. Luo, Theoretical Study on the Mechanism of Photoreduction of CO₂ to CH₄ on the Anatase TiO₂(101) Surface, *ACS Catal.* 6 (2016) 2018–2025.

60. J.-C. Wang, H.-C. Yao, Z.-Y. Fan, L. Zhang, J.-S. Wang, S.-Q. Zang, Z.-J. Li, Indirect Z-Scheme BiOI/g-C₃N₄ Photocatalysts with Enhanced Photoreduction CO₂ Activity under Visible Light Irradiation, *ACS Appl. Mater. Interfaces*. 8 (2016) 3765–3775.
61. J.-C. Wang, L. Zhang, W.-X. Fang, J. Ren, Y.-Y. Li, H.-C. Yao, J.-S. Wang, Z.-J. Li, Enhanced Photoreduction CO₂ Activity over Direct Z-Scheme α -Fe₂O₃/Cu₂O Heterostructures under Visible Light Irradiation, *ACS Appl. Mater. Interfaces*. 7 (2015) 8631–8639.
62. P. Tamilarasan, S. Ramaprabhu, Sub-ambient carbon dioxide adsorption properties of nitrogen doped graphene, *J. Appl. Phys.* 117 (2015) 144301-144308.
63. W. Xing, C. Liu, Z. Zhou, L. Zhang, J. Zhou, S. Zhuo, Z. Yan, H. Gao, G. Wang, S.Z. Qiao, Superior CO₂ uptake of N-doped activated carbon through hydrogen-bonding interaction, *Energy Environ. Sci.* 5 (2012) 7323–7327.
64. N. Daems, X. Sheng, I.F.J. Vankelecom, P.P. Pescarmona, Metal-free doped carbon materials as electrocatalysts for the oxygen reduction reaction, *J. Mater. Chem. A*. 2 (2014) 4085–4110.
65. L. Jia, D.-H. Wang, Y.-X. Huang, A.-W. Xu, H.-Q. Yu, Highly Durable N-Doped Graphene/CdS Nanocomposites with Enhanced Photocatalytic Hydrogen Evolution from Water under Visible Light Irradiation, *J. Phys. Chem. C*. 115 (2011) 11466–11473.
66. H.-C. Hsu, I. Shown, H.-Y. Wei, Y.-C. Chang, H.-Y. Du, Y.-G. Lin, C.-A. Tseng, C.-H. Wang, L.-C. Chen, Y.-C. Lin, K.-H. Chen, Graphene oxide as a promising photocatalyst for CO₂ to methanol conversion, *Nanoscale*. 5 (2013) 262–268.
67. D. Uner, M.M. Oymak, On the mechanism of photocatalytic CO₂ reduction with water in the gas phase, *Catal. Today*. 181 (2012) 82–88.
68. H. Wang, T. Maiyalagan, X. Wang, Review on Recent Progress in Nitrogen-Doped Graphene: Synthesis, Characterization, and Its Potential Applications, *ACS Catal.* 2 (2012) 781–794.
69. Y. Xu, Y. Mo, J. Tian, P. Wang, H. Yu, J. Yu, The synergistic effect of graphitic N and pyrrolic N for the enhanced photocatalytic performance of nitrogen-doped graphene/TiO₂ nanocomposites, *Appl. Catal. B Environ.* 181 (2016) 810–817.
70. A. Sayari, Y. Belmabkhout, Stabilization of Amine-Containing CO₂ Adsorbents: Dramatic Effect of Water Vapor, *J. Am. Chem. Soc.* 132 (2010) 6312–6314.

71. L.-C. Chen, Facile Preparation of Nitrogen-Doped Activated Carbon for Carbon Dioxide Adsorption, *Aerosol Air Qual. Res.* (2014) 916–927.

Chapter 5 Supporting Information

Table of Contents

S5.1 Estimated band gap energies

S5.2 Effect of the GO amount on the catalytic performance

S5.3 TG/DTA profiles

S5.4 Linear sweep voltammetry scan

S5.5 Quantum efficiency calculation

S5.6 CO production rate under Xe lamp (with UV cut-off filter) irradiation.

S5.1 Estimated band gap energies of TiO₂, TiO₂/rGO and TiO₂/NrGO samples.

Table S5.1 Estimated band gap energies of TiO₂, TiO₂/rGO and TiO₂/NrGO samples.

Sample	Estimated band gap energy (eV)
TiO ₂	3.15
TiO ₂ /rGO	2.95
TiO ₂ /NrGO-100	2.95
TiO ₂ /NrGO-200	2.95
TiO ₂ /NrGO-300	2.93
TiO ₂ /NrGO-400	2.93
TiO ₂ /NrGO-500	2.95

S5.2 The effect of the GO amount on the catalytic performance of the prepared TiO₂/NrGO-300 composites for CO₂ photoreduction.

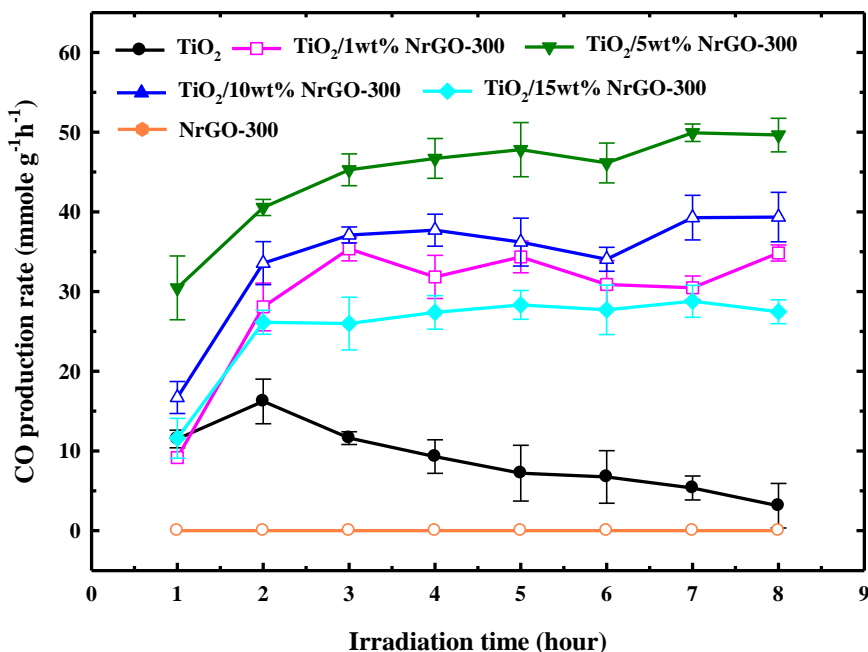


Fig. S5.1 The effect of the GO amount on the catalytic performance of the prepared TiO₂/NrGO-300 composites for CO₂ photoreduction.

Fig. S5.1 displays the CO₂ photoreduction results for TiO₂/NrGO composites synthesized at a fixed weight ratio of urea/GO = 300, with different GO amounts in the precursor solution. It is clear to see that all of the TiO₂/NrGO-300 exhibit much higher activity and stability than the bare TiO₂. Moreover, the GO amount has a strong influence on the photocatalytic activity of the TiO₂/NrGO-300 composites, and the photocatalytic activity follows the order of TiO₂/5wt% NrGO-300 > TiO₂/10wt% NrGO-300 > TiO₂/1wt% NrGO-300 > TiO₂/15wt% NrGO-300. These results suggest a synergistic effect between the NrGO-300 and TiO₂. Therefore, it is important to control the composition ratio in the composite material to achieve the optimal photocatalytic activity. One should note that a high addition ratio of GO (10 wt % and 15 wt %) lowered the photocatalytic activity of the TiO₂/NrGO-300 composites for CO₂ photoreduction. The higher addition ratio of GO into the composites may lower the contact surface of TiO₂ particles with the light illumination, leading to decrease the photocatalytic performance.^{1,2}

S5.3 The TG/DTA profiles of the TiO₂/rGO and TiO₂/NrGO composites.

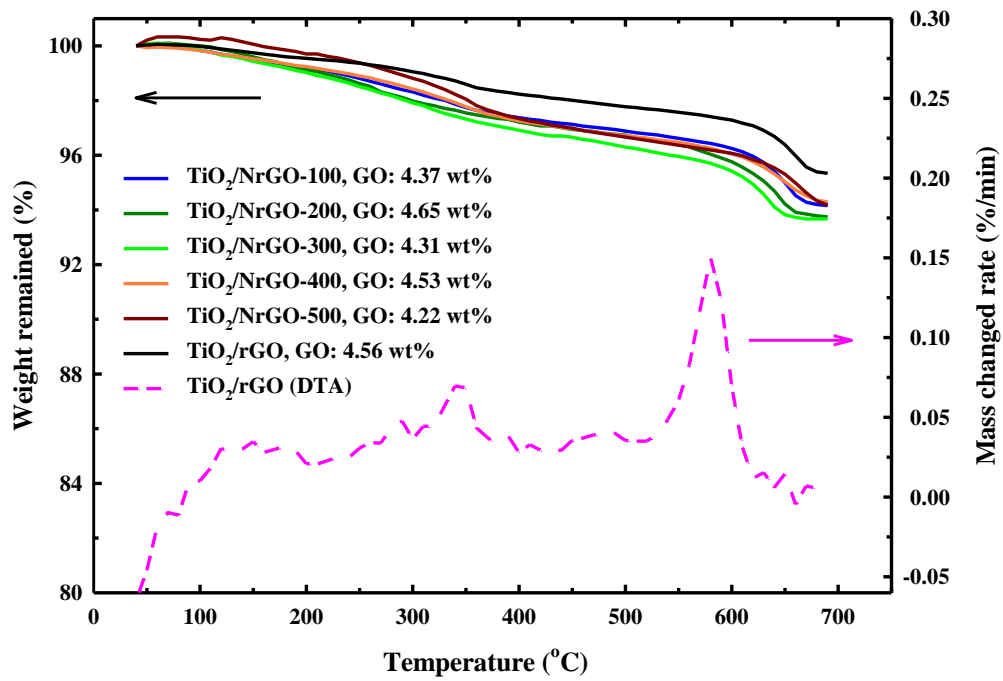


Fig. S5.2 The TG/DTA profiles of the TiO₂/rGO and TiO₂/NrGO composites.

S5.4 Linear sweep voltammetry (a) Cathodic scan and (b) anodic scan for TiO₂/rGO, TiO₂/NrGO-300 and TiO₂/NrGO-500 composite

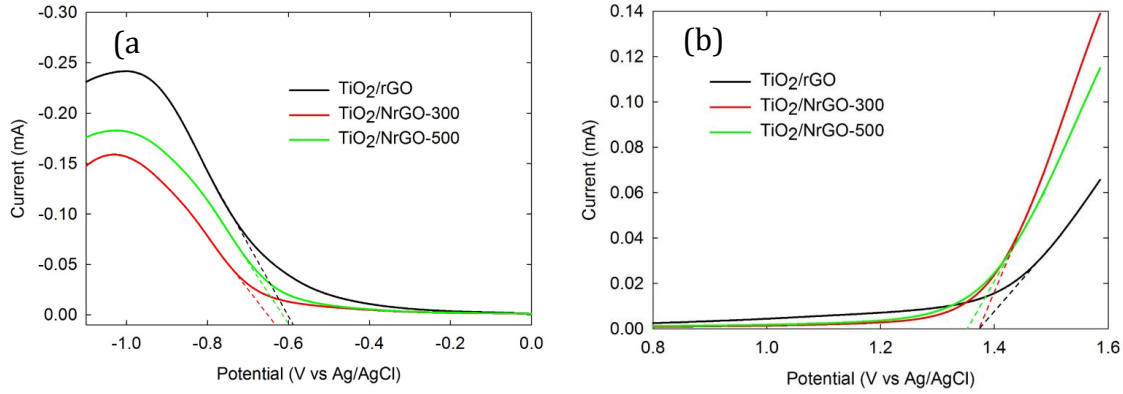


Fig. S5.3 Linear sweep voltammetry (a) Cathodic scan and (b) anodic scan for TiO₂/rGO, TiO₂/NrGO-300 and TiO₂/NrGO-500 composite

S5.5 Quantum efficiency calculation

The photoreduction performance can also be characterized by the photochemical quantum efficiency (quantum yield), ϕ , which is defined as a measure of the molar fraction of incident photons that result in CO₂ reduction products.³ For the case that CO is the product, quantum efficiency can be calculated by the following equation, as two electrons are required to convert one CO₂ molecule to one CO molecule.³

$$\phi(\%) = \frac{2 \times CO \text{ yield (mol)}}{\text{photon absorbed by catalyst (mol)}} \times 100\% \quad (\text{S5.1})$$

The highest CO yield within the 8 hours UV irradiation was taken for calculation of quantum efficiency. The moles of photo absorbed by catalyst were calculated using the following equation:

$$\text{photon absorbed by catalyst (mol)} = \frac{\text{total energy absorbed by catalyst}}{\text{average photon energy} \times N_A} \quad (\text{S5.2})$$

where N_A is the Avogadro's constant.

The photon energy at a certain wavelength can be calculated by:

$$E = \frac{hc}{\lambda} \quad (\text{S5.3})$$

where h , c and λ are Planck constant, speed of light and wavelength of light, respectively. The average photon energy can be estimated by averaging the photon energy from 250 to 400 nm.

The constants that were used for the calculations are listed as below:

Light intensity in the effective light range: 11.5 mW/cm²

Deposited film diameter (circle): 4.2 cm

Average photon energy: 6.85×10^{-19} J

Yield of CO: 50 $\mu\text{mol g}^{-1}\text{h}^{-1}$

Mass of the catalyst used: 10 mg

Based on Eq. (1), the ϕ was calculated to be 0.0072%.

S5.6 CO production rate as a function of time-on-stream over bare TiO₂, TiO₂/rGO, and TiO₂/NrGO-300 under Xe lamp (with UV cut-off filter) irradiation.

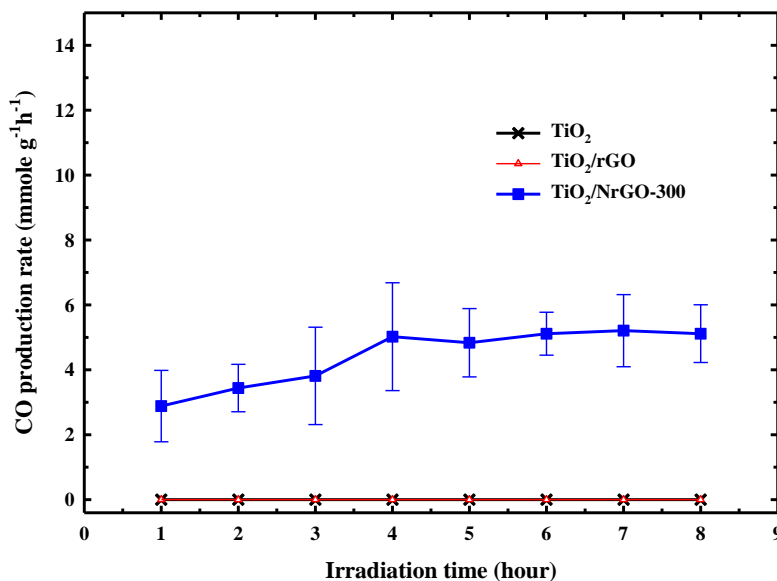


Fig. S5.4 CO production rate as a function of time-on-stream over bare TiO₂, TiO₂/rGO, and TiO₂/NrGO-300 under Xe lamp (with UV cut-off filter) irradiation.

References

1. P. Wang, J. Wang, X. Wang, H. Yu, J. Yu, M. Lei, Y. Wang, One-step synthesis of easy-recycling TiO₂-rGO nanocomposite photocatalysts with enhanced photocatalytic activity, *Appl. Catal. B Environ.* 132–133 (2013) 452–459.
2. Y. Zhang, Z.-R. Tang, X. Fu, Y.-J. Xu, TiO₂-Graphene Nanocomposites for Gas-Phase Photocatalytic Degradation of Volatile Aromatic Pollutant: Is TiO₂-Graphene Truly Different from Other TiO₂-Carbon Composite Materials?, *ACS Nano.* 4 (2010) 7303–7314.
3. X. An, K. Li, J. Tang, Cu₂O/Reduced Graphene Oxide Composites for the Photocatalytic Conversion of CO₂, *ChemSusChem.* 7 (2014) 1086–1093.

**Chapter 6 Surface Defect-Induced Performance Enhancement
in CO₂ Photoreduction: An Applied Electric Potential
Approach**

To be submitted for publication, August 2018

Abstract

The CO₂ photoreduction over TiO₂ is significantly limited by the wide band gap (3.2 eV for anatase), low surface area, and rapid recombination of electrons and holes. Surface defects engineering is commonly used approach to overcome these barriers, however, the existing methods usually require high energy input, and an intense and special synthesis environment. This work reports a new method to generate oxygen vacancies and Ti-related defects (OTDs) in columnar titanium dioxide (TiO₂) thin film under UV irradiation with an applied potential to the substrate. The defective TiO₂ (TiO_{2-x}) showed a significant performance enhancement in carbon dioxide (CO₂) photoreduction with the highest CO yield of 375 μmol/g/hr, which is about 4 times higher than that of pristine TiO₂ (95 μmol/g/hr). The roles of the applied electric power and substrate used in the enhancement of photocatalytic performance were investigated systematically. Besides, the OTDs in the samples exhibit excellent reversibility, and the formation and recovery of OTDs were deliberately analyzed with high-resolution transmission electron microscopy (HRTEM), ultraviolet–visible spectroscopy, Raman spectroscopy, and X-ray photoelectron spectroscopy (XPS). The results reveal that the enhancement of the TiO_{2-x} in CO₂ photoreduction created by electric potential can be attributed to 1) the narrowed band gap energy, 2) the enhanced CO₂ adsorption and molecule activation, and 3) the better separation of electrons and holes. This study offers new insights into engineering OTDs in TiO₂ for photocatalysis, using an easy and gentle method in ambient environment.

6.1 Introduction

Photocatalytic reduction of carbon dioxide (CO₂) with water (H₂O) vapor is an attractive approach to address the CO₂ emission problem, because it is a “green chemistry” technique to convert CO₂ into useful fuels (e.g., carbon monoxide (CO), methane, and methanol) by directly harnessing inexpensive and abundant solar energy.¹⁻² Titanium dioxide (TiO₂) is a widely used semiconductor for photocatalysis, due to its comparatively low cost, low toxicity,³ and ability to resist photo-corrosion.⁴ However, the CO₂ photoreduction efficiency of TiO₂ materials is typically low, which results from the wide band gap (3.2 eV for anatase), low surface area, and rapid recombination of electrons and holes. A number of methods have been reported to modify TiO₂ to address these limitations, such as metal⁵⁻⁶ or non-metal doping,⁷⁻⁸ morphology modification,⁹⁻¹⁰ and defects engineering.¹¹⁻¹³

The surface properties of TiO₂ are largely influenced by defects, and the dominant defects are oxygen vacancies and Ti-related defects (OTDs).¹⁴⁻¹⁶ It has been reported that OTDs can not only work as adsorption active sites for heterogeneous catalysis,¹⁷ but also affect the electron-hole recombination process in photocatalysis.¹⁸ In addition, to avoid introducing excess foreign elements, the effects of OTDs have been widely studied as a form of so-called “self-doping”,¹⁹ which is considered a green and promising strategy for efficient and environmentally friendly engineering of photocatalysts. Therefore, the introduction of OTDs in TiO₂ is a useful method to enhance its photocatalytic performance. OTDs can be generated via diverse mechanisms, such as hydrogen thermal treatment,²⁰⁻²¹ high-energy particle bombardment,²²⁻²³ doping of metal or nonmetal ions,²⁴⁻²⁵ photo-induced reactions,²⁶⁻²⁷ and thermal treatment in an oxygen depleted environment.²⁸⁻²⁹

These methods usually require high energy input, and an intense and special synthesis environment in order to remove the oxygen atom in the lattice and to form OTDs. Developing a method, which uses a low energy input and requires only an ambient environment would be a large environmental step forward and broaden the application of defective TiO₂.

Single crystal-phase TiO₂ nanostructures with one-dimensional (1D) orientation, such as nanotubes, nanowires, and nanocolumns, have demonstrated better photocatalytic capability than those of planar or random orientation structures,³⁰⁻³¹ because these 1D structures have a large surface area,^{9, 32} minimized boundary effects,³³ and enhanced electron mobility.³⁰ In this study, the aerosol chemical vapor deposition (ACVD) process was used to synthesize TiO₂ thin films with columnar morphologies, which were then used for CO₂ photoreduction. The ACVD technique, which has been well demonstrated in our previous work,^{9, 34} has several outstanding advantages over other existing methods: it is a one-step process, operated in the ambient environment, and easy to scale up.

Here, we reported a method to in-situ generate OTDs in these columnar TiO₂ thin films by simultaneously applying electric potential and UV irradiation. To the best of our knowledge, the method has never been reported in this field. In comparison with the existing methods to create OTDs in TiO₂, applying electric potential under UV irradiation in the ambient environment is both more simple and convenient. Besides, these OTDs created by this method can be recovered, indicating that the electric potential and UV approach is reversible and nearly non-destructive to TiO₂ structure. The effects of electric power and substrates on the enhanced CO₂ photoreduction was investigated systematically. The formation and recovery of OTDs were carefully analyzed with high-resolution

transmission electron microscopy (HRTEM), ultraviolet–visible spectroscopy, Raman spectroscopy, and X-ray photoelectron spectroscopy (XPS). Furthermore, a mechanistic understanding of the formation of OTDs and the enhanced CO₂ photoreduction with electric potential, was proposed. Our study offers new insights into engineering OTDs in TiO₂ for photocatalysis.

6.2 Materials and methods

6.2.1 Synthesis of columnar TiO₂ single crystals

In our previous studies,^{9,34} ACVD system was used to synthesize TiO₂ thin films with different morphologies, including planar, columnar, and granular structures (more details can be found in the Supporting Information, S6.1). The experimental conditions for ACVD deposition of columnar TiO₂ thin films in this study are briefly described here. Titanium tetraisopropoxide (TTIP, 97%, Sigma-Aldrich) was used as a precursor and loaded in a homemade bubbler at a constant temperature of 297 K. Fluorine doped tin oxide (FTO)-, indium tin oxide (ITO)-coated glass and stainless steel (SS) were used as deposition substrates (1 inch × 1 inch), which were maintained at 773 K for all samples. The flow rate of carrier gas, nitrogen (N₂), entering the bubbler was controlled at 0.45 liter per minute (lpm), which was equivalent to 1.46 μmol/min of TTIP fed into the reactor. The total flow rate was 0.9 lpm, leading to a residence time of TTIP of 20 ms. For all samples, the total deposition time of TiO₂ was fixed at 50 min. The mass of each thin film sample was measured to be 0.7 mg.

6.2.2 Materials characterization

The morphology and structure of the columnar TiO₂ single crystals were examined by field emission scanning electron microscopy (FE-SEM, NOVA NanoSEM 230, FEI

Co.), transmission electron microscopy (TEM, Tecnai TM Spirit, FEI Co.), and high resolution-TEM (HRTEM, JEOL 2100). The crystal phase was determined by X-ray diffraction (XRD) (Geigerflex D-MAX/A, Rigaku Denki) over scattering angles from 20° to 60° with Cu K α radiation ($\lambda = 1.548 \text{ \AA}$). The diffuse reflectance spectra were measured using a UV-Vis spectrophotometer (Varian Bio 50). The surface chemical compositions and properties were analyzed by laser Raman spectrometry (Renishaw InVia Reflex confocal Raman spectrometer, with a 514 nm laser) and X-ray photoelectron spectroscopy (XPS, PHI 5000 VersaProbe II equipped with a monochromatic Al K α (1486.6 eV) X-ray source). XPS data analysis was performed using the PHI MultiPak software, after performing a Shirley background correction. Calibration was carried out by aligning the spectra with reference to the C 1s line at 284.5 eV.

6.2.3 Design of the configuration to apply electric potential

To investigate the effect the electric potential on the enhanced CO₂ photoreduction, two possible configurations shown in Figure S6.2 (see Supporting Information) were considered. In Figure S6.2(a), an electric field can be added to the columnar TiO₂ by applying electric potential to two FTO substrates, with columnar TiO₂ on one of the substrate and towards the other one. With this configuration, photo-generated electrons and holes can have higher mobility driven by the electric field, resulting in a better separation of electrons and holes. Another configuration, as shown in Figure S6.2(b), is applying the electric potential directly to the FTO substrate with columnar TiO₂, which can result in electric current passing through the substrate. In this study, the second configuration was used, due the simpler design and easier exposure of the columnar TiO₂ to UV irradiation, than the first configuration.

6.2.4 CO₂ photoreduction analysis

Figure 6.1 shows a schematic diagram of the CO₂ photoreduction system. Compressed CO₂ (Instrument Gr. 4, Airgas, Inc.) was the carbon source, and was passed through a water bubbler to generate a mixture of CO₂ and water vapor. The gaseous mixture was then introduced into a homemade continuous flow reactor where the columnar TiO₂ thin film samples were loaded. To investigate the effect of electric potential, the sample was connected to a direct-current (DC) power supply (Tekpower TP3005D, 0-30V, 0-5A). The reactor was cylindrical, with a quartz window vertically facing the light source, which was a Xe lamp (Oriol 66021, Newport Co.) operating at 450 W (the light spectrum was measured by a spectroradiometer (ILT-900R, Polytec GmbH), see **Figure S3**, Supporting Information). The photoreduction analysis system was reported in detail in our previous publications.^{10, 35-36} Before each test, the reactor loaded with samples and support glass fiber was initially purged with CO₂ and water vapor at 16 ml/min for 1 hr, and then the flow rate was decreased and maintained at 1 ml/min for the test period. The light source was turned on (t = 0 hr) and measurements were made for 8 hours. The concentrations of effluent gases (CO₂, CO, CH₄, O₂, and N₂) as a function of irradiation time were recorded automatically by gas chromatography (GC, 6895N, Agilent Technologies, Inc.) through an automated gas valve, using helium as the carrier gas. The GC was equipped with a PLOT capillary column (Supelco Carboxen-1010) and a thermal conductivity detector (TCD). An overall experimental plan is outlined in Table 6.1.

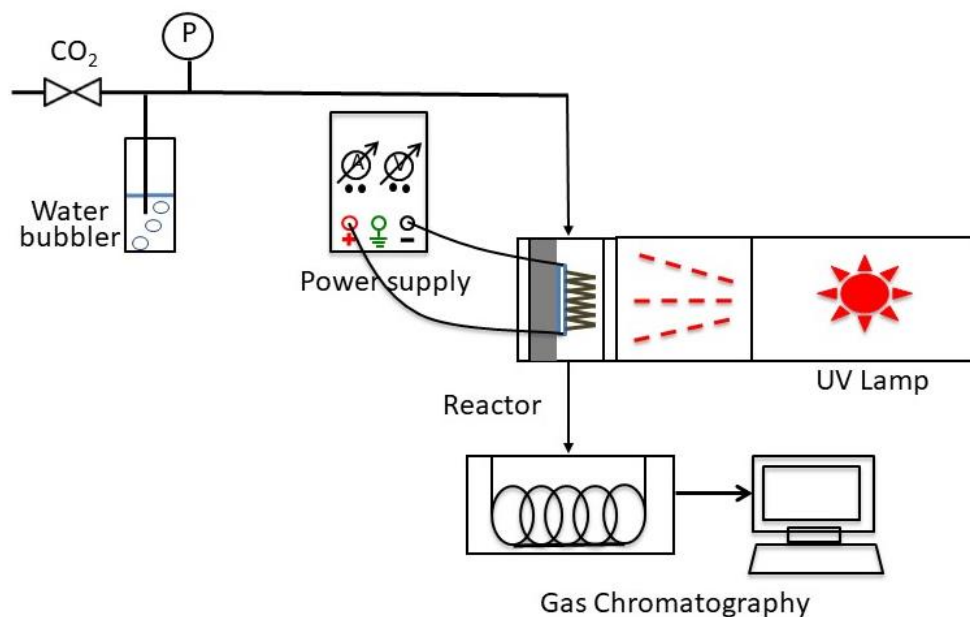


Figure 6.1 Schematic diagram of the CO₂ photoreduction system.

Table 6.1 Experimental plan.

Test number	Objectives	Instruments/ methodology	Results
1	Material characterization (morphology)	SEM, TEM	Figure 6.2
2	CO ₂ photoreduction test	CO ₂ photoreduction analysis system	Effect of electric power: Figure 6.3a Effect of substrate: Figure 6.3b
3	Material characterization before and after CO ₂ photoreduction (crystalline structure and surface chemistry)	HRTEM, XRD UV-vis, Raman, XPS, in-situ DRIFTS	HRTEM: Figure 6.4 XRD: Figure S6.4 UV-Vis: Figure 6.5 Raman: Figure 6.6 XPS: Figure 6.7 In-situ DRIFTS: Figure 6.9
4	Recyclability test	CO ₂ photoreduction analysis system	Figure 6.8

6.2.5 In situ diffuse reflectance infrared Fourier transform spectroscopy (DRIFTS) analysis

To identify the intermediates formed during the adsorption process, in situ DRIFTS analysis were carried out in the Praying Mantis™ reaction chamber. The experimental procedures were similar to those in our previous studies.³⁷⁻³⁸ Firstly, the loaded samples were heated at 150 °C under the helium flow (30 mL/min) for 30 min. Then, the heater was switched off and a background spectrum was collected after chamber was cooled down to 25 °C. Subsequently, the helium gas flow was turned off, and CO₂/helium gas mixture (volume ratio: 1:9, 4 mL/min) was fed into the chamber after passing through a water bubbler. Meanwhile, the IR spectra were continuously recorded during the adsorption process.

6.3 Results and discussion

The morphology of a representative columnar TiO₂ thin film was characterized by FESEM (Figure 6.2a) and TEM (Figure 6.2b). As shown in Figure 6.2a, the TiO₂ film has a highly oriented 1D structure with a height of around 1 μm, and a typical column diameter of around 250 nm (Figure 6.2b). These highly oriented columnar structures significantly increase the effective surface area compared to a dense planar film, providing more active sites for CO₂ and H₂O adsorption as well as photocatalytic reactions.

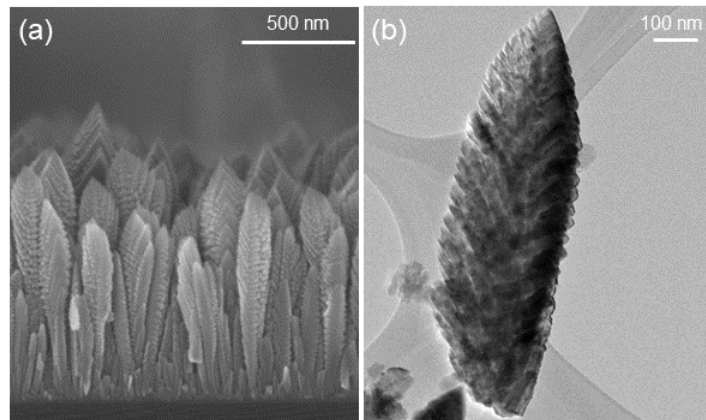


Figure 6.2 (a) SEM image and (b) TEM image of a typical columnar TiO₂ sample.

6.3.1 CO₂ photoreduction analysis

As reported in our previous work,³⁵ a series of background tests were conducted to confirm that any carbon-containing products in the effluent gas measured by GC originated from the photo-conversion of the CO₂ reactant, and not from the catalysts. The following three cases were tested: (1) CO₂ source gas only, no columnar TiO₂ nor glass fiber (the support for the samples) in the reactor, (2) CO₂ source gas with blank glass fiber in the reactor, and (3) N₂ source gas, columnar TiO₂ and glass fiber in the reactor. In all cases, no CO₂ conversion products (e.g., CO or CH₄) were detected whether the light was on or off. Therefore, if carbon-containing products were detected during the CO₂ photoreduction process when the columnar TiO₂ was placed in the reactor, then these products could only be from photo-conversion of the CO₂ source.

6.3.2.1 Effect of electric potential

CO₂ photoreduction results for columnar TiO₂ thin film on FTO substrates with different electric powers are shown in Figure 6.3a. Each experiment was repeated for three times and error bars are included. The resistance of a typical columnar TiO₂ thin film on a FTO substrate is about 25 Ω. The voltage was maintained from 2.5 V to 10 V to provide

currents in the range from 0.1 A to 0.4 A. The applied electric power can be calculated accordingly. In Figure 6.3a, the CO yield increases with an increase in electric power applied. The highest CO yield of the columnar TiO₂ thin film obtained with a power of 4 W was 375 μmol/g/hr (the apparent quantum efficiency is 0.045%, see Supporting Information, S5 for detailed calculations), which was about 4 times higher than that without electric potential (95 μmol/g/hr). The CO yield remained at a high value for the whole 8-hr experiment. The enhancement of CO yield by electric potential could be caused by the better separation of photo-generated electrons and holes due to enhanced movement under the electric field, but this mechanism needs further characterization.

6.3.2.2 Effect of substrate

Further investigation was conducted with columnar TiO₂ thin films on various substrates. Columnar TiO₂ on ITO substrate has a very large resistance (about 1 MΩ) due to the loss of conductivity of ITO coating material under high temperature (the synthesis temperature in the ACVD system is 773 K). As shown in Figure 6.3b, the CO yield of a columnar TiO₂ sample on ITO substrate is about 30 μmol/g/hr, which is relatively lower than that of a sample on FTO substrates. When 12 V was applied to the ITO sample, the electric power was still almost 0, and no significant enhancement was observed. It can be inferred that the substrates need to be conductive, then the applied electric potential can show enhancement in CO₂ photoreduction.

Figure 6.3b also shows the CO yield of columnar TiO₂ on SS substrate with different powers. The resistance of a typical sample on SS substrate is about 0.5 Ω. To provide a 0.4 A - 0.9 A current, less than 0.5 V was needed. There is only small difference in the CO yields among SS samples with different powers, which might be due to the

relatively lower power than that for FTO substrate. Due to the limitation of the current of the power supply, a current larger than 1 A cannot be achieved, and only lower than 0.5 V voltage can be applied. In the following material characterization section, the band gap energy of different TiO₂ samples were estimated to be in range 2.87-3.2 eV (Table 6.2). If voltage around or higher than the band gap energy of TiO₂ is applied, it may help more electrons be excited from valence band to conduction band under UV irradiation. Because the voltages applied to SS samples were all smaller than 0.5 V, this effect may not be significant. Therefore, the enhancement of electric potential added to SS samples on CO₂ photoreduction performance was not significant. It can be concluded that both the conductivity of the substrate and the voltage applied played an important role in CO₂ photoreduction. Because significant enhancement by electric potential was only observed in only FTO samples, these samples were used for the following study.

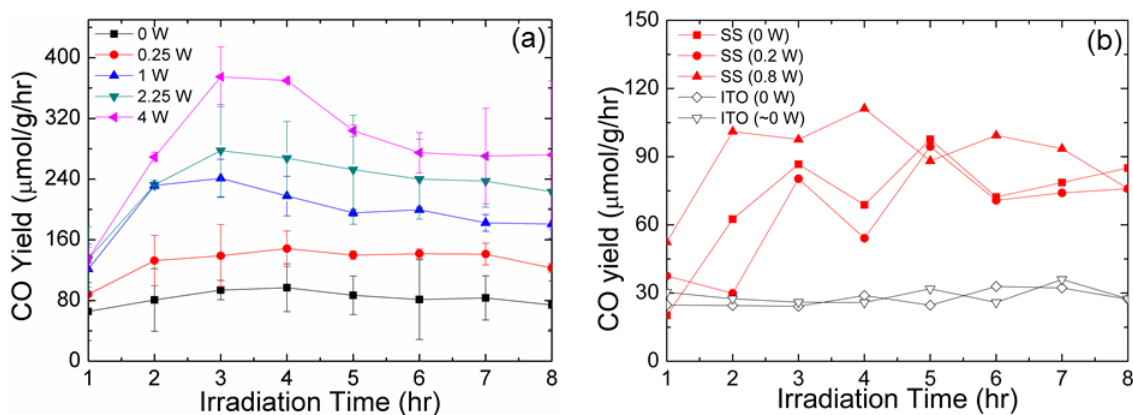


Figure 6.3 CO₂ photoreduction of columnar TiO₂ on (a) FTO substrate, (b) SS substrate and ITO substrate, with different electric powers. (Note: 0 W means no voltage applied; ~ 0 W means 12 V voltage applied, almost 0 A current, and 0 W power obtained.)

6.3.2 Characterizations of OTDs

It is worth noting that the color of the columnar TiO₂ thin film with electric potential changed from white to yellow during the CO₂ photoreduction process, as shown in the insets of Figure 6.4a and 6.4b. The yellow sample turned back to white when exposed to CO₂ under UV irradiation. To exclude the possibility of carbon-containing composites deposited on the TiO₂ surface that might cause the color change, the experiment was repeated in a helium (He). We still observed the change of color from white to yellow when UV irradiation and electric potential were simultaneously applied. However, in the He environment, the sample remained yellow with only UV irradiation. To investigate if similar color change can appear in the ambient environment, the experiment was also repeated in room air. Also, the white sample turned to yellow with simultaneous electric potential and UV irradiation, and the yellow sample became light with UV irradiation only. Because the color change of TiO₂ sample is normally due to the formation of OTDs (oxygen vacancy and Ti³⁺),³⁹⁻⁴⁰ we assume that OTDs might have formed in the columnar TiO₂ thin film under UV irradiation with the assistance of electric potential. In addition, these defects could also be gradually healed in oxygen rich environment, because the color of sample becomes lighter over time and was finally nearly white when the yellow sample was placed in an ambient environment for a very long time. And CO₂ photoreduction, which generates many active intermediates, can promote the healing of OTDs, because the yellow sample turned back to white in CO₂ environment under 8-hr UV irradiation.

To verify the hypothesized of formation of defects in columnar TiO₂ thin film, we performed material characterizations of the sample before and after the CO₂ photoreduction, with or without electric potential. Figure 6.4a and 6.4b show HRTEM

images of pristine columnar TiO_2 and columnar TiO_2 after CO_2 photoreduction with a 4 W electric power (denoted as 4W TiO_2), and Figure 6.4c and 6.4d show the related fast Fourier transform (FFT) analysis of these two samples, respectively. In both Figure 6.4a and 6.4b, a clear lattice pattern is observed with a single-crystal phase, and the measured inter-plane distance is 0.35 nm. However, crystalline defects can be seen in both images. Notably, the FFT image of the 4W TiO_2 shows fuzzier and more elongated dots,⁴⁰ compared to the relatively sharp dots of the pristine sample, which indicates the formation of defects in 4W TiO_2 . However, further crystalline structure and surface chemistry characterizations were needed.

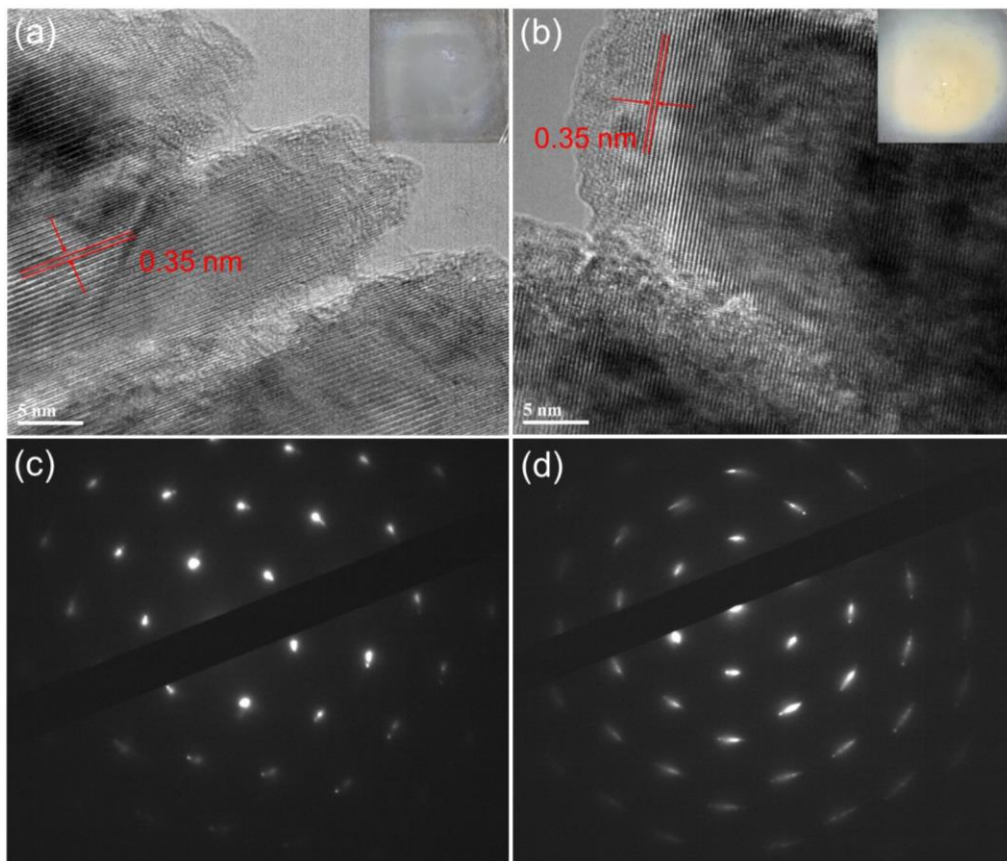


Figure 6.4 HRTEM images of (a) pristine TiO_2 (inset is the digital picture), (b) 4W TiO_2 (inset is the digital picture). FFT analysis of (c) pristine TiO_2 , and (d) 4W TiO_2 .

The XRD patterns of pristine TiO₂, 4W TiO₂, 4W TiO₂ after CO₂ photoreduction (denoted as 4W_postUV TiO₂), and TiO₂ after CO₂ photoreduction without electric potential (denoted as photo_only TiO₂) show almost the same pattern (Figure S6.4, Supporting Information, reference anatase TiO₂ is also included⁴¹). All the peaks in the XRD patterns exhibit characteristic features of pure crystalline anatase TiO₂. Furthermore, both the intensity and the full width at half maximum (FWHM) of the peaks in all these samples are also similar, which indicate that both the crystal structure and the crystallinity of the columnar TiO₂ did not change due to the UV irradiation or electric potential treatment.

As mentioned above (insets of Figure 6.4a and 6.4b), the color of the columnar TiO₂ changed to yellow during UV irradiation with electric potential, and the yellow sample turned back to white after the removal of electric potential (i.e., with UV irradiation only). The UV-vis absorption spectra of pristine TiO₂, TiO₂ after CO₂ photoreduction with 0.25 W electric power (denoted as 0.25W TiO₂), 1W TiO₂, 2.25W TiO₂, 4W TiO₂, 4W_postUV TiO₂, and photoreduced TiO₂ are shown in **Figure 5a**. For pristine TiO₂, no absorption was observed above 380 nm. TiO₂ samples treated with UV irradiation and electric potential exhibited a new absorption in the visible light region from 380-600 nm. The higher the electric power provided, the stronger the new absorption, which was in good agreement with the enhanced CO₂ photoreduction performance (Figure 6.3a).

In Figure 6.5a, the shift in the absorption edge suggests a change in the band gap energies of the TiO₂. To determine these band gap energies, a Tauc plot of the modified Kubelka-Munk function versus the energy of light absorbed is shown in **Figure 6.5b**.

Compared to pristine TiO₂, all samples treated with UV irradiation and electric potential exhibited reduced band gap energies, as shown in Table 6.2, and the 4W TiO₂ showed the lowest band gap energy of 2.87 eV, which is attributable to the possible existence of OTDs.⁴²⁻⁴⁴ These defects can create states in the band gap, which can potentially absorb sub-bandgap photon and affect the absorption spectrum, leading to a lower band gap energy than the defect-free samples.⁴⁵ It is interesting that the absorption spectrum of the 4W_postUV TiO₂ is almost same as that of the pristine TiO₂, which implies the healing of OTDs after CO₂ photoreduction. In addition, the spectrum of photo_only TiO₂ is also similar to that of pristine TiO₂, indicating both UV irradiation and electric potential are necessary to form OTDs in TiO₂.

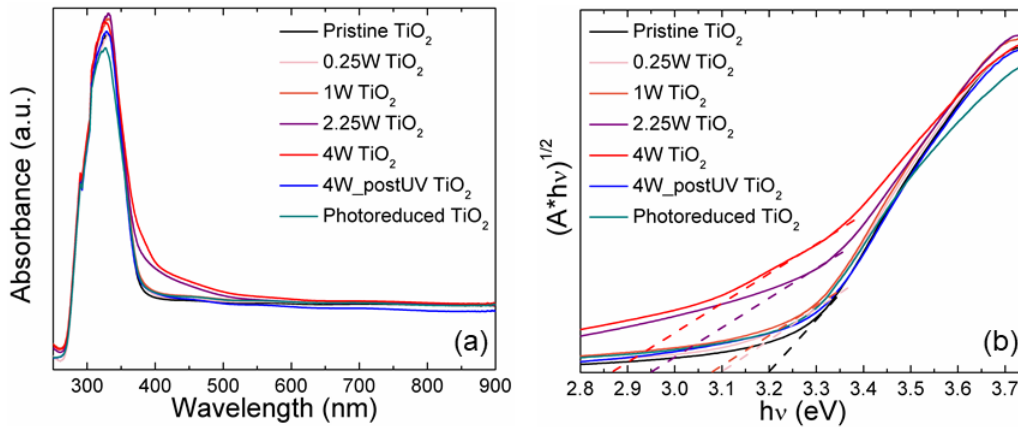


Figure 6.5 (a) UV-vis adsorption spectra and (b) Tauc's plot obtained for different columnar TiO₂ samples.

Table 6.2 Estimated band gap energies of different TiO₂ samples: pristine, 0.25 W, 1 W, 2.25 W, 4 W.

Sample	Estimated band gap energy (eV)
Pristine	3.20
0.25 W	3.13

1 W	3.11
2.25 W	2.95
4 W	2.87

Raman spectroscopy, a characterization technique to measure molecular vibrations, was employed to further detect the changes on the surface of the columnar TiO₂ thin film. As shown in Figure 6.6a, pristine TiO₂ shows three E_g modes (143 cm⁻¹, 198 cm⁻¹, and 639 cm⁻¹), a B_{1g} mode (399 cm⁻¹), and an A_{1g} mode (515 cm⁻¹), all of which are in good agreement with pure anatase TiO₂.⁴⁶ However, besides these peaks appearing in pristine TiO₂, the Raman peaks of the 4W TiO₂ are slightly noisier and two new peaks appear, at 448 cm⁻¹ and 605 cm⁻¹ (magnified Raman spectra in range of 300 to 800 nm, Figure 6.6b). It has been reported that oxygen vacancy can result in new weak modes at wavenumbers higher than 300 cm⁻¹.⁴⁷ These two peaks could not be assigned to any type of anatase Raman-active modes, which might result from formation of oxygen vacancy at the surface due to UV irradiation with electric potential. These two new peaks are weaker in the Raman spectrum of 4W_postUV TiO₂, which indicates the healing of oxygen vacancies after CO₂ photoreduction. Besides, the photo_only TiO₂ did not show these two new peaks, verifying that only the co-existence of UV irradiation and electric potential could cause the formation of oxygen vacancies. These results are consistent with the color change and the UV-vis adsorption results.

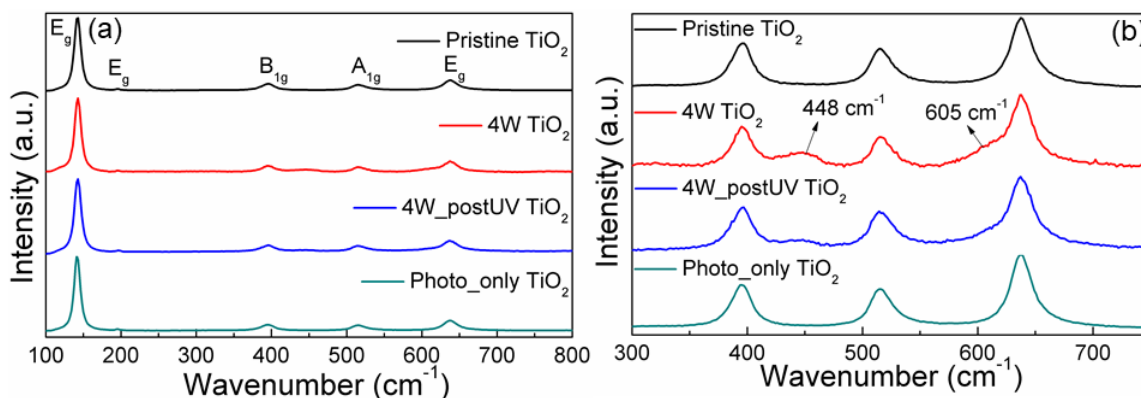


Figure 6.6 (a) Raman spectra and (b) magnified Raman spectra in range of 300 to 800 nm, of different columnar TiO₂ samples, including pristine TiO₂; 4W TiO₂; 4W_postUV TiO₂; photoreduced TiO₂.

Figure 6.7a shows the XPS spectra of the Ti 2p doublet region of the pristine, 4W, and 4W_postUV TiO₂. Compared with those of pristine and 4W_postUV TiO₂, the spectrum of 4W TiO₂ shows a slight shift to lower binding energy, indicating the presence of lower valance states of Ti.⁴⁰ Figure 6.7b, c, and d show the deconvolution of the peaks of pristine, 4W, and 4W_postUV TiO₂, respectively. The main sharp peaks of Ti 2p_{3/2}, located at 458.6 eV, and Ti 2p_{1/2}, at 464.3 eV, were assigned to Ti⁴⁺ in TiO₂. However, two small peaks appeared in the spectrum of 4W TiO₂, at 458.0 eV for Ti 2p_{3/2} and 464.0 eV for Ti 2p_{1/2}, which clearly verified the presence of Ti³⁺. The XPS results further demonstrate the formation of defects of Ti³⁺ in the columnar TiO₂ after UV irradiation with electric potential.

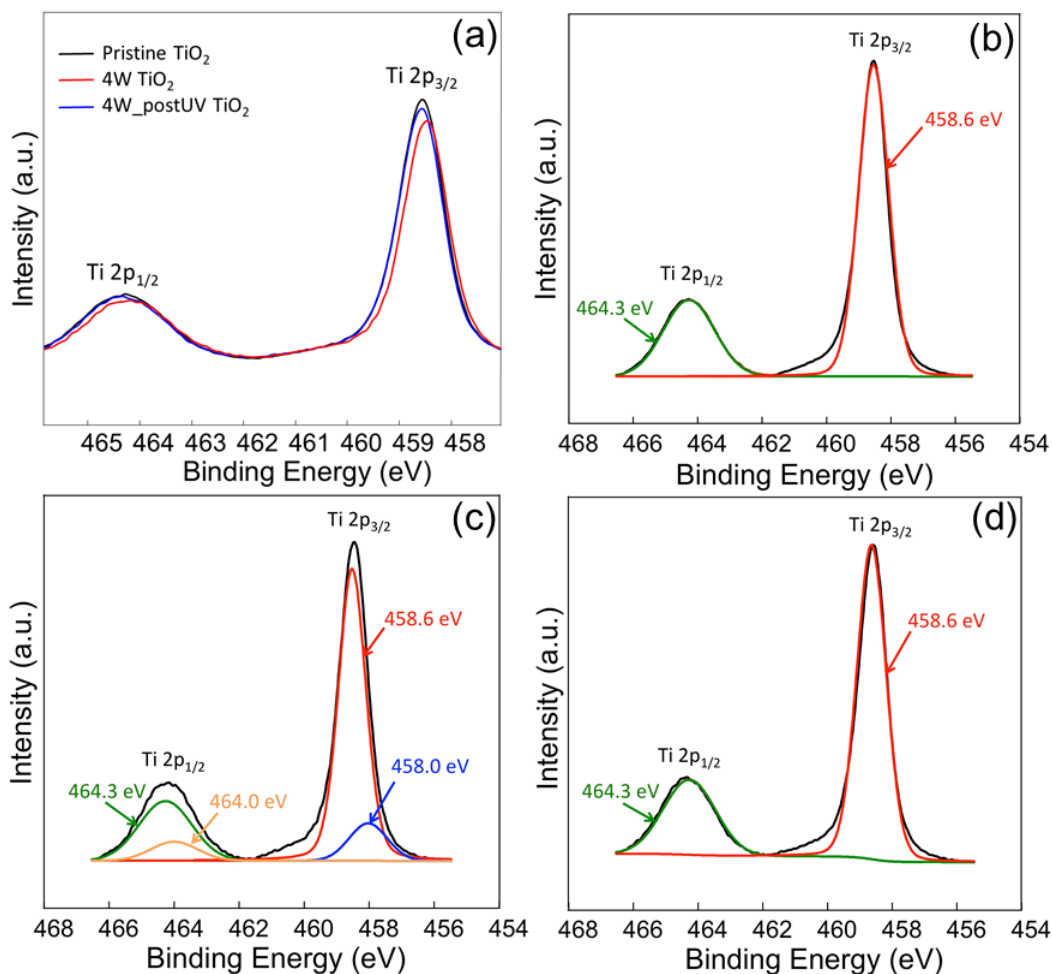


Figure 6.7 (a) Ti 2p XPS spectra of different columnar TiO₂ samples, including pristine TiO₂, 4W TiO₂, and 4W_postUV TiO₂. Deconvoluted Ti 2p XPS spectra of (b) pristine TiO₂; (c) 4W TiO₂; and (d) 4W_postUV TiO₂.

6.3.3 Recyclability test

To investigate the recyclability of the defective TiO₂, the same sample was used for the CO₂ photoreduction test with or without electric potential for several sequential cycles, and the results are shown in Figure 6.8. For example, in the first cycle, the electric power was kept at 4W, then it was turned off for the second cycle and on for the third cycle, and so on. Figure S6.5 (Supporting Information) shows digital pictures of the samples before and after each cycle. Whenever the electric potential was on, the CO yield stayed at a high

value and the sample became yellow. However, in the next cycle, without electric potential the CO yield dropped gradually, and the sample became white. It can be inferred that the formation of OTDs in the sample is reversible and that columnar TiO₂ can retain its high catalytic capability with the assistance of electric potential.

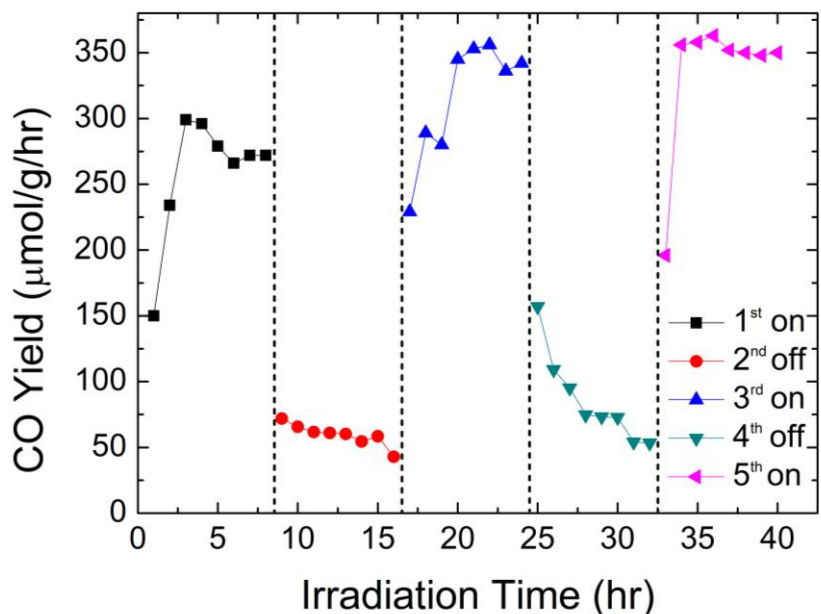


Figure 6.8 CO₂ photoreduction of the columnar TiO₂ for five cycles (1st 4W on; 2nd off; 3rd 4W on; 4th off; 5th 4W on).

6.3.4 Proposed mechanisms

As discussed in the introduction, there are several different approaches to forming defects in TiO₂. In most cases, high temperature treatment (generally above 400 °C) is needed to provide enough energy to form defects. The temperature in our reactor under different conditions was measured using a K-type thermal couple, with the following results: 1) UV + 4 W electric power, 92.8 °C; 2) UV only, 58.3 °C; and 3) 4 W electric power only, 66.8 °C. The temperatures in all the cases may not be high enough to activate the formation of defects. To verify this speculation, a heating taper was used to heat the

reactor to around 93 °C, no significant enhancement in CO₂ photoreduction and no color change of the sample was observed. The color change and OTDs status of TiO₂ samples under different conditions is summarized in Table 6.3. The possible reactions are listed below:

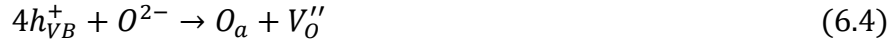
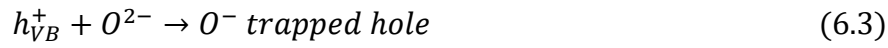
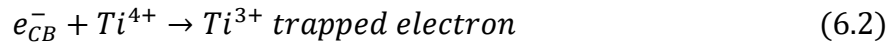


Table 6.3 Color change and OTDs status change of TiO₂ samples under different conditions.

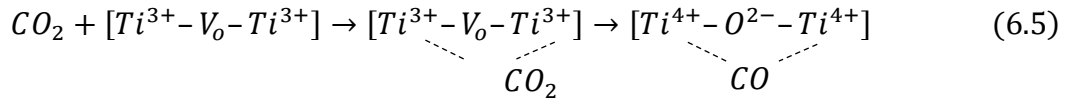
Fill gas	Light	Electric power	Other	Color change	OTDs status	Sample notation
CO ₂	On	Off	Heat to 93 °C	Keep white	No formation	
CO ₂	Off	4 W	N.A.	Keep white	No formation	
CO ₂	On	Off	N.A.	Keep white	No formation	Photo_only TiO ₂
CO ₂	On	0.25 W	N.A.	White to yellow	Formation	0.25W TiO ₂
CO ₂	On	1 W	N.A.	White to yellow	Formation	1W TiO ₂
CO ₂	On	2.25 W	N.A.	White to yellow	Formation	2.25W TiO ₂
CO ₂	On	4 W	N.A.	White to yellow	Formation	4W TiO ₂
CO ₂	On	Off	N.A.	Yellow to white	Recovery	4W_postUV TiO ₂

He	On	4 W	N.A.	White to yellow	Formation
He	On	Off	N.A.	Keep yellow	No recovery
Air	On	4 W	N.A.	White to yellow	Formation
Air	On	Off	N.A.	Lighter yellow	Partial recovery

TiO₂ can be photo-excited under UV irradiation to generate electrons in the conduction band and holes in the valance band. The electric potential can improve the separation of electrons and holes by increasing their mobility. The photo-generated electrons are trapped by Ti⁴⁺ in the lattice and reduce it to Ti³⁺. At the same time, the photo-generated holes are trapped by O²⁻ in the lattice and oxidize the O²⁻ to O[·], further oxidize it to atomic O_a with the assistance of electric potential in our study, leaving an oxygen vacancy (V_O'').

The mechanism of the enhanced CO₂ photoreduction performance with defective anatase TiO₂ was further analyzed by using in situ DRIFTS. In particular, CO₂ adsorption kinetics were obtained by plotting the areas of corresponding IR peaks (2340 and 2360 cm⁻¹)^{37-38, 48} as a function of adsorption time. As shown in Figure 6.9a, the capacity of defective TiO₂ to adsorb CO₂ is about five times higher than that of pristine TiO₂, which is attributable to enhanced interaction of CO₂ with the defective sites. In addition, the defective sites also have a substantial effect on intermediates formed during the adsorption process (Table 6.4 and Figures 6.9b-c). As exhibited in Figure 6.9b, the surface of pristine TiO₂ were dominated by carbonate (1325, 1498 and 1590 cm⁻¹) and bicarbonate (1402 cm⁻¹). While, more active intermediates were observed on the surface of defective TiO₂, such as formic acid (1710 and 1765 cm⁻¹). The existence of these active intermediates can

significantly facilitate the CO₂ photoreduction process.³⁷ The IR peak at 1825 cm⁻¹ can be assigned to bridge-bonded CO, which indicates that defective TiO₂ can reduce CO₂ to CO even without UV irradiation. Moreover, hydroxyl species (3596 and 3625 cm⁻¹) were also identified on the surface of defective TiO₂, which stems from the dissociation of water molecules during the adsorption process,³⁸ once again demonstrating high reactivity of defective TiO₂. The formation mechanism of the active intermediates during the CO₂ adsorption process are proposed as below:



To be specific, it has been verified that strong bonding can be formed between CO₂ and the bridging V_o sites,⁴¹ and the adsorbed CO₂ would be reduced to CO by oxidizing V_o to perfect site (Reaction (6.5)).⁴⁵ In addition, the existence of Ti³⁺ in the defective TiO₂ can activate adsorbed CO₂ to formic acid in the presence of protons (Reaction (6.7)). The formic acid is an active intermediate and can be reduced to CO by photo-generated electrons as shown below:

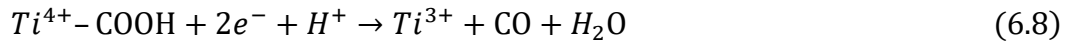


Table 6.4 Assignment of the IR bands

Wavenumber (cm ⁻¹)	Assignment	Ref.
1277	linear adsorbed CO ₂	49
1325	bidentate carbonate, b-CO ₃ ²⁻	37
1375	linear adsorbed CO ₂	49
1402	monodentate bicarbonate, m-HCO ₃ ⁻	50
1498	monodentate carbonate, m-CO ₃ ²⁻	51
1590	bidentate carbonate, b-CO ₃ ²⁻	52
1640	adsorbed water molecules	37
1710	formic acid	53
1765	formic acid	54
1825	bridge-bonded CO	55
3596	hydroxyl species	56
3625	hydroxyl species	38
3700	Fermi resonance of linear adsorbed CO ₂	57
3728	Fermi resonance of linear adsorbed CO ₂	57

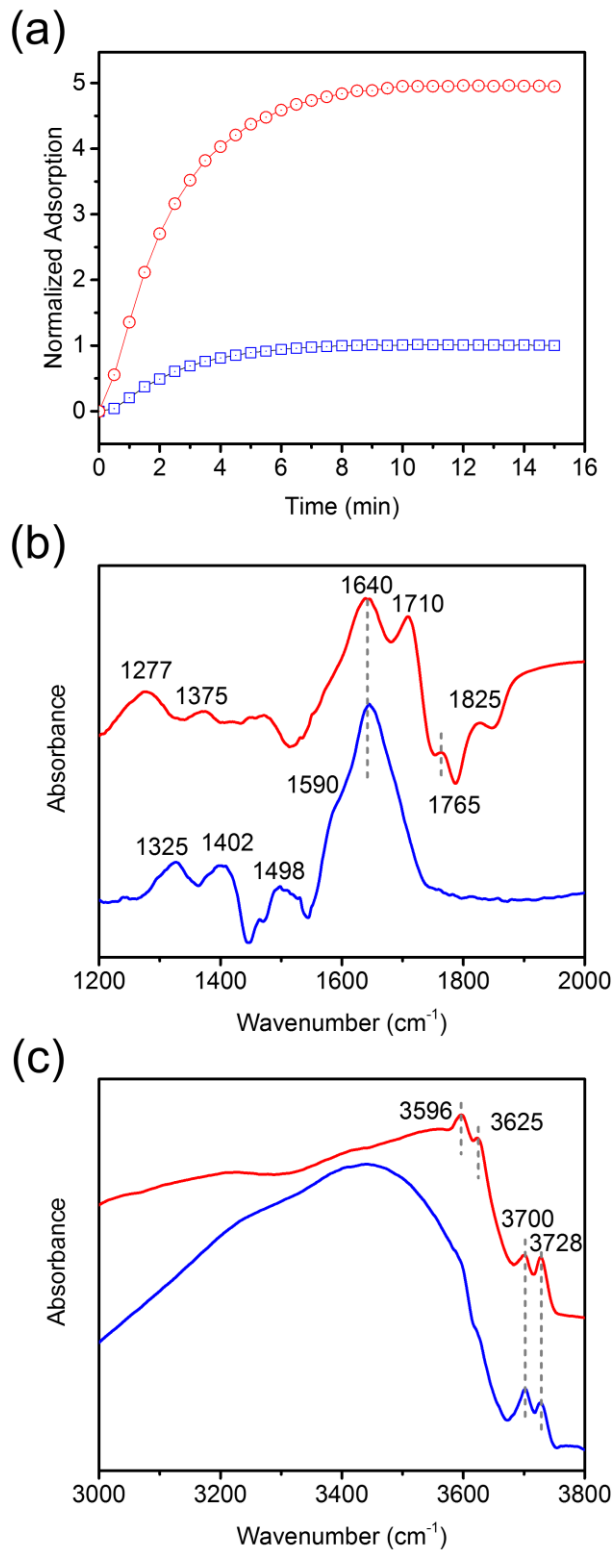


Figure 6.9 In situ DRIFTS analysis (red: defective TiO₂ (4W TiO₂), blue: pristine TiO₂): (a) CO₂ adsorption kinetics; (b) and (c) IR spectra obtained after adsorption for 15 min.

As the defective yellow sample would turn to white after CO₂ photoreduction, it can be inferred that the reaction (5), where CO₂ is reduced, and the V_o sites are healed, is also enhanced under UV irradiation. The overall formation and healing of OTDs and the CO₂ photoreduction mechanisms over the columnar TiO₂ thin films are shown in Figure 6.10.

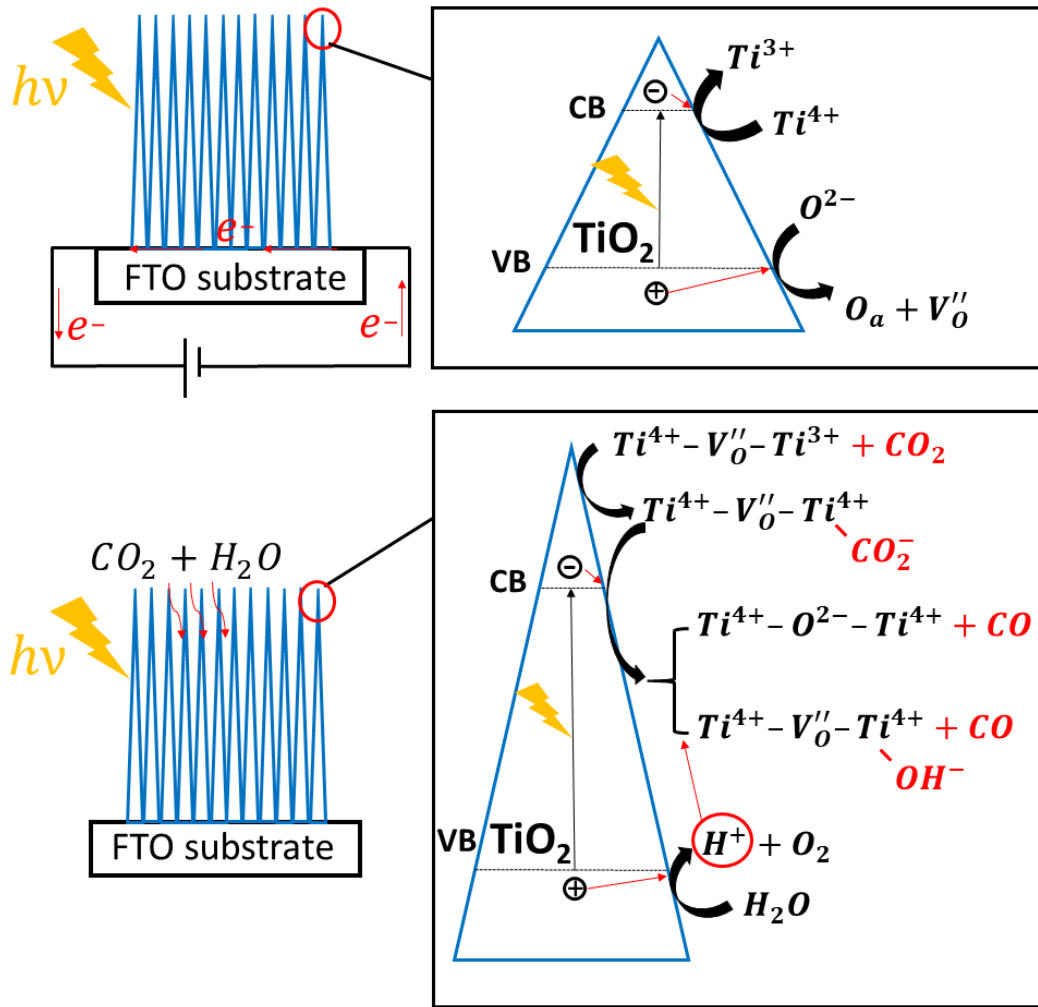


Figure 6.10 Schematic diagram of OTDs formation and healing and CO₂ photoreduction mechanism for the columnar TiO₂ with electric potential.

6.4 Conclusions

OTDs were generated in columnar TiO₂ thin film under UV irradiation with electric potential. The defective TiO_{2-x} showed a significant enhancement in CO₂ photoreduction. The effects on CO₂ photoreduction performance of the substrate, and electric power applied were investigated systematically. The best performing sample showed the highest CO yield of 375 μmol/g/hr, which was about 4 times higher than that without potential (95 μmol/g/hr). The formation of OTDs is reversible in CO₂ photoreduction, with or without electric potential. The formation and healing of OTDs were confirmed by the color change and HRTEM images, UV-vis adsorption, Raman spectroscopy, and XPS spectra analysis. The enhancement of the TiO_{2-x} in CO₂ photoreduction with electric potential can be attributed to 1) the narrowed band gap energy, 2) the enhanced CO₂ adsorption and molecule activation, and 3) the better separation of electrons and holes.

Acknowledgements

Y.N. thanks the McDonnell International Scholars Academy and the McDonnell Academy Global Energy and Environment Partnership (MAGEEP) for partial support of this work and through a fellowship to pursue a Ph.D. at Washington University in St. Louis. W.-N. W and X. H. thank the American Chemical Society Petroleum Research Fund (57072-DNI10) for financial support.

References

1. Roy, S. C.; Varghese, O. K.; Paulose, M.; Grimes, C. A., *Acs Nano* **2010**, 4 (3), 1259-1278.
2. Indrakanti, V. P.; Kubicki, J. D.; Schobert, H. H., *Energy Environ. Sci.* **2009**, 2 (7), 745-758.
3. Fujishima, A.; Zhang, X.; Tryk, D. A., *Surf. Sci. Rep.* **2008**, 63 (12), 515-582.
4. Carp, O.; Huisman, C. L.; Reller, A., *Prog. Solid State Chem.* **2004**, 32 (1), 33-177.
5. Xu, Y.; Schoonen, M. A., *Am. Mineral.* **2000**, 85 (3-4), 543-556.
6. Mao, J.; Ye, L.; Li, K.; Zhang, X.; Liu, J.; Peng, T.; Zan, L., *Appl. Catal., B* **2014**, 144, 855-862.
7. Hou, W.; Hung, W. H.; Pavaskar, P.; Goeppert, A.; Aykol, M.; Cronin, S. B., *ACS Catalysis* **2011**, 1 (8), 929-936.
8. Zhou, S.; Liu, Y.; Li, J.; Wang, Y.; Jiang, G.; Zhao, Z.; Wang, D.; Duan, A.; Liu, J.; Wei, Y., *Appl. Catal., B* **2014**, 158, 20-29.
9. Asahi, R.; Morikawa, T.; Irie, H.; Ohwaki, T., *Chem. Rev.* **2014**, 114 (19), 9824-9852.
10. An, W.-J.; Thimsen, E.; Biswas, P., *J. Phys. Chem. Lett.* **2009**, 1 (1), 249-253.
11. Wang, W.-N.; An, W.-J.; Ramalingam, B.; Mukherjee, S.; Niedzwiedzki, D. M.; Gangopadhyay, S.; Biswas, P., *J. Am. Chem. Soc.* **2012**, 134 (27), 11276-11281.
12. Liu, L.; Chen, X., *Chem. Rev.* **2014**, 114 (19), 9890-9918.
13. Liu, L.; Peter, Y. Y.; Chen, X.; Mao, S. S.; Shen, D., *Phys. Rev. Lett.* **2013**, 111 (6), 065505.
14. Teng, F.; Li, M.; Gao, C.; Zhang, G.; Zhang, P.; Wang, Y.; Chen, L.; Xie, E., *Appl. Catal., B* **2014**, 148, 339-343.
15. Shi, J.; Chen, J.; Feng, Z.; Chen, T.; Lian, Y.; Wang, X.; Li, C., *J. Phys. Chem. C* **2007**, 111 (2), 693-699.
16. Liu, H.; Ma, H.; Li, X.; Li, W.; Wu, M.; Bao, X., *Chemosphere* **2003**, 50 (1), 39-46.
17. Bak, T.; Nowotny, J.; Nowotny, M., *The Journal of Physical Chemistry B* **2006**, 110 (43), 21560-21567.
18. Polarz, S.; Strunk, J.; Ischenko, V.; Van den Berg, M. W.; Hinrichsen, O.; Muhler, M.; Driess, M., *Angew. Chem. Int. Ed.* **2006**, 45 (18), 2965-2969.

19. Wang, J.; Liu, P.; Fu, X.; Li, Z.; Han, W.; Wang, X., *Langmuir* **2008**, 25 (2), 1218-1223.
20. Lo, H.-H.; Gopal, N. O.; Ke, S.-C., *Appl. Phys. Lett.* **2009**, 95 (8), 083126.
21. Zheng, Z.; Huang, B.; Lu, J.; Wang, Z.; Qin, X.; Zhang, X.; Dai, Y.; Whangbo, M.-H., *Chem. Commun.* **2012**, 48 (46), 5733-5735.
22. Chen, X.; Liu, L.; Peter, Y. Y.; Mao, S. S., *Science* **2011**, 331 (6018), 746-750.
23. Wang, L.-Q.; Baer, D. R.; Engelhard, M. H.; Shultz, A. N., *Surf. Sci.* **1995**, 344 (3), 237-250.
24. Eriksen, S.; Egdell, R., *Surf. Sci.* **1987**, 180 (1), 263-278.
25. Wu, Q.; Zheng, Q.; van de Krol, R., *J. Phys. Chem. C* **2012**, 116 (12), 7219-7226.
26. Takata, T.; Domen, K., *J. Phys. Chem. C* **2009**, 113 (45), 19386-19388.
27. Panayotov, D. A.; Morris, J. R., *J. Phys. Chem. C* **2009**, 113 (35), 15684-15691.
28. Vedin, J. C.; Coudurier, G.; Millet, J.-M. M., *Catal. Today* **1997**, 33 (1-3), 3-13.
29. Thompson, T. L.; Yates, J. T., *Top. Catal.* **2005**, 35 (3), 197-210.
30. Liu, L.; Zhao, C.; Li, Y., *J. Phys. Chem. C* **2012**, 116 (14), 7904-7912.
31. Thimsen, E.; Rastgar, N.; Biswas, P., *J. Phys. Chem. C* **2008**, 112 (11), 4134-4140.
32. Mor, G. K.; Shankar, K.; Paulose, M.; Varghese, O. K.; Grimes, C. A., *Nano Lett.* **2005**, 5 (1), 191-195.
33. van de Krol, R.; Liang, Y.; Schoonman, J., *J. Mater. Chem.* **2008**, 18 (20), 2311-2320.
34. Aduda, B. O.; Ravirajan, P.; Choy, K.; Nelson, J., *Int J Photoenergy* **2004**, 6 (3), 141-147.
35. An, W.-J.; Jiang, D. D.; Matthews, J. R.; Borrelli, N. F.; Biswas, P., *J. Mater. Chem.* **2011**, 21 (22), 7913-7921.
36. Nie, Y.; Wang, W.-N.; Jiang, Y.; Fortner, J.; Biswas, P., *Catal. Sci. Technol.* **2016**, 6 (16), 6187-6196.
37. Lin, L.-Y.; Nie, Y.; Kavadiya, S.; Soundappan, T.; Biswas, P., *Chem. Eng. J.* **2017**, 316, 449-460.
38. Shah, M. W.; Zhu, Y.; Fan, X.; Zhao, J.; Li, Y.; Asim, S.; Wang, C., *Sci. Rep.* **2015**, 5, 15804.
39. Jiang, X.; Zhang, Y.; Jiang, J.; Rong, Y.; Wang, Y.; Wu, Y.; Pan, C., *J. Phys. Chem. C* **2012**, 116 (42), 22619-22624.

40. Nakamura, I.; Negishi, N.; Kutsuna, S.; Ihara, T.; Sugihara, S.; Takeuchi, K., *J. Mol. Catal. A: Chem.* **2000**, 161 (1), 205-212.
41. Mehta, M.; Kodan, N.; Kumar, S.; Kaushal, A.; Mayrhofer, L.; Walter, M.; Moseler, M.; Dey, A.; Krishnamurthy, S.; Basu, S., *J. Mater. Chem. A* **2016**, 4 (7), 2670-2681.
42. Breckenridge, R. G.; Hosler, W. R., *Physical Review* **1953**, 91 (4), 793.
43. Zhang, W.; He, Y.; Zhang, M.; Yin, Z.; Chen, Q., *J. Phys. D: Appl. Phys.* **2000**, 33 (8), 912.
44. Liu, G.; Li, F.; Wang, D.-W.; Tang, D.-M.; Liu, C.; Ma, X.; Lu, G. Q.; Cheng, H.-M., *Nanotechnology* **2007**, 19 (2), 025606.
45. Liu, L.; Zhao, H.; Andino, J. M.; Li, Y., *Acs Catalysis* **2012**, 2 (8), 1817-1828.
46. Lehn, J.-M.; Ziessel, R., *Proc. Natl. Acad. Sci. U. S. A.* **1982**, 79 (2), 701-704.
47. Freund, H.-J.; Roberts, M. W., *Surf. Sci. Rep.* **1996**, 25 (8), 225-273.

Chapter 6 Supporting Information

Table of Contents

S6.1 Schematics of ACVD system

S6.2 Schematic configurations to apply electric potential

S6.3 Light spectrum of the Xe lamp

S6.4 XRD patterns of FTO substrate and different columnar TiO₂ samples

S6.5 Apparent quantum efficiency calculation

S6.6 Digital pictures of the columnar TiO₂ before and after each cycle test.

S6.1 Columnar TiO₂ single crystals synthesized by aerosol chemical vapor deposition (ACVD)¹⁻²

ACVD method, was designed to synthesize metal oxide films with controlled morphologies including planar, columnar, and granular structures. Different synthesis conditions affect the characteristic times, such as residence time (τ_{res}), reaction time of the precursor (τ_{rxn}), sintering time (τ_{sin}), collision time (τ_{col}), and particle arrival time (t_{arv}) of the process. The relationship of these characteristic times determines the deposition regimes and film growth mechanisms and the final morphology of the film, which is detailed in our previous work (Figure S6.1).¹ Three different deposition regimes of vapor dominant, vapor-particle mixed, and particle dominant lead to planar, columnar and granular morphologies, respectively. In this study, synthesis conditions were controlled to form the vapor-particle mixed region where t_{arv} is similar or faster than τ_{sin} . Columnar TiO₂ thin films were obtained for further use.

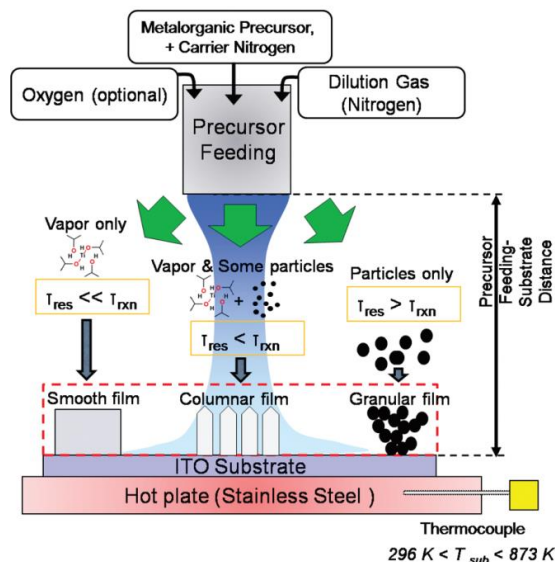


Figure S6.1 Schematic diagram of ACVD with three different deposition and film growth pathways.¹

S6.2 Schematic configurations to apply electric potential.

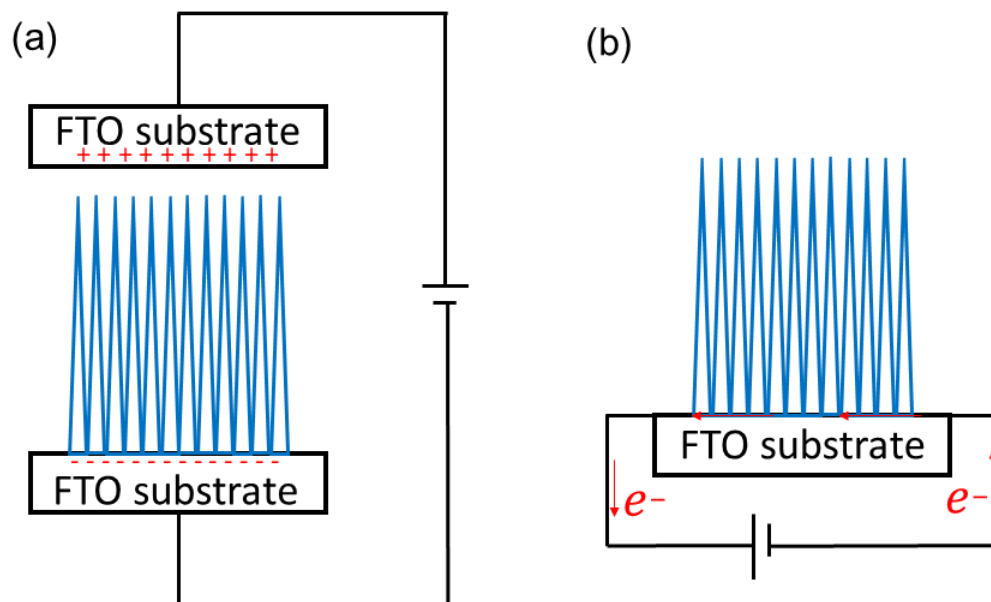


Figure S6.2 Schematic configurations to apply electric potential.

S6.3 Light spectrum of the Xe lamp.

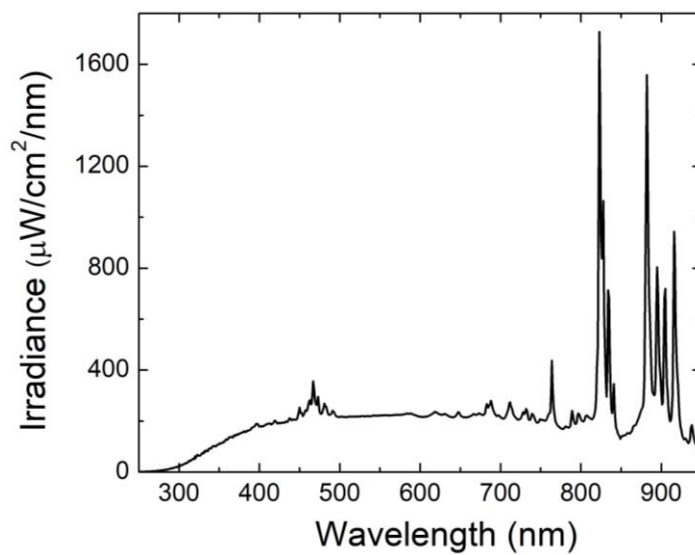


Figure S6.3 Light spectrum of the Xe lamp.

S6.4 XRD patterns of FTO substrate and different columnar TiO₂ samples, including pristine TiO₂; 0.4A TiO₂; 0.4A_postUV TiO₂; and photo-reduced TiO₂.

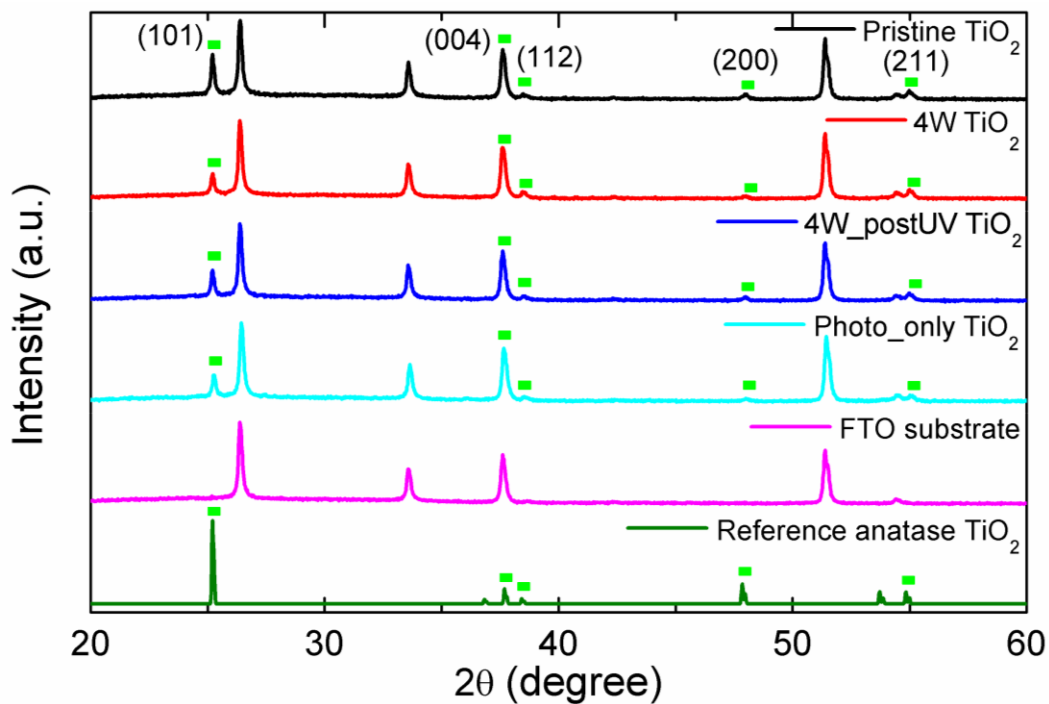


Figure S6.4 XRD patterns of FTO substrate and different columnar TiO₂ samples, including pristine TiO₂; 0.4A TiO₂; 0.4A_postUV TiO₂; and photo-reduced TiO₂.

S6.5 Apparent quantum efficiency calculation

The photoreduction performance can be characterized by the photochemical apparent quantum efficiency (quantum yield), ϕ , which is defined as a measure of the molar fraction of incident photons that result in CO₂ reduction products.³ In our case that CO is the product, ϕ can be calculated by the following equation:

$$\phi(\%) = \frac{2 \times \text{CO yield (mol)}}{\text{incident photon (mol)}} \times 100\% \quad (\text{S6.1})$$

The highest CO yield within the 8 hours UV irradiation was taken for calculation of quantum efficiency. The moles of incident photon were calculated using the following equation:

$$\text{incident photon (mol)} = \frac{\text{total incident energy}}{\text{average photon energy} \times N_A} \quad (\text{S6.2})$$

where N_A is the Avogadro's constant.

The photon energy at a certain wavelength can be calculated by:

$$E = \frac{hc}{\lambda} \quad (\text{S6.3})$$

where h , c and λ are Planck constant, speed of light and wavelength of light, respectively. As the band gap of 0.4A TiO₂ is 2.87 eV, the effective UV range is 250-433 nm. By integration the light spectrum (Fig. S2), the accumulated intensity in this effective UV range was calculated to be 17.5 mW/cm². The average photon energy can be estimated by averaging the photon energy from 250 to 433 nm.

The constants that were used for the calculations are listed as below:

Light intensity in the effective light range:	17.5 mW/cm ²
Deposited film side length (square):	1 inch (2.54 cm)
Average photon energy:	5.82×10 ⁻¹⁹ J
Yield of CO:	375 μmol/g/h
Mass of the catalyst used:	0.7 mg

Based on Eq. (1), the ϕ was calculated to be 0.045%.

S6.6 Digital pictures of the columnar TiO₂ before and after each cycle test.

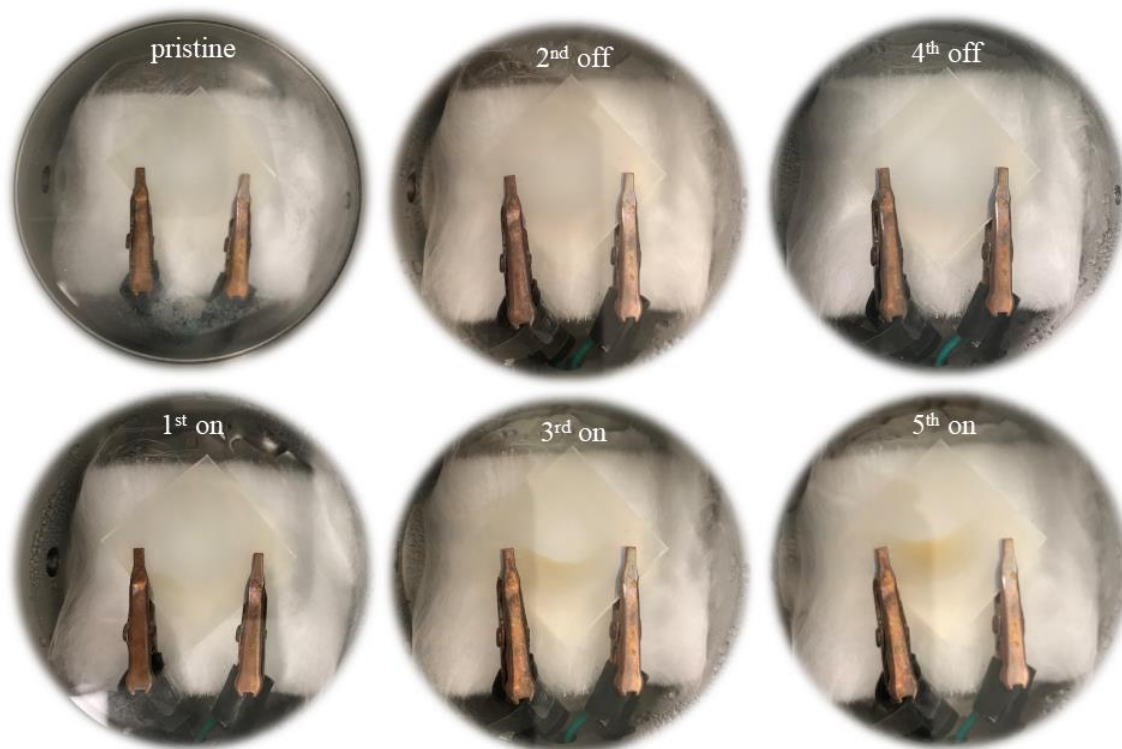


Figure S6.5 Digital pictures of the columnar TiO₂ before and after each cycle test.

Supplementary References

1. An, W.-J.; Thimsen, E.; Biswas, P., *J. Phys. Chem. Lett.* **2009**, 1 (1), 249-253.
2. An, W.-J.; Jiang, D. D.; Matthews, J. R.; Borrelli, N. F.; Biswas, P., *J. Mater. Chem.* **2011**, 21 (22), 7913-7921.
3. Morris, A. J.; Meyer, G. J.; Fujita, E., *Acc. Chem. Res.* **2009**, 42 (12), 1983-1994.

**Chapter 7 A Kinetic Model of Gas-Phase Photoreduction of
CO₂ over TiO₂ Thin Films with Different Morphologies in A
Continuous Flow Reactor**

To be submitted for publication, August 2018

Abstract

Columnar TiO₂ thin films were synthesized using an aerosol chemical vapor deposition (ACVD) method that we designed to deposit metal oxide thin films with controlled morphologies. The size and morphology of these thin films were characterized by SEM and AFM, and the optical absorption coefficient was calculated from the UV-Vis absorption spectrum. These thin films were used for gas-phase CO₂ photoreduction in a continuous flow reactor, and CO was the only reduction product detected by GC. A kinetic model was developed based on the mechanistic steps, including the photo-generation of electrons and holes, the adsorption of the reactants on the surface of the thin films, and reaction kinetics. Reaction rate constants were obtained by fitting the model with the experimental data. Predictions of the CO₂ photoreduction performance of the TiO₂ thin films with different morphologies and size parameters were made using the kinetic model with the calculated reaction rate constants. Both catalyst mass based CO yield and irradiation area based CO yield were discussed. The results of this study emphasize the strong effect of morphology and size parameters on photoactivity. Depending on morphology, the catalyst mass based CO yield and irradiation area based CO yield can have similar trends or different trends. This study offers new insights into designing the morphology of highly efficient CO₂ photoreduction catalysts.

7.1 Introduction

The increasing burning of fossil fuels is the main anthropogenic source of atmospheric carbon dioxide (CO₂), a major greenhouse gas.¹⁻² With global atmospheric CO₂ levels reaching 400 ppm,³ developing an approach that can not only reduce CO₂ emissions, but also convert CO₂ to valuable products, such as hydrocarbon fuels,⁴ is a significant environmentally-friendly and energy-saving step forward. In this regard, photoreduction of CO₂, which uses abundant solar energy and inexpensive coreactants (e.g., water), is a promising technique.⁵⁻⁷ However, the low conversion yield and quantum efficiencies, which result from a narrow light absorption spectrum and fast electron-hole recombination,⁸⁻⁹ still limit the broad application of CO₂ photoreduction beyond lab scale. To overcome these limitations, it is urgent to develop a highly efficient and low cost photocatalyst.

Titanium dioxide (TiO₂), a semiconductor which is commonly used as photocatalyst, shows great potential in CO₂ photoreduction, due to its low cost, and low toxicity,¹⁰ and high photo-corrosion resistance.¹¹ However, it has been reported that the synthesis conditions of TiO₂ can significantly affect its photoactivity, by altering its size, structure, and morphology.¹²⁻¹³ To both reduce cost and guide synthesis procedures, we need to predict the CO₂ photoreduction performance of TiO₂ with different sizes, structures and morphologies. Developing a simple but practical kinetic model of CO₂ photoreduction is the foundation that will ultimately enable such prediction.

Kinetic models of typical photocatalytic processes presented in the literature are usually for liquid phase reactions and continuous stirred-tank reactors (CSTRs).¹⁴⁻¹⁶ However, in this study, we focus on gas phase reactions and a mixed flow reactor (MFR).

The aerosol chemical vapor deposition (ACVD) technique,¹⁷⁻¹⁸ which can be used to synthesize TiO₂ thin films with dense, columnar and granular morphologies. Here, we employed ACVD to synthesize the synthesis of columnar TiO₂, then used scanning electron microscopy and atomic force microscopy for morphology and size characterization of the columnar TiO₂. Light absorption was examined by a UV-Vis spectrophotometer. CO₂ photoreduction experiments were conducted in a homemade continuous flow reactor, in which well mixed conditions were assumed.

In developing the kinetic model, we considered three aspects in the following order: 1) light activation, 2) surface adsorption of reactants and products, and 3) reaction kinetics. For light activation, the optical absorption coefficient of the columnar TiO₂ films was calculated from UV absorption spectrum experiments, and was used for other TiO₂ film morphologies, assuming similar light absorption properties. Concerning the surface adsorption of the reactants and products, the amount of available adsorption sites is the limitation and is a function of surface area. As reactions proceed, more sites are occupied by un-desorbed reaction intermediates and products, causing a plateau in the reaction rates. Thirdly, reaction kinetics were solved by assuming photostationary state of reaction intermediates. By combining these three factors, a CO yield rate model was developed, as a function of reaction rate constants as well as the morphology and size parameters of the TiO₂ thin films.

These reaction rate constants were estimated by fitting the model with the experimental data, and used to further predict the CO yield for TiO₂ thin films with different morphology and size parameters. Notably, both catalyst mass based CO yield ($Y_{CO,m}$) and irradiation area based CO yield ($Y_{CO,A}$) are important, when discussing the

photocatalytic capabilities of different catalysts, but these two values have not been fully compared. In this study, $Y_{CO,m}$ and $Y_{CO,A}$ were calculated in prediction the CO₂ photoreduction performance, and both similar and opposite trends were observed. The underlying mechanisms of the predicted CO yield trends for TiO₂ thin films with different morphologies were also discussed. This study offers new insights into designing the morphology of highly efficient CO₂ photoreduction catalysts.

7.2 Experimental methods

7.2.1 Material synthesis

In our previous studies,¹⁷⁻¹⁸ an ACVD system was used to synthesize TiO₂ thin films with different morphologies, including dense, columnar, and granular. In this study, columnar TiO₂ thin films were synthesized by ACVD and used for material characterization and CO₂ photoreduction performance testing. In the synthesis, titanium tetraisopropoxide (TTIP, 97%, Sigma-Aldrich) was used as a precursor and loaded in a homemade bubbler at a constant temperature of 297 K. Fluorine-doped tin oxide (FTO)-coated glass slides (1 inch × 1 inch) were used as deposition substrates, and maintained at 773 K for all samples. The flow rate of N₂ carrier gas entering the bubbler was controlled at 0.45 L per minute (lpm), which was equivalent to 1.46 μmol/min of TTIP fed into the reactor. The total flow rate, including the dilution flow, was 0.9 lpm, which corresponded to 20 ms of TTIP residence time. For all samples, the total deposition time was fixed at 50 min. The mass of each thin film sample, deposited over a one-inch wide circle area directly beneath the nozzle, was measured to be 0.7 mg.

7.2.2 Material characterization

Detailed characterizations of the TiO₂ thin films with different morphologies can be found in our previous papers.¹⁷⁻¹⁹ Here, we report only some basic characteristics of the columnar TiO₂ thin film which was used in the following model fitting. The morphology of the columnar TiO₂ thin films was examined by field emission scanning electron microscopy (FE-SEM, NOVA NanoSEM 230, FEI Co.) and atomic force microscopy (AFM, Dimension 3100 Nanoman, Veeco Instruments, Inc.). The light transmission spectrum was measured using a UV-Vis spectrophotometer (Varian Bio 50).

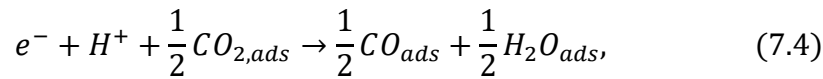
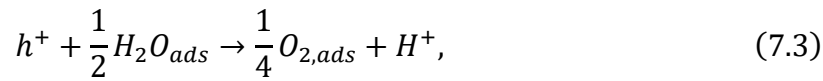
7.2.3 CO₂ photoreduction analysis

The photoreduction analysis system was reported in detail in our previous publications,¹⁹⁻²¹ and is briefly described here. The gaseous mixture was introduced into a homemade continuous flow reactor where the columnar TiO₂ thin film samples were loaded. The reactor was cylindrical, with a top quartz window vertically facing the light source, which was a Xe lamp (Oriel 66021, Newport Co.) operating at 450 W (the light spectrum was measured by a spectroradiometer (ILT-900R, Polytec GmbH). The concentrations of effluent gases (CO₂, CO, CH₄, O₂, and N₂) as a function of irradiation time were recorded automatically by gas chromatography (GC, 6895N, Agilent Technologies, Inc.) through an automated gas valve, using helium as the carrier gas. The GC was equipped with a PLOT capillary column (Supelco Carboxen-1010) and a thermal conductivity detector (TCD).

7.3 Model development

In heterogeneous photocatalysis of CO₂ on TiO₂, the mechanism usually includes a set of complicated steps. First, TiO₂ needs to be activated by absorbing light energy (E_{hv})

equal to or higher than its bandgap (E_g) (3.2 eV for anatase TiO_2). Electrons and holes are formed in the conduction band (CB) and valence band (VB) separately, due to the photoexcitation, as shown in Eqn. (7.1). These electrons and holes can recombine, generating only heat, Eqn. (7.2). The holes can also react with adsorbed H_2O to oxidize it to O_2 , generating H^+ at the same time, Eqn. (7.3). Meanwhile, electrons, together with the generated H^+ , can reduce adsorbed CO_2 to a set of products. In our case, only CO was detected and is considered here in Eqn. (7.4). A simplified reduction scheme is shown in Figure 7.1, and the related reaction equations are



where the subscript *ads* represents the adsorbed species on the surface of the catalysts.

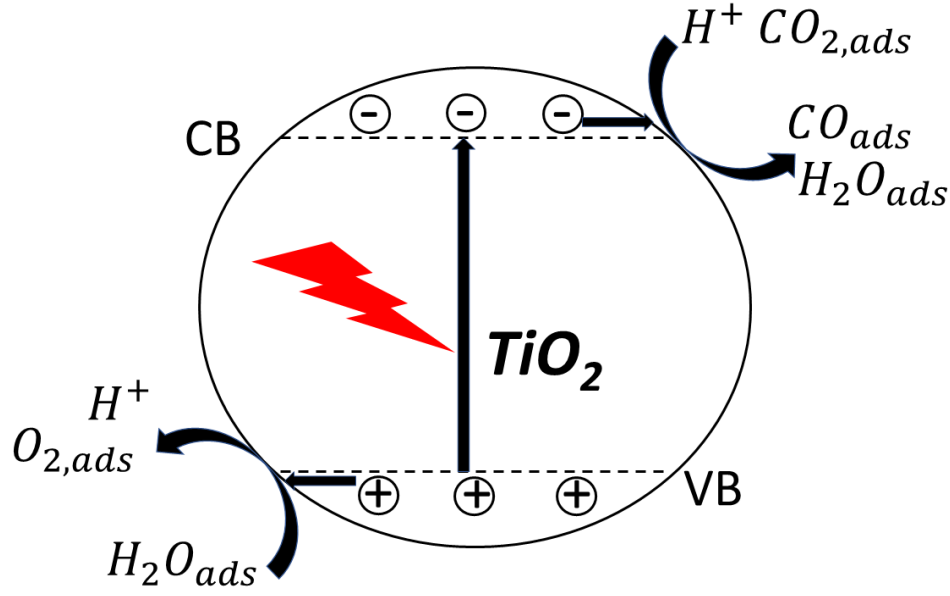


Figure 7.1 Reaction scheme of an illuminated TiO₂ particle.

To simplify the model that describes the CO production rate with a reasonable number of fitting parameters, three basic assumptions were made: 1) Only the recombination of electrons and holes that occurs at the surface of the catalysts is considered, and the bulk recombination is negligible;²² 2) The surface of the catalyst is totally accessible for all the reactants, without any diffusion limitation through the pores; and 3) The incident light source is from the collimated light source, and it decays only as it penetrates the catalyst film.

7.3.1 Light-induced generation of electron and hole pairs

To solve for the CO production rate, the first step is to calculate the total generation rate of electrons and holes, g . The generation rate of electrons and holes is dependent on the incident light profile and the optical and physical properties of the TiO₂ thin films, and the equation is given by Butler²³

$$g(x, \lambda) = k_1 I_0(\lambda) \alpha(\lambda) \exp(-\alpha(\lambda)x). \quad (7.5)$$

Here, k_1 is reaction rate constant in Eqn (7.1) (mol W^{-1}), $I_0(\lambda)$ is the incident light profile at a certain wavelength ($\text{W m}^{-2} \text{ nm}^{-1}$), α is the optical absorption coefficient of the catalyst film (m^{-1}), x is the depth into the catalyst film (m), and λ is the wavelength of the incident light (nm). The optical absorption coefficient α is calculated as a function of the wavelength for columnar TiO_2 , using the following equation:²⁴

$$\alpha(\lambda) \approx \frac{1}{d_F} \ln\left(\frac{1}{T(\lambda)}\right), \quad (7.6)$$

where d_F is the thickness of the catalyst film (m), and T is its transmittance, measured experimentally (%). The optical absorption coefficient α is assumed to be the same for TiO_2 thin film with different morphologies and used as a known parameter in the following calculations.

For the whole catalyst film, the total rate of electron-hole generation by light with a specific wavelength can be calculated from Eqn. (7.5) by integration over the thickness of the film:

$$g(\lambda) = I_0(\lambda) - I_0(\lambda) \exp(-\alpha(\lambda)d_F). \quad (7.7)$$

To obtain the total generation rate, $g(\lambda)$ should be integrated over the wavelengths below 380 nm (the longest wavelength to active anatase TiO_2) in the spectrum of the lamp:

$$g = \int_{\lambda_1}^{\lambda_2} g(\lambda) d\lambda, \quad (7.8)$$

where λ_1 is the shortest wavelength in the spectrum of the lamp, and λ_2 is 380 nm.

7.3.2 Adsorption of reactants and products on the accessible surface of TiO_2

All the reactants must be first adsorbed onto the surface of the TiO_2 thin film to further participate in the reactions. In addition, the products of the reactions are first adsorbed on the surface and then desorbed into the gas phase. Therefore, CO_2 , H_2O , CO ,

and O_2 are competing for the limited adsorption sites on the surface of the TiO_2 film. Because this is a CO_2 -and H_2O -saturated environment, all the available adsorption sites are assumed to be occupied by one of these four species:

$$[CO_{2,ads}] + [H_2O_{ads}] + [CO_{ads}] + [O_{2,ads}] = C_{tot}A_s, \quad (7.9)$$

where $[CO_{2,ads}]$, $[H_2O_{ads}]$, $[CO_{ads}]$, and $[O_{2,ads}]$ represent the total amount of the corresponding specie adsorbed on the surface of the catalyst (mol), C_{tot} is the concentration of all the available adsorption sites on the surface of the catalyst ($mol\ m^{-2}$), and A_s is the surface area of the catalyst (m^2).

The relationship between the adsorption species and their corresponding species in gas phase should satisfy the following adsorption equilibrium equations

$$[CO_{2,ads}] = k_{CO_2}P_{CO_2}, \quad (7.10)$$

$$[H_2O_{ads}] = k_{H_2O}P_{H_2O}, \quad (7.11)$$

$$[CO_{ads}] = k_{CO}P_{CO}, \quad (7.12)$$

$$[O_{2,ads}] = k_{O_2}P_{O_2}, \quad (7.13)$$

where P_{CO_2} , P_{H_2O} , P_{CO} , and P_{O_2} are the partial pressures of the certain species (Pa), and k_{CO_2} , k_{H_2O} , k_{CO} , k_{O_2} are the specific adsorption constants ($mol\ Pa^{-1}$).

Because P_{CO} and P_{O_2} were monitored by GC over the irradiation time, and P_{CO} and P_{O_2} were found to follow a similar trend, it is assumed that

$$P_{O_2} = mP_{CO}, \quad (7.14)$$

where m is a constant.

Because the feed rate of H₂O and CO₂ is fixed, the reactor is saturated with H₂O and CO₂, and the conversion of CO₂ and H₂O is very low, the ratio of P_{CO_2} and P_{H_2O} are assumed to a constant. Then $[CO_{2,ads}]$ and $[H_2O_{ads}]$ can be represented by P_{CO} :

$$[CO_{2,ads}] = \frac{C_{tot}A_s - k_{CO}P_{CO} - k_{O_2}mP_{CO}}{1 + \frac{k_{H_2O}P_{H_2O}}{k_{CO_2}P_{CO_2}}}, \quad (7.15)$$

$$[H_2O_{ads}] = \frac{C_{tot}A_s - k_{CO}P_{CO} - k_{O_2}mP_{CO}}{1 + \frac{k_{CO_2}P_{CO_2}}{k_{H_2O}P_{H_2O}}}. \quad (7.16)$$

7.3.3 Photostationary state assumption for the reaction intermediates

Assuming the reactions reach photostationary state on the whole surface of the catalyst, then the following equations are obtained:

$$\frac{d[e^-]}{dt} = gA_L - k_2C_e-C_h+A_s^2 - k_4C_e-C_H+A_s^2\sqrt{[CO_{2,ads}]} \approx 0, \quad (7.17)$$

$$\frac{d[h^+]}{dt} = gA_L - k_2C_e-C_h+A_s^2 - k_3C_h+A_s\sqrt{[H_2O_{ads}]} \approx 0, \quad (7.18)$$

$$\frac{d[H^+]}{dt} = k_3C_h+A_s\sqrt{[H_2O_{ads}]} - k_4C_e-C_H+A_s^2\sqrt{[CO_{2,ads}]} \approx 0, \quad (7.19)$$

in which $[e^-]$, $[h^+]$, and $[H^+]$ are the total amounts of the photo-generated electrons, holes, and protons on the surface of the catalyst (mol). C_e^- , C_{h^+} and C_{H^+} is the corresponding surface concentrations (mol m⁻²), A_L is the irradiation area (m²), k_2 is the reaction rate constant of reaction (2) (mol⁻¹ s⁻¹), k_3 is the reaction rate constant of reaction (3) (mol^{-1/2} s⁻¹), and k_4 is the reaction rate constant of reaction (4) (mol^{-3/2} s⁻¹).

To simplify the calculation, C_{H^+} is assumed to be a constant for a given catalyst in a CO₂ and H₂O saturated environment. The reaction rate constants are re-denoted as

$$k'_3 = k_3\sqrt{[H_2O_{ads}]}, \quad (7.20)$$

$$k'_4 = k_4 C_{H^+} \sqrt{[CO_{2,ads}]}. \quad (7.21)$$

Eqn. (7.17) and Eqn. (7.18) are used to derive an expression for the surface concentration of the photo-generated electrons C_{e^-} , and a quadratic expression is obtained as

$$\frac{k_2 k'_4 A_s^3}{k'_3} C_{e^-}^2 + k'_4 A_s^2 C_{e^-} - g A_L \approx 0. \quad (7.22)$$

Solve Eqn. (7.22) for C_{e^-} , and Eqn. (7.23) is obtained

$$C_{e^-} = \frac{\sqrt{(k'_3 k'_4 A_s^2)^2 + 4k_2 k'_4 A_s^3 g A_L} - k'_3 k'_4 A_s^2}{2k_2 k'_4 A_s^3}. \quad (7.23)$$

7.3.4 CO yield rate as a function of different reaction parameters

The generation rate of $[CO_{ads}]$ can be obtained from reaction (7.4) as

$$\frac{d[CO_{ads}]}{dt} = \frac{1}{2} k'_4 C_{e^-} A_s^2. \quad (7.24)$$

By substituting Eqn. (7.23) into Eqn. (7.24), Eqn. (7.25) is obtained

$$\frac{d[CO_{ads}]}{dt} = \frac{\sqrt{(k'_3 k'_4 A_s)^2 + 4k_2 k'_4 A_s g A_L} - k'_3 k'_4 A_s}{4k_2}. \quad (7.25)$$

Then substituting Eqn. (7.12) into Eqn. (7.25), Eqn. (7.26) is obtained

$$\frac{dP_{CO}}{dt} = \frac{\sqrt{(k'_3 k'_4 A_s)^2 + 4k_2 k'_4 A_s g A_L} - k'_3 k'_4 A_s}{4k_2 k_{CO}}. \quad (7.26)$$

To calculate the CO yield rate per catalyst mass, $Y_{CO,m}$ (mol g⁻¹ hr⁻¹), the ideal gas law is used

$$Y_{CO,m} = \frac{P_{CO} v}{RTM}, \quad (7.27)$$

in which v is the flow rate of the feed gas that passes through the reactor (L min^{-1}), R is the ideal gas law constant ($\text{J mol}^{-1} \text{K}^{-1}$), T is the temperature in the reactor (K), and M is the mass of the catalyst (g).

In some situations, the CO yield rate per irradiation area, $Y_{CO,A}$ ($\text{mol g}^{-1} \text{m}^{-2}$), is also an important factor indicating the efficiency of the catalyst, and it can easily be deduced from $Y_{CO,m}$:

$$Y_{CO,A} = Y_{CO,m} \frac{M}{A_L}. \quad (7.28)$$

7.4 Results and discussions

7.4.1 Material characterizations

The morphology of a representative columnar TiO_2 thin film was characterized by FESEM (Figure 7.2a), and AFM (Figure 7.2b). As shown in Figure 7.2a, the TiO_2 film has a highly oriented 1D structure with a height of around $1.1 \mu\text{m}$, which is consistent with the AFM observation, and the diameter of a typical column diameter is around 250 nm . The AFM image presents a top view of the thin film, where individual columns can also be identified. These separate columnar structures significantly increase the surface area compared to a dense film with the same height, providing more active sites for CO_2 and H_2O adsorption, and for photocatalytic reactions.

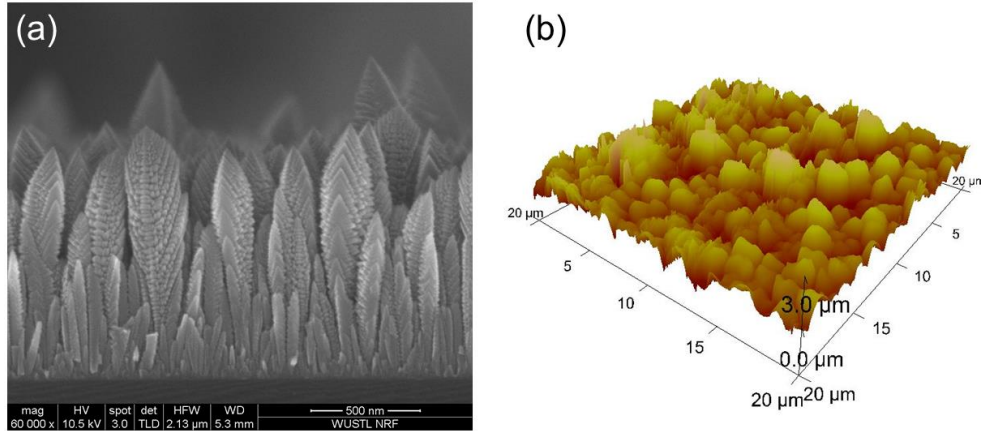


Figure 7.2 (a) SEM and (b) AFM images of a typical columnar TiO₂ thin film.

Figure 7.3a and 7.3b present respectively the incident light intensity spectrum and the light transmission spectrum of a representative columnar TiO₂ thin film. The incident light has a broad spectrum from 250 to 950 nm, and the TiO₂ thin film has a significant absorption peak from 280 to 410 nm. These experimental data were used to calculate the optical absorption coefficient α and the total electron-hole generation rate g , using Eqns. (7.6), (7.7), and (7.8). With all these known data substituted in, g is a function of the thickness of only the thin film d_F .

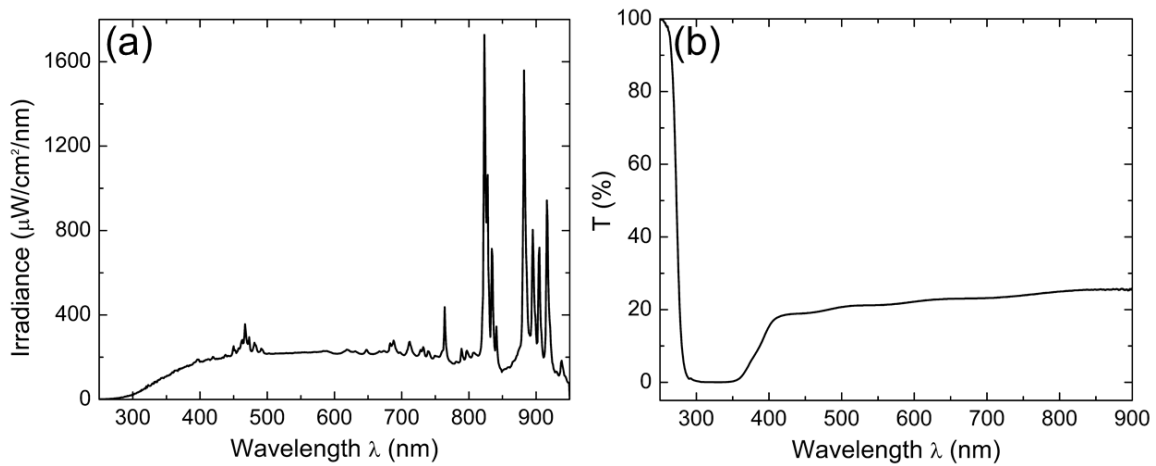


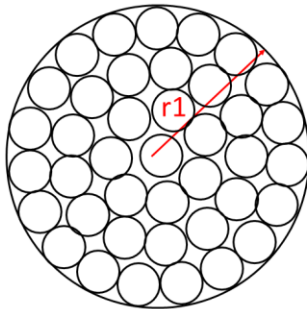
Figure 7.3 (a) Incident light intensity spectrum. (b) Light transmission spectrum of a typical TiO₂ thin film.

7.4.2 Model parameters of TiO₂ thin films with different morphologies

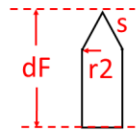
In addition to d_F , the surface area A_S and the projection area towards the light A_L have important effects on the photocatalytic performance, as shown in Eqn. (7.27). For TiO₂ thin films with different morphologies, A_S and A_L are dependent on different parameters, and the calculation methods are different. Figure 7.4 shows schematic diagrams of the top view and the side view of different TiO₂ thin films, where different parameters considered in the model are presented.

(a) Columnar film

Top view

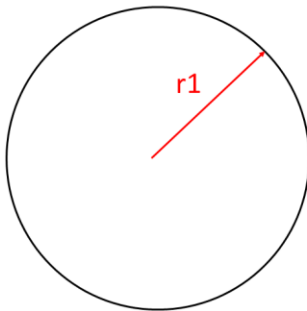


Side view of one column

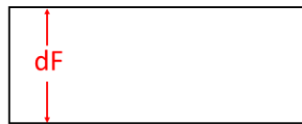


(b) Dense film

Top view

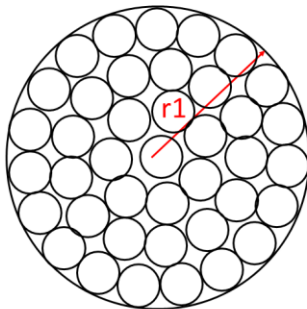


Side view



(c) Granular film

Top view



Side view

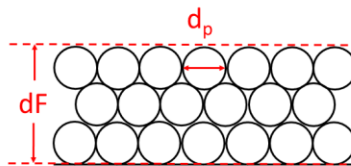


Figure 7.4 Schematic diagram of top and side views of TiO_2 thin films with different morphologies: (a) columnar film, (b) dense film, and (c) granular film.

7.4.2.1 Columnar film

For columnar film, which we used in this study, a hexagonal packing arrangement ($\eta_1 = \frac{\pi}{\sqrt{12}} \approx 0.9069$)²⁵ of the individual columns is assumed. Three parameters of a single column are labeled: the radius r_2 (nm), the top cone taper length s (nm), and the height d_F (μm) (same as the thickness of the film) (Figure 7.4a). The equations to calculate the irradiation area A_L , surface area A_S , and the total mass M of the columnar film are derived and shown in Supporting Information.

7.4.2.2 Dense film

From Figure 7.4b, the only varying parameter for different dense films is the thickness, d_F , and the corresponding A_L , A_S , and M are discussed in Supporting Information.

7.4.2.3 Granular film

Figure 7.4c shows the top view and side view of a granular film, and a 3D hexagonal packing arrangement ($\eta_2 = \frac{\pi}{3\sqrt{2}} \approx 0.7405$)²⁶ is assumed for the primary particles. Two parameters are labeled: the thickness of the film d_F , and the diameter of the primary particle, d_p (nm). Hence, the corresponding A_L , A_S and M can be calculated and the details are shown in Supporting Information.

7.4.3 Solving for the reaction parameters by fitting the model with experimental data

From the material characterization discussed above, $d_F = 1.1 \mu m$, $r_2 = 125 nm$, $s = 250 nm$, and $M = 0.7 mg$ for a typical columnar TiO_2 thin film sample used for a CO_2 photoreduction test. Then A_L and A_S can be calculated using Eqns. (S7.1) and (S7.4),

and substituted into Eqn. (7.27). By numerically fitting Eqn. (7.27) using the experimental data, the involved reaction constants can be estimated. A comparison of the experimental and model results is shown in Figure 7.5. The experimental data presents a slight decrease after 4 hr, while the model data shows a plateau, which might be from the build-up of diffusion limitation and the gradual de-activation of the catalyst with time (not included in the model). Except for this, the model shows a good match with the experimental data. These simulated reaction parameters are used for the following predictions of the photocatalytic performance of different TiO₂ thin films.

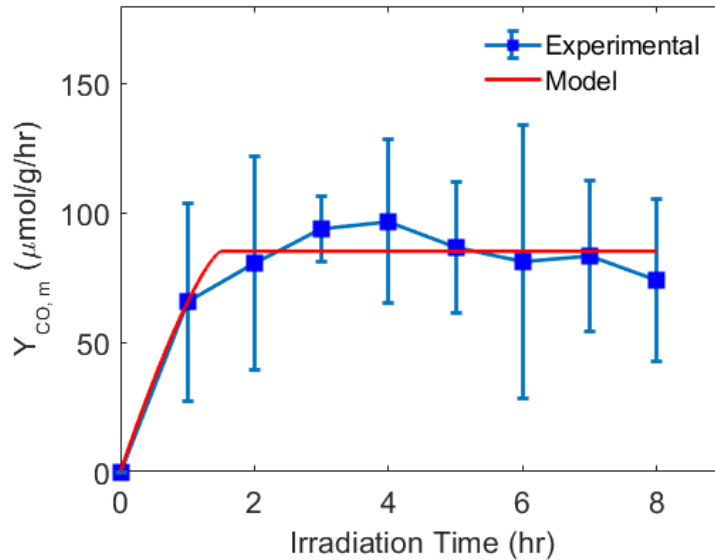


Figure 7.5 Fitting of the kinetic model with the experimental data.

7.4.4 CO₂ photoreduction predictions of TiO₂ thin films with different morphologies

7.4.4.1 Columnar film

The CO₂ photoreduction performance of columnar TiO₂ thin films with different r_2 , s , and d_F is shown in Figure 7.6. By comparing Figure 7.6(a) and 7.6(b), Figure 7.6(c) and 7.6(d), and Figure 7.6(e) and 7.6(f), the difference in $Y_{CO,m}$ and $Y_{CO,A}$ can be clearly seen. For $Y_{CO,m}$, the effect of different parameters follows the order $r_2 > s > d_F$. Here, r_2

has an increase from 25 nm to 300 nm, with a step size of 25 nm in the model prediction, and r_2 was measured to be 125 nm in the experimental test. With decreasing r_2 , $Y_{CO,m}$ increases significantly, especially in the small r_2 range. The range of s in the model prediction is from 50 nm to 1000 nm, with a step of 100 nm, and the experimental value is 250 nm. A slight increase in $Y_{CO,m}$ can be seen with the increase of s . However, d_F (range from 0.5 μm to 1.5 μm , step size of 0.2 μm) has the smallest effect on $Y_{CO,m}$. From Eqn. (S7.4) and (S7.5), A_s is inversely proportional to r_2 , while M is proportional to r_2 . Thus smaller r_2 leads to larger A_s and smaller M , which are two effects that positively enhance $Y_{CO,m}$. The effect of s on A_s is not monotonic, because A_s of the cone increases with the increase of s , while A_s of the cylinder decreases with the increase of s . Taking together the effect of s on M (increasing s leads to decreasing M), $Y_{CO,m}$ shows a monotonic positive relationship with s , which suggests that the effect of M plays a dominant role. Eqn. (7.7) and Eqn. (S7.5) show that both g and M increase with increasing d_F . In Figure 7.6(e), $Y_{CO,m}$ increases with a decrease of d_F , but the effect of d_F on $Y_{CO,m}$ is not significant, which means that the effect of g balances the effect of M .

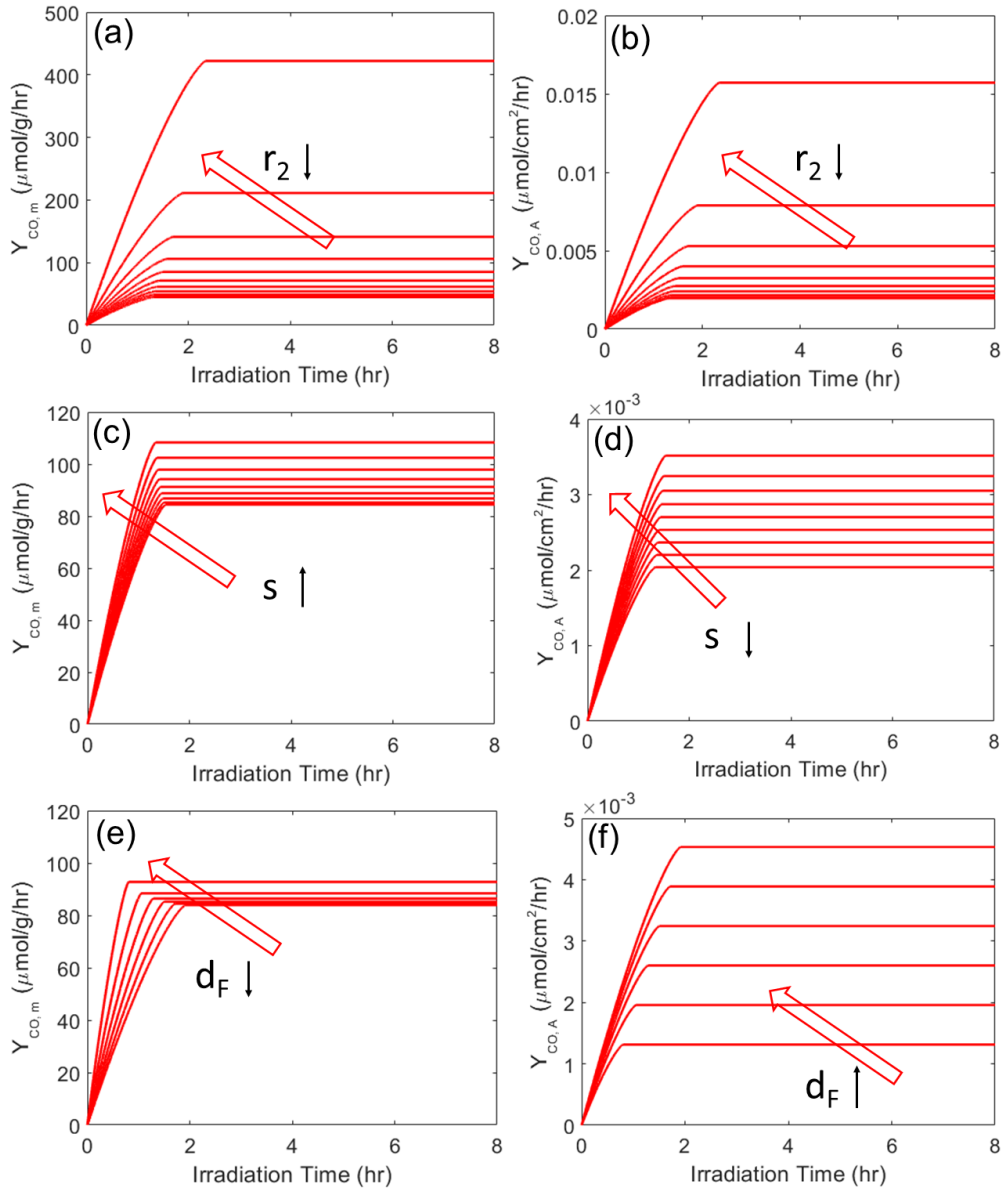


Figure 7.6 Model predictions for columnar TiO₂ thin films. (a) $Y_{CO,m}$ and (b) $Y_{CO,A}$ as a function of a radius of the single column (r_2); (c) $Y_{CO,m}$ and (d) $Y_{CO,A}$ as a function of the top cone taper length (s); (e) $Y_{CO,m}$ and (f) $Y_{CO,A}$ as a function of the thickness of the film (d_F).

With respect to $Y_{CO,A}$, a similar trend for the effect of r_2 , and an opposite trend for the effects of s and d_F are observed. Columnar TiO₂ thin films with different values of those parameters have the same A_L . Therefore, the effect of M , which is considered in

discussing $Y_{CO,m}$, can be neglected here. $Y_{CO,A}$ increases with a decrease of r_2 , which is due to the increasing of A_s with the decrease of r_2 . $Y_{CO,A}$ also increases with a decrease of s , because a smaller s leads to a larger A_s of the cylinder part, and thus to a larger total A_s . The difference between $Y_{CO,A}$ and $Y_{CO,m}$ with different d_F is the most significant: A larger d_F leads to a larger g , and a higher $Y_{CO,A}$.

Because these structural parameters of the columnar TiO₂ thin films can have similar or opposite effects on $Y_{CO,A}$ and $Y_{CO,m}$, it is proper to report both $Y_{CO,A}$ and $Y_{CO,m}$ when comparing the photocatalytic capabilities of different catalysts, which have not always been reported.²⁷⁻²⁸ Thus, in designing catalysts, we need to carefully choose the optimal parameters based on whether $Y_{CO,A}$ and $Y_{CO,m}$ is more important in a specific case. In most cases, higher A_s can enhance both $Y_{CO,A}$ and $Y_{CO,m}$. Therefore, to obtain a better performing columnar TiO₂ thin film, decreasing the radius of a single column is quite important.

7.4.4.2 Dense film

Figure 7.7(a) and (b) present $Y_{CO,m}$ and $Y_{CO,A}$ as a function of the thickness of dense TiO₂ thin films, d_F , respectively. The range of d_F is from 0.1 μm to 1.2 μm , with a step size of 0.2 μm . $Y_{CO,m}$ increases, but $Y_{CO,A}$ decreases with decreasing d_F . In most cases, the $Y_{CO,m}$ of dense films is predicted to be much lower compared than that of the columnar films used in the experiment, except for the case where $d_F = 0.1 \mu\text{m}$. The reason could be the much lower specific surface area of the dense film than that of the columnar film with the same thickness. However, if the dense film is thin enough (thinner than 0.1 μm), $Y_{CO,m}$ is predicted to increase greatly, which accounts for why a nano thin film is desirable.

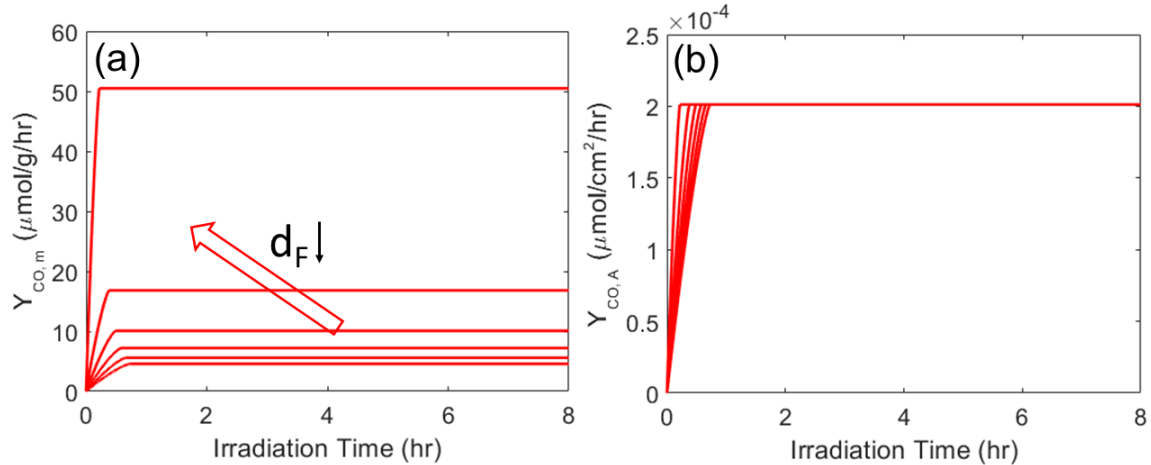


Figure 7.7 Model prediction for dense TiO₂ thin films. (a) $Y_{CO,m}$ and (b) $Y_{CO,A}$ as a function of the thickness of the film (d_F).

When the effect of M is not considered, $Y_{CO,A}$ shows very similar trend with different d_F . As discussed for columnar thin films, a larger d_F leads to a larger total generation rate of electrons and holes, g . However, A_s also increases with an increase in d_F . These two counterfactors together can result in a much smaller difference in $Y_{CO,A}$ with different d_F than that for the case of columnar films. Thus, in designing dense thin film, making it thinner is more effective in terms of $Y_{CO,m}$, and more material saving in terms of $Y_{CO,A}$.

7.4.4.3 Granular film

The values of $Y_{CO,m}$ and $Y_{CO,A}$ of granular films as a function of primary particle size, d_p , and the thickness of the film, d_F , are shown in Figure 7.8(a) and (b), and (c) and (d). Both $Y_{CO,m}$ and $Y_{CO,A}$ increase significantly with a decrease in d_p (the range from 30 nm to 100 nm, with a step size of 10 nm), which is mainly due to the increase of A_s caused by the decrease in d_p . Because compact packing is assumed, M is a function of d_F only, and A_L is a constant for different d_p . Therefore, $Y_{CO,m}$ and $Y_{CO,A}$ show similar trends with

respect to d_p . As for the effect of d_F , $Y_{CO,m}$ is almost the same for different d_F values, while $Y_{CO,A}$ increases with an increase in d_F . Because Eqn. (S7.10) and Eqn. (S7.11) show the linear relationship between A_s , M , and d_F , the increase of $Y_{CO,m}$ due to the increase of A_s is neutralized by the decrease of $Y_{CO,m}$ due to the increase of M , causing no observable change, despite different d_F .

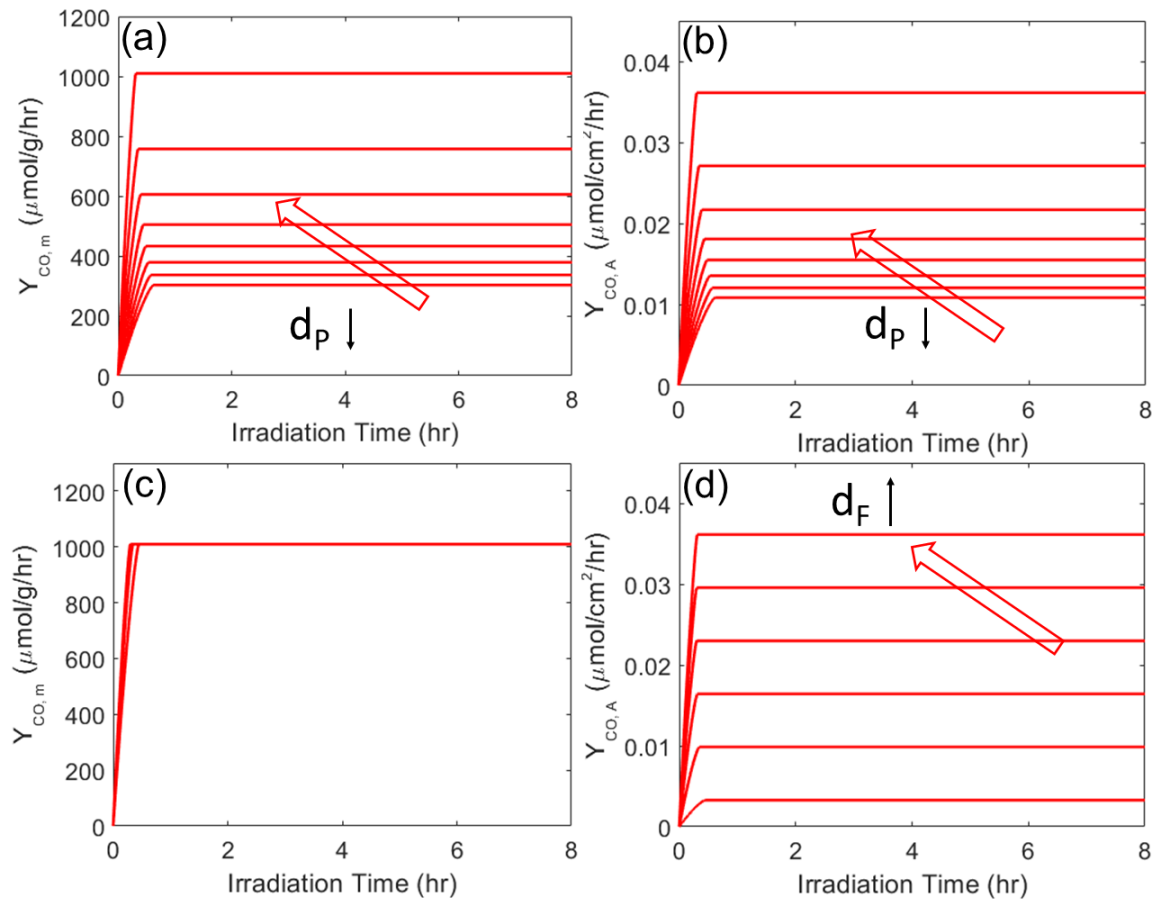


Figure 7.8 Model prediction for granular TiO₂ thin films. (a) $Y_{CO,m}$ and (b) $Y_{CO,A}$ as a function of a radius of the primary particle diameter (d_p); (c) $Y_{CO,m}$ and (d) $Y_{CO,A}$ as a function of the thickness of the film (d_F).

However, when considering $Y_{CO,A}$, because only the effect of d_F on A_s is counted, $Y_{CO,A}$ clearly shows a positive relationship with d_F (range from 0.1 μm to 1.1 μm , with a step size of 0.2 μm). Notably, this model prediction for granular films has several biases.

First, diffusion limitations of reactants and products, which are neglected in this model, need to be taken into account in a real situation, especially as d_F increases. In addition, aggregation of the particles cannot be avoided; therefore, A_s is not linearly and positively related to d_F . Both factors could significantly affect the real $Y_{CO,m}$ and $Y_{CO,A}$. Overall, a smaller d_p and d_F are preferred to obtain a larger A_s and lower diffusion resistance, and thus a higher $Y_{CO,m}$.

7.5 Conclusions

A simple kinetic model was developed to describe gas-phase CO₂ photoreduction in a continuous flow reactor. The optical absorption coefficient and the reaction rate constants were determined by experimental measurements and model fitting. Predictions of the CO yields as a function of the morphology parameters of the TiO₂ thin films were made and discussed. $Y_{CO,m}$ and $Y_{CO,A}$ can show similar or different trends. The results showed that a larger surface area and a smaller thickness usually result in a larger $Y_{CO,m}$. However, a smaller thickness can usually cause a smaller $Y_{CO,A}$. Diffusion limitations need to be considered for further improvement of the model.

Acknowledgements

Y.N. thanks the McDonnell International Scholars Academy and the McDonnell Academy Global Energy and Environment Partnership (MAGEEP) for partial support of this work and through a fellowship to pursue a Ph.D. at Washington University in St. Louis.

References

1. Meinshausen, M.; Smith, S. J.; Calvin, K.; Daniel, J. S.; Kainuma, M.; Lamarque, J.-F.; Matsumoto, K.; Montzka, S.; Raper, S.; Riahi, K., *Clim. Change* **2011**, 109 (1-2), 213.
2. Raupach, M. R.; Marland, G.; Ciais, P.; Le Quéré, C.; Canadell, J. G.; Klepper, G.; Field, C. B., *Proc. Natl. Acad. Sci. U. S. A.* **2007**, 104 (24), 10288-10293.
3. Barnosky, A. D.; Hadly, E. A.; Bascompte, J.; Berlow, E. L.; Brown, J. H.; Fortelius, M.; Getz, W. M.; Harte, J.; Hastings, A.; Marquet, P. A., *Nature* **2012**, 486 (7401), 52.
4. Wang, W.; Wang, S.; Ma, X.; Gong, J., *Chem. Soc. Rev.* **2011**, 40 (7), 3703-3727.
5. Indrakanti, V. P.; Kubicki, J. D.; Schobert, H. H., *Energy Environ. Sci.* **2009**, 2 (7), 745-758.
6. Inoue, T.; Fujishima, A.; Konishi, S.; Honda, K., *Nature* **1979**, 277 (5698), 637-638.
7. Usubharatana, P.; McMartin, D.; Veawab, A.; Tontiwachwuthikul, P., *Industrial & engineering chemistry research* **2006**, 45 (8), 2558-2568.
8. Fujishima, A.; Zhang, X.; Tryk, D. A., *Surf. Sci. Rep.* **2008**, 63 (12), 515-582.
9. Linsebigler, A. L.; Lu, G.; Yates Jr, J. T., *Chem. Rev.* **1995**, 95 (3), 735-758.
10. Carp, O.; Huisman, C. L.; Reller, A., *Prog. Solid State Chem.* **2004**, 32 (1), 33-177.
11. Mao, J.; Ye, L.; Li, K.; Zhang, X.; Liu, J.; Peng, T.; Zan, L., *Appl. Catal., B* **2014**, 144, 855-862.
12. Peral, J.; Domenech, X.; Ollis, D. F., *J. Chem. Technol. Biotechnol.* **1997**, 70 (2), 117-140.
13. Sclafani, A.; Palmisano, L.; Schiavello, M., *J. Phys. Chem.* **1990**, 94 (2), 829-832.
14. Almquist, C. B.; Biswas, P., *J. Catal.* **2002**, 212 (2), 145-156.
15. Dijkstra, M.; Panneman, H.; Winkelman, J.; Kelly, J.; Beenackers, A., *Chem. Eng. Sci.* **2002**, 57 (22-23), 4895-4907.
16. Manassero, A.; Zacarías, S. M.; Satuf, M. L.; Alfano, O. M., *Chem. Eng. J.* **2016**, 283, 1384-1391.
17. An, W.-J.; Thimsen, E.; Biswas, P., *J. Phys. Chem. Lett.* **2009**, 1 (1), 249-253.
18. An, W.-J.; Jiang, D. D.; Matthews, J. R.; Borrelli, N. F.; Biswas, P., *J. Mater. Chem.* **2011**, 21 (22), 7913-7921.
19. Wang, W.-N.; An, W.-J.; Ramalingam, B.; Mukherjee, S.; Niedzwiedzki, D. M.; Gangopadhyay, S.; Biswas, P., *J. Am. Chem. Soc.* **2012**, 134 (27), 11276-11281.

20. Nie, Y.; Wang, W.-N.; Jiang, Y.; Fortner, J.; Biswas, P., *Catal. Sci. Technol.* **2016**, 6 (16), 6187-6196.
21. Lin, L.-Y.; Nie, Y.; Kavadiya, S.; Soundappan, T.; Biswas, P., *Chem. Eng. J.* **2017**, 316, 449-460.
22. Kelly, J.; Vanmaekelbergh, D., *Electrochim. Acta* **1998**, 43 (19-20), 2773-2780.
23. Butler, M., *J. Appl. Phys.* **1977**, 48 (5), 1914-1920.
24. Jacques, I. P., by Prentice-Hall. Englewood Cliffs. Inc. New Jersey, (1ed) **1971**, 87.
25. Chang, H.-C.; Wang, L.-C., *arXiv preprint arXiv:1009.4322* **2010**.
26. Gauß, C. F., *Göttingische Gelehrte Anzeigen* **1831**, 2, 188-196.
27. Wang, W.-N.; Wu, F.; Myung, Y.; Niedzwiedzki, D. M.; Im, H. S.; Park, J.; Banerjee, P.; Biswas, P., *ACS Appl. Mater. Interfaces* **2015**, 7 (10), 5685-5692.
28. Li, Y.; Wang, W.-N.; Zhan, Z.; Woo, M.-H.; Wu, C.-Y.; Biswas, P., *Appl. Catal., B* **2010**, 100 (1), 386-392.

Chapter 7 Supporting Information

Table of Contents

S7.1 Calculation of irradiation area, surface area and total mass of the TiO₂ thin films with different morphologies.

S7.1 Calculation of irradiation area, surface area and total mass of the TiO₂ thin films with different morphologies.

(1) Columnar film

We assume compact packing for all the thin films with a radius of r_1 (1 inch for all the samples), so A_L is a constant for all the columnar films:

$$A_L = \eta_1 \pi r_1^2. \quad (S7.1)$$

The surface area of a single column is the sum of the surface area of the top cone and the bottom cylinder, a_s :

$$a_s = \pi r_2^2 + 2\pi r_2 \left(d_F - \sqrt{s^2 - r_2^2} \right). \quad (S7.2)$$

The mass of a single column is the sum of the mass of the top cone and the bottom cylinder, \dot{m} (mg):

$$\dot{m} = \left[\frac{1}{3} \pi r_2^2 \sqrt{s^2 - r_2^2} + \pi r_2^2 \left(d_F - \sqrt{s^2 - r_2^2} \right) \right] \rho, \quad (S7.3)$$

where ρ is the density of the TiO₂ material, $mg\ m^{-3}$.

Then A_s and M are respectively the product of a_s and the total number of columns N , and the product of \dot{m} and N :

$$A_s = a_s N = a_s \frac{\eta_1 r_1^2}{r_2^2}, \quad (S7.4)$$

$$M = \dot{m} N = \eta_1 \pi r_1^2 \left(d_F - \frac{2}{3} \sqrt{s^2 - r_2^2} \right) \rho. \quad (S7.5)$$

(2) Dense film

$$A_L = \pi r_1^2, \quad (S7.6)$$

$$A_s = \pi r_1^2 + 2\pi r_1 d_F, \quad (S7.7)$$

$$M = \pi r_1^2 d_F \rho. \quad (S7.8)$$

(3) Granular film

$$A_L = \eta_1 \pi r_1^2, \quad (\text{S7.9})$$

$$A_s = \frac{6\eta_2 \pi r_1^2 d_F}{d_p}, \quad (\text{S7.10})$$

$$M = \eta_2 \pi r_1^2 d_F \rho, \quad (\text{S7.11})$$

Chapter 8 Conclusions and Future Directions

8.1 Conclusions

This dissertation focused on the synthesis and engineering of crumpled graphene and TiO₂ based novel materials, the investigation of their chemical and physical properties, and their application to CO₂ photoreduction. Conclusions drawn from this work are applicable in such fields as aerosol processing of materials and morphological design of photocatalysts.

The major conclusions from this dissertation can be categorized by three aspects, corresponding to the objectives in the Introduction.

1. An experimental method to synthesize CGO nanoparticles was described and their mobility and charging characteristics were systematically investigated. Crumpled graphene formed as a by-product in a NASA plasma reactor was characterized and used in Li-ion batteries.

(1) The projected area equivalent diameter was found to be approximately equal to the electrical mobility diameter for the CGO particles, regardless of their morphology. DMA can be employed as a convenient and efficient tool to classify CGO particles according to their physical diameters. This classification is advantageous when the application of CGO nanoparticles requires a uniform size and structure distribution, such as in membranes and solar cell assembly.

(2) In the charging characteristics study, Fuch's theory fits the experimental data better than the Boltzmann's theory for most of the measured charging fractions, indicating that the conductivity of CGO particles plays an important role in affecting their charging characteristics. CGO particles synthesized at 400 °C provided the highest charging fraction,

which may be a result of higher particle conductivity, resulting from the thermal reduction of CGO under the optimal temperature.

(3) The carbon material formed as a side product in a NASA plasma reactor for methane post-processing was characterized as crumpled graphene with a low oxygen content and only a few layers in thickness. This crumpled graphene material was used to synthesize the anodes of LIBs, which showed high electrochemical performance. Considering the high electrochemical performance of the crumpled graphene LIBs, our study provided an interesting possibility for recycling this by-product and better supporting long-duration space missions.

2. N-modified graphene-TiO₂ nanocomposites and defective TiO₂ thin films were synthesized and tested for enhanced CO₂ photoreduction.

(4) CGOATI nanocomposites were synthesized by a one-step aerosol technique to enable simultaneous CO₂ adsorption and photoreduction. The 3D structure largely prevented the crumpled graphene nanosheets from restacking by minimizing π - π interactions, thus enhancing the stability of the catalyst by retaining its higher surface area. A combination of a 20% mass percentage of TiO₂/GO, a 15:1 mass ratio of EDA/GO in precursor solution, and a 200 °C synthesis temperature led to the highest CO yield (65 $\mu\text{mol/g/h}$, with a quantum efficiency of 0.0094%), which was two-fold higher than that of crumpled reduced GO-TiO₂ (CGOTI) and four-fold higher than that of TiO₂ alone. The enhancement of CO₂ photoreduction was attributed to higher CO₂ adsorption on the amine-functionalized reduced-GO (r-GO) surface and the strong electron trapping capability of r-GO.

(5) A series of TiO₂/nitrogen doped reduced graphene oxide (TiO₂/NrGO) nanocomposites with varying concentrations and bonding configurations of nitrogen were synthesized by a one-step urea-assisted hydrothermal method, and were used for CO₂ photoreduction. TiO₂/NrGO-300, with a 300:1 mass ratio of urea/GO in precursor solution had the highest CO production yield (356.5 μmole g⁻¹), manifesting significant 4.4- and 2.2-fold enhancements of CO yield over pure TiO₂ and TiO₂/rGO, respectively. TiO₂/NrGO showed excellent catalytic stability during the prolonged reaction, but catalytic deactivation was observed for both pristine TiO₂ and TiO₂/rGO after a few hours. It was demonstrated that NrGO with an appropriate N quantity and N-bonding configuration acted as a dual-functional promoter, simultaneously enhancing CO₂ adsorption on the catalyst surface and facilitating electron-hole separation, and eventually boosting the photocatalytic performance.

(6) Oxygen vacancies and Ti-related defects (OTDs) were generated in columnar titanium dioxide (TiO₂) thin film under UV irradiation with electric potential. The defective TiO₂ (TiO_{2-x}) showed a significant enhancement in CO₂ photoreduction. The best performing sample showed a highest CO yield of 375 μmol/g/hr, with an apparent quantum efficiency of 0.045%, which was about 4 times higher than that without potential (95 μmol/g/hr). A recyclability test demonstrated the reversibility of the OTDs in CO₂ photoreduction, with or without electric potential. The enhancement of the TiO_{2-x} in CO₂ photoreduction with electric potential can be attributed to 1) the narrowed band gap energy, 2) the enhanced chemical adsorption of CO₂, and 3) the better separation of electrons and holes.

3. A kinetic model of gas-phase CO₂ photoreduction over TiO₂ thin films in a continuous flow reactor was developed and used for the predictions of CO₂ photoreduction of TiO₂ with different morphology parameters.

(7) A kinetic model of gas-phase CO₂ photoreduction over TiO₂ thin films in a continuous flow reactor was developed based on mechanistic steps, including the photo-generation of electrons and holes, the adsorption of the reactants on the surface of the thin films, and the reaction kinetics. Reaction rate constants in the model were obtained by fitting the model with the experimental data.

(8) The CO₂ photoreduction performances of the TiO₂ thin films with different morphology parameters were predicted using the kinetic model with the calculated reaction rate constants. Both catalyst-mass-based and irradiation-area-based CO yields were discussed. The results of this study elucidate the strong effect of morphology parameters on photoactivity. This study offers new insights for designing the morphology of highly efficient CO₂ photoreduction catalysts.

8.2 Future directions

8.2.1 Material synthesis

(1) The scale-up of the photocatalysts is a very important step, to increase their applicability. For crumpled graphene, a better design of the geometry of the tube furnace is needed to decrease the loss of particles passing through the tube. For TiO₂ thin films, in the ACVD process, a movable and flexible substrate and multi-nozzles can be employed to synthesize large-size TiO₂ thin films with a more uniform height distribution.

(2) For the defect engineering of metal oxide materials, only TiO₂ thin films were tested. It is worth trying to apply a similar electric-potential-UV-induced technique for

other metal oxide based photocatalysts. The optimal synthesis conditions and the long-cycle recyclability of these defective TiO₂ films can be further investigated.

(3) Because the decay in CO₂ photoreduction performance can usually be observed for many different types of photocatalyst, a systematic study of the reason for decay and the effects that affect the decay rate is needed. Regeneration methods for photocatalyst are also worth investigating.

(4) The design of hybridized catalysts that can use normal solar irradiation for CO₂ photoreduction would fundamentally advance the CO₂ photoreduction technique beyond lab-scale, into pilot-scale or even full scale.

8.2.2 CO₂ Photocatalytic mechanisms

(5) An in-situ FTIR system can be used for a better understanding of changes of functional groups during the CO₂ photoreduction process. A multi-channel GC can be employed to measure different types of CO₂ photoreduction products, at the same time, such as small-molecule products (e.g., CH₄ and CO) and possibly large-molecule products (e.g., methanol and ethanol). With these new tools, detailed CO₂ photocatalytic mechanisms can be investigated. Design of photocatalysts for specific products can be next step.

8.2.3 Model development

(6) Adding diffusion limitations of both reactants and products into the kinetic model will provide a better description of the real reaction conditions. The effects of CGO can be also considered, enabling the model to predict the CO₂ photoreduction performance of hybridized materials.

(7) With a better understanding of CO₂ photocatalytic mechanisms, adding reactions of all possible CO₂ photoreduction products into the model will improve the capability to predict the possible products over catalysts with different morphology parameters.

**Appendix A. MATLAB Code of the Kinetic Modeling of the CO₂
photoreduction over TiO₂ thin films**

A.1 Obtaining the model coefficients by fitting the model with experimental data

```
function ypred = pred8p(Coef)

stepsize = 0.001;
ypred = nan(8, 1);

y = 0;

for iStep = 1:int64(8/stepsize)

    slope = sqrt(Coef(1) * (Coef(2) - y) * (Coef(2) * Coef(3)
- y) + Coef(4) * sqrt(Coef(2) - y)) - sqrt(Coef(1) * (Coef(2)
- y) * (Coef(2) * Coef(3) - y));
    y = min(Coef(2), y + stepsize * slope);

    if mod(iStep, 1/stepsize) == 0
        ypred(int64(iStep * stepsize)) = y;
    end

end

function S = TargetFuc(Coef)

ypred = pred8p(Coef);

ydata = [
65.51737
80.74518
93.6772
96.81575
86.69536
81.25374
83.40424
74.03216
];

S = sum((ydata - ypred).^2);
end

clearvars; close all; clc;
```

```

nTrial = 100;
Coef_history = nan(4, nTrial);
sse_history = nan(1, nTrial);
ypred_history = nan(8, nTrial);

xdata = 0:8;

ydata = [
65.51737
80.74518
93.6772
96.81575
86.69536
81.25374
83.40424
74.03216
];

ydata_error = [
38.20064
41.24189
12.67875
31.50165
25.40887
52.6466
29.17962
31.54275
];

for iTrial = 1:nTrial

disp(iTrial)

Coef0 = rand(4,1) * 100;

options = optimset('MaxIter',1e12);
[Coef, fval] = fmincon(@TargetFuc, Coef0, [], [], [], [], [0,
70, 1, 0], [Inf, 100, Inf, Inf], [], options);

Coef_history(:, iTrial) = Coef;
sse_history(:, iTrial) = fval;

ypred_history(:, iTrial) = pred8p(Coef);

end

best_ind = find(sse_history == min(sse_history));

```

```

figure(1)
clf
errorbar(xdata, [0; ydata], [0; ydata_error/2], 'b')
hold on
plot(xdata, ypred_history(:, 71), 'r')
axis([0 9 0 120])

plot(Coef_history(:,best_ind), Coef_history(:,75))
[~, pos_order] = sort(sse_history)
log10(sort(sse_history))

Coef_history(:, 71)'

Coef      =      [1.79776093123739e-07;      85.2317535717502;
1.05899273091047; 621.943276461112];

ypred = [0; pred8p(Coef)];

close all
figure(1)
errorbar(xdata, [0; ydata],[0; ydata_error], '-
s','MarkerSize', 10, ...
'MarkerEdgeColor','blue','MarkerFaceColor','blue',
'LineWidth', 2)
hold on
plot(xdata, ypred, 'r', 'LineWidth', 2)
set(gca, 'FontSize', 16)
legend({'Experimental', 'Model'}, 'FontSize',14)
legend('boxoff')
xlabel('Irradiation Time (hr)', 'FontSize',16)
ylabel('Y_{\fontsize{10}CO, m} (\mumol/g/hr)',
'FontSize',16)
axis([0 9 0 180])

```

A.2 Predictions of the CO yield of the TiO₂ films with different morphologies

A.2.1 Columnar film

A.2.1.1 Effect of the radius of a single column (r₂) and the top cone taper length (s)

```
clearvars; close all; clc;

load('simulation_data.mat')

% cut lambda2 and I at 900
I_lambda2 = I_lambda2(~(lambda2 > 900));
lambda2 = lambda2(~(lambda2 > 900));

I_lambda = interp1(lambda2, I_lambda2, lambda1, 'linear');
T_lambda = T_lambda1;
lambda_wavelength = lambda1;

clearvars -except I_lambda T_lambda lambda_wavelength

figure(1)
semilogy(lambda_wavelength, [T_lambda, I_lambda]);

%% data & general paras

% packing factor for circle and sphere
packingf_2d = 0.9069;
packingf_3d = 0.74048;

% data
r1 = 2.54e+4; % substrate size
height = 1.1; %
r2_expr = 0.125;
s_expr = 0.250;
AreaSur_expr = (pi * r2_expr * s_expr + 2 * pi * r2_expr *
(height - sqrt(s_expr^2 - r2_expr^2))) * r1^2 * packingf_2d
/ r2_expr^2;
AreaLig_expr = pi * r1^2 * packingf_2d;
M_expr = pi * r1^2 * packingf_2d * (height - 2 / 3 *
sqrt(s_expr^2 - r2_expr^2));

%% columnar structure - fixed height

dF_range = height;
```

```

r2_range = 0.025: 0.025: 0.3;
s_range = 0.05: 0.1 : 1;

AreaLig_col = nan(numel(r2_range), numel(s_range));
AreaSur_col = nan(numel(r2_range), numel(s_range));
M_col = nan(numel(r2_range), numel(s_range));

for i_r2 = 1:numel(r2_range)
    for i_s = 1:numel(s_range)
        if s_range(i_s) >= r2_range(i_r2)
            AreaLig_col(i_r2, i_s) = pi * r1^2 * packingf_2d;
            AreaSur_col(i_r2, i_s) = ...
                (pi * r2_range(i_r2) * s_range(i_s) + ...
                 2 * pi * r2_range(i_r2) * (dF_range -
sqrt(s_range(i_s)^2 - r2_range(i_r2)^2))) ...
                 * r1^2 * packingf_2d / r2_range(i_r2)^2;
            M_col(i_r2, i_s) = pi * r1^2 * packingf_2d *
(dF_range - 2 / 3 * sqrt(s_range(i_s)^2 - r2_range(i_r2)^2));
        end
    end
end
clearvars i_r2 i_s

g_integral_store = nan(numel(dF_range), 1);

for i_dF = 1:numel(dF_range)
    dF = dF_range(i_dF);

    alpha_lambda = log(1./T_lambda)./dF;

    g_lambda = I_lambda .* alpha_lambda .* exp(-alpha_lambda
.* dF);

    begin_wavelength_idx = find(lambda_wavelength == 250);
    end_wavelength_idx = find(lambda_wavelength == 380);

    g_lambda_height = nan(end_wavelength_idx -
begin_wavelength_idx, 1);
    for iStep = begin_wavelength_idx:(end_wavelength_idx -
begin_wavelength_idx)
        g_lambda_height(iStep) = ...
            (g_lambda(iStep) + g_lambda(iStep + 1)) / 2;
    end
end

```

```

        g_integral          =          sum(g_lambda_height          .*
diff(lambda_wavelength(begin_wavelength_idx:end_wavelength_
idx)));
        g_integral_store(i_dF) = g_integral;
end

g_integral_store = ones(numel(r2_range), numel(s_range)) *
g_integral_store;

AS_ratio = AreaSur_col./ AreaSur_expr;
AL_ratio = AreaLig_col./ AreaLig_expr;
g_expr = g_integral_store(dF_range == 1.1);
g_ratio = g_integral_store / g_expr;
M_ratio = M_col / M_expr;

% plot the effect by changing r2_range and s_range
xdata = 0:8;
ydata = [
    0
    65.51737
    80.74518
    93.6772
    96.81575
    86.69536
    81.25374
    83.40424
    74.03216
];

Coef_fit = [1.79776093123739e-07;    85.2317535717502;
1.05899273091047; 621.943276461112];

ypred_store = nan(size(ydata, 1), numel(r2_range),
numel(s_range));
ypred_store_Madjust = nan(size(ydata, 1), numel(r2_range),
numel(s_range));

for i_r2 = 1:numel(r2_range)
    for i_s = 1:numel(s_range)
        if s_range(i_s) >= r2_range(i_r2)

            Coef(1) = Coef_fit(1) * AS_ratio(i_r2, i_s)^2; %
C1

            Coef(4) = Coef_fit(4) * AS_ratio(i_r2, i_s) *
AL_ratio(i_r2, i_s) * g_ratio(i_r2, i_s); % C2

            Coef(2) = Coef_fit(2) * AS_ratio(i_r2, i_s); % K1

```

```

        Coef(3) = Coef_fit(3) * Coef(2); % K2

        ypred = [0; pred8p(Coef)];

        ypred_store(:, i_r2, i_s) = ypred;
        ypred_store_Madjust(:, i_r2, i_s) =
ypred/M_ratio(i_r2, i_s);
    end
end
end

```

```

figure(2)
plot(0:8, squeeze(real(ypred_store_Madjust(:, :, s_range ==
0.25))), 'r', 'LineWidth', 2)
xlabel('Irradiation Time (hr)', 'FontSize', 16)
ylabel('Y_{\fontsize{10}CO, m} (\mumol/g/hr)',
'FontSize', 16)
axis([0 8 0 500])
set(gca, 'FontSize', 16)

```

```

figure(3)
plot(0:8, squeeze(real(ypred_store_Madjust(:, r2_range ==
0.125, :))), 'r', 'LineWidth', 2)
xlabel('Irradiation Time (hr)')
ylabel('Mass-Based CO Yield (\mumol/g/hr)')
xlabel('Irradiation Time (hr)', 'FontSize', 16)
ylabel('Y_{\fontsize{10}CO, m} (\mumol/g/hr)',
'FontSize', 16)
axis([0 8 0 120])
set(gca, 'FontSize', 16)

```

```

ydata_surf = ydata * 0.7 * 10 ^ (-3) / (AreaLig_expr / 10 ^
8);
ypred_store_surf = ypred_store * 0.7 * 10 ^ (-3) ./
(AreaLig_expr / 10 ^ 8);

```

```

figure(4)
plot(0:8, squeeze(real(ypred_store_surf(:, :, s_range ==
0.25))), 'r', 'LineWidth', 2)
xlabel('Irradiation Time (hr)')
ylabel('Y_{\fontsize{10}CO, A} (\mumol/cm^{\fontsize{10}2}/hr)')
axis([0 8 0 2e-2])
set(gca, 'FontSize', 16)

```

```

figure(5)

```



```

plot(0:8, squeeze(real(ypred_store_surf(:, r2_range ==
0.125, :))), 'r', 'LineWidth', 2)
xlabel('Irradiation Time (hr)')
ylabel('Y_{\fontsize{10}CO, A}
(\mumol/cm^{\fontsize{10}2}/hr)')
axis([0 8 0 4e-3])
set(gca, 'FontSize', 16)

```

A.2.1.2 Effect of the thickness of the film (d_f)

```

clearvars; close all; clc;

load('simulation_data.mat')

% cut lambda2 and I at 900
I_lambda2 = I_lambda2(~(lambda2 > 900));
lambda2 = lambda2(~(lambda2 > 900));

I_lambda = interp1(lambda2, I_lambda2, lambda1, 'linear');
T_lambda = T_lambda1;
lambda_wavelength = lambda1;

clearvars -except I_lambda T_lambda lambda_wavelength

figure(1)
semilogy(lambda_wavelength, [T_lambda, I_lambda]);

%% data & general paras

% packing factor for circle and sphere
packingf_2d = 0.9069;
packingf_3d = 0.74048;

% data
r1 = 2.54e+4; % substrate size
height = 1.1; %
r2_expr = 0.125;
s_expr = 0.250;
AreaSur_expr = (pi * r2_expr * s_expr + 2 * pi * r2_expr *
(height - sqrt(s_expr^2 - r2_expr^2))) * r1^2 * packingf_2d
/ r2_expr^2;
AreaLig_expr = pi * r1^2 * packingf_2d;
M_expr = pi * r1^2 * packingf_2d * (height - 2 / 3 *
sqrt(s_expr^2 - r2_expr^2));

%% columnar structure - fixed r2 and s

```

```

dF_range = 0.5:0.2:1.5;
AreaSur_col = (pi * r2_expr * s_expr + 2 * pi * r2_expr *
(dF_range - sqrt(s_expr^2 - r2_expr^2))) * r1^2 * packingf_2d
/ r2_expr^2;
AreaLig_col = pi * r1^2 * packingf_2d * ones(size(dF_range));
M_col = pi * r1^2 * packingf_2d * (dF_range - 2 / 3 *
sqrt(s_expr^2 - r2_expr^2));

g_integral_store = nan(numel(dF_range), 1);

for i_dF = 1:numel(dF_range)
    dF = dF_range(i_dF);

    alpha_lambda = log(1./T_lambda)./dF;

    g_lambda = I_lambda .* alpha_lambda .* exp(-alpha_lambda
.* dF);

    begin_wavelength_idx = find(lambda_wavelength == 250);
    end_wavelength_idx = find(lambda_wavelength == 380);

    g_lambda_height = nan(end_wavelength_idx -
begin_wavelength_idx, 1);
    for iStep = begin_wavelength_idx:(end_wavelength_idx -
begin_wavelength_idx)
        g_lambda_height(iStep) = ...
            (g_lambda(iStep) + g_lambda(iStep + 1)) / 2;
    end

    g_intergral = sum(g_lambda_height .*
diff(lambda_wavelength(begin_wavelength_idx:end_wavelength_
idx)));
    g_integral_store(i_dF) = g_intergral;
end

AS_ratio = AreaSur_col./ AreaSur_expr;
AL_ratio = AreaLig_col./ AreaLig_expr;
g_expr = g_integral_store(dF_range == 1.1);
g_ratio = g_integral_store / g_expr;
M_ratio = M_col / M_expr;

% plot the effect by change dF_range
xdata = 0:8;
ydata = [
    0
    65.51737

```

```

80.74518
93.6772
96.81575
86.69536
81.25374
83.40424
74.03216
];

Coef_fit = [1.79776093123739e-07; 85.2317535717502;
1.05899273091047; 621.943276461112];

ypred_store = nan(size(ydata, 1), numel(dF_range));
ypred_store_Madjust = nan(size(ydata, 1), numel(dF_range));

for i_dF = 1:numel(dF_range)

    disp(i_dF)
    Coef(1) = Coef_fit(1) * AS_ratio(i_dF)^2; % C1
    Coef(4) = Coef_fit(4) * AS_ratio(i_dF) * AL_ratio(i_dF)
* g_ratio(i_dF); % C2

    Coef(2) = Coef_fit(2) * AS_ratio(i_dF); % K1
    Coef(3) = Coef_fit(3) * Coef(2); % K2

    ypred = [0; pred8p(Coef)];

    ypred_store(:, i_dF) = ypred;
    ypred_store_Madjust(:, i_dF) = ypred / M_ratio(i_dF);

end

figure(2)
plot(xdata, ypred_store_Madjust, 'r','LineWidth', 2)
xlabel('Irradiation Time (hr)', 'FontSize',16)
ylabel('Y_{\fontsize{10}CO, m} (\mumol/g/hr)',
'FontSize',16)
axis([0 8 0 120])
set(gca, 'FontSize', 16)

ydata_surf = ydata * 0.7 * 10 ^ (-3) / (AreaLig_expr / 10 ^
8);
ypred_store_surf = ypred_store * 0.7 * 10 ^ (-3) ./
(AreaLig_expr / 10 ^ 8);

figure(3)
plot(xdata, ypred_store_surf, 'r','LineWidth', 2)

```

```
xlabel('Irradiation Time (hr)', 'FontSize',16)
ylabel('Y_{\fontsize{10}CO,
(\mumol/cm^{\fontsize{10}2}/hr)')
axis([0 8 0 5e-3])
set(gca, 'FontSize', 16)
```

A}

A.2.2 Dense film

A.2.2.1 Effect of the thickness of the film (d_F)

```
clearvars; close all; clc;

load('simulation_data.mat')

% cut lambda2 and I at 900
I_lambda2 = I_lambda2(~(lambda2 > 900));
lambda2 = lambda2(~(lambda2 > 900));

I_lambda = interp1(lambda2, I_lambda2, lambda1, 'linear');
T_lambda = T_lambda1;
lambda_wavelength = lambda1;

clearvars -except I_lambda T_lambda lambda_wavelength

figure(1)
semilogy(lambda_wavelength, [T_lambda, I_lambda]);

%% data & general paras

% packing factor for circle and sphere
packingf_2d = 0.9069;
packingf_3d = 0.74048;

% data
r1 = 2.54e+4; % substrate size
height = 1.1; %
r2_expr = 0.125;
s_expr = 0.250;
AreaSur_expr = (pi * r2_expr * s_expr + 2 * pi * r2_expr *
(height - sqrt(s_expr^2 - r2_expr^2))) * r1^2 * packingf_2d
/ r2_expr^2;
AreaLig_expr = pi * r1^2 * packingf_2d;
M_expr = pi * r1^2 * packingf_2d * (height - 2 / 3 *
sqrt(s_expr^2 - r2_expr^2));

%% dense film
```

```

dF_range = 0.1:0.2:1.2;
AreaLig_dense = ones(1, numel(dF_range)) * pi * r1^2;
AreaSur_dense = pi * r1^2 + 2 * pi * r1 * dF_range;
M_dense = pi * r1^2 * dF_range;

g_integral_store = nan(numel(dF_range), 1);

for i_dF = 1:numel(dF_range)
    dF = dF_range(i_dF);

    alpha_lambda = log(1./T_lambda)./dF;

    g_lambda = I_lambda .* alpha_lambda .* exp(-alpha_lambda
.* dF);

    begin_wavelength_idx = find(lambda_wavelength == 250);
    end_wavelength_idx = find(lambda_wavelength == 380);

    g_lambda_height = nan(end_wavelength_idx -
begin_wavelength_idx, 1);
    for iStep = begin_wavelength_idx:(end_wavelength_idx -
begin_wavelength_idx)
        g_lambda_height(iStep) = ...
            (g_lambda(iStep) + g_lambda(iStep + 1)) / 2;
    end

    g_intergral = sum(g_lambda_height .*
diff(lambda_wavelength(begin_wavelength_idx:end_wavelength_
idx)));
    g_integral_store(i_dF) = g_intergral;
end

AS_ratio = AreaSur_dense./ AreaSur_expr;
AL_ratio = AreaLig_dense./ AreaLig_expr;
g_expr = g_integral_store(dF_range == 1.1);
g_ratio = g_integral_store / g_expr;
M_ratio = M_dense / M_expr;

% plot the effect by change dF_range
xdata = 0:8;
ydata = [
    0
    65.51737
    80.74518
    93.6772
    96.81575
    86.69536

```

```

81.25374
83.40424
74.03216
];

Coef_fit = [1.79776093123739e-07; 85.2317535717502;
1.05899273091047; 621.943276461112];
ypred_store = nan(size(ydata, 1), numel(dF_range));
ypred_store_Madjust = nan(size(ydata, 1), numel(dF_range));

for i_dF = 1:numel(dF_range)

    Coef(1) = Coef_fit(1) * AS_ratio(i_dF)^2; % C1
    Coef(4) = Coef_fit(4) * AS_ratio(i_dF) * AL_ratio(i_dF)
* g_ratio(i_dF); % C2

    Coef(2) = Coef_fit(2) * AS_ratio(i_dF); % K1
    Coef(3) = Coef_fit(3) * Coef(2); % K2

    ypred = [0; pred8p(Coef)];

    ypred_store(:, i_dF) = ypred;
    ypred_store_Madjust(:, i_dF) = ypred / M_ratio(i_dF);

end

figure(2)
clf
plot(xdata, ypred_store_Madjust, 'r','LineWidth', 2)
xlabel('Irradiation Time (hr)', 'FontSize',16)
ylabel('Y_{\fontsize{10}CO, m} (\mumol/g/hr)',
'FontSize',16)
axis([0 8 0 60])
set(gca, 'FontSize', 16)

ydata_surf = ydata * 0.7 * 10 ^ (-3) / (AreaLig_expr / 10 ^
8);
ypred_store_surf = ypred_store * 0.7 * 10 ^ (-3) ./
(AreaLig_dense / 10 ^ 8);

figure(3)
clf
plot(xdata, ypred_store_surf, 'r','LineWidth', 2)
xlabel('Irradiation Time (hr)', 'FontSize',16)
ylabel('Y_{\fontsize{10}CO, A}
(\mumol/cm^{\fontsize{10}2}/hr)', 'FontSize',16)
axis([0 8 0 0.25e-3])

```

```
set(gca, 'FontSize', 16)
```

A.2.3 Granular film

A.2.2.1 Effect of the diameter of the primary particle (d_p) and the thickness of the film

(dF)

```
clearvars; close all; clc;

% lambda1 = xlsread('simulation data.xlsx', 'Sheet2',
'A2:A1302');
% % var(diff(lambda1)), 0, setpsize = 0.5
% T_lambda1 = xlsread('simulation data.xlsx', 'Sheet2',
'E2:E1302');
% % plot(lambda1, T_lambda1)
%
% lambda2 = xlsread('simulation data.xlsx', 'Sheet2',
'G2:G702');
% % var(diff(lambda2)), % 0, setpsize = 1
% I_lambda2 = xlsread('simulation data.xlsx', 'Sheet2',
'H2:H702');
% % plot(lambda2, I_lambda2)
%
% save('simulation_data.mat')

load('simulation_data.mat')

% cut lambda2 and I at 900
I_lambda2 = I_lambda2(~(lambda2 > 900));
lambda2 = lambda2(~(lambda2 > 900));

I_lambda = interp1(lambda2, I_lambda2, lambda1, 'linear');
T_lambda = T_lambda1;
lambda_wavelength = lambda1;

clearvars -except I_lambda T_lambda lambda_wavelength

figure(1)
semilogy(lambda_wavelength, [T_lambda, I_lambda]);

%% data & general paras

% packing factor for circle and sphere
packingf_2d = 0.9069;
packingf_3d = 0.74048;
```

```

% data
r1 = 2.54e+4; % substrate size
height = 1.1; %
r2_expr = 0.125;
s_expr = 0.250;
AreaSur_expr = (pi * r2_expr * s_expr + 2 * pi * r2_expr *
(height - sqrt(s_expr^2 - r2_expr^2))) * r1^2 * packingf_2d
/ r2_expr^2;
AreaLig_expr = pi * r1^2 * packingf_2d;
M_expr = pi * r1^2 * packingf_2d * (height - 2 / 3 *
sqrt(s_expr^2 - r2_expr^2));

%% particle

dF_range = (1:2:12)*0.1;
dP_range = 0.03:0.01:0.1;
AreaLig_particle = ones(numel(dF_range), numel(dP_range)) *
pi * r1^2 * packingf_2d;
AreaSur_particle = nan(numel(dF_range), numel(dP_range));
for i_dF = 1:numel(dF_range)
    for i_dP = 1:numel(dP_range)
        AreaSur_particle(i_dF, i_dP) = 6 * dF_range(i_dF) *
pi * r1^2 * packingf_3d / dP_range(i_dP);
    end
end

M_particle = pi * r1^2 * dF_range * packingf_3d;

g_integral_store = nan(numel(dF_range), 1);

for i_dF = 1:numel(dF_range)
    dF = dF_range(i_dF);

    alpha_lambda = log(1./T_lambda)./dF;
    % plot(lambda_wavelength, alpha_lambda)

    g_lambda = I_lambda .* alpha_lambda .* exp(-alpha_lambda
.* dF);
    % plot(lambda_wavelength, [I_lambda, g_lambda])

    begin_wavelength_idx = find(lambda_wavelength == 250);
    end_wavelength_idx = find(lambda_wavelength == 380);

    g_lambda_height = nan(end_wavelength_idx -
begin_wavelength_idx, 1);

```



```

    for iStep = begin_wavelength_idx:(end_wavelength_idx -
begin_wavelength_idx)
        g_lambda_height(iStep) = ...
            (g_lambda(iStep) + g_lambda(iStep + 1)) / 2;
    end

    g_intergral = sum(g_lambda_height .*
diff(lambda_wavelength(begin_wavelength_idx:end_wavelength_
idx)));
    g_integral_store(i_dF) = g_intergral;
end

AS_ratio = AreaSur_particle./ AreaSur_expr;
AL_ratio = AreaLig_particle./ AreaLig_expr;
g_expr = g_integral_store(dF_range == 1.1);
g_ratio = g_integral_store / g_expr;
M_ratio = M_particle / M_expr;

% plot the effect by change dF_range
xdata = 0:8;
ydata = [
    0
    65.51737
    80.74518
    93.6772
    96.81575
    86.69536
    81.25374
    83.40424
    74.03216
];

% Coef_fit = [1.02882859264177e-08; 85.2323044060049;
635.162186435740; 624.312408023546];
Coef_fit = [1.79776093123739e-07; 85.2317535717502;
1.05899273091047; 621.943276461112];
ypred_store = nan(size(ydata, 1), numel(dF_range),
numel(dP_range));
ypred_store_Madjust = nan(size(ydata, 1), numel(dF_range),
numel(dP_range));

for i_dF = 1:numel(dF_range)
    disp(i_dF)
    for i_dP = 1:numel(dP_range)

        Coef(1) = Coef_fit(1) * AS_ratio(i_dF, i_dP)^4; % C1
    end
end

```

```

    Coef(4) = Coef_fit(4) * AS_ratio(i_dF, i_dP)^3 *
AL_ratio(i_dF, i_dP) * g_ratio(i_dF); % C2

    Coef(2) = Coef_fit(2) * AS_ratio(i_dF, i_dP); % K1
    Coef(3) = Coef_fit(3) * Coef(2); % K2

    ypred = [0; pred8p(Coef)];

    ypred_store(:, i_dF, i_dP) = ypred;
    ypred_store_Madjust(:, i_dF, i_dP) = ypred /
M_ratio(i_dF);

    end
end

figure(2)
plot(0:8, squeeze(real(ypred_store_Madjust(:, :, dP_range ==
0.03))), 'r', 'LineWidth', 2)
xlabel('Irradiation Time (hr)', 'FontSize', 16)
ylabel('Y_{\fontsize{10}CO, m} (\mumol/g/hr)',
'FontSize', 16)
%legend({'Model'}, 'FontSize', 14)
%legend('boxoff')
axis([0 8 0 1300])
set(gca, 'FontSize', 16)

figure(3)
plot(0:8, squeeze(real(ypred_store_Madjust(:, dF_range ==
1.1, :))), 'r', 'LineWidth', 2)
xlabel('Irradiation Time (hr)', 'FontSize', 16)
ylabel('Y_{\fontsize{10}CO, m} (\mumol/g/hr)',
'FontSize', 16)
%legend({'Model'}, 'FontSize', 14)
%legend('boxoff')
axis([0 8 0 1200])
set(gca, 'FontSize', 16)

ydata_surf = ydata * 0.7 * 10 ^ (-3) / (AreaLig_expr / 10 ^
8);
ypred_store_surf = ypred_store * 0.7 * 10 ^ (-3) ./
(AreaLig_expr / 10 ^ 8);

figure(4)
plot(0:8, squeeze(real(ypred_store_surf(:, :, dP_range ==
0.03))), 'r', 'LineWidth', 2)
xlabel('Irradiation Time (hr)', 'FontSize', 16)

```

```

ylabel('Y_{\fontsize{10}CO,                                     A}
(\mumol/cm^{\fontsize{10}2}/hr)', 'FontSize',16)
%legend({'Model'}, 'FontSize',14)
%legend('boxoff')
axis([0 8 0 0.04])
set(gca, 'FontSize', 16)

figure(5)
plot(0:8, squeeze(real(ypred_store_surf(:, dF_range == 1.1,
:))), 'r', 'LineWidth', 2)
xlabel('Irradiation Time (hr)', 'FontSize',16)
ylabel('Y_{\fontsize{10}CO,                                     A}
(\mumol/cm^{\fontsize{10}2}/hr)', 'FontSize',16)
%legend({'Model'}, 'FontSize',14)
%legend('boxoff')
axis([0 8 0 0.04])
set(gca, 'FontSize', 16)

```

Appendix B. Curriculum Vitae

Curriculum Vitae

Yao Nie

EDUCATION

Washington University in St. Louis, MO, USA Ph.D. Energy, Environmental and Chemical Engineering	2013-2018
Washington University in St. Louis, MO, USA M.S Energy, Environmental and Chemical Engineering	2013-2017
Tsinghua University, Beijing, China B.E. Environmental Engineering	2009-2013
Tsinghua University, Beijing, China B.S. Economics	2010-2013

HONORS AND AWARDS

McDonnell Fellowship, Washington University in St. Louis, US	2013-2018
Travel Grant, American Association for Aerosol Research Conference	2015
Distinguished Graduate Award (Top 5%), Tsinghua University, China	2013
Distinguished Undergraduate Thesis, Tsinghua University, China	2013
Hach Water Quality Scholarship (Top 1), Hach Company, US	2012
Outstanding Research Scholarship, <i>Tsinghua University, China</i>	2012
Boeing Scholarship, <i>Boeing Company, US</i>	2012
Veolia outstanding creative integrated scholarship, <i>Veolia Environment Company, France</i>	2012
Veolia excellent research individual, <i>Veolia Environment Company, France</i>	2012
3 rd Award in the 7 th National Environmental-Friendly Technology Competition	2012
Second Prize in the 30 th Challenge Cup, Tsinghua University, China	2012
National Scholarship for Excellent Students, Ministry of Education, China	2011
First Prize Integrated Scholarship, Meishang International Group, China	2010

PUBLICATIONS

1. **Nie, Yao**, Clayton Kacica, Marit E. Meyer, Robert D. Green, and Pratim Biswas. "Graphene Synthesized as By-Product of Gas Purification in Long-term Space Missions and its Lithium-ion Battery Application." Submitted to *Advances in*

- Space Research*, 62 (2018): 1015-1024.
2. Lin, Liang-Yi, Shalinee Kavadiya, Bedia Begum Karakocak, **Yao Nie**, Ramesh Raliya, Steven T. Wang, Mikhail Y. Berezin and Pratim Biswas. "ZnO_{1-x}/Carbon Dots Composite Hollow Spheres: Facile Aerosol Synthesis and Superior CO₂ Photoreduction under UV, Visible and Near-Infrared Irradiation." *Applied Catalysis B: Environmental* 230 (2018): 36-48.
 3. **Nie, Yao**, Yang Wang, and Pratim Biswas. "Mobility and Bipolar Diffusion Charging Characteristics of Crumpled Reduced Graphene Oxide Nanoparticles Synthesized in a Furnace Aerosol Reactor." *The Journal of Physical Chemistry C* 121.19 (2017): 10529-10537.
 4. Lin, Liang-Yi, **Yao Nie**, Shalinee Kavadiya, Thiagarajan Soundappan, and Pratim Biswas. "N-doped Reduced Graphene Oxide Promoted Nano TiO₂ as A Bifunctional Adsorbent/Photocatalyst for CO₂ Photoreduction: Effect of N Species." *Chemical Engineering Journal* 316 (2017): 449-460.
 5. **Nie, Yao**, Wei-Ning Wang, Yi Jiang, John Fortner, and Pratim Biswas. "Crumpled Reduced Graphene Oxide–Amine–Titanium Dioxide Nanocomposites for Simultaneous Carbon Dioxide Adsorption and Photoreduction." *Catalysis Science & Technology* 6 (2016): 6187-6196. (**Back cover paper**)
 6. Jiang, Yi, Wei-Ning Wang, Di Liu, **Yao Nie**, Wenlu Li, Jiewei Wu, Fuzhong Zhang, Pratim Biswas, and John D. Fortner. "Engineered Crumpled Graphene Oxide Nanocomposite Membrane Assemblies for Advanced Water Treatment Processes." *Environmental science & technology* 49, no. 11 (2015): 6846-6854.
 7. Deng, Shubo, **Yao Nie**, Ziwen Du, Qian Huang, Pingping Meng, Bin Wang, Jun Huang, and Gang Yu. "Enhanced Adsorption of Perfluorooctane Sulfonate and Perfluorooctanoate by Bamboo-derived Granular Activated Carbon." *Journal of hazardous materials* 282 (2015): 150-157.
 8. **Nie, Yao**, Shubo Deng, Bin Wang, Jun Huang, and Gang Yu. "Removal of Clofibric Acid from Aqueous Solution by Polyethylenimine-modified Chitosan Beads." *Frontiers of Environmental Science & Engineering* 8, no. 5 (2014): 675-682.
 9. Wei, Haoran, Shubo Deng, Qian Huang, **Yao Nie**, Bin Wang, Jun Huang, and Gang Yu. "Regenerable Granular Carbon Nanotubes/Alumina Hybrid Adsorbents for Diclofenac Sodium and Carbamazepine Removal from Aqueous Solution." *Water research* 47, no. 12 (2013): 4139-4147.
 10. Deng, Shubo, Qiaoying Zhang, **Yao Nie**, Haoran Wei, Bin Wang, Jun Huang, Gang Yu, and Baoshan Xing. "Sorption Mechanisms of Perfluorinated Compounds on Carbon Nanotubes." *Environmental pollution* 168 (2012): 138-144.
 11. **Nie, Yao**, John D. Fortner, and Pratim Biswas. "Applied Potential to Substrate to Induce Formation of Defects in Columnar TiO₂ Single Crystals under UV

Irradiation for Enhanced CO₂ Photoreduction.” In preparation.

12. **Nie, Yao** and Pratim Biswas. “A Kinetic Model of Gas-Phase Photoreduction of CO₂ over TiO₂ Thin Films with Different Morphologies in A Continuous Flow Reactor.” In preparation.
13. An Siyuan, Jiewei Wu, **Yao Nie**, and John Fortner. “Photoenhanced Transformation of Graphene Oxide by Free Chlorine: Reaction Kinetics and Product Characterization.” In preparation.
14. Hu, Yanjie, Nan Xu, Yang Wang, **Yao Nie**, Yi Jiang, Pratim Biswas, and Chunzhong Li. “Anatase Porous TiO₂ Microspheres: Aerosol Spray Pyrolysis Synthesis and Tailored Photocatalytic Activity.” In preparation.

SELECTED PRESENTATIONS (Presenter with *)

1. **Nie, Y.***, Lin, L. Y., Wang, W. N., Biswas, P., Role of nitrogen addition to reduced graphene oxide-TiO₂ nanocomposites in enhancing CO₂ photoreduction, The AIChE Conference, Minneapolis, MN, October 29-November 3, 2017.
2. **Nie, Y.***, Biswas, P., Synthesis of crumpled graphene oxide-based materials and their energy related applications, The AIChE Conference, Minneapolis, MN, October 29-November 3, 2017. (Poster)
3. **Nie, Y.***, Lin, L. Y., Wang, W. N., Fortner, J. D., Biswas, P., Role of nitrogen addition to reduced graphene oxide-TiO₂ nanocomposites in enhancing CO₂ photoreduction, Mid-America Environmental Engineering Conference, Washington University in St. Louis, St. Louis, MO, October 7th, 2017.
4. Kavadiya, S.*, **Nie, Y.**, Biswas, P., Determination of mass mobility exponent and fractal dimension of crumpled graphene oxide synthesized in furnace aerosol reactor, The 36th AAAR Annual Conference, Raleigh, NC, October 16-20, 2017.
5. **Nie, Y.***, Wang, Y., Jiang, Y., Biswas, P., Mobility and charging characteristics of crumpled reduced graphene oxide synthesized by aerosol process, The 34th AAAR Annual Conference, Minneapolis, MN, October 12-16, 2015. (Poster)
6. **Nie, Y.***, Wang, W. N., Jiang, Y., Fortner J. D., Biswas, P., Aminated reduced graphene oxide-titanium dioxide nanocomposites (AGOTi) for carbon dioxide capture and photoreduction, The 33rd AAAR Annual Conference, Orlando, FL, October 21-24, 2014
7. Jiang, Y.*, Wang, W. N., Liu, D., **Nie, Y.**, Li, W., Wu, J., Zhang, F., Biswas, P., Fortner, J. D., Engineered crumpled graphene oxide nanocomposite membrane assemblies for advanced water treatment processes. Mid-America Environmental Engineering Conference, Missouri University of Science and Technology, Rolla, MO, November 15th, 2014
8. Jiang, Y.*, Wang, W. N., **Nie, Y.**, An, S., Biswas, P., Fortner, J. D., Engineered crumpled graphene nanocomposites for photocatalytic environmental reduction

applications. The 248th ACS National Meeting, San Francisco, CA, August 10-14, 2014

9. Jiang, Y.*, **Liu, D.**, Wang, W. N., **Nie, Y.**, Li, W., Wu, J., Zhang, F., Biswas, P., Fortner, J. D., Crumpled graphene oxide nanocomposites for multifunctional water treatment membrane structures. The 248th ACS National Meeting, San Francisco, CA, August 10-14, 2014

JOURNAL REVIEW ACTIVITY

Journal of Aerosol Science, RSC Advances, New Journal of Chemistry, Desalination and Water Treatment, and Nanomaterials and Nanotechnology